

Supercell electrostatics of charged defects in periodic density functional theory

Thomas Robert Durrant

A dissertation submitted in partial fulfillment
of the requirements for the degree of
Doctor of Philosophy
of
University College London.

Department of Physics and Astronomy
University College London
Gower street, London, WC1E 6BT

October 21, 2019

I, Thomas Robert Durrant, confirm that the work presented in this thesis is my own. Where information has been derived from other sources, I confirm that this has been indicated in the work.

Abstract

Charged defects are often studied using density functional theory (DFT). However, the use of periodic boundary conditions (PBC) introduces a fictitious jellium background required to maintain charge neutrality, along with periodic images of the defect. As a consequence, the calculations are found to be sensitive to the size of the supercell used. Several competing correction methods have been developed for bulk materials, but do not provide a completely satisfactory solution to this problem.

One source of error in these corrections is suggested to be the simple density models employed. I propose a new electrostatic correction based on calculating electronic charge density differences between reference DFT calculations, and then solving Poisson equation for these charge models. For bulk materials, I demonstrate that this new correction is in agreement with the existing Lany-Zunger (LZ) method. This demonstrates that using more realistic density models is not sufficient to improve the corrections, but the new method does allow an improved understanding of potential alignment. I found that alignment errors are introduced by adding or removing atoms from the supercell to form the defect, and that these errors are related to their atomic radius. Secondly, the charge models I constructed are found to be in good agreement with the predictions of classical electrostatics, corresponding to both bound and free charges. I derive a new analytic charge correction based on this model, but it produces smaller corrections than anticipated.

Further calculations demonstrate that the remaining unexplained finite-size error is introduced by the finite-size dependence of the exchange-correlation energy of the screening bound charge, rather than on electrostatic grounds. Improved empirical corrections are constructed, which display differences between unrelaxed

and relaxed defects. The developed arguments are extended to surface slab models, where the observed errors are found to be dependent on the shape of the supercell employed.

Impact Statement

Within academia, this thesis deals with several topics of fundamental interest. Firstly, the interplay between DFT and classical electrostatics enables an enhanced understanding of dielectric screening in real materials. The results of this thesis demonstrate how classical dielectric screening is achieved quantum mechanically.

The section on Koopmans' theorem (KT) contributes to the growing interest in this area. It seems clear that KT can be leveraged to develop improved hybrid functionals for materials, with better treatment of self interaction errors. However, the accuracy of these methods is damaged if the finite-size errors discussed in this thesis are not understood and corrected. The results of this thesis demonstrate that exchange-correlation plays an important role in the observed finite-size errors, and underlines the requirement that these two problems must be tackled consistently.

Additionally, there is a significant amount of interest in extending our understanding of charged defects to surfaces and 2D materials. It is shown that bound depletion charges are expelled to surfaces in these cases. Methods are developed in order to validate calculated formation energies for these kinds of system, and it is demonstrated that consistent charged defect formation energies can be calculated and compared between bulk and surface calculations. These methods can be developed further in the future in order to understand in more detail the role surfaces may play in stabilizing the formation of charged defects.

Outside of academia, charged defects play an important role in many technological applications, including radiation damage, microelectronics, photovoltaics, catalysts and sensors. As the behavior of many materials in their desired application can be strongly effected by charged defects, understanding their behavior is

Impact Statement

vital in order to bring new materials to market. First principles simulation allows insight into defect properties, but the need to use large supercells in order to produce reliable results can greatly increase the cost of such investigations. The methods developed in this thesis allow smaller supercells to be used reliably, increasing the availability of these calculations to industry.

Acknowledgements

The work presented in this PhD thesis would not have been possible without the contributions of many people. I am especially indebted to my supervisor Prof. Alex Shluger for his constant encouragement and guidance. His enduring support on both a professional and personal level has been key to the completion of my thesis.

I am grateful to group members past and present for the help they have given me. Mathew Watkins, Samuel Murphy, Jack Strand, Julian Gaberle, David Gao, Al-moatasem El-Sayed and Oliver Dicks deserve particular mention.

I would like to thank Phil Hasnip for his help with Castep, in particular for his help in understanding the non-Coulombic energy. Without this key intervention, this project would have gone poorly. I am additionally grateful to Sanliang Ling for his help with cp2k, where his practical guidance has been invaluable.

I would like to acknowledge both the EPSRC and the London Centre for Nanotechnology for their financial support. Additionally, the ARCHER national super-computing service played a key role in enabling this research.

I would also like to thank my friends for keeping my spirits high whilst I was finishing my writing, especially Doug and Esther Hogg, Andrew Crawley, Peter Mansfield, Rachel Haines and Paul Lee. All now know more about crystallographic defects than they were previously aware they wanted.

Finally, I would like to thank my parents and my brother Jack for their constant help and encouragement over the course of my project. Without them I would not be where I am today.

Contents

0.1	List of publications	33
0.2	Mathematical notation	33
0.3	Key terminology	33
1	Introduction	35
1.1	Charged point defects	35
1.2	Thesis outline	39
2	Established theory	42
2.1	Many-body quantum mechanics	42
2.2	Density functional theory	43
2.2.1	Total energy in a planewave basis	44
2.2.1.1	Electrostatic terms and charged systems	47
2.2.2	Planewave basis	49
2.2.3	Brillouin zone sampling	49
2.2.4	Gaussian planewave basis	50
2.2.5	Exchange-Correlation functionals	51
2.2.5.1	LDA functional	51
2.2.5.2	PBE functional	51
2.2.5.3	PBEsol functional	52
2.2.5.4	PBE0 functional	52
2.2.5.5	Auxiliary density matrix method	53
2.2.5.6	PBE0_TC_LRC functional	54
2.2.6	Koopmans' theorem	55

2.3	Density functional perturbation theory	56
2.4	Supercell defect formation energies	56
2.4.1	Known finite-size scaling rules	57
3	Defect electrostatics in the bulk	59
3.1	Electrostatic corrections	59
3.1.1	The method of Makov and Payne	59
3.1.1.1	Energy of a point charge	61
3.1.1.2	Original derivation of the MP method	61
3.1.2	The method of Dabo, Kozinsky, Singh-Miller and Marzari	63
3.1.3	The method of Lany and Zunger	64
3.1.4	The method of Freysoldt, Neugebauer and Van de Walle	66
3.1.5	The method of Taylor and Bruneval	67
3.1.6	The method of Murphy and Hine	68
3.1.7	The method of Kumagai and Oba	69
3.1.8	Discussion of present bulk methods	69
3.1.8.1	Usage of present methods	70
4	Development of the DEFECT_SOLVER code	71
4.1	Electrostatic corrections	71
4.1.1	Definition of electrostatic corrections	71
4.1.2	Extension to dielectric materials	72
4.1.3	Electrostatic libraries: PSPFFT	74
4.1.4	Electrostatic libraries: DL_MG	75
4.2	Description of main subroutines	75
4.2.1	get_hartree_isolated	75
4.2.2	get_hartree_periodic	76
4.2.3	get_hartree_isolated_super	77
5	Jellium and potential alignment	80
5.1	The jellium background and DFT	80
5.2	Potential alignment and its causes	83

Contents

5.2.1	Calculating the potential alignment in practice	83
5.2.2	Model system: Gaussian charge in a box	85
5.2.3	A new decomposition of potential alignment	90
5.2.3.1	The ΔV_{AB} component	90
5.2.3.2	The ΔV_{BC} component	92
5.2.3.3	The ΔV_{CD} component	95
5.2.3.4	Discussion of all components	96
5.2.4	Finite-size scaling of the ΔV_{AB} component	98
5.2.5	Model system: classical structureless atom	102
5.2.6	Environment dependence of potential alignment	103
6	Application of methods in the bulk	108
6.1	Overview of bulk calculations	108
6.2	Case study: Vacancies in bulk diamond	110
6.3	Case study: Vacancies in bulk MgO	114
6.4	Case study: Vacancies in bulk SnO ₂	115
6.5	Figures of merit	117
7	Structure of the bound charges	120
7.1	Classical electrostatics	121
7.1.1	Electrostatics in vacuum	121
7.1.2	Electrostatics within a dielectric	122
7.1.3	The multipole expansion	122
7.1.4	The polarization density	123
7.1.5	Ideal problem: Point charge in an infinite dielectric	125
7.1.6	Ideal problem: Point charge in a dielectric sphere	126
7.2	Modeling of the defect charge	128
7.3	Defect charge in the bulk	131
7.4	Calculation of the dielectric constant from the density response	134
7.5	Role of boundary conditions and jellium	135
7.6	New derivations of point charge corrections	137

Contents

7.6.1	Mathematical preliminaries	137
7.6.2	Solution in vacuum	140
7.6.3	Solution in a dielectric medium	141
7.7	Bound surface charges	142
8	Less electrostatic errors	145
8.1	Improving electrostatic models through potential alignment	146
8.2	Further example systems	152
8.3	Applying linear extrapolation	153
8.4	Separating the exchange-correlation energy	158
8.5	Model calculations and the exchange-correlation energy	161
8.6	Parameterizing a new bulk correction	162
8.7	Role of relaxation	164
9	Ionization of surfaces and surface defects	168
9.1	Eigenvalue vs numerical ionization approaches	169
9.2	KT for ionization of the bulk	172
9.3	KT for ionization of surfaces	175
9.3.1	Workfunction dependence on number of layers	175
9.3.2	Workfunction dependence on vacuum gap size	178
9.3.3	Workfunction dependence on cubic volume	180
9.4	KT for charged defects in the bulk	186
9.5	Applying linear extrapolation to surfaces	188
10	Conclusions	195
10.1	General Conclusions	195
10.2	Avenues for future work	197
10.2.1	Hybrid functionals and defect states	198
10.2.2	Role of ionic relaxation for surfaces	200
10.2.3	Comparison with 2D boundary conditions	200
	Bibliography	203

List of Figures

1.1	Several example point defects, using GaAs as an example. The defects are labeled with modified Kröger-Vink notation, as introduced below. Figure by Prof Kai Nordlund, and released into the public domain.	36
1.2	Schematic representation of embedded cluster and supercell approaches to the simulation of point defects. The two approaches have different drawbacks and advantages	38
3.1	A periodic DFT calculation containing a defect is shown on the left, which is used to construct the simplified classical model on the right. The model charge q interacts through a classical dielectric background, represented by the shaded background. The interaction of the classical model is removed from the final formation energy. Two possible models for q are shown in Fig. 3.2.	60
3.2	Comparison of defect charge models for V_O^{+2} defect in MgO. The total charge is plotted in y and z. a) is a model constructed as a charge density difference between two DFT calculations, and b) is a Gaussian model, as commonly used in the FNV method. The zero density isosurface is shown as a solid black line.	65
3.3	Dependence of the LZ correction for cubic supercells on the dielectric constant. When $\epsilon=1$ (i.e. a molecule in vacuum), then the LZ method correctly reduces to the MP method. As the dielectric of the material increases, the LZ correction removes more of the MP correction.	66

List of Figures

- 4.1 Error in the total energy calculated using DEFECT_SOLVER and the PSPFFT library for a Gaussian charge distribution with spread $\sigma = 1.0$ on a $20 \times 20 \times 20$ Å grid, with increasing grid size N . The energy is calculated on a grid with $N \times N \times N$ total points. 76
- 4.2 Comparison between the analytic Madelung correction and the energy correction calculated using a Gaussian charge model in the DEFECT_SOLVER code. The difference between the two calculations tends to zero as the size of the simulation supercell is increased. This is the anticipated result if the code is performing correctly. . . . 77
- 4.3 Error in calculated isolated interaction energy using the GET_HARTREE_ISOLATED_SUPER subroutine, against the GET_HARTREE_ISOLATED method, as the size of the classical simulation region is increased. The error in energy decreases linearly with inverse supercell size. The blue dashed line shows a linear fit to the two largest cells considered. The test example is a defect charge from the $2 \times 2 \times 2$ supercell containing the defect charge model of the unrelaxed V_C^{+1} defect in diamond. 78
- 4.4 Example of a $3 \times 3 \times 3$ simulation region used for the GET_HARTREE_ISOLATED_SUPER method. The orange cube in the middle contains the charge distribution for which Poisson's equation is being solved. The blue cubes contain empty space, and the potential is set to zero at the edges of the composite cube. 79
- 5.1 The difference between the xy-averaged electrostatic potential of a V_C^{-2} defect in a $2 \times 2 \times 2$ diamond supercell (with full ionic relaxation), and an equivalent bulk cell of the same size. The defect is placed at the center of the cubic supercell. A potential difference of zero (denoted by the dotted line) is not recovered far from the defect. For this example, $\Delta V_{q/b} = 0.56$ V. The bulk potential is most strongly modified near to the defect, at the center of the supercell. . . 85
- 5.2 Charge distribution of a Gaussian charge, with $\sigma = 1.0$ Å, at the center of a 40 Å cubic box. 86

- 5.3 The resultant electrostatic potentials of the charge shown in Fig. 5.2, under both PBC and isolated boundary conditions. The shape of the two potentials is very similar, but due to neglect of the average potential, there is a uniform shift ΔV between the two potentials. Even when this shift is removed, the potentials are not identical, due to the interaction of the Gaussian charge with its images in neighboring cells. These interactions tend to zero as the the volume of the cell tends to infinity. 87
- 5.4 Dependence of the electrostatic energies under PBC (blue line) and isolated boundary conditions (orange line), on the size of the cubic supercell containing the charge. Note that application of an electrostatic correction E_{corr} (green dashed line) converts the PBC energy into the isolated energy, as expected. Note that as all the energies are calculated using the DEFECT_SOLVER code, this correction is ideal. 88
- 5.5 Electrostatic errors of various correction strategies, defined as the difference between the PBC energy and the isolated energy calculated using DEFECT SOLVER. The uncorrected results are shown by the blue line. As the size of the cell is increased, the interaction with images decreases, and the error in the uncorrected results reduces. The electrostatic correction shows ideal performance (orange line), but also including a potential alignment (PA) correction makes the results worse. Adding just a potential alignment term produces the green line, and adding both potential alignment and the calculated electrostatic correction produces the red line. 89

- 5.6 Schematic process of forming a charged defect in a periodic DFT calculation. Each lettered square denotes a DFT single-point calculation. In A, the host material is simulated, without a defect. In B, atoms are removed to form a vacancy (or added to form an interstitial), but the ionic structure is not yet relaxed. In C, the final ionic structure of the relaxed charged defect is adopted, but the charge is kept neutral. Finally, in D, electrons are exchanged to reach the required charge state. The ionic geometry in C is maintained, which is the relaxed geometry of this system. Configurations A and D are real states of the system, but B and C are artificial configurations used to break the defect formation process into steps. Only the final configuration D has a formal net charge compensated by a jellium background. The notation given below the figure is chosen to be similar to the conventional notation, but we prefer the alphabetical labels in this paper, to emphasize that we are not only using the conventional reference configurations. 91
- 5.7 Comparison of all the potential delta components of a V_C^{-2} defect in a $2 \times 2 \times 2$ diamond supercell. The ΔV_{AB} component is explored in Fig. 5.8, and the ΔV_{CD} component is explored more detail in Fig. 5.10. For this example, $\Delta V_{AB}=0.32$ V, $\Delta V_{BC}=0.01$ V, and $\Delta V_{CD}=0.23$ V. 92
- 5.8 Comparison between the ΔV_{AB} alignment component of a $2 \times 2 \times 2$ supercell of diamond when a carbon atom is removed, with the potential of a carbon atom placed in an empty periodic cell of the same size. In this example, $\Delta V_{AB}(z=0) = 0.325$ V and $V_{C \text{ atom}}(z=0) = 0.297$ V. 93

- 5.9 Schematic diagram of the approximation of ΔV_{AB} potential alignment component, as in Fig. 5.8. Our results show that this is approximated by a calculation on an isolated atom. This is justified as shown in the diagram, because the crystal appears to play only a secondary role. It changes the electrostatic distribution of charge associated with the atom, but this is a modification rather than a total change in character. The case of an isolated atom is simple enough to attack analytically, and predicts that the potential shift introduced will be volume dependent, as in Eq. 5.13. 93
- 5.10 Comparison of the ΔV_{CD} alignment component of a V_C^{2-} defect in a $2 \times 2 \times 2$ supercell, with the correction potentials constructed. The inset shows a $\times 50$ magnification. 96
- 5.11 Finite-size convergence of the formation energy of the V_O^{+2} defect in MgO, depending on the potential alignment utilized. Results are shown without any correction (UC, blue dashed line) and with the screened Poisson electrostatic correction proposed in Chapter 4 (C, dark green line). Additionally, results also including a potential alignment correction are shown. Using only the ΔV_{AB} component (red line) yields the best finite-size scaling. Additionally including the ΔV_{BC} (cyan line) and ΔV_{CD} (purple line) components appears to make the scaling worse. A dotted line is shown for the result of the screened Poisson correction and ΔV_{AB} potential alignment for the largest supercell, to demonstrate how little size dependence remains in these results. 97

- 5.12 Electrostatic potential of an Sn atom at the center of a 10 Å cubic box, using different pseudopotentials and DFT codes. In solid green, the potential under isolated boundary conditions is shown (only available for CP2K). The blue dashed line shows the potential when periodic boundary conditions are applied. The red dotted line shows the potential alignment predicted from the atomic radius, by the fit in Fig. 5.13. For each individual pseudopotential, the electrostatic potentials are identical in shape for both boundary conditions, but the potential in the periodic system is shifted upwards by ΔV_{atom} . The convention of setting $\langle V \rangle = 0$, introduces this shift ΔV_{atom} far from the atom, as the isolated atom has a non-zero average potential. Equivalently, calculations on atoms using isolated boundary conditions are always correctly referenced to the vacuum level, but this level is shifted within the PBC calculations. From left to right, $V_{\text{atom}} = 0.33, 0.27$ and 0.31 V. 99
- 5.13 Comparison between the potential alignment shift introduced by an isolated atom in a 10 Å cubic box, with the atomic radius of that species. Elements from the same row of the periodic table share the same color. We find the potential alignment constants are dependent on pseudopotential and XC functional used, but that all choices produced similar linear fits, to that shown by the solid black line ($m = 0.097$ V/Å, $c = 0.045$ V). One standard deviation is shown by the dashed black line. Atomic radius is a characteristic of the element, rather than the particular DFT approximations used. 101
- 5.14 Schematic representation of the model atom, as a 2D slice of the 3D sphere. A positively charged red sphere sits inside a larger negatively charged blue sphere. Both spheres are uniformly charged (and overlap inside the red sphere). The origin of our co-ordinate system is placed at the center of the spheres. 102

- 5.15 Example sphere models (upper right), and their observed electrostatic potentials (as given in Eq. 5.15). Total charges of $Q_A = -1$ and $Q_B = 1$ a.u. were employed. For all three figures $R_A = 1.0$ Bohr, and R_B takes a value of 1.0, 4.95 and 9.45 Bohr respectively. It is observed that as the sphere of negative charge is increased in radius that the depth of the total electrostatic potential well increases. Both the total potential, and the individual contributions of the positive and negative charge are shown. 104
- 5.16 Dependence of the calculated average electrostatic potential of the model on the R_B parameter, which is the radius of the outer sphere representing electrons. R_A is held fixed at 1 Bohr. Total charges of $Q_A = -1$ and $Q_B = 1$ a.u. were employed. As R_B is increased, the average potential is observed to also increase. The potentials are averaged over a sphere of radius 9.4 Bohr. 105
- 5.17 The ΔV_{AB} alignment shift introduced by the removal of an oxygen atom from the indicated chemical systems, as related to the Bader charge of the atom. Negative relative charges on the considered oxygen atom are consistent with a reduction in the produced alignment shift. 106
- 5.18 The ΔV_{AB} alignment shift introduced by the removal of a magnesium atom from the indicated chemical systems, as related to the Bader charge of the atom. Positive relative charges on the considered magnesium atom are consistent with an increase in the produced alignment shift. 107

6.1	Formation energy diagrams of the V_C^{+1} defect in diamond. Uncorrected denotes formation energies calculated using Eq. 2.23, without any explicit corrections. ΔV_{AB} denotes results where AB potential alignment has been performed. MP denotes the Makov-Payne correction, SP (screened Poisson) denotes the correction of Eq. 4.1, LZ denotes the Lany-Zunger correction, and FNV denotes the Freysoldt-Neugebauer-van de Walle correction. Additionally, a linear extrapolation from the two best aligned results (red dashed line) and a traditional extrapolation in terms of inverse volume and length is shown (dotted black line).	111
6.2	Formation energy diagrams of the V_C^{+2} defect in diamond. Follows the same notation as Fig. 6.1.	112
6.3	Formation energy diagrams of the V_C^{-1} defect in diamond. Follows the same notation as Fig. 6.1.	112
6.4	Formation energy diagrams of the V_C^{-2} defect in diamond. Follows the same notation as Fig. 6.1.	112
6.5	Formation energy diagrams of the V_O^{+1} defect in MgO. Follows the same notation as Fig. 6.1.	115
6.6	Formation energy diagrams of the V_O^{+2} defect in MgO. Follows the same notation as Fig. 6.1.	115
6.7	Formation energy diagrams of the V_{Sn}^{-4} defect in SnO ₂ . Follows the same notation as Fig. 6.1. This example demonstrates a large ΔV_{AB} alignment term. By eye, it appears that the MP correction is too large in this case, and that the LZ and SP methods are more effective.	117
7.1	Schematic illustration of the charge decomposition introduced in Eq. 7.27. The magnitudes of the charge components are shown below the figure. The localized charges, ρ_q and ρ_s are well localized with respect to the size of the simulation cells.	129

7.2 Defect density components of the V_O^{+1} defect in a $2 \times 2 \times 2$ supercell of MgO. The total defect charge neglecting jellium ($\rho - J$) is shown by the blue line. The defect free charge (ρ_q) is shown by the green line. The screening charge (ρ_s) is shown by the red dotted line, which when smoothed becomes the cyan line. The depletion charge (ρ_d) is shown by the red line. 131

7.3 Defect density components of the V_O^{+1} defect in a $7 \times 7 \times 7$ supercell of MgO. The same notation is used as in Fig. 7.2. 132

7.4 The density overlap (defined in Eq. 7.35) is considered separately for both the defect charge (excluding jellium) and for the defect free charge (defined in Eq. 7.32). The comparisons are made with respect to the densities of the $7 \times 7 \times 7$ supercell, so the overlaps are one by definition for this cell. It can be seen directly that convergence of the defect free charge ρ_q is achieved rapidly, but that convergence of the defect charge $\rho - J$ is slow. From the gradient, it is clear that even in a $7 \times 7 \times 7$ supercell, that a fully converged defect charge has not been achieved. The V_O^{+1} defect in bulk MgO is considered. 133

7.5 Comparison between the inter-supercell and intra-supercell interactions present in an electrostatic correction calculated using the definitions introduced in Eqs. 7.37 and 7.38. 136

7.6 Defect charge models for the unrelaxed V_O^+ defect in MgO slabs. The red markers denote atoms. The charge density is shown in $e\text{\AA}^{-2}$. The models demonstrate a bound surface depletion charge that only weakly depends on the number of layers contained in the model. 143

7.7	Total charges (excluding the jellium background), integrated radially from the defect site. The density shows two regions, firstly a near region $\sim 5 \text{ \AA}$ in radius that is not highly sensitive to the number of layers and which contains approximately $\frac{q}{\epsilon}$ of charge. Secondly, the charge outside this sphere is sensitive to the number of MgO layers in the model, and moves further from the defect as the surface is moved further away. This can be interpreted as the first region containing the screened defect ($\rho_q + \rho_s$), and the second region the surface depletion charge, ρ_d	144
8.1	Comparison between optimized electrostatic model (Eq. 8.4, cyan line) and DFT CD alignment component (green line), for a 1x1x1 supercell of diamond, containing a V_C^+ defect. The model potential is also shown when its average value is not neglected (red line). The change in the XC potential is also shown (dark blue line).	148
8.2	Comparison between optimized electrostatic model and DFT CD alignment component, for a 2x2x2 supercell of diamond, containing a V_C^+ defect. The same notation as in Fig. 8.1 is used.	149
8.3	Comparison between optimized electrostatic model and DFT CD alignment component, for a 3x3x3 supercell of diamond, containing a V_C^+ defect. The same notation as in Fig. 8.1 is used.	149
8.4	Comparison between optimized electrostatic model and DFT CD alignment component, for a 4x4x4 supercell of diamond, containing a V_C^+ defect. The same notation as in Fig. 8.1 is used.	150
8.5	Dependence of calculated optimal value of σ on supercell size for the example of a V_C^+ defect in diamond.	151
8.6	Available analytic approximations to f on electrostatic grounds. Both the Makov-Payne and Lany-Zunger are significantly larger than the electrostatic correction previously derived in this thesis (FS). All three terms reduce to the known Madelung correction at the limit of $\epsilon = 1$ i.e. in the absence of a dielectric.	155

8.7	Finite-size dependence of the formation energy of the unrelaxed V_O^+ defect in MgO. Formation energies are shown using Γ -point sampling (blue), using a Monkhorst-Pack \mathbf{k} -point sampling (orange), using a Monkhorst-Pack \mathbf{k} -point sampling and AB potential alignment (green), the same with the addition of a MP correction (red) and finally when the MP correction is reduced by the calculated f -value (purple).	155
8.8	Finite-size dependence of the formation energy of the unrelaxed V_O^+ defect in CaO. Note the importance of \mathbf{k} -point sampling in reaching a linear regime.	156
8.9	Finite-size dependence of the formation energy of the unrelaxed V_{Cl}^+ defect in KCl. Same notation as Fig. 8.7.	156
8.10	The red points show the extrapolated f values for the different defects considered. The dielectric constants are calculated using DFPT. The calculated defects fall between the predictions of the Makov-Payne and the Lany-Zunger correction. All observed f values are significantly larger than would be predicted by the electrostatic derivation we carried out (yielding Eq. 7.55), here denoted as f^{FS}	157
8.11	Demonstrated f -value size dependence for unrelaxed vacancy defects in MgO and LiF. The points are plotted at the average size of the two supercells that the f -value was evaluated from. The f -values calculated using both potential alignment and \mathbf{k} -point sampling (orange line) and with only \mathbf{k} -point sampling (blue line). The blue dashed lines show the predictions of the MP and LZ methods. An extrapolation is performed according to Eq. 8.6.	158
8.12	Plot of ΔE_{xc} (as defined in Eq. 8.7 against inverse supercell for the unrelaxed V_O^+ defect in MgO using CP2K. The energy term tends to linear behavior for the largest supercells considered.	160

8.13 Exchange-correlation energies of the developed charge models for the V_C^+ defect. The simple model tends to linear error, but the magnitude of the error is too small to explain the XC errors seen in Tab. 8.5. 161

8.14 Dependence of extrapolated f -values on dielectric constant for the +1 vacancy defects, compared against the predictions of the MP and LZ correction methods. All the calculated values fall between the two correction methods, and lie nearer to the MP method. The round markers show the f -value extrapolated using Eq. 8.6, and the squares show the largest supercell calculated. For LiF, KCl, NaCl and MgO, a 5x5x5 supercell was calculated, and the extrapolation only changes the value slightly. For CaO, SrO and C, the largest supercell calculated was 4x4x4, and the extrapolation has a larger impact. 162

8.15 The same data as Fig. 8.14, but plotted against the magnitude of the bound charge. A linear fit to the data is shown, as defined through Eq. 8.8. For this fit, $A = 1.03$ and $B = -0.11$ 163

8.16 Demonstrated f -value size dependence for relaxed vacancy defects in MgO and LiF. An extrapolation according to Eq. 8.6 is shown, but it no longer appears to be reliable. 164

8.17 Observed dependence of f -values on dielectric constant, for both unrelaxed (circles) and relaxed (diamonds) vacancy defects. Due to the lack of a reliable extrapolation, the relaxed defects are expected to display larger errors. 165

8.18 Observed dependence of f -values on magnitude of the bound charge, for both unrelaxed (circles) and relaxed (diamonds) vacancy defects. Due to the lack of a reliable extrapolation, the relaxed defects are expected to display larger errors. Linear fits are shown to both datasets, which display different behavior 166

-
- 9.1 Comparison between the highest occupied molecular orbital ϵ_{homo} and the ionization energy I (Eq. 9.1) for different cubic supercells of MgO. The eigenvalue displays less finite-size dependence compared to the ionization energy. 172
- 9.2 Koopmans' errors calculated for bulk MgO supercells, using the PBE functional. The Koopmans' error is small for all the supercells considered, and does display finite-size dependence. A linear extrapolation to the four largest supercells is shown in red, which predicts a Koopmans' error of 0.0018 eV for an infinite supercell. Addition of an E_{PBC} correction (Eq. 4.5) does reduce the inferred error for larger supercells. 174
- 9.3 Calculated $-E_{PBC}$ corrections calculated from the density differences between a bulk supercell and an equivalent supercell of the same size with an electron removed. The interaction energy is low because the deoccupied state is a negative charge delocalized across the whole cell, immersed in a positive jellium background delocalized across the whole supercell. The similarity of the two charge distributions leads to almost complete screening, with the interaction only present because the bulk state is not perfectly uniform. . . 175
- 9.4 Example surface unit cells in the layers data set. A constant supercell is applied to a model that contains varying numbers of layers, effectively leading to a reduction in vacuum gap as the number of layers increases. A constant 4×4 surface net is maintained across the dataset. 176
- 9.5 Comparison between work function values for the layers dataset using both eigenvalue (Eq. 9.3) and numerical ionisation definitions (Eq 9.4). In blue, the w_ϵ definition quickly converges with respect to the number of MgO layers contained in the model. In contrast, w_I definition converges significantly slower, as shown by the green line. According to both definitions, the monolayer is an outlier. . . . 177

9.6 Koopmans' errors, as defined in Eq. 9.5, for the layers dataset. Addition of a E_{PBC} correction to the numerical ionization energy removes most of the Koopmans' error demonstrated by the dataset. . . . 178

9.7 Example surface unit cells in the gap scan data set. A four layer system is considered in supercells with various vacuum gap sizes. A surface net of 4×4 is maintained across the calculations. The vacuum gap is defined as the extra separation over a bulk supercell, rather than the standard definition of separation between surface layers (using the standard definition yields a non-zero vacuum gap in the bulk case). Hence, vac 0 represents a rectangular bulk supercell. Note that an even number of layers is required to avoid a stacking fault in the bulk limit. 179

9.8 Dependence of the calculated Koopmans' error on the size of the vacuum gap. Uncorrected results (blue line) are contrasted with a periodic correction, E_{PBC} (green line). 180

9.9 Example surface unit cells in the cubic data set. A three layer system is considered in supercells of various sizes, which are always constructed to be cubic. The size of the surface net and the size of the vacuum region increase in lockstep. Observe that this produces vacuum gaps that are smaller than would normally be considered acceptable in the literature. 181

9.10 Calculated workfunctions following the definitions given in Eqs. 9.3 and 9.4. The eigenvalue definition shows very little finite-size dependence, and the total energy definition is mildly concave. The two methods differ in the calculated value of the workfunction by ~ 0.1 eV. 182

-
- 9.11 Koopmans' errors, as defined in Eq. 9.5, for the cubic dataset. Addition of a E_{PBC} correction to the numerical ionization removes the majority of the observed Koopmans' error. Equally, the observed Koopmans' errors are small in comparison to the calculations performed with a large vacuum gap ($> 15 \text{ \AA}$). 183
- 9.12 Calculated electrostatic corrections with respect to inverse supercell size. The form of the curve is quite complex, and does not demonstrate a systematic improvement. The requirement that the correction term tends to zero as $L \rightarrow \infty$ suggests that the correction drops off quite rapidly for larger models. 184
- 9.13 Observed changes in the electronic density as electrons are removed from the cubic slab models, averaged along the y-axis (the surface normal). The three layers of the slab are clearly visible, and as the size of the box is increased, the total amount of charge placed on the surfaces increases. 185
- 9.14 Finite-size dependence of the calculated Koopmans' errors for removal of an electron from an F-center in a bulk MgO supercell. The observed finite-size dependence appears to be dominated by a L^{-1} term. The total error increases with supercell size, saturating at a value of 1.06 eV. Additionally, the Makov-Payne correction well approximates the observed finite-size dependence (the low dielectric of this example yields $f \approx 1$). 187

9.15 Dependence of the formation energy on size of the cubic model employed for a trilayer of MgO. Data is shown only with AB potential alignment (blue line), both with potential alignment and the addition of a fE_{MP} correction (green line), and finally with both AB alignment and the Komsa *et al.* electrostatic correction (orange line). The behavior appears to become linear once large enough cells are considered, and a fit of the Makov-Payne correction to the best two cells yields the shown fit, along with a value of $f = 1.65$, showing enhancement of the finite-size error with respect to the bulk case. 189

9.16 Dependence of the formation energy on size of the cubic model employed for a pentalayer of MgO. Same notation as Fig. 9.15. Linear behaviour is achieved significantly more rapidly than in the trilayer case in Fig. 9.15, but the implied correction is not as large. 190

9.17 Dependence of the formation energy on size of the cubic model employed for a heptalayer of MgO. Same notation as Fig. 9.15. Again, linear scaling is quickly achieved, with a further reduction in the value of f calculated. 191

9.18 Average electrostatic potential (blue line) along the y-axis, for a 8x8x8 cubic supercell containing a heptalayer of MgO. A smoothed electrostatic potential (green line) is also shown. The average value of the potential within the MgO system is inferred as the difference between the smoothed potential in the middle of the vacuum gap and in the middle of the slab model. 192

-
- 9.19 Comparison between formation energies calculated in the bulk, and for layered systems. The dashed lines and squares show the formation energies calculated in the bulk. The round markers show the formation energies calculated for the layered systems. The charged formation energies shown have been corrected with AB potential alignment, and with MP electrostatic corrections, that have been scaled based on a linear fit of f based on the two largest cubic supercells considered. Both the uncorrected formation energies for the F^0 and the corrected values for the F^+ center converge to the bulk values as the number of layers in the model is increased. The formation energies for the charged defects are referenced to the vacuum level, rather than the more typical ϵ_{VBM} 193
- 10.1 Finite-size dependence of the calculated Koopmans' errors for the removal of an electron from the F-centre in a bulk MgO supercell, using the PBE_TC_LRC functional. The observed behavior is qualitatively similar to that seen for the PBE functional in Fig. 9.14, but the limit of the error is significantly reduced. This suggests a improved description of the self interaction error on the state. 199
- 10.2 Gradient in the formation energy with cubic supercell volume. Calculations without XC demonstrate significantly weaker finite-size dependence than calculations including it. There is a change in finite-size scaling moving from PBE to PBE0, but is significantly smaller. In this case, the use of Fock exchange slightly increases the observed finite-size dependence. 200

10.3 Formation energy dependence on supercell shape for an unrelaxed F^+ defect in an MgO trilayer, under two different boundary conditions. On the left, 3D boundary conditions (with ΔV_{AB} alignment) and a cubic supercell are employed. On the right, 2D boundary conditions (an essentially infinite vacuum gap) is utilized. Note that potential alignment is not required in the 2D case, as these calculations are correctly referenced to the vacuum level. A linear fit to the largest three cells is shown for both boundary conditions. The extrapolations approximately agree, but the 2D results have a higher gradient, suggesting that the encountered errors are larger under 2D boundary conditions. Formation energies are referenced to the vacuum level rather than the bulk VBM, and hence are not directly comparable with bulk formation energies. 201

List of Tables

5.1	Pseudopotential dependence of formation energy on the way the E_{NC} is calculated. For the calculation of E_{NC} , Eq. 5.1 was used. In contrast, for E_{NC}^* , this was corrected to multiplication of a factor of $(N_e + q)/\Omega$. The definition of E_{NC} only affects total energies and has no impact on potentials, and hence potential alignment. Standard deviations are shown in the last row. We note that CASTEP incorrectly neglected this component of the jellium energy when we started this project. We ensured that this was corrected in version 16.1.2. of CASTEP	82
5.2	Comparison between alignment constants calculated between configurations A and B, with the potential alignment introduced by an isolated atom of the type being removed. The percentage errors reveal that there is a strong relationship between the alignment constants, but that this is a significant variance. The V_{atom} terms scale ideally with inverse volume. The ΔV_{AB} potential alignment terms retain an approximate inverse volume scaling, but the introduced noise prevents highly accurate extrapolation via Eq. 2.25.	94
5.3	Dependence of the ΔV_{AB} neutral alignment component on pseudopotential, for the example of a $2 \times 2 \times 2$ diamond supercell containing a carbon vacancy.	102

6.1	Energy difference between the two largest supercells considered for all materials and defects considered, that produced cubic supercells. This table is for the unrelaxed defect formation energies. All figures in eV.	118
6.2	Energy difference between the two largest supercells considered for all materials and defects considered, that produced cubic supercells. This table is for the relaxed defect formation energies. All figures in eV.	119
7.1	Comparison of the dielectric constants calculated using DFPT, and by inspection of the defect density via Eq. 7.36, for +1 vacancy defects in $3 \times 3 \times 3$ supercells of the listed materials. The strong agreement between the dielectric constants calculated through the two methods justifies the developed charge model.	135
8.1	Calculated correction energies for the considered diamond supercells containing a V_C^+ defect. The relative error between the correction given by Eq. 7.55, and the energy calculated from the density model in Eq. 8.3 is shown. On electrostatic grounds, the change in the width of the bound screening charge doesn't significantly alter the error expected for large cells.	151
8.2	DFT parameters used to calculate the additional systems. \mathbf{k} -points is the Monkhorst-Pack grid used for the conventional unit cell, and E_{cut} is the cutoff energy of the planewave basis employed. The calculated equilibrium lattice constants are compared with their experimentally reported values.	152
8.3	Comparison between experimentally measured and calculated dielectric properties for the additional systems considered.	153

8.4 Calculated f values for the V_O^+ vacancy in MgO, using respectively both \mathbf{k} -point sampling and AB potential alignment, using Γ -point sampling and AB potential alignment, and using \mathbf{k} -point sampling but neglecting potential alignment. If the finite-size errors were perfectly inverse length dependant, then f would be a constant, independent of cell size. It can be directly observed that the use of both AB potential alignment and \mathbf{k} -point sampling causes the remaining finite-size errors to be significantly closer to ideal linear errors, as the size dependence of f is greatly reduced. 154

8.5 Observed finite-size dependence for unrelaxed +1 vacancy defects in the listed materials. The dielectric constants ϵ_∞ are calculated using DFPT. The f_{elec} values listed are those predicted by Eq. 7.55. The values of f_{xc} and f are determined through the linear extrapolations outlined. Δf is the difference between the extrapolated f and the prediction of $f_{\text{elec}} + f_{\text{xc}}$ 160

0.1 List of publications

The following publication includes work presented in this thesis. I produced the original manuscripts and performed all calculations referenced in the paper.

1. T. R. Durrant, S. T. Murphy, M. B. Watkins and A. L. Shluger, “Relation between image charge and potential alignment corrections for charged defects in periodic boundary conditions”, *J. Chem. Phys.* **149** 024103 (2018)

0.2 Mathematical notation

The following conventions are adopted in this thesis.

$n(\mathbf{r})$		An electron density (typically from DFT)
$\rho(\mathbf{r})$		A classical electrostatic charge density
q		Total charge, either of a defect or a classical charge density
J		A uniform jellium charge density

0.3 Key terminology

The following key terms take on specific meanings in this thesis. Terms marked with an asterisk are not in common usage.

Finite-size error A total energy component that is an artifact of the finite size of the supercell used in a periodic defect calculation. If an infinitely big supercell was used, these energy terms would be zero by definition.

Electrostatic correction A correction to a defect formation energy that attempts to remove finite-size errors introduced by the incorrect features of a supercell model (principally due to the inclusion of a jellium background and periodic images) of a charged defect.

Inter-supercell interaction* That part of an electrostatic correction that represents unwanted finite-size dependent interactions between a defect containing supercell and its periodic images.

Intra-supercell interaction* That part of an electrostatic correction that represents unwanted finite-size dependent interactions within a defect containing supercell.

0.3. KEY TERMINOLOGY

Potential alignment correction A finite-size correction required due to an implicit change in the value of the unknown average potential of a supercell.

Atomic alignment* That part of a potential alignment correction that is introduced by a change in the number of atoms in a supercell.

Electrostatic alignment* That part of a potential alignment correction that is introduced by the same finite-size interactions (principally with a jellium background and with periodic images) included in an electrostatic correction.

Displacement alignment* That part of a potential alignment correction that is caused by long range ionic relaxations within a material. Potential alignment requires a region like the perfect lattice in the defect supercell to be calculated accurately, but long range atomic relaxations can prevent this from being done accurately.

Free charge A fixed charge that is placed within a dielectric medium, which the dielectric is then allowed to respond to.

Bound charge Those charges which are induced within a dielectric as its polarization response to free charges.

Bound screening charge Bound charges that are induced in order to screen a free charge present within the dielectric, producing the observed dielectric screening.

Bound depletion charge Charge conservation requires that bound screening charge has to have been removed from some other part of the supercell. The bound depletion charge is this removed charge.

Chapter 1

Introduction

1.1 Charged point defects

The last century has been marked by an extraordinary pace of technological discovery. The invention of the first semiconductor transistor in 1947 has led to the modern day, where we have smart phones in our pockets that contain billions of transistors. This rapid pace of the technological development of computers has ushered in the information age, where computer technology touches every aspect of our lives and societies.

Semiconductors can be used to make transistors because their electrical conduction can be tailored by addition of defects, a process known as doping. As an example, adding only one boron defect per one hundred thousand atoms in a crystal of pure silicon increases the conductivity one hundred times [1]. By selectively doping silicon, the complex electronic components in modern microelectronics can be built up. In order to have the required degree of control over the defects present, highly pure Silicon is needed, demanding impurity levels below one atom per 10^{10} [2]. The ability to grow crystals of such high purity is one of the main advantages of Silicon based technologies, which are now ubiquitous [3, 4]. Understanding these dopant defects is vital to functionalizing the host semiconductor.

Equally, defects can hinder the performance of devices. One direct example is given by solar cells. There is great interest in the development of cheap and efficient solar cells, as one possible solution to the problem of man-made global

1.1. CHARGED POINT DEFECTS

warming [5]. Solar cells operate on a two step process. First, the absorption of light excites an electron-hole pair, followed by separation of the pair, which yields useful electricity [6]. If the pair is able to recombine before being separated, the solar cell does not function [7]. Defects can act as traps, holding either the electrons or holes in place, and greatly enhancing their chance to recombine [8, 9]. Defects of this type are called recombination centers, and they can badly damage the performance of solar cells [6, 10]. Predicting and controlling these kinds of defects is a clear goal of theory.

This thesis is about point defects. In these defects, the ideal crystal structure of a material is disturbed near a particular lattice point [1, 11]. Typical examples are shown in Fig. 1.1, and normally involve a few extra or missing atoms in the crystal structure. Materials found in nature also contain more extended defects, such as line defects like dislocations, as well as planar defects such as grain boundaries. However I don't consider extended defects in this thesis, and when I refer to defects I always mean point defects.

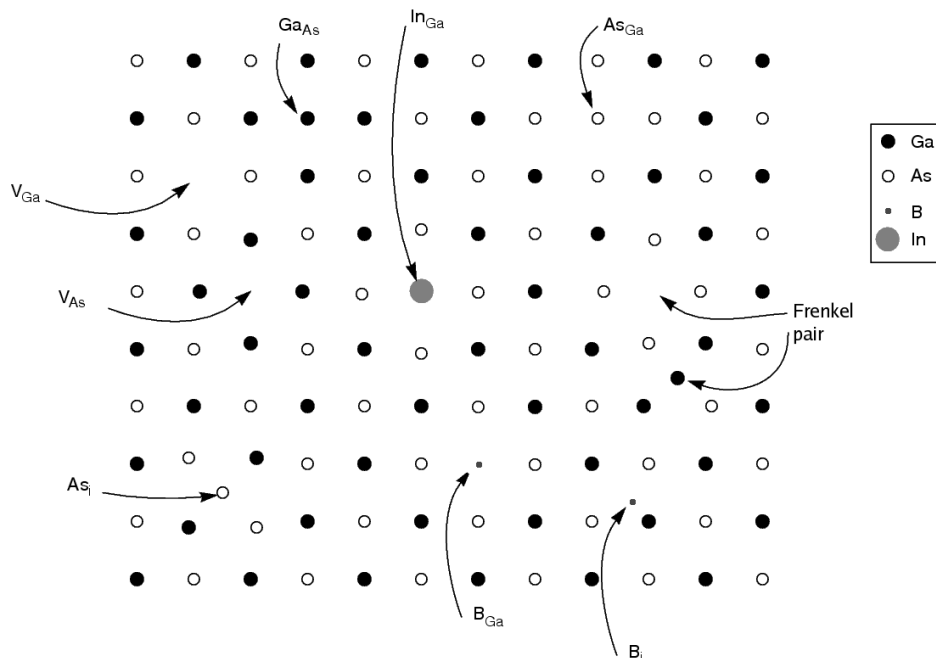


Figure 1.1: Several example point defects, using GaAs as an example. The defects are labeled with modified Kröger-Vink notation, as introduced below. Figure by Prof Kai Nordlund, and released into the public domain.

1.1. CHARGED POINT DEFECTS

Kröger and Vink introduced a compact notation for labeling crystallographic point defects [12]. In this notation, a particular defect is labeled,

$$D_S^C,$$

where D represents the element present at (or the special symbol V for a vacancy) at the defect site, S represents the site in the crystal occupied by the defect, and C represents the net charge on the defect. The site S should be an element present in the host crystal, or the special label I for interstitial defects.

Some typical examples of point defects, using GaAs an example, are shown in Fig. 1.1. Example native point defects in GaAs would include the gallium vacancy (V_{Ga}), the arsenic vacancy (V_{As}), the gallium interstitial (Ga_I), and finally the arsenic interstitial (As_I). Native defects are defects that can be formed without the introduction of impurity atoms, and have a special importance as they are intrinsic to the material and can form no matter how high a chemical purity is archived in the experimental growth process. Examples of impurity defects shown in the figure would include substitutional indium (In_{Ga}) and interstitial boron (B_I).

The above rules define point defects in terms of the chemical elements that make them up. Point defects often also have localised electrons associated with them. If extra electrons are added or removed from the defect, it changes its charge state of the defect. In the considered example, the V_{As}^0 acts as a shallow donor defect, requiring ~ 0.1 eV of energy [13] to release an electron into the conduction band, leaving a charged V_{As}^{+1} vacancy behind. Under realistic growth conditions, this intrinsic defect controls the position of the Fermi level within the material [13], controlling the degree of doping that can be achieved.

Kröger-Vink notation as originally introduced uses dashes and circles to denote the charge state of the defect. Hence, the version of the notation introduced above is sometimes called modified Kröger-Vink notation. In the literature on charged defects, this modified version is typically preferred.

The enormous technological relevance of defects outlined above explains the theoretical interest in predicting both the energy costs to form defects and their prop-

erties. However, point defects present an obvious challenge because they destroy the perfect lattice symmetry that normally renders the physics of crystals mathematically approachable [14]. For this reason, computational simulation approaches are the most fruitful. Still, this reduction of symmetry is a significant barrier, and computational costs are inevitably increased for calculations of point defects, compared with simulations of pure crystalline materials without defects.

The important technological abilities of point defects to act as dopants and recombination centers both involve a charge transfer between bulk band states in the material containing the defect, and with the defect itself. This raises the second main theoretical problem encountered in this thesis, that of describing point defects with net charge. Whatever approach we employ needs to be able to describe both localized defect states and bulk band states within a material, and accurately describe the energy separations between them. In practice, this becomes an involved problem because methods using periodic boundary conditions are well suited to describe band states, but encounter new problems when the charge state of the system being studied changes. In fact, the use of periodic boundary conditions almost demands that we study systems that are electrostatically neutral, as the properties of an infinite array of net charges is very poorly defined.

Broadly, the two most popular approaches for simulating charged defects are embedded cluster methods and supercell methods. These two approaches are summarized pictorially in Fig 1.2.

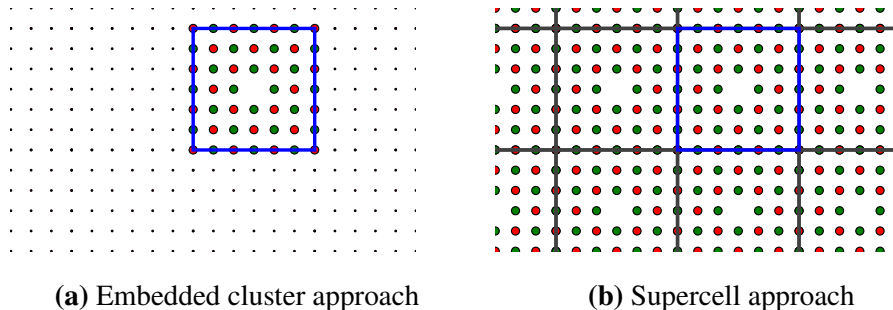


Figure 1.2: Schematic representation of embedded cluster and supercell approaches to the simulation of point defects. The two approaches have different drawbacks and advantages

In embedded cluster methods, we attempt to embed a cluster containing a defect in a large continuum that contains no further defects (as shown in Fig. 1.2a). Typically, the cluster is described using a more accurate but expensive method, with a cheaper method being used to represent the bulk of the crystal. This bulk region seeks to reproduce the boundary conditions present around the defect. In these methods, it can be challenging to describe the interactions between the cluster and the continuum it is embedded in. However, if this can be successfully done, reliable energies can be calculated.

In supercell methods, we take a different approach and periodically repeat the defect containing system in some way (as shown in Fig. 1.2b). In this case, we simulate a periodic array of defects, rather than just an individual defect. This introduces challenges because the defect being considered is able to interact with its own images, interactions which would not be present in the case of an isolated defect.

Supercell methods are generally expected (although some authors disagree) to converge to the desired isolated case as the size of the supercell model is systematically increased, but practical limitations in the computer power available can prevent us from achieving this in practice. Instead, we need to understand the extra interactions the use of a periodic model introduces, so that they can be removed from any properties we calculate for the system.

The supercell method is used far more widely in the context of density functional theory (DFT) studies on charged defects, as a high level of expertise is normally required to use the embedded cluster approach successfully. In contrast, methods to remove the finite-size dependence for supercells are well developed, and observed to be generally reliable [15].

1.2 Thesis outline

In Chapter 2, density functional theory is introduced with a focus on the supercell approach in order to study point defects. It is shown that this produces a method that demonstrates finite-size dependence, as the results calculated depend on the size of

the supercell employed.

Then in Chapter 3, present correction methods for charged defects are presented and discussed. The different approximations made in the derivations of these methods and the different approximations they make for the density response on formation of a charged defect are highlighted.

In Chapter 4, code is developed and validated to solve Poisson's equation for density models constructed from DFT density differences. An extension of the density countercharge method (DCC) to material is presented.

In Chapter 5, other possible sources of error to defect electrostatics are investigated. A decomposition of potential alignment is introduced that helps to understand the different sources of this error. It is investigated how these potential alignment terms can be approximated in practice.

In Chapter 5, several example charged defects in the bulk are introduced. The various existing correction methods introduced in Chapter 3 are compared with the new method developed in Chapter 4. This investigation demonstrates that the new method introduced shows the same behavior as the existing LZ (Lany-Zunger) method. The performance of the completing methods is evaluated by looking at the remaining supercell finite-size dependence.

Following on from this in Chapter 6, the defect charge models constructed in Chapter 5 are studied in more detail. It is discovered that the density response observed is in agreement with the predictions of classical electrostatics, where the density difference can be understood as being composed of bound and free charges. A new electrostatic correction is derived, where both these charges are included consistently, and this produces a significantly smaller correction than the other electrostatic methods already discussed.

Next, in Chapter 8, it is demonstrated that that relaxing the approximation of the free and bound screening as point like is not sufficient to explain the larger finite-size errors observed in practical calculations. Instead, the finite-size dependence observed is broken up into its separate DFT energy terms. This shows that the remaining finite-size error once both potential alignment and the smaller electro-

static correction have been applied is contained in the exchange-correlation energy. As only localised densities produce a change in this energy, and as it was already demonstrated in Chapter 6 that the defect free charge displays little finite-size dependence, this energy error is related to the bound screening charge. New empirical corrections are constructed, that are justified as combined electrostatic-exchange-correlation errors. These new corrections are similar to the MP (Makov-Payne) correction for unrelaxed defects, and switch from LZ-like to MP-like for relaxed defects as the dielectric constant increases.

Chapter 9 is the final results chapter, where ionization problems are considered for both bulk and surface calculations. A strong link between the finite-size errors of charged formation energies and the observed errors to obey Koopmans' theorem (KT) is reported. It is discovered that for ionization calculations on surfaces, the error to obey KT is reduced for cubic cells, due to favorable electrostatic interactions with the neutralizing jellium background. For charged defects in surface calculations, it is demonstrated that the same inverse linear errors reported in Chapter 8 are maintained for unrelaxed defects as long as cubic supercells are used. This allows the internal consistency of bulk and surface defects to be demonstrated for the first time, using the oxygen vacancy in MgO as an example.

Finally, general conclusions are presented. Avenues for future work are discussed, where the role of ionic relaxation in surface calculations can be developed. Additionally, the role of functional dependence and 2D boundary conditions are highlighted as important goals of future work.

Chapter 2

Established theory

Aims: In order to understand and predict the properties of materials and their defects, we rely on quantum mechanics. This fundamental theory describes materials and the defects within them, but is sufficiently complex that major approximations need to be introduced to produce practical calculations. In this thesis, I use the method of density functional theory to approximate quantum mechanics. This theory is highly successful, but is generally constructed differently depending on whether molecular or crystalline systems are being studied. I will introduce the plane wave pseudopotential (PWP) method, developed specifically for crystals. I will then explore how the PWP method introduces extra complexities when systems with net charge are considered.

2.1 Many-body quantum mechanics

The starting point for calculating the properties of materials and their defects is the many-body Schrödinger equation,

$$\hat{H}\Psi(\mathbf{x}_1, \dots, \mathbf{x}_N) = E\Psi(\mathbf{x}_1, \dots, \mathbf{x}_N), \quad (2.1)$$

where \hat{H} is Hamilton operator, $\Psi(\mathbf{x}_1, \dots, \mathbf{x}_N)$ is the many-body wavefunction as a function of the electron coordinates \mathbf{x} , and E is the total energy of the system. The electron coordinates x encapsulate both a position and a spin state, such that

$x = (\mathbf{r}, \sigma)$. The Hamilton operator is given as,

$$\hat{H} = T + V_{e-e} + V_{\text{ext}}, \quad (2.2)$$

where T is the many-body kinetic energy, V_{e-e} is the many-body electron-electron interaction and V_{ext} is the interaction with an external potential, which in the absence of external fields is the interaction with point ions.

In the above treatment, we have already implicitly made the Born-Oppenheimer approximation [16], that the electronic and nuclear wavefunctions of the system can be separated. We first calculate the electronic wavefunction given a set of nuclear positions. Then, the forces experienced by the nuclei can be calculated using this electronic wavefunction, via the Hellmann-Feynman theorem [17, 18, 19, 20]. This process can be repeated until the lowest energy state is found. This approximation is justified as electrons have a much lower mass than ions, meaning that it is an effective approximation to allow the electrons to instantly respond the positions of the atomic nuclei [21].

Even though significant approximations have already been introduced, Eq. 2.1 is still a formidable equation to solve, rapidly growing in complexity as the number of electrons increases. Even when limited to two electrons, only one analytic solution of Eq. 2.1 is known, for a hypothetical system that does not exist in nature [22]. In order to study materials, we need to introduce further approximations to make the problem computationally accessible.

2.2 Density functional theory

Density functional theory (DFT) is presently the most popular quantum mechanical computational method used in condensed matter physics. This popularity is due to the method being very accurate given its relative computational cost. Other competing methods such as configuration interaction (CI) [23, 24] and Møller–Plesset perturbation theory [25, 26, 27, 28] are significantly more computationally demanding, and could be expected to be significantly more accurate. However, continuing experience demonstrates that practical DFT calculations can be far more accurate

than would be naively expected from their reduced numerical complexity. The reasons for this continue to be a rapidly moving area of research.

DFT is based on the Hohenberg-Kohn Theorems [29], which state that there is a one to one mapping between the ground-state wavefunction $\Psi(\mathbf{x}_1, \dots, \mathbf{r}_N)$ and the electron density $n(\mathbf{r})$. This appears to be an enormous reduction in complexity, as the electron density is a function of only one position coordinate, rather than N .

In Kohn-Sham density functional theory, the total energy is calculated as,

$$E = T_{\text{KS}} + V_{\text{Hart}} + V_{\text{ext}} + E_{\text{xc}}, \quad (2.3)$$

where T_{KS} is the kinetic energy of the fictitious Kohn-Sham electrons, V_{Hart} is the semiclassical Hartree electron-electron interaction, V_{ext} is the interaction with an external potential, and V_{xc} is the exchange-correlation energy.

2.2.1 Total energy in a planewave basis

There are several ways that DFT can be practically implemented, depending on the basis functions used to expand the KS orbitals and on which electrons in the system are treated explicitly. The planewaves and pseudopotentials (PWP) approach is the original implementation of DFT for bulk systems, and continues to enjoy several advantages. In particular, the PWP method takes the simplest form for bulk calculations, and as such is often used to implement new methods first.

The total energy expression in this formalism can be given as,

$$E = E_{\text{kin}} + E_{\text{xc}} + \boxed{E_{\text{PP}} + E_{\text{Hart}} + E_{\text{Ewald}} + E_{\text{NC}}}, \quad (2.4)$$

where E_{kin} is the single particle kinetic energy of the Kohn-Sham electrons, E_{xc} is the exchange-correlation energy, E_{PP} is the energy contribution from the pseudopotentials of the ions, E_{Hart} is the Hartree electronic interaction energy, E_{Ewald} is the ion-ion interaction energy and E_{NC} is the non-Coulombic energy of the local pseudopotential.

I use the name of the E_{NC} term as given in a standard textbook [30] and as used in the CASTEP code, although I believe it is misleading as the pseudopotential

itself contains Coulomb interactions that contribute to this term. In this context non-Coulombic only means that this energy term is not included in the evaluation of the Hartree energy, E_{Hart} .

In calculating all the energy terms shown in a box in Eq. 2.4, an assertion has been made that the total system has a net charge of zero. I discuss this point in more detail in Sec. 2.2.1.1, as this has important consequences when systems with net charge are considered.

First the non-interacting single-particle kinetic energy of the Kohn-Sham electrons is calculated as,

$$E_{\text{kin}} = 2 \sum_i \int \phi_i \left[-\frac{\hbar^2}{2m} \right] \nabla^2 \phi_i d^3 \mathbf{r}, \quad (2.5)$$

where a sum is performed over all i occupied Kohn-Sham orbitals ϕ . This is not the correct kinetic energy for the interacting system, but a good approximation to it. The E_{xc} term should include a correction for the kinetic energy of the interacting system.

The energy of interaction between ions and electrons is calculated as,

$$E_{\text{PP}} = \int v_{\text{PP}}(\mathbf{r}) n(\mathbf{r}) d^3 \mathbf{r}, \quad (2.6)$$

where v_{PP} is the local part of the potential of the pseudoions in the system.

The exchange-correlation energy is calculated as,

$$E_{\text{xc}} = \int \epsilon_{\text{xc}}[n(\mathbf{r})] d^3 \mathbf{r}, \quad (2.7)$$

where the exchange-correlation energy is a functional of the electron density. As this functional is not known exactly, an approximate functional must be employed in practical calculations. These approximations are discussed in more detail in Section 2.2.5.

The semiclassical Hartree interaction between electrons is calculated as,

$$E_{\text{Hart}} = \frac{e^2}{2} \int \frac{n(\mathbf{r})n(\mathbf{r}')}{|\mathbf{r}-\mathbf{r}'|} d^3\mathbf{r}d^3\mathbf{r}', \quad (2.8)$$

where n is the electronic density. The Hartree energy is not the interaction energy of the true interacting system for two reasons. Firstly, it neglects electron exchange and correlation, both quantum mechanical effects with no classical analogue, which modify the effective distance between electrons. Secondly, the Hartree integral causes electrons to interact with themselves, introducing a self-interaction that would be absent in the real system. Both these errors should be compensated by a corresponding part of the exchange-correlation energy.

The ion-ion interaction energy (between the point charges that model the pseudoions) is calculated as,

$$E_{\text{Ewald}} = \frac{1}{2} \sum_{I,J} Z_I Z_J e^2 \left\{ \sum_{\mathbf{I}} \frac{\text{erfc}(\eta|\mathbf{R}_I + \mathbf{I} - \mathbf{R}_J|)}{|\mathbf{R}_I + \mathbf{I} - \mathbf{R}_J|} - \frac{2\eta}{\sqrt{\rho}} \delta_{IJ} + \frac{4\pi}{\Omega} \sum_{\mathbf{G} \neq 0} \frac{1}{|\mathbf{G}|^2} \exp\left(-\frac{|\mathbf{G}|^2}{4\eta^2}\right) \cos[(\mathbf{R}_I - \mathbf{R}_J) \cdot \mathbf{G}] - \frac{\pi}{\eta^2 \Omega} \right\}, \quad (2.9)$$

where a sum is performed over both the direct lattice vectors \mathbf{I} and the reciprocal lattice vectors \mathbf{G} . This term describes the interaction of point charges representing the ions (or pseudoions) with each other. It is performed using the method of Ewald summation [31], which is introduced in Sec. 3.1.1.1.

Finally, a non-Coulombic energy must also be calculated,

$$E_{\text{NC}} = \frac{Z}{\Omega} \sum_{\alpha} v_{\alpha, \text{core}}, \quad (2.10)$$

where Z is the total ionic charge present in the cell, Ω is the volume of the simulation cell and $v_{\alpha, \text{core}}$ is a pseudopotential dependent contribution. Part of the Coulomb interaction between atomic nuclei and electrons has been drawn into the pseudopotential constructed, so care is required in order to ensure that the electrostatic energy is still calculated consistently.

2.2.1.1 Electrostatic terms and charged systems

The total energy expression given in Eq. 2.4 is constructed with care, due to fundamental challenges in evaluating Coulomb interactions under periodic boundary conditions. One aspect of this is that the total charge in the system has been set to zero.

Even when considering a charge neutral lattice, the conditionally convergent nature of the Coulomb interaction means that methods that seem physically meaningful can still give incorrect total energies. The most common example is given by evaluation of the energy of a molecular dynamics simulation of NaCl. If the interaction energy for an individual ion is calculated by adding spheres of atoms to the summation then the sum never converges. In contrast, if the crystal is built by adding cubes, the correct energy is calculated. This behavior demonstrates that the behavior of the Coulomb interaction under periodic boundary conditions is not simple [32]. Although this behavior is now understood, a flawed treatment was previously given in many respected textbooks [1, 33]. These kind of past failures mean that many still consider the calculation of meaningful formation energies using supercells to be impossible, as argued in a recent paper [34].

The $\mathbf{G}=0$ term is divergent and neglected in both the E_{Hart} and E_{Ewald} energies. The electronic subsystem contains only negative charge, and an infinite amount of negative charge would have an infinite repulsive energy under periodic boundary conditions. The positive atomic nuclei would also infinitely repel themselves. The sum of these two terms is more meaningful, as the combination of electronic and nuclear charges is overall charge neutral and these two divergences cancel. The use of pseudopotentials complicates the argument, and both the E_{PP} and E_{NC} terms are also required to maintain this property when pseudopotentials are employed, as the description of ions as perfect point charges becomes too simplistic. As long as the average potential (the $\mathbf{G}=0$ term) of all local potentials is neglected, we can avoid needing to attempt to calculate any of these difficult $\mathbf{G}=0$ terms at all.

In fact, it has been mathematically proved that a meaningful calculation of the average potential of an infinite crystal is impossible [35, 36, 37, 38, 39, 40]. This

surprising result follows from the conditionally convergent nature of Coulomb summation, and physically means that we need to understand the surface of a crystal in order to fully determine the potential in its interior [38]. The difficulty in calculating the average potential in the PWP DFT approach is actually due to the fact that this average potential lacks any fundamental meaning.

For comparing the total energy of charge neutral systems, the PWP scheme produces robust results. The average value of the potential has not been evaluated, can not be evaluated even in principle, and makes no difference to the total energy in any case, as both the ions and electrons would experience this average potential, which have a combined charge of zero. If a negative average potential was added to the system, then the increase in the energy of the negative electrons caused would be exactly canceled by the reduction in energy of the positive nuclei.

In fact, if a system with net charge is considered using these equations, the formalism enforces the presence of neutralizing jellium charge in the system. This is the standard way systems with net charge are simulated, although this background ensures that the supercells are in fact formally charge neutral. This jellium charge is only present implicitly in the four terms shown in the box in Eq. 2.4. Notably, this jellium charge is not included in the calculation of the exchange-correlation energy, E_{xc} . This introduces a natural way for finite-size errors to be introduced, as part of the charge present in the supercell is present in the evaluation of E_{Hart} , but not in E_{xc} , even though the second term includes corrections to the first.

The above discussed uncertainties in the average potential do in fact produce practical difficulties when comparing neutral calculations. As both calculations are referenced to an unknown average potential, it is not formally possible to directly compare their eigenvalues. This can be practically seen by adding a uniform potential directly to a PWP planewave calculation. The total energies remain unchanged and can still be compared, but all eigenvalues in the system are shifted by the uniform amount.

2.2.2 Planewave basis

In order to calculate the total energy in a PWP calculation using Eq. 2.4, a basis set for the Kohn-Sham orbitals also needs to be selected. In turn, this will define the basis that the total electron density is expressed on. The Kohn-Sham orbitals are expanded in a basis of planewaves, yielding,

$$\phi(\mathbf{r}) = \sum_{\mathbf{G}}^{G < G_{\max}} C_{\mathbf{G}} e^{i(\mathbf{G} \cdot \mathbf{r})}, \quad (2.11)$$

where a summation is performed over all \mathbf{G} vectors below a cutoff length of G_{\max} . As the magnitude of a \mathbf{G} vector is quite an abstract concept, it is customary to convert these values to energies, using the energies of the ideal Bloch states they describe. The highest Fourier mode G_{\max} is mapped onto its kinetic energy,

$$E_{\text{cut}} = \frac{\hbar^2 \mathbf{G}_{\max}^2}{2}, \quad (2.12)$$

in Hartree atomic units.

Higher values of E_{cut} correspond to planewaves with more nodes. The completeness of the basis set improves as E_{cut} is increased.

In this project I used the CASTEP code for DFT calculations using a planewave basis.

2.2.3 Brillouin zone sampling

The above approach is almost sufficient to describe crystalline materials accurately. Accurate calculations of crystals also requires \mathbf{k} -point sampling if a small unit cell is used [30]. This is needed because the symmetry of the wavefunction within a crystal has more freedom than the real space crystal lattice, allowing for components of the wavefunction with longer wavelength than the lattice cell used to define the atomic positions.

In order to well describe band states in a crystal, it is necessary to either use supercells significantly larger than those required to describe the atomic symmetry of the crystal, or to instead directly sample the extra freedom of the wavefunction by

averaging over different \mathbf{k} -points. For defect-free crystals, these two approaches are mathematically identical, as long as the symmetry of the chosen \mathbf{k} -points and supercell models are identical [41]. The approach of \mathbf{k} -point sampling is traditionally preferred over the competing supercell approaches as it enjoys numerical advantages [42]. A regular grid of \mathbf{k} -points is commonly employed, and referred to as Monkhorst-Pack [43] sampling.

When considering defects, the situation is more complex as this direct correspondence between supercell methods and \mathbf{k} -point sampling breaks down. As we are interested in only a single defect in an infinite crystal, then any localized states associated with the defect should have no \mathbf{k} -point dependence at all. However, the finite-size of the host supercell can cause a non-physical \mathbf{k} -point dependence for defect states to be calculated. In the worst cases, this causes non-physical charge transfers from occupied defect states at unfavorable \mathbf{k} -points to favorable ones. Band-filling corrections have been suggested to resolve this problem [44]. In this thesis, I always avoid this problem by increasing the quality of the \mathbf{k} -point grid until the effect is no longer observed, which is another solution to this problem reported in the literature [45].

2.2.4 Gaussian planewave basis

I also used CP2K for calculations using a Gaussian planewave basis [46, 47]. This method is similar to the PWP method described in more detail in this thesis. The main difference is that the Kohn-Sham orbitals are extended in local basis functions, as well as in planewaves. The electrostatics is carried out in the same way as in the PWP approach, making the two methods very similar in the way Coulomb interactions are evaluated. However, this slightly more complex approach has advantages in allowing cheaper evaluation of non-local exchange-correlation functionals, by implementing the methods outlined in Sec. 2.2.5.5 and Sec. 2.2.5.6.

Note that when using CP2K, I always sample the Brillouin zone using only a single \mathbf{k} -point, at the Γ -point. Although efforts have been made to add \mathbf{k} -point sampling to CP2K, its implementation is not presently considered to be reliable.

2.2.5 Exchange-Correlation functionals

In practical DFT calculations, the Exchange-Correlation energy E_{xc} is not known exactly, and must be approximated. Many such approximations now exist, providing a ladder of approximations of increasing computational cost and (hopefully) increased accuracy [48].

2.2.5.1 LDA functional

The simplest approximate exchange correlation functional is the local density approximation [49]. It is defined as,

$$E_{xc}^{\text{LDA}} = \int \epsilon_{xc}(\mathbf{r}) n(\mathbf{r}) d^3\mathbf{r}, \quad (2.13)$$

where ϵ_{xc} is the local exchange correlation energy density of a homogeneous electron gas of the same local density. The energy contribution ϵ_{xc} can be calculated accurately for the homogeneous electron gas using Monte Carlo methods [50, 51]. As a very simple exchange-correlation functional, the success of the LDA was originally quite surprising. This accuracy is now commonly believed to be because the LDA is able to well approximate the radial average of the XC hole [52, 53].

In the context of the solid state, the LDA overbinds crystals, leading to a consistent error of predicting smaller lattice constants than those measured experimentally. The method is the cheapest approximation to the exchange-correlation energy that can still be described as successful for solid state calculations.

2.2.5.2 PBE functional

The LDA only uses the local density to calculate the exchange-correlation energy, but improvements can be seen if the local density gradient is also used. This produces generalized gradient approximations (GGAs), of which PBE [54] functional is the most commonly used for solid state calculations. The GGA xc energy is defined as,

$$E_{xc}^{\text{GGA}} = \int \epsilon_{xc}^{\text{GGA}}[n(\mathbf{r}), \nabla n(\mathbf{r})] n(\mathbf{r}) d^3\mathbf{r}, \quad (2.14)$$

where the semilocal xc energy density ϵ_{xc} is a functional of both the local density and its gradient.

In the context of the solid state, the PBE underbinds crystals, leading to an overprediction of the lattice constant. Although GGAs are more complex than the LDA, the computational cost of calculations is not meaningfully increased in practice. The PBE functional does normally improve on the LDA for non-metallic materials [55].

2.2.5.3 PBEsol functional

The original PBE functional was designed for both solid state and atomic calculations, but growing experience shows that no GGA can well treat both classes of system [56]. PBEsol [57] is a reparameterization of PBE for solid state systems, that aims to improve the prediction of lattice constants. The two functionals are very similar, as only two constants are modified from their PBE values to produce the PBEsol functional. It should improve the description of solid state systems, but at a corresponding cost of an accuracy loss for atomic systems[58].

2.2.5.4 PBE0 functional

A further popular class of exchange-correction functionals are hybrid functionals, where the approximations given above are mixed with Hartree-Fock (HF) exchange. Although originally developed in an *ad hoc* way, hybrid methods can be rigorously developed through the adiabatic connection [59]. One of the most popular hybrid functionals in the context of solids is the PBE0 functional [60, 61]. In this method,

$$E_{xc}^{\text{PBE0}} = aE_x^{\text{HF}} + (1 - a)E_x^{\text{PBE}} + E_c^{\text{PBE}}, \quad (2.15)$$

where E_x^{HF} is the Hartree-Fock exchange energy. The value of a can be varied, but a standard value of $a=0.25$ is most commonly used. This number is justified as being in good agreement with MP4 results for small molecules [61].

The Hartree-Fock exchange energy is given as,

$$E_x^{\text{HF}} = -\frac{1}{2} \sum_{i,j} \int \int \phi_i^*(\mathbf{r}_1) \phi_j^*(\mathbf{r}_1) \frac{1}{r_{12}} \phi_i(\mathbf{r}_2) \phi_j(\mathbf{r}_2) d^3\mathbf{r}_1 d^3\mathbf{r}_2, \quad (2.16)$$

which as a double integral of position, is extremely costly to evaluate computation-

ally.

More recent work has suggested that a can be self-consistently determined in the solid state by calculating the electronic contribution to the dielectric constant, ϵ [62]. This produces the self-consistency condition,

$$a = \frac{1}{\epsilon_{\infty}}, \quad (2.17)$$

which should be evaluated until the input value of the mixing fraction a produces the predicted high-frequency dielectric constant ϵ_{∞} . Satisfying this self consistency condition typically only requires around five iterations. Such a procedure can be justified through many-body perturbation theory [63, 64].

One significant downside of hybrid functionals (such as PBE0) is that they greatly increase the computational cost and memory requirements of DFT calculations, making the calculation of the exchange-correlation energy the most computationally demanding part of the calculation.

2.2.5.5 Auxiliary density matrix method

One way of reducing the computational cost of hybrid exchange is to use the auxiliary density matrix method (ADMM) [65].

In this approach, we introduce a new auxiliary density matrix,

$$n(\mathbf{r}) \approx \hat{n}(\mathbf{r}), \quad (2.18)$$

such that the new auxiliary density \hat{n} approximates the charge density n . Crucially, \hat{n} is calculated on a new auxiliary basis set of lower numerical complexity, containing simpler basis functions. The costly Fock operator can then be evaluated on this simplified basis.

However, to do this directly would introduce large errors, as the exchange energy on this new reduced basis set will be quite different as a result of its reduced quality. In order to introduce a fruitful approximation, a correction must also be applied for this effect. The CP2K code uses a correction based on the following

approximation,

$$\begin{aligned} E_x^{\text{HF}}[n] &= E_x^{\text{HF}}[\hat{n}] + (E_x^{\text{HF}}[n] - E_x^{\text{HF}}[\hat{n}]) \\ &\approx E_x^{\text{HF}}[\hat{n}] + (E_x^{\text{PBE}}[n] - E_x^{\text{PBE}}[\hat{n}]), \end{aligned} \quad (2.19)$$

that the difference in the exchange energy on this change of basis at the PBE level mimics the same change in energy at the HF level. The difference in energy at the PBE level can be rapidly calculated and subtracted from the calculated energy. Reference calculations on atomic and molecular systems demonstrate that performing this correction can reduce the introduced error by more than 50% [65].

2.2.5.6 PBE0_TC_LRC functional

Even with ADMM, the PBE0 functional can still be prohibitively expensive for large simulation cells. A cheaper alternative is given in the PBE0_TC_LRC functional [66]. In this method, the exchange-correlation energy is given as,

$$E_{xc}^{\text{PBE0_TC_LRC}} = aE_x^{\text{HF,TC}} + aE_x^{\text{PBE,LRC}} + (1-a)E_x^{\text{PBE}} + E_c^{\text{PBC}}, \quad (2.20)$$

where the only difference from Eq. 2.15 is in the way that the Hartree-Fock term (now split into $E_x^{\text{HF,TC}}$ and $E_x^{\text{PBE,LRC}}$) has been calculated.

Firstly, the Fock integral is truncated in this approximation, at a cutoff radius of R_c ,

$$E_x^{\text{HF}}(\mathbf{r}_1, \mathbf{r}_2) = \begin{cases} E_x^{\text{HF}}(\mathbf{r}_1, \mathbf{r}_2) & \text{if } r_{12} \leq R_c \\ 0 & \text{if } r_{12} > R_c \end{cases} \quad (2.21)$$

This reduces the computational cost with decreasing R_c , at the cost of neglecting part of the exchange energy. As $R_c \rightarrow 0$, PBE results are recovered.

Secondly, a long range correction, $E_x^{\text{PBE,LRC}}$, is applied, which aims to reduce the loss of accuracy introduced by the truncation of the Fock integral. This energy correction has a rather complex form, but can be evaluated analytically. It should act to reduce the loss of accuracy introduced by the truncation radius R_c .

Taken together, the outlined approximations allow CP2K calculations using

hybrid functionals on systems with thousands of atoms [66].

2.2.6 Koopmans' theorem

The eigenvalues of the fictitious Kohn-Sham electrons do not directly correspond with properties of the real many-body system, with one important exception. According to Koopmans' theorem (KT) [67],

$$I = -\epsilon_{\text{homo}}, \quad (2.22)$$

where I is the ionization energy, the energy required to remove one electron from the system, and ϵ_{homo} is the eigenvalue of the highest occupied Kohn-Sham orbital.

Koopmans' theorem was originally discovered in the context of Hartree-Fock [67], where the theorem is only approximate as it makes the frozen orbital approximation. This means that orbital relaxation upon removal of an electron is neglected.

In the context of DFT, KT was proved by Almladh and von Barth [68], both for isolated systems, and for semi-infinite surfaces. Unexpectedly, the theorem turns out to be exact for ideal DFT, and does not require the frozen orbital approximation. The first context allows application of the theorem to molecules, and the second enables calculations of surface work functions.

For DFT practical calculations, Eq. 2.22 is not expected to be an exact condition. This is because the theorem is exact only for the universal XC functional, and the use of approximate XC functionals will introduce an error to obey KT [69]. In particular, approximate functionals struggle to describe non-local features of the universal XC functional, that ensure the correct charge transfer between isolated subsystems [70]. As a consequence, KT is a useful tool for developing improved functionals. Secondly, the theorem only strictly applies to isolated or semi-infinite surface systems. So, other errors may be introduced when considering systems not of this type.

Koopmans' theorem has also been proved for exact generalized Kohn-sham theory [71], meaning that KT is also applicable to hybrid functionals. As in ordi-

nary DFT, the use of approximate XC functionals may cause KT to fail in practical calculations.

2.3 Density functional perturbation theory

Perturbation theory can be applied within the framework of DFT in order to produce Density functional perturbation theory (DFPT) [72, 73], which enables the calculation of response properties such as phonons, polarizabilities and Raman spectra.

As already described in Sec. 2.1, if the electron density $n(\mathbf{r})$ is known for a given atomic geometry, the force experienced by atoms in response to this electron density can be calculated analytically using the Hellmann-Feynman theorem. In typical DFPT implementations, the approximation is made that there is a linear relationship between the displacement of an individual atom and the forces experienced by the other atoms. By considering all the available linear perturbations of a given ionic structure, the phonon structure of a given material can be calculated numerically. This enables the calculation of physical properties that are described by atomic displacements, such as low frequency dielectric constants.

In this thesis, DFPT is employed to calculate both static (ϵ_0) and high frequency (ϵ_∞) dielectric constants, using the implementation of DFPT available in CASTEP [74]. The calculation of ϵ_∞ keeps ionic positions fixed, and represents physical processes that take place too fast for ions to move in response. In contrast, ϵ_0 represents slower processes where the atomic positions have time to respond, and its calculation requires computation of the phonon spectrum of the material.

2.4 Supercell defect formation energies

When using DFT, defect formation energies can be calculated, which are the energy cost to form a particular defect. The standard definition [75] of the defect formation energy E_f is given as:

$$E_f = E_{\text{defect}}^{\text{DFT}} - E_{\text{bulk}}^{\text{DFT}} - \sum_i n_i \mu_i + q \mu_e, \quad (2.23)$$

where $E_{\text{defect}}^{\text{DFT}}$ and $E_{\text{bulk}}^{\text{DFT}}$ are the total energies of the supercell containing the defect, and an equivalently shaped supercell of the perfect bulk crystal respectively. Additionally, this raw energy difference is modified by the energy required to exchange n_i ions with some reservoir of chemical potential μ_i , along with the cost to exchange electrons with some external reservoir μ_e . Note that the change in number of electrons in the system is just the opposite of the charge of the system q , as each electron has a charge of -1 . The chemical potentials μ_i and μ_e make a statement about the chemical environments being considered.

When the definition given in Eq. 2.23 is used in combination with the supercell method, as introduced in Sec. 1.1, the results are found to be highly sensitive to the size and shape of the supercell model employed. In order to attempt to remove this non-physical model dependence, two main corrections are commonly employed, yielding the corrected formation energy,

$$E_f^{\text{corr}} = E_f + E_{\text{corr}} + q\Delta V_{\text{PA}}, \quad (2.24)$$

which includes the finite-size corrections E_{corr} and $q\Delta V_{\text{PA}}$, which should act to reduce finite-size dependence. These corrections are the main topic of this thesis.

2.4.1 Known finite-size scaling rules

Detailed studies on supercell size dependence of the formation energy of charged defects have been carried out. The study of Castleton *et al.* [76] has produced the following empirical scaling rule for cubic supercells,

$$E_f(L) = E_f(L \rightarrow \infty) + \frac{a_1}{L} + \frac{a_3}{L^3}, \quad (2.25)$$

which demonstrates an inverse size dependence on both the length of the considered supercell, L , and the volume of the supercell $\Omega=L^3$. Knowledge of this scaling rule doesn't inform us about the origin of a_1 and a_3 , and several plausible suggestions have been offered in the literature [77, 78].

The expression in Eq. 2.25 is often used to extrapolate charged defect formation energies to the dilute limit [76]. This is then used to test the performance of

2.4. SUPERCELL DEFECT FORMATION ENERGIES

charge correction methods in several papers [78, 79, 80, 81]. But, as long as the origin of Eq. 2.25 is not clearly understood, it remains unclear how accurate such extrapolations are.

Chapter 3

Defect electrostatics in the bulk

Aims: In this chapter I introduce electrostatic corrections, commonly used in DFT calculations on the formation energies of charged defects, in order to reduce the finite-size dependence observed in such calculations. These corrections are required because the electrostatics of the supercell model includes interactions that would not be present in the limit of an infinitely large supercell. I introduce several electrostatic correction methods that are commonly used in the literature and explain the differences between the approaches used by the methods.

3.1 Electrostatic corrections

As the use of periodic boundary conditions replaces an isolated charged defect with an array of periodic images, calculations using the supercell methodology also include an energy error (if one is interested in the dilute limit) due to the interactions with images, E_{corr} . In order to remove these unwanted interactions, they can be modeled separately using classical electrostatics, and then removed. This is shown pictorially in Fig. 3.1.

Bulk correction methods have been developing over the last 25 years, and several different approaches now exist in the literature. The performance of the methods has been harder to assess.

3.1.1 The method of Makov and Payne

The simplest electrostatic model that can be applied is approximating the defect as a point charge (PC). In Fig. 3.1, this represents the charges q as ideal points.

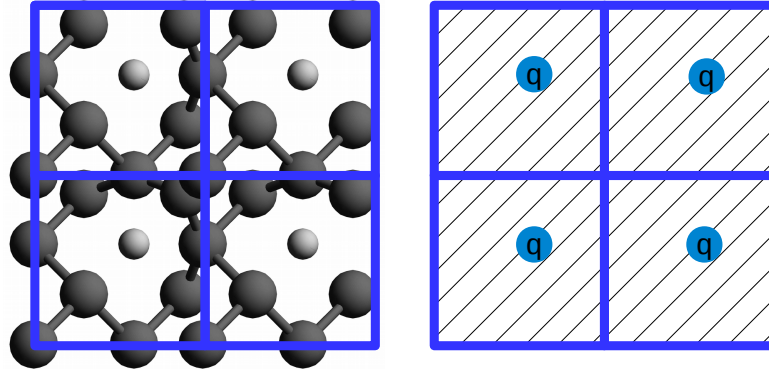


Figure 3.1: A periodic DFT calculation containing a defect is shown on the left, which is used to construct the simplified classical model on the right. The model charge q interacts through a classical dielectric background, represented by the shaded background. The interaction of the classical model is removed from the final formation energy. Two possible models for q are shown in Fig. 3.2.

These corrections were first applied to defect calculations using classical molecular dynamics by Leslie and Gillan [82]. In the context of DFT, this is the first order Makov-Payne (MP) correction for cubic supercells: [83]

$$E_{\text{corr}}^{\text{MP}} = \frac{q^2 \alpha_M}{2\epsilon L}, \quad (3.1)$$

where ϵ is the dielectric constant of the material containing the defect, L is the separation between defects and α_M is the Madelung constant, which depends only on the shape of the supercell containing the defect. This provides the exact interaction energy of an array of point charges immersed in neutralizing jellium. The appropriate dielectric constant is the static dielectric constant ϵ_0 when ionic relaxation of the defect is performed, or the high frequency dielectric constant ϵ_∞ when the ionic structure is kept fixed. This simple method has been extended to general supercell shapes and to anisotropic dielectrics [39, 84]. For cubic cells, this produces a L^{-1} dependent term that could explain the origin of the a_1 term in Eq. 2.25.

However, a point charge is a highly idealized model, which is known to overestimate the size of the unwanted image interactions. Charged defects are often not point-like, but instead have charge distributed over some defect dependent region,

such as a vacancy site, dangling bonds or neighboring ions. More complex interaction corrections attempt to capture this in a more distributed charge model $q(\mathbf{r})$, which tends to reduce the interaction correction.

Makov and Payne [83] were motivated by these considerations to suggest a multipole expansion to generate higher order terms that could also be calculated. Such an expansion yields:

$$E_{\text{corr}}^{\text{MP2}} = \frac{q^2 \alpha_M}{2\epsilon L} - \frac{2\pi q Q}{3L^3} + O(L^{-5}), \quad (3.2)$$

where Q is the quadrupole moment of the defect charge model. This expression contains only odd L terms, because the even L terms are zero for charge distributions with cubic symmetry. Hence, Eq. 3.2 is correct up to the fifth order, for cubic supercells. However, the MP paper [83] does not provide a systematic way of calculating Q , so this quadrupole term is rarely calculated within the MP method.

3.1.1.1 Energy of a point charge

The energy of an infinite array of interacting point charges, embedded in a neutralizing jellium background can be calculated using the first term in Eq. 3.2. In turn, this requires calculation of the relevant Madelung constant α_M . This can be achieved using the well known method of Ewald summation,

$$\frac{\alpha_M}{L} = \sum_{\mathbf{R}_i}^{i \neq 0} \frac{\text{erfc}(\gamma \sqrt{|\mathbf{R}_i|})}{|\mathbf{R}_i|} + \sum_{\mathbf{G}_i}^{i \neq 0} \frac{4\pi}{\Omega} \frac{\exp(-\mathbf{G}_i^2/4\gamma^2)}{\mathbf{G}_i^2} - \frac{2\gamma}{\sqrt{\pi}} - \frac{\pi}{\Omega\gamma^2}. \quad (3.3)$$

It can be seen that the value of α_M only depends on the shape of the supercell containing the defect.

3.1.1.2 Original derivation of the MP method

To derive the MP method, consider the charge density,

$$\rho(\mathbf{r}) = \rho_c(\mathbf{r}) + J, \quad (3.4)$$

3.1. ELECTROSTATIC CORRECTIONS

where the total charge density $\rho(\mathbf{r})$ is made of a charge distribution for the defect $\rho_c(\mathbf{r})$, embedded in a uniform jellium background J . The neutralizing jellium background ensures charge neutrality, with a density of q/Ω .

Makov and Payne took Eq. 3.4, and added and removed a point charge of magnitude q at position \mathbf{r}_o . This leads to the expression,

$$\rho(\mathbf{r}) = \left[q\delta(\mathbf{r} - \mathbf{r}_o) + J \right] + \left[\rho_c(\mathbf{r}) - q\delta(\mathbf{r} - \mathbf{r}_o) \right]. \quad (3.5)$$

The two point charges would cancel and leave the density unchanged. Then, charge distributions are defined using the bracketed sections, yielding

$$\rho_1(\mathbf{r}) = \left[q\delta(\mathbf{r} - \mathbf{r}_o) + J \right], \quad (3.6)$$

and

$$\rho_2(\mathbf{r}) = \left[\rho_c(\mathbf{r}) - q\delta(\mathbf{r} - \mathbf{r}_o) \right]. \quad (3.7)$$

Both of the charge distributions ρ_1 and ρ_2 have a net charge of zero. Additionally, in the case of a cubic cell, \mathbf{r}_o can be taken as both the center of the cell and the defect site. These choices ensure that both ρ_1 and ρ_2 have a dipole moment of zero, due to symmetry arguments. This ensures that the highest order interactions are quadruples.

Then, linear superposition is used to calculate the three energy components and know the total interactions of the charge distributions. These components are E_{11} , the interaction energy of ρ_1 with itself, E_{22} the interaction of ρ_2 with itself, and finally E_{12} , the interaction of ρ_1 with ρ_2 .

Makov and Payne note that E_{11} is the known result for a point charge embedded in neutralizing jellium, yielding,

$$E_{11} = -\frac{q^2\alpha}{2L}. \quad (3.8)$$

Then, they make the assumption that ρ_c is well localized within the cell, and hence is size independent. This means that E_{22} is the interaction of a well localized

neutral charge with no monopole or quadrupole moment. This interaction would be well approximated as 0, so they let E_{22} equal zero.

Finally they consider the energy E_{12} . Makov and Payne argue that the only non-zero contribution to this energy is given as,

$$E_{12} = \frac{2\pi q}{3\Omega} \int_{\Omega} \rho_2(\mathbf{r}) r^2 d^3r + O(L^{-5}). \quad (3.9)$$

This would lead to a total energy formula for a cubic lattice of,

$$E = E_0 - \frac{q^2 \alpha}{2L} - \frac{2\pi q Q}{3L^3} + O(L^{-5}), \quad (3.10)$$

where Q is the quadrupole moment defined through Eq. 3.9.

Note that the only non-zero energy terms that have been included in this final expression are interactions between a charge distribution and a jellium background.

3.1.2 The method of Dabo, Kozinsky, Singh-Miller and Marzari

Quite a different approach was introduced by Dabo, Kozinsky, Singh-Miller and Marzari [85], who introduced what they termed the density countercharge method (DCC).

In this approach, a corrective potential v_{corr} is constructed,

$$v_{\text{corr}} = v_{\text{iso}} - v_{\text{PBC}}, \quad (3.11)$$

where v_{iso} is the electrostatic potential under isolated boundary conditions, and v_{PBC} is the corresponding electrostatic potential under periodic boundary conditions.

Once such a potential has been calculated, the total correction to the energy is calculated as,

$$E_{\text{corr}} = \frac{1}{2} \int v_{\text{corr}}(\mathbf{r}) n(\mathbf{r}) d\mathbf{r}, \quad (3.12)$$

where $n(\mathbf{r})$ is the electronic charge of the system.

Unlike the other correction strategies considered, this method enables on the fly corrections during the SCF loop of a DFT calculation. The potential defined in

Eq. 3.11 can be added to the electrostatic potential during the calculation. Calculations demonstrate that this procedure is successful at removing finite-size dependence from the simulation of charged molecules under periodic boundary conditions [85].

The DCC method is not applicable to the problem of charged defects in crystals, as the method removes all inter-supercell interactions indiscriminately. In the case of a crystal, this would introduce enormous errors as interactions with both defects and the crystal bulk in image cells would be removed. I consider how the DCC method can be adapted to the problem of crystalline defects in Sec. 4.

3.1.3 The method of Lany and Zunger

As discussed, the MP correction in principle includes a quadrupole correction term. However, no systematic construction for this term was given. The Lany-Zunger (LZ) correction [80, 86] directly attacks this problem by making a practical approximation to Q . This method is derived by assuming that the defect draws polarization charge, as in a classical model. This is given by:

$$\rho_{\text{screen}}^{\text{LZ}}(\mathbf{r}) \underset{\mathbf{r} \rightarrow \infty}{\approx} \frac{q}{\Omega} \left(1 - \frac{1}{\epsilon}\right). \quad (3.13)$$

This charge present across the whole supercell is used to define the quadrupole moment Q , and leads to a reduction in the magnitude of the correction. In fact, this is shown to reduce the MP correction by about a third. Charge models constructed from DFT density differences are found to include this screening charge, as shown in Fig. 3.2 a.

Generally, we may express this reduction in interaction with images by defining an internal polarization ratio f . The MP correction is too large and needs to be reduced by a scaling factor. Then, the complete interaction correction is given as:

$$E_{\text{corr}} = fE^{\text{MP}}. \quad (3.14)$$

3.1. ELECTROSTATIC CORRECTIONS

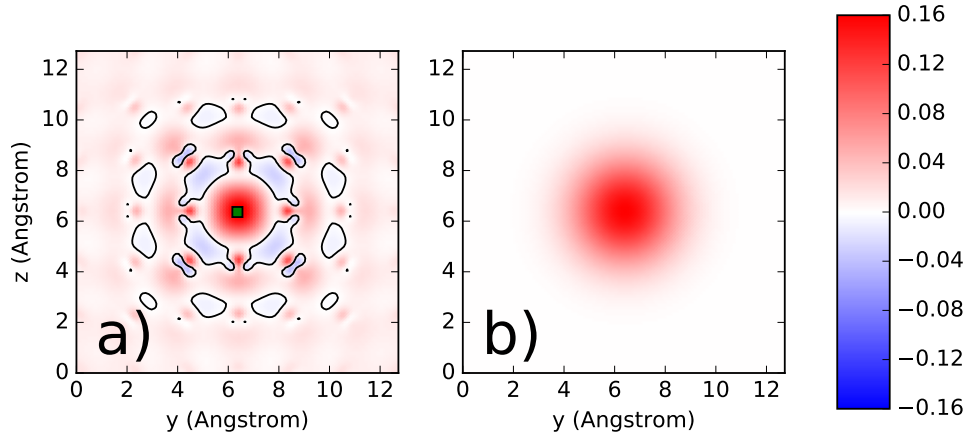


Figure 3.2: Comparison of defect charge models for V_O^{+2} defect in MgO. The total charge is plotted in y and z . a) is a model constructed as a charge density difference between two DFT calculations, and b) is a Gaussian model, as commonly used in the FNV method. The zero density isosurface is shown as a solid black line.

The LZ method provides a practical approximation to f in the form:

$$f^{\text{LZ}} = 1 - c_{\text{sh}} (1 - \epsilon^{-1}), \quad (3.15)$$

where the shape factor, c_{sh} , depends only on the shape of the defect containing supercell. Note that Lany and Zunger originally defined c_{sh} as $-c_{\text{sh}}$, but we follow the definition given by Pasquarello *et al.* [79], as this notation makes it clearer that the LZ method leads to a reduced correction. These factors have been calculated for common supercells[86]. As the LZ method is derived from Eq. 3.2, it is also partly underpinned by an assumption of a cubic supercell. For cubic cells with a high dielectric constant ($\epsilon \rightarrow \infty$) this yields $f^{\text{LZ}} = 0.631$. In contrast, the original MP correction is recovered when $f = 1$. As the LZ method reduces to a scaling of the original MP correction, it also leads to a L^{-1} dependent correction that could produce the a_1 term in Eq. 2.25.

As in Eq. 3.15, the final Lany-Zunger correction is dependent on the dielectric constant of the material being considered. For cubic systems, this dependence is shown in Fig. 3.3.

We note that the LZ method was also introduced with a potential alignment technique based on atomic site averages, performed over a large volume of the cell.

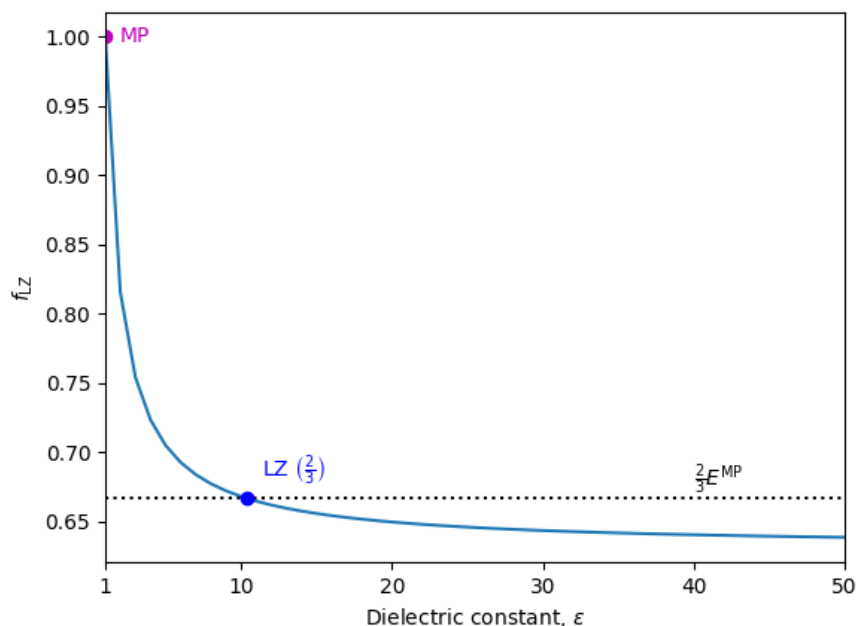


Figure 3.3: Dependence of the LZ correction for cubic supercells on the dielectric constant. When $\epsilon=1$ (i.e. a molecule in vacuum), then the LZ method correctly reduces to the MP method. As the dielectric of the material increases, the LZ correction removes more of the MP correction.

Hence, when LZ results are presented in the literature, they may also include this more complex alignment procedure. I discuss the problem of potential alignment in more detail in Chapter 5.

3.1.4 The method of Freysoldt, Neugebauer and Van de Walle

Another distinct conceptual approach is the defect correction method of Freysoldt, Neugebauer, and Van de Walle (FNV) [87]. This method models the charge as a Gaussian distribution like that shown in Fig. 3.2 b) (or other simple localized distribution), which normally make only a very minor change to the interaction strength E_{corr} , and produces an energy almost identical to $E_{\text{corr}}^{\text{MP}}$. Then, the electrostatic potentials of the model system and the DFT calculation are matched far from the defect, introducing extra polarization effects into the correction. In this method f is not calculated directly, but can be inferred via Eq. 3.14. We would understand the charged potential alignment carried out in this method as improving the description of f .

In this method, the correction is given as:

$$E_{\text{corr}}^{\text{FNV}} = E^{\text{FNV}} - q(\Delta\tilde{V}_{q/0}), \quad (3.16)$$

where E^{FNV} is the interaction energy of the defect charge model used, and $\Delta\tilde{V}_{q/0}$ is the shift in potential between the charged and neutral defect, beyond that introduced by the calculation of E^{FNV} . (Potential alignment is discussed in more detail in Chapter. 5). Eq. 3.16 contains two terms, where E^{FNV} can be identified with the a_1 term, and $-q(\Delta\tilde{V}_{q/0})$ can be associated with the a_3 term, in Eq. 2.25.

3.1.5 The method of Taylor and Bruneval

Taylor and Bruneval [78] argue that the image electrostatics of point defects is already described adequately, and that to make improvements, other sources of error should be considered instead. They introduced the following correction formula,

$$E_{\text{corr}} = \frac{q\alpha_M}{\epsilon L} + q\Delta V + nV, \quad (3.17)$$

where the first correction term is the standard MP interaction correction, the second term is a potential alignment, and the last term is a defect state hybridization correction.

They suggest that the potential alignment should be calculated as,

$$\langle V_{\text{KS}} \rangle = \frac{1}{\Omega} \int_{\Omega} v_{\text{KS}}(\mathbf{r}) d^3\mathbf{r} \quad (3.18)$$

Following from Eq. 3.18, the potential alignment can then be defined as,

$$\Delta V = \langle V_{\text{KS}}^{\text{bulk}} \rangle - \langle V_{\text{KS}}^{\text{defect}} \rangle, \quad (3.19)$$

where the average in Eq. 3.18 is performed for the perfect bulk cell and the supercell containing the charged defect, respectively.

As the average of the electrostatic potential is zero under periodic boundary conditions, Taylor and Bruneval argue that constructing the potential alignment in

this way avoids double counting of the electrostatic potential shift introduced by the image interaction. This argument essentially requires a belief that the electrostatic shift introduced by the charged defect is entirely a finite-size error.

Additionally, they also suggest adding a further correction, allowing for the possibility of defect state hybridization, which they argue can be a significant source of error in some situations. In order to do this, they define the following Hamiltonian for iteration with n nearest neighbors,

$$H_n = H_0 + nV \quad (3.20)$$

where the effective Hamiltonian H_n is made up of H_0 , the Hamiltonian without neighbor interactions, and V is the magnitude of the neighbor interactions.

In order to calculate H_0 and V , they suggest a second calculation where the length of the supercell is doubled. In their argument, this halves the number of nearest neighbors N , allowing the calculation of these terms.

3.1.6 The method of Murphy and Hine

Murphy and Hine [84] extended the Makov-Payne correction to cells of arbitrary shape and dielectric tensor. They defined the screened Madelung potential as,

$$v_M^s = \sum_{\mathbf{R}_i}^{i \neq 0} \frac{1}{\sqrt{\det \underline{\underline{\epsilon}}}} \frac{\operatorname{erfc}\left(\gamma \sqrt{\mathbf{R}_i \cdot \underline{\underline{\epsilon}}^{-1} \cdot \mathbf{R}_i}\right)}{\sqrt{\mathbf{R}_i \cdot \underline{\underline{\epsilon}}^{-1} \cdot \mathbf{R}_i}} + \sum_{\mathbf{G}_i}^{i \neq 0} \frac{4\pi}{\Omega} \times \frac{\exp\left(-\mathbf{G}_i \cdot \underline{\underline{\epsilon}} \cdot \mathbf{G}_i / 4\gamma^2\right)}{\mathbf{G}_i \cdot \underline{\underline{\epsilon}} \cdot \mathbf{G}_i} - \frac{2\gamma}{\sqrt{\pi \det \underline{\underline{\epsilon}}}} - \frac{\pi}{\Omega \gamma^2}, \quad (3.21)$$

where γ is a suitably chosen convergence parameter, and $\underline{\underline{\epsilon}}$ is a 3x3 dielectric matrix.

Following on from the definition in Eq. 3.21, the anisotropic MP correction becomes,

$$E = -\frac{q^2 v_M^s}{2} \quad (3.22)$$

Note that this method assumes that the defect charge present in the defect con-

taining supercell is well approximated by a point charge.

3.1.7 The method of Kumagai and Oba

Kumagai and Oba [81] introduced a systematic way of combining the corrections of Murphy and Hine with that of Freysoldt, Neugebauer and Van de Walle. They realized that the MH expression for the defect site potential given in Eq. 3.21 could be generalized to calculate the potential anywhere in the cell. They presented the following formula,

$$\begin{aligned}
 v_M^s(\mathbf{r} \neq \mathbf{0}) = & \sum_{\mathbf{R}_i} \frac{q}{\sqrt{|\underline{\underline{\epsilon}}|}} \frac{\gamma \sqrt{(\mathbf{R}_i - \mathbf{r}) \cdot \underline{\underline{\epsilon}}^{-1} \cdot (\mathbf{R}_i - \mathbf{r})}}{\sqrt{(\mathbf{R}_i - \mathbf{r}) \cdot \underline{\underline{\epsilon}}^{-1} \cdot (\mathbf{R}_i - \mathbf{r})}} - \frac{\pi q}{\Omega \gamma^2} \\
 & + \sum_{\mathbf{G}_i}^{i \neq 0} \frac{4\pi q}{\Omega} \frac{\exp\left(-\mathbf{G}_i \cdot \underline{\underline{\epsilon}} \cdot \mathbf{G}_i\right)}{\mathbf{G}_i \cdot \underline{\underline{\epsilon}} \cdot \mathbf{G}_i} \cdot \exp(i\mathbf{G}_i \cdot \mathbf{r}).
 \end{aligned} \tag{3.23}$$

As this gives the potential at any point in the cell, this can be used to extend the FNV method.

3.1.8 Discussion of present bulk methods

Out of the considered methods, the FNV approach offers the most flexibility, because both the charge model used and the region over which potential alignment is calculated can be varied, effectively leading to a whole family of charge corrections. These options can allow some fine tuning of the magnitude of the correction to the specific defect being studied. More recent work on the method has looked at fitting these charge models to defect state orbitals directly [88].

The FNV method has the advantage of being extensible to more complex situations, such as surfaces and interfaces [89]. However, it can be complicated in practice by the effects of atomic relaxation, as the movement of ions introduces long range changes in potential not related to alignment effects [79, 81]. The Kumagai-Oba (KO) method [81] has been suggested to circumvent these limitations.

The LZ method requires the dielectric of the system to be constant and isotropic, limiting its application to bulk systems. In this case, the method can be

applied very straightforwardly. Both of these methods are expected to improve the description of finite-size screening, and generally reduce the total correction given by the MP method.

One important question is whether we should expect image charge corrections to have different magnitudes for positive and negative values of q . The corrections based on analytic theory (MP and LZ) are identical for positively and negatively charged defects. The FNV method is observed to break this symmetry when it is applied, a flexibility introduced by the $\Delta\tilde{V}_{q/0}$ term.

3.1.8.1 Usage of present methods

I present the present citation counts for the above methods (using the most highly cited paper if more than one reference paper exists) for the above methods. Although this only allows a very approximate insight into their usage, it still allows us to see the relative popularity of the methods.

Method	Citations ¹	Year
MP [83]	1912	1995
DCC [85]	99	2008
LZ [80]	750	2008
FNV [87]	519	2009
TB [78]	80	2011
MH [84]	51	2013
KO [81]	99	2014

This comparison suggests that the MP, LZ and FNV corrections are the most popular, and that the KO method is gaining popularity very rapidly, considering that the method is the newest considered.

¹Google scholar citations, accessed 23/08/2018.

Chapter 4

Development of the DEFECT_SOLVER code

Aims: In this chapter I develop a new electrostatic correction method based on the use of DFT electronic density differences. A new computer code, DEFECT_SOLVER is developed to calculate the corrections of this new method. To validate the developed code, I demonstrate that this code can reproduce available analytic results.

4.1 Electrostatic corrections

In this thesis, I introduce a new correction method where I calculate interaction corrections from DFT electronic densities directly, rather than approximating the defect charge distribution.

To do this, we follow very similar conceptual lines to the density countercharge method (DCC) of Dabo *et al.* [85], where the charge due to the defect is modeled by an explicit charge distribution and a full electrostatic model system is solved (in the DCC method, corrections are then applied self-consistently within the DFT calculation, in contrast to our approach where corrections are applied after the calculation).

4.1.1 Definition of electrostatic corrections

As originally derived by Dabo *et al.* [85], and then later generalised by Komsa *et al.* [79], electrostatic corrections can be defined as,

$$E_{\text{corr}} = E_{\text{iso}} - E_{\text{PBC}}, \quad (4.1)$$

namely that the correction E_{corr} is defined as the difference in energy of an isolated defect charge, E_{iso} , and the energy of the same defect charge under periodic boundary conditions, E_{PBC} . This defect charge should be picked in order to replicate the errors observed in DFT calculations on charged defects.

Given a defect charge model $\rho(\mathbf{r})$, Poisson's equation can be solved with both kinds of boundary condition, in order to generate the required potentials,

$$\nabla^2 v_{\text{iso}}(\mathbf{r}) = \rho(\mathbf{r}) \quad (\text{Isolated boundary conditions}), \quad (4.2)$$

$$\nabla^2 v_{\text{PBC}}(\mathbf{r}) = \rho(\mathbf{r}) \quad (\text{Periodic boundary conditions}), \quad (4.3)$$

where $v_{\text{iso}}(\mathbf{r})$ is the electrostatic potential of the defect charge under isolated boundary conditions, and $v_{\text{PBC}}(\mathbf{r})$ is the electrostatic potential of the defect charge under periodic boundary conditions.

From these two solutions of Poisson's equation, the two correction energies required in Eq. 4.1 are then defined as,

$$E_{\text{iso}} = \frac{1}{2} \int \rho(\mathbf{r}) v_{\text{iso}}(\mathbf{r}) d\mathbf{r}, \quad (4.4)$$

$$E_{\text{PBC}} = \frac{1}{2} \int \rho(\mathbf{r}) v_{\text{PBC}}(\mathbf{r}) d\mathbf{r}, \quad (4.5)$$

where the same charge model $\rho(\mathbf{r})$ is employed.

The above approach works well for molecules, where the defect charge model can be the entire charge of the molecule, $\rho(\mathbf{r}) = n(\mathbf{r})$. At the Hartree level, this replaces a periodic charged molecule with an isolated charged molecule. This is the basis of the DCC approach [85]. However, this definition of the defect charge is too simplistic for charged defects in dielectric materials.

4.1.2 Extension to dielectric materials

In order to produce a correction method using the approach outlined in Sec. 4.1.1, we first need to pick a defect charge model $\rho(\mathbf{r})$ that is appropriate for charged defects within DFT.

When considering DFT, neutral defects do not display the same supercell size

4.1. ELECTROSTATIC CORRECTIONS

dependence observed for charged defects. Hence, we must distinguish between electronic charge which is present in the case of a neutral defect from that introduced by charging the point defect itself. When ions are not allowed to relax, this can be directly defined as the electronic density difference between the neutral defect and the charged defect in state q . This yields a charge distribution with total magnitude q :

$$\rho(\mathbf{r}) = n_{q=q}^{\text{defect}}(\mathbf{r}) - n_{q=0}^{\text{defect}}(\mathbf{r}), \quad (4.6)$$

where $n_{q=q}^{\text{defect}}$ is the electronic density of the supercell containing the charged defect and $n_{q=0}^{\text{defect}}$ is the electronic density when the defect is in a charge neutral state. If relaxation around the defect is not allowed, the atomic structure is identical in both calculations.

When the defect geometry is allowed to relax, there is more flexibility in the construction of the defect charge model, $\rho(\mathbf{r})$. I fully relax the atomic geometry of the charged defect in the calculation of $n_{q=q}^{\text{defect}}$. Then, I use this same ionic geometry in the calculation of $n_{q=0}^{\text{defect}}$. This matches the ionic structure that is present in the image cells. Effectively, this replaces charged defects in the image cells with neutral defects of the same ionic structure. If the geometry is also relaxed in the calculation of $n_{q=0}^{\text{defect}}$, large fluctuations are introduced into $\rho(\mathbf{r})$, reflecting the movement of ions.

This charge model $\rho(\mathbf{r})$ includes a jellium background only implicitly, and hence is of total magnitude q . When the interaction potential v_{corr} is calculated, a jellium background is effectively introduced in exactly the same way as for DFT calculations. This is because we follow the same convention as the DFT calculation that generated the charge model [90, 30], and set the average value of the periodic part of the interaction correction model v_{PBC} to zero, in the same way as the average electrostatic potential V within the DFT calculation is set to zero.

Secondly, as this defect charge is present inside a dielectric material, the Poisson equations in Eqs. 4.2 and 4.3 should be replaced by the appropriate screened

equations, producing

$$\nabla[\boldsymbol{\varepsilon}(\mathbf{r})\nabla v_{\text{iso}}(\mathbf{r})] = \rho(\mathbf{r}) \quad (\text{Isolated boundary conditions}), \quad (4.7)$$

$$\nabla[\boldsymbol{\varepsilon}(\mathbf{r})\nabla v_{\text{PBC}}(\mathbf{r})] = \rho(\mathbf{r}) \quad (\text{Periodic boundary conditions}), \quad (4.8)$$

where the dielectric tensor $\boldsymbol{\varepsilon}$ has been introduced at each point in space.

Once both $\boldsymbol{\varepsilon}(\mathbf{r})$ and $\rho(\mathbf{r})$ are defined, the corrective potentials can be calculated by solving Eqs. 4.7 and 4.7. Then, these potentials are used to calculate the required energy components E_{PBC} and E_{iso} , from their definitions in Eqs. 4.4 and 4.5. Finally, these energies are combined using Eq. 4.1 into the final correction.

When using both the defect charge model defined in Eq. 4.6 and the screened potentials given in Eqs. 4.7 and 4.8, we term the resultant correction the screened Poisson (SP) correction.

I use the open source libraries `DL_MG` [91, 92, 93] and `PSPFFT` [94] to solve these electrostatic problems directly, without the introduction of further approximations. `DL_MG` is an iterative multigrid solver [95]. `PSPFFT` is an FFT based solver for isolated boundary conditions. I describe these libraries in more detail in the next section.

4.1.3 Electrostatic libraries: PSPFFT

The first library I used is called `PSPFFT` [94], for **P**oisson **S**olver **P**arallel **F**FT. This library is written in Fortran 95 in an object oriented style. The library takes advantage of the `FFTW` [96] library to perform highly efficient FFTs. Additionally, the library supports both MPI and OpenMP parallelization. The `PSPFFT` library was developed with gravitational problems in mind, so can only be used for problems where the dielectric is a constant scalar and the Poisson equation is solved under isolated boundary conditions.

Using this code, Poisson’s equation is solved using the “transform method” [97]. Although limited to problems with a uniform dielectric constant and isolated boundary techniques, the method is able to solve this limited problem rapidly [98, 99]. Additionally, as the quality of the integration grid is improved, the exact isolated

solution is approached [94].

4.1.4 Electrostatic libraries: DL_MG

The DL_MG [93, 92] library is more versatile, allowing a diagonal dielectric constant to be defined at each point in space. The library is parallel 3D geometric high order finite difference multigrid solver for Poisson's equation. This method is more flexible, although computationally more demanding.

Multigrid methods are well established [95], and this particular library was already developed with DFT applications in mind [93]. It will probably be available to perform 2D calculations in CASTEP in the future.

4.2 Description of main subroutines

I encapsulated calls to the above libraries in the following functions of the DE-FECT_SOLVER code.

4.2.1 get_hartree_isolated

This function solves Poisson's equation under isolated boundary conditions (Eq. 4.2), given an input charge distribution $\rho(\mathbf{r})$ and a uniform scalar dielectric constant. In order to validate this part of the code, I used Gaussian charge distributions, where the isolated interaction energy is known analytically [89].

Given the Gaussian charge distribution defined as,

$$\rho(\mathbf{r}) = \frac{q}{\sigma^3 (2\pi)^{\frac{3}{2}}} \exp\left(-\frac{r^2}{2\sigma^2}\right) \quad (4.9)$$

where σ is the standard deviation of the charge and q is the total charge, then the total interaction energy under isolated boundary conditions is given as,

$$E = \frac{q^2}{2\sqrt{\pi}\epsilon\sigma}. \quad (4.10)$$

The PSPFFT library cannot be expected to exactly reproduce this result, due to discretization error [100]. Instead, it should tend to this result as the quality of the integration grid is increased.

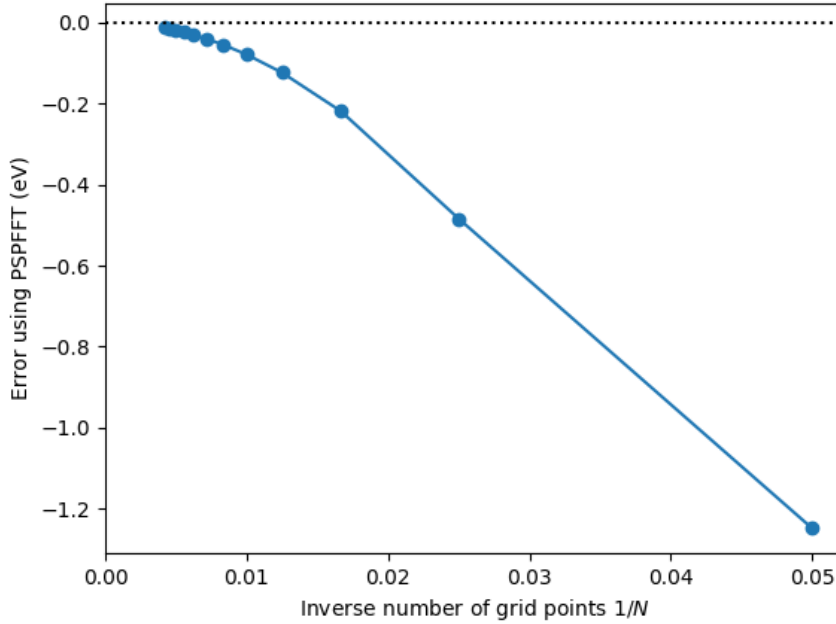


Figure 4.1: Error in the total energy calculated using `DEFECT_SOLVER` and the `PSPFFT` library for a Gaussian charge distribution with spread $\sigma = 1.0$ on a $20 \times 20 \times 20$ Å grid, with increasing grid size N . The energy is calculated on a grid with $N \times N \times N$ total points.

Fig. 4.1 demonstrates that the correct analytic solution is approached as the quality of the integration grid is improved. This validates this part of the `DEFECT_SOLVER` code, and provides the tool to calculate E_{iso} for materials with a uniform dielectric constant.

4.2.2 `get_hartree_periodic`

Secondly, I consider solving the Poisson equation under periodic boundary conditions within a dielectric (Eq. 4.8). Just as in DFT, such calculations implicitly incorporate a jellium background. The `GET_HARTREE_PERIODIC` routine calls the `DL_MG` library to solve Eq. 4.8, so it can be used for any space varying diagonal dielectric profile. To test this routine, I used the analytic Madelung sum, which gives the energy difference between a point charge in free space under isolated and periodic boundary conditions. As the width of the Gaussian test charge becomes small in comparison to width of the simulation supercell, the calculated energy should tend to the energy of a point charge. The width of the test Gaussian charge was kept

constant at 0.53 \AA (1 Bohr).

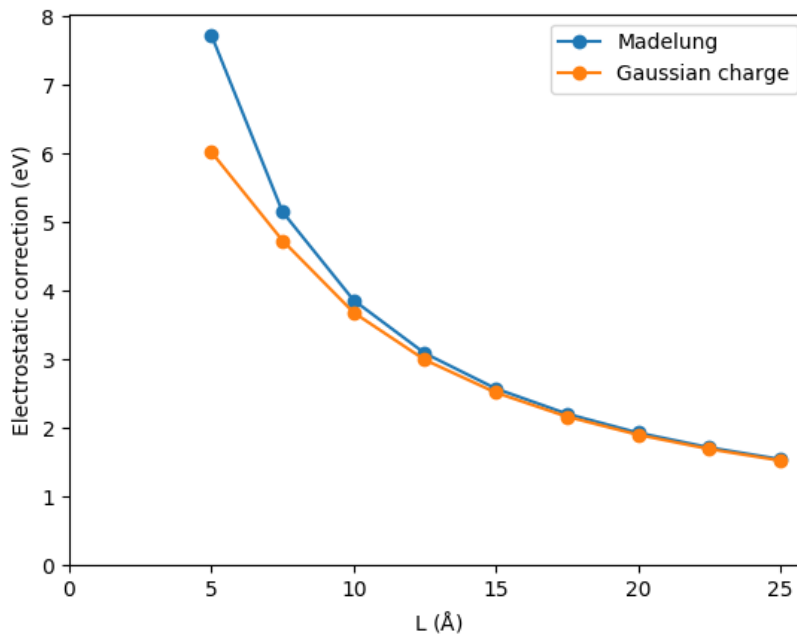


Figure 4.2: Comparison between the analytic Madelung correction and the energy correction calculated using a Gaussian charge model in the `DEFECT_SOLVER` code. The difference between the two calculations tends to zero as the size of the simulation supercell is increased. This is the anticipated result if the code is performing correctly.

As shown in Fig. 4.2, my code passes this consistency test. This also demonstrates the result often mentioned in regard to the FNV method, that the use of a Gaussian charge model in this approach doesn't introduce much difference from a Madelung correction [87, 88].

4.2.3 `get_hartree_isolated_super`

The function `GET_HARTREE_ISOLATED` described above only works for a uniform dielectric constant (Eq. 4.2). To solve the same problem for a diagonal dielectric tensor that can vary at each point in space (Eq. 4.7) requires a different approach. I used the `DL_MG` library to do this, but it wasn't able to solve this problem directly as it doesn't implement isolated boundary conditions.

Instead, I set $v = 0$ boundary conditions at the edges, and then increased the size of the simulation region, until the error of this approximation was minimised.

4.2. DESCRIPTION OF MAIN SUBROUTINES

This works, as the potential of any isolated charge distribution tends to zero as the distance from the charge increases. In this approach, there is no electric charge outside of the original simulation region, but the size of the dielectric region is increased, placing the $\nu = 0$ boundary conditions further from the charge distribution of interest. An example of this procedure is shown in Fig. 4.3, where the calculated energies are compared for an example defect in diamond. In this example, the dielectric is constant and the method can be compared against the use of GET_HARTREE_ISOLATED for the same problem.

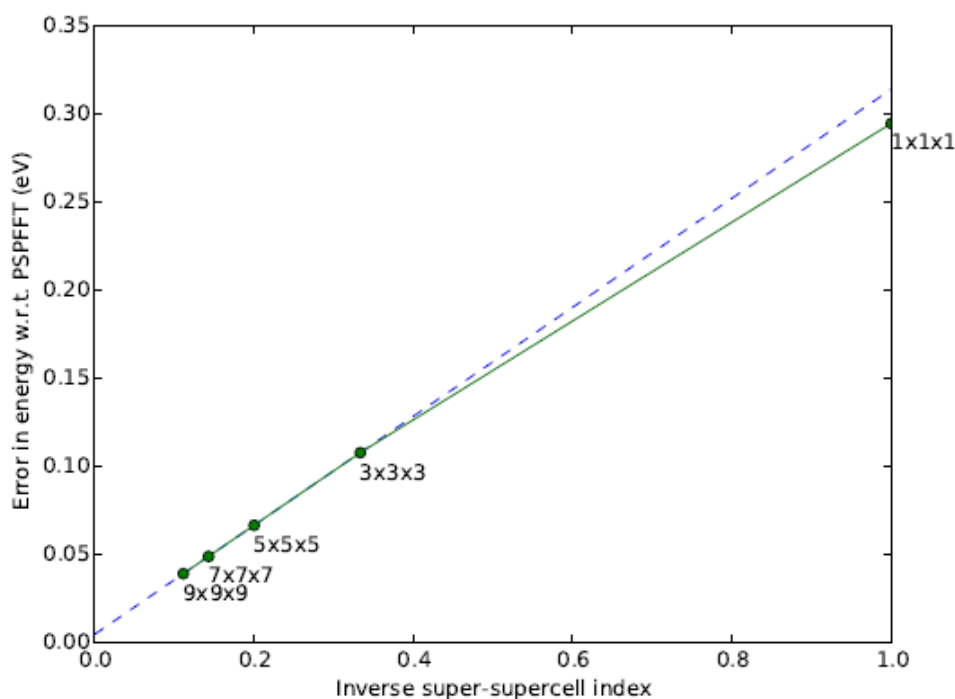


Figure 4.3: Error in calculated isolated interaction energy using the GET_HARTREE_ISOLATED_SUPER subroutine, against the GET_HARTREE_ISOLATED method, as the size of the classical simulation region is increased. The error in energy decreases linearly with inverse supercell size. The blue dashed line shows a linear fit to the two largest cells considered. The test example is a defect charge from the 2x2x2 supercell containing the defect charge model of the unrelaxed V_C^{+1} defect in diamond.

In order to make the implementation of this method simpler, the simulation region was only increased in integer multiples. An example of a 3x3x3 supercell is shown in Fig. 4.4.

In principle, the size of the simulation box should be increased until the re-

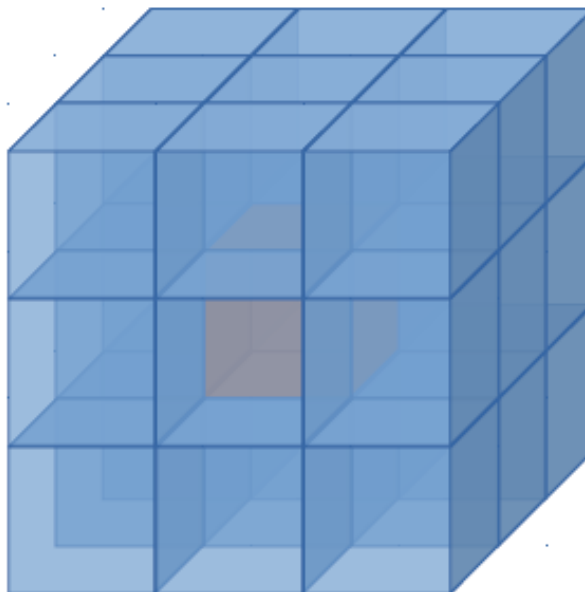


Figure 4.4: Example of a $3 \times 3 \times 3$ simulation region used for the GET_HARTREE_ISOLATED_SUPER method. The orange cube in the middle contains the charge distribution for which Poisson's equation is being solved. The blue cubes contain empty space, and the potential is set to zero at the edges of the composite cube.

quired accuracy is achieved. In practice, I found that the linear extrapolation introduced was accurate enough for the calculations performed in this thesis. This linear extrapolation method remained reliable when a spatially varying dielectric profile was used, and the GET_HARTREE_ISOLATED method could no longer be employed. The errors introduced by linear extrapolation were typically less than 0.005 eV. Unlike for DFT supercells, these electrostatic supercells could be simulated significantly more cheaply, and $13 \times 13 \times 13$ models could be simulated and used to validate the method.

Conclusions: An extension to the method of Dabo *et. al.* was constructed for charged defects in dielectrics, and code was developed to calculate these corrections.

Chapter 5

Jellium and potential alignment

In this chapter I consider other kinds of finite-size corrections, that could be required in addition to the electrostatic corrections considered in Chapter 3. First I consider the role of neutralizing jellium in more detail, finding a significant bug in past versions of the CASTEP DFT code. Then, I consider the more common topic of potential alignment, which is known to be partly linked to electrostatic corrections. I decompose the defect formation process into steps and demonstrate that significant alignment shifts are introduced by changes in the number of atoms in the supercells being compared, which are unrelated to electrostatic corrections.

5.1 The jellium background and DFT

One additional problem in charged DFT calculations is that of neutralization. Formally, the energy of a periodic system with net charge will always be infinite. As a result, DFT calculations on charged systems actually contain neutralization charge, so that the total charge is zero [82, 101]. The extra charge placed into the cell in order to charge neutralize the system should be distributed across the cell, so that it is diffuse and hence only weakly interacts with the 'real' charge in the system. In periodic DFT calculations, charge neutralization is almost always achieved with a uniform jellium background. The density of this jellium background is $-q/\Omega$, where Ω is the total volume of the cell, and q is the net charge of the cell (excluding the jellium background itself).

This jellium background can be implemented in DFT codes in several ways,

either as implicit or explicit charge. If the jellium background is included explicitly, it is included in the charge density when electrostatics is performed, otherwise it is not included in the density matrix, but only implicitly included in the way the total energy is evaluated. The DFT codes `CASTEP`, `VASP` and `CP2K` include the jellium background implicitly. In contrast, `QUANTUM ESPRESSO` includes the jellium background explicitly in the electronic density, $n(\mathbf{r})$. The way in which a DFT code internally handles a jellium background is not visible to an end user, as when the DFT code outputs the electronic density, the jellium background is normally removed in both cases.

The jellium background is also present in the electrostatic model used for image charge correction, so the main non-physical contribution made by the jellium background to the total energy is removed in the calculation of E^{int} . This effect can be seen most clearly in the corrections required for periodic slab models [89], where the interaction with the jellium background is often the dominant source of error.

The contribution of jellium to defect formation energies is confused in the literature, as sometimes the total energy for charged systems is not correctly calculated by the underlying DFT code.

The energy expression originally derived is correct for neutral systems, and hence works for charged systems that have been charged neutralized by a jellium background tool [102]. In order to calculate meaningful energies, all the electrostatic energy components must be calculated consistently, which is the case if the originally derived expressions are implemented correctly. Generally, the jellium contribution to the ion-ion and electron-electron interaction energies is calculated correctly, as both of these terms require an assumption of charge neutrality. However, one of the contributions of the interaction of pseudo-ions with the valence electrons and jellium is not always correct. This E_{NC} term should be defined in terms of the ionic charge, as the expression is given in Eq. 2.10. Instead, in a standard textbook [30] it is given as:

$$E_{\text{NC}} = \left(\sum_i \alpha_i \right) \frac{N_e}{\Omega}, \quad (5.1)$$

Table 5.1: Pseudopotential dependence of formation energy on the way the E_{NC} is calculated. For the calculation of E_{NC} , Eq. 5.1 was used. In contrast, for E_{NC}^* , this was corrected to multiplication of a factor of $(N_e + q)/\Omega$. The definition of E_{NC} only affects total energies and has no impact on potentials, and hence potential alignment. Standard deviations are shown in the last row. We note that CASTEP incorrectly neglected this component of the jellium energy when we started this project. We ensured that this was corrected in version 16.1.2. of CASTEP

Pseudopotential	E_{NC} (eV)	E_{NC}^* (eV)	$E_{\text{NC}}^* + q\Delta V_{\text{AB}}$ (eV)
NC	-2.751	7.305	7.078
US	0.299	7.311	7.116
QC5	-1.445	7.226	7.080
OTFG	3.195	7.324	7.121
σ	1.685	0.016	0.011

where each individual ion i in the system contributes a pseudopotential dependent term α_i to the total energy, interacting with the average electronic density, given by the number of electrons N_e in the cell, divided by the cell volume Ω . But this form of the expression neglects the charge contribution of the jellium to the electronic charge density (N_e/Ω) and gives the wrong energy for the charged case. Instead, this term should become $(N_e + q)/\Omega$, where q is net charge of the system that is being compensated by jellium. If this is not the case, then the system is not properly charge neutralized. This problem is avoided if the original definition given in Eq. 2.10 is used.

The most clear signature of this problem is that defect formation energies become strongly pseudopotential dependent. I used the F center in MgO as an illustrative example in Table 5.1. In the worst case, we find a 5 eV shift in formation energy between two different pseudopotentials. Using a different pseudopotential modifies all energy terms in the formation energy, but Eq. 2.23 should still yield meaningful results if jellium has been introduced consistently. This error becomes less severe for larger cells as N_e increases relative to q .

The energy shifts shown in Table 5.1 demonstrate that the total energy does include electrostatic interaction between the jellium background and the full electron+ion system, in direct contrast with the traditional view [86]. This energy contribution is required for a pseudopotential independent formation energy.

A further warning sign of this implementation problem is a significant failure

to obey Koopman’s DFT theorem [68, 103], as the energy of the charged system (with an electron removed) will be incorrectly calculated. Although this theorem is not expected to be exact, it is already established that failures to obey this condition for bulk band states should be very small in correctly implemented DFT codes, and should be introduced by failures of approximate exchange-correlation functionals.

If a formation energy calculation contains an incorrect energy for the charged state $E_{\text{defect}}^{\text{DFT}}$, then there are several additional schemes in the literature that compensate this error. One choice is to re-define μ_e as the numerical ionization energy I , rather than the valence band maximum ε_{VBM} [104]. I is directly calculated as the change in energy when an electron is removed from the bulk system. This resolves the problem, as the error introduced into μ_e compensates the error in $E_{\text{defect}}^{\text{DFT}}$. This choice only leads to significant energy contributions when Koopman’s condition is not obeyed. Another choice would be to perform a ‘jellium neutralization’ procedure [105], performing a similar role. These kinds of procedure should not be required when using the correct expression for total energy.

5.2 Potential alignment and its causes

A further problem in defect calculations is “potential alignment”. This was first discussed in the literature for calculations on charged defects in 1992 [106]. As in periodic DFT, the average potential is neglected and set to zero, this unknown and neglected average could change between the calculations on the bulk and the charged defects. If this is the case, it would introduce an energy difference for charged systems:

$$\Delta E_{\text{PA}} = q\Delta V, \quad (5.2)$$

where there is an energy change ΔE_{PA} that is introduced by the neglected change in the average potential, ΔV . q is the charge state of the system. This energy shift is introduced as we have referenced the energies of our cells to ε_{VBM} in the bulk cell.

5.2.1 Calculating the potential alignment in practice

Generally speaking, when using PBC DFT, total energies of neutral systems can be directly compared between different DFT calculations, but the eigenvalues can

always be shifted by an unknown amount, this unknown amount being introduced by neglect of the average potential. If the system has a net charge of zero, then any arbitrary shift in potential will effect the positive and negative charges equally, and produce no change in total energy. In contrast, when the system is charged, both the eigenvalues and the total energy can be affected by the implicit neglect of the average potential.

If the shift in the electrostatic potential introduced by neglect of the average potential can be identified, it's non-physical contribution to the formation energy can be removed. In order to determine the shift, a potential difference between a supercell containing the charged defect and a supercell of the same size containing the bulk crystal can be calculated,

$$\Delta V_{q/b}(\mathbf{r}) = V_q(\mathbf{r}) - V_b(\mathbf{r}), \quad (5.3)$$

where the electrostatic potential of the supercell containing the charged defect, V_q is compared against the potential of a bulk supercell of the same shape, V_b . As the average of both the electrostatic potentials V_q and V_b is zero, the average of $\Delta V_{q/b}$ over the entire supercell will also be zero. To determine a scalar potential shift, $\Delta V_{q/b}$ between the two configurations, it must be averaged over some region of the supercell that is chosen to reproduce bulk properties [88]:

$$\Delta V_{q/b} = \Delta V_{q/b}(\mathbf{r}) \Big|_{\text{far}}. \quad (5.4)$$

If the 'far region' that $\Delta V_{q/b}$ is averaged over does reproduce bulk properties in the defective cell, then the difference between the potentials must be the unphysical potential shift introduced into the calculation by neglect of the average potential. Hence,

$$\Delta V_{\text{PA}} \approx \Delta V_{q/b}. \quad (5.5)$$

Eq. 5.4 inevitably introduces a lot of choice in the way the far region that is averaged over is defined, potentially leading to different values of the scalar alignment shift $\Delta V_{q/b}$. I normally restrict myself to one of the simplest averaging techniques,

calculating the xy planar average of $\Delta V_{q/b}(\mathbf{r})$ and then taking the z-value furthest from the defect. In this case, the far region is the xy plane furthest from the defect. Note that Eq. 5.5 is approximate, as the scalar potential shift introduced by neglect of the average potential will only be correctly identified if the 'far' region the average is performed over does in fact reproduce bulk properties. An example of the xy planar average is shown in Fig. 5.1, where the alignment term would be taken far from the defect, at $z=0$.

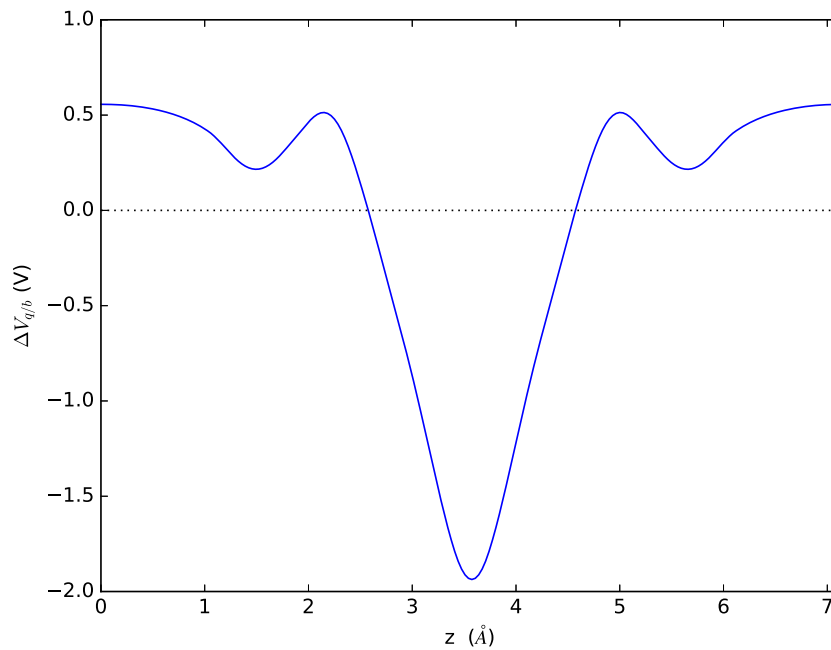


Figure 5.1: The difference between the xy-averaged electrostatic potential of a V_C^2 defect in a $2 \times 2 \times 2$ diamond supercell (with full ionic relaxation), and an equivalent bulk cell of the same size. The defect is placed at the center of the cubic supercell. A potential difference of zero (denoted by the dotted line) is not recovered far from the defect. For this example, $\Delta V_{q/b} = 0.56$ V. The bulk potential is most strongly modified near to the defect, at the center of the supercell.

5.2.2 Model system: Gaussian charge in a box

In the present literature, the methodological comparison paper by Komsa *et al.* is influential [79]. It discusses the example of point and Gaussian charges in a box, and uses this to explain potential alignment. I will consider the example of a Gaussian charge in an otherwise empty box in more detail. First, I show an example charge

distribution in Fig. 5.2.

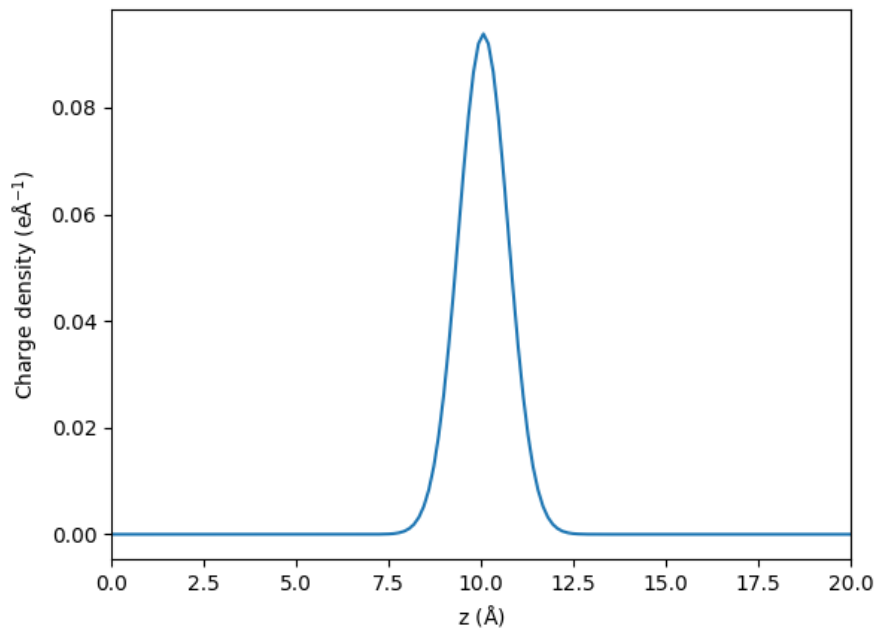


Figure 5.2: Charge distribution of a Gaussian charge, with $\sigma = 1.0 \text{ \AA}$, at the center of a 40 \AA cubic box.

I used the DEFECT_SOLVER code (as described in Chapter 4) to calculate the interactions of this charge under both PBC and isolated boundary conditions, producing Fig. 5.3. Note the high similarity between the shapes of the two potentials. This is the case as the only additional interaction under PBC is that the charge will interact with its own images. The images are far away compared to the self interaction within the cell, and hence is a weaker interaction. Secondly, neglect of the average potential introduces a large energy shift, as the average electrostatic potential under isolated boundary conditions is not zero.

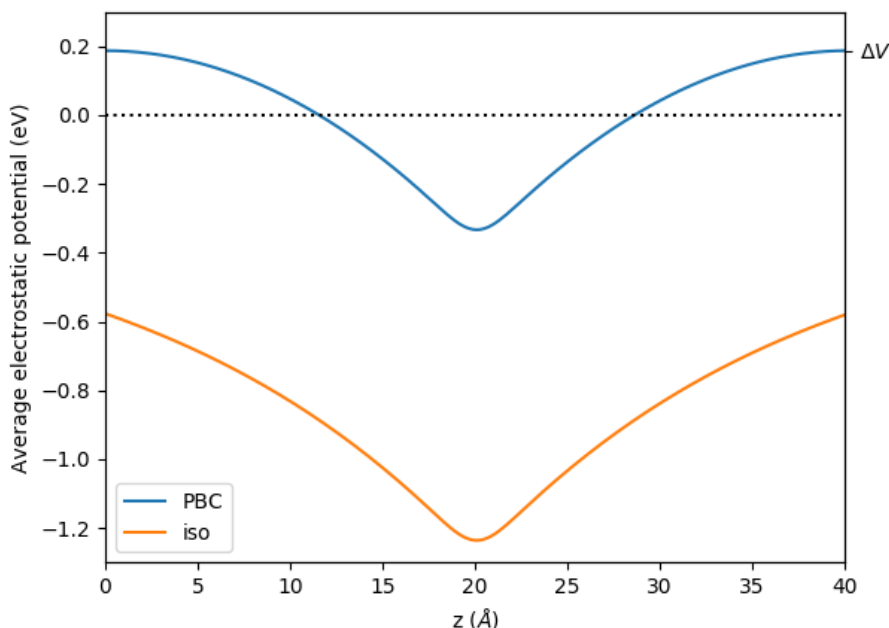


Figure 5.3: The resultant electrostatic potentials of the charge shown in Fig. 5.2, under both PBC and isolated boundary conditions. The shape of the two potentials is very similar, but due to neglect of the average potential, there is a uniform shift ΔV between the two potentials. Even when this shift is removed, the potentials are not identical, due to the interaction of the Gaussian charge with its images in neighboring cells. These interactions tend to zero as the the volume of the cell tends to infinity.

Applying an electrostatic correction using the DEFECT SOLVER code converts the PBC energies into isolated energies, as we would expect, shown in Fig. 5.4. This is the aim when we apply an electrostatic correction. As this is a simple model calculation, rather than a DFT calculation, this is a trivial result.

In the case of a DFT calculation, the electrostatic system requiring correction (the DFT calculation containing the charged defect) and corrective model (the calculation of the E_{corr} correction) will not be identical.

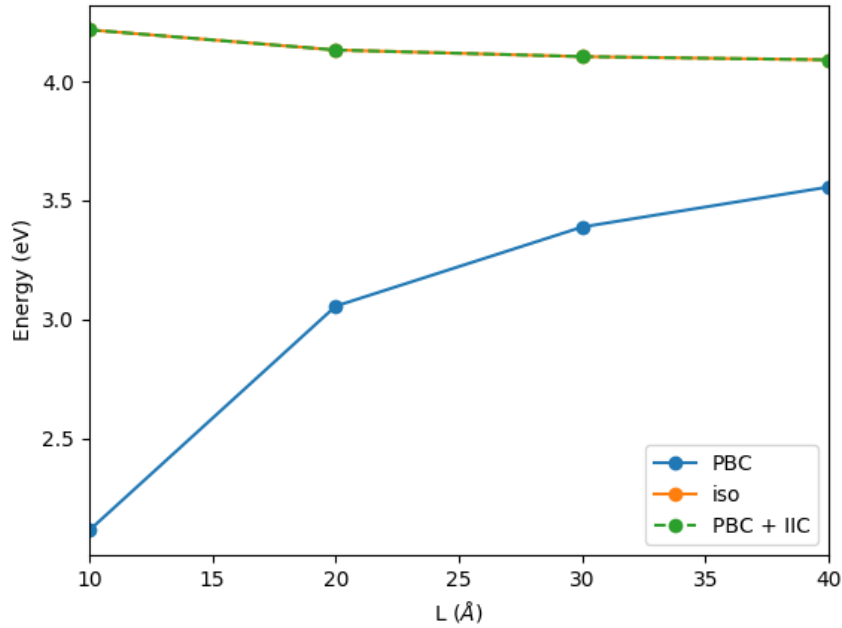


Figure 5.4: Dependence of the electrostatic energies under PBC (blue line) and isolated boundary conditions (orange line), on the size of the cubic supercell containing the charge. Note that application of an electrostatic correction E_{corr} (green dashed line) converts the PBC energy into the isolated energy, as expected. Note that as all the energies are calculated using the DEFECT_SOLVER code, this correction is ideal.

As the energies are no longer size-dependent, performing additional potential alignment can only make the results worse. In Fig. 5.5, we compare the errors in the PBC energy recreating the isolated energy, given several possible corrections. Including potential alignment between the charged and neutral calculations introduces error.

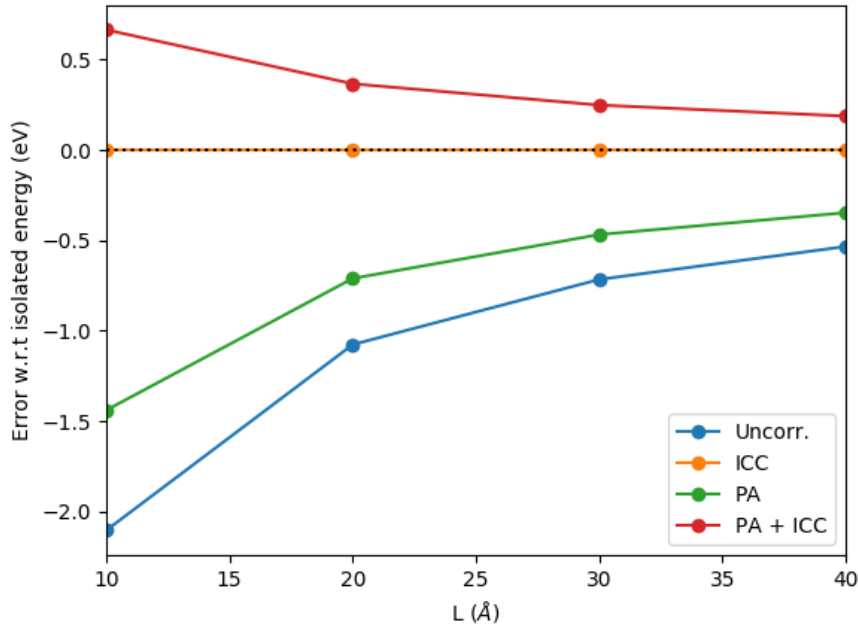


Figure 5.5: Electrostatic errors of various correction strategies, defined as the difference between the PBC energy and the isolated energy calculated using DEFECT SOLVER. The uncorrected results are shown by the blue line. As the size of the cell is increased, the interaction with images decreases, and the error in the uncorrected results reduces. The electrostatic correction shows ideal performance (orange line), but also including a potential alignment (PA) correction makes the results worse. Adding just a potential alignment term produces the green line, and adding both potential alignment and the calculated electrostatic correction produces the red line.

The above example justifies the FNV method. In this method, the potential alignment produced by E_{PBC} is removed from the potential alignment correction. In the Gaussian example, this will produce an alignment correction of zero. Hence, the FNV method shows ideal performance on this model problem. Additionally, the model clearly shows that potential shifts present in E_{PBC} can be double counted in the potential alignment scheme, if care is not taken.

Although this example is useful and interesting, it does contain two shortcomings that can lead to the wrong conclusions being drawn. Firstly, the cell is empty, apart from the charge present, and hence $\epsilon=1$. Secondly, as there are no atoms in the cell, there is no change in atom number. We find that both these features are important to understand potential alignment in the case of charged defects.

5.2.3 A new decomposition of potential alignment

In the standard approach, ΔV_{PA} is inferred by comparing the electrostatic potentials of a supercell of the bulk material and a supercell containing the charged defect, via Eqs. 5.3, 5.4 and 5.5. However, when the problem is approached in this way, it remains unclear what aspect of the calculation is introducing an unphysical potential shift. In order to further explore the causes of potential alignment, we split the process of forming a charged defect into steps, and compare the potentials of four DFT calculations. Such a procedure is illustrated in Figure 5.6. As the start and end DFT calculations are identical to the standard approach, splitting up the alignment in this way produces a total potential alignment $\Delta V_{q/b}(\mathbf{r})$ which is identical. This leads to the following expression for the total alignment,

$$\Delta V_{q/b}(\mathbf{r}) = \Delta V_{AB}(\mathbf{r}) + \Delta V_{BC}(\mathbf{r}) + \Delta V_{CD}(\mathbf{r}), \quad (5.6)$$

where the total change in potential of the bulk and defective systems $\Delta V_{q/b}$ is composed of the three alignment terms between the four configurations introduced via Fig. 5.6. Evaluating the potential in this way does require two additional single-point DFT calculations that would not otherwise be carried out (configurations B and C), whereas traditional approaches use only configurations that already have been calculated to evaluate the formation energy. We note the charge model we defined in Eq. 4.6 is the charge density difference between configurations C and D. I show below an example of this decomposition of the total potential difference in Fig. 5.7, for a V_C^{-2} defect in diamond.

5.2.3.1 The ΔV_{AB} component

Interesting, in our example in Fig. 5.7, we observe that a significant potential shift is introduced far from the defect by the removal of a carbon atom from the supercell alone, producing the ΔV_{AB} component. This particular alignment component is shown in Fig. 5.8, for the diamond supercell.

The ΔV_{AB} component is extremely local to the defect site, so bulk properties are quickly recovered far from the defect. This is shown by how quickly ΔV_{AB} takes

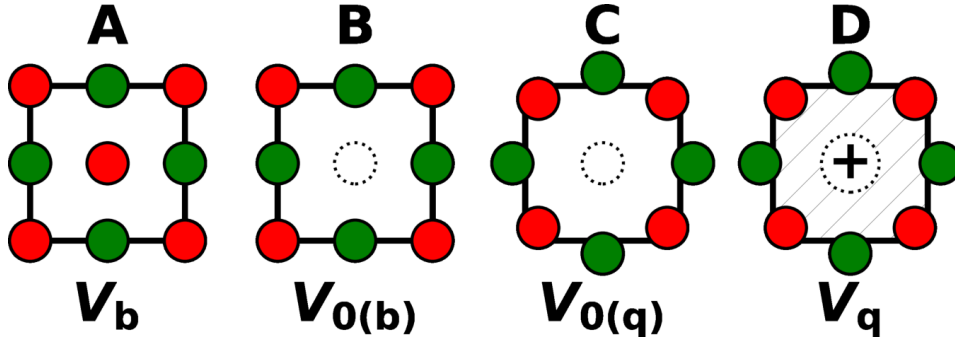


Figure 5.6: Schematic process of forming a charged defect in a periodic DFT calculation. Each lettered square denotes a DFT single-point calculation. In A, the host material is simulated, without a defect. In B, atoms are removed to form a vacancy (or added to form an interstitial), but the ionic structure is not yet relaxed. In C, the final ionic structure of the relaxed charged defect is adopted, but the charge is kept neutral. Finally, in D, electrons are exchanged to reach the required charge state. The ionic geometry in C is maintained, which is the relaxed geometry of this system. Configurations A and D are real states of the system, but B and C are artificial configurations used to break the defect formation process into steps. Only the final configuration D has a formal net charge compensated by a jellium background. The notation given below the figure is chosen to be similar to the conventional notation, but we prefer the alphabetical labels in this paper, to emphasize that we are not only using the conventional reference configurations.

a constant value far from the defect. This ensures that the average in Eq. 5.4 can be carried out easily and without ambiguity – any sensible averaging technique will return the same value. As a result, for this component of potential alignment, we expect the approximate Eq. 5.5 to be very accurate.

ΔV_{AB} can be readily approximated by simply placing an atom of the type being exchanged in a periodic box of the same size, as justified in Fig. 5.9. This approximation is accurate to $\sim 30\%$ for the examples we considered, as shown in Table 5.2. Each atom present in the periodic DFT supercell makes a contribution to the average potential (which is conventionally neglected and set to zero) and hence changing the number of atoms in the supercell modifies the potential shift introduced by neglect of the average potential.

The electrostatic potentials depend on the exact distribution of electric charge within the atom. As a consequence, any component of a DFT calculation that modifies the electron density can also modify the potential shift associated with each

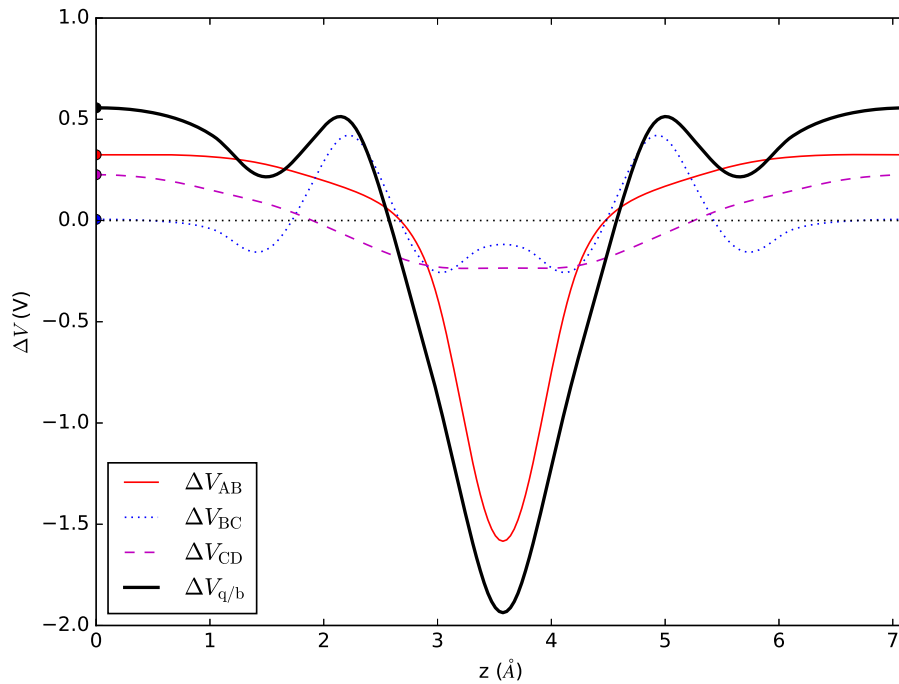


Figure 5.7: Comparison of all the potential delta components of a V_C^2 defect in a $2 \times 2 \times 2$ diamond supercell. The ΔV_{AB} component is explored in Fig. 5.8, and the ΔV_{CD} component is explored more detail in Fig. 5.10. For this example, $\Delta V_{AB}=0.32$ V, $\Delta V_{BC}=0.01$ V, and $\Delta V_{CD}=0.23$ V.

atom. The atomic species is clearly the most important, but the chemical environment the atom is present in also makes an important contribution to the distribution of its electric charge.

We will further develop these ideas in section 5.2.4, in order to predict how ΔV_{AB} scales with the size of the supercell.

5.2.3.2 The ΔV_{BC} component

The ΔV_{BC} component is the most challenging to interpret. This potential change is introduced when the final ionic configuration of charged defect is introduced. Hence, this component is zero by definition when the formation energy of an unrelaxed defect is considered. An example of all three components, along with the total change in potential is shown in Fig. 5.7. For the example of diamond, this last alignment component makes the smallest contribution to the total potential shift far from the defect. In this example, the relaxation of ions makes almost no change to the electrostatic potential far from the defect. In this case, it appears that neglect

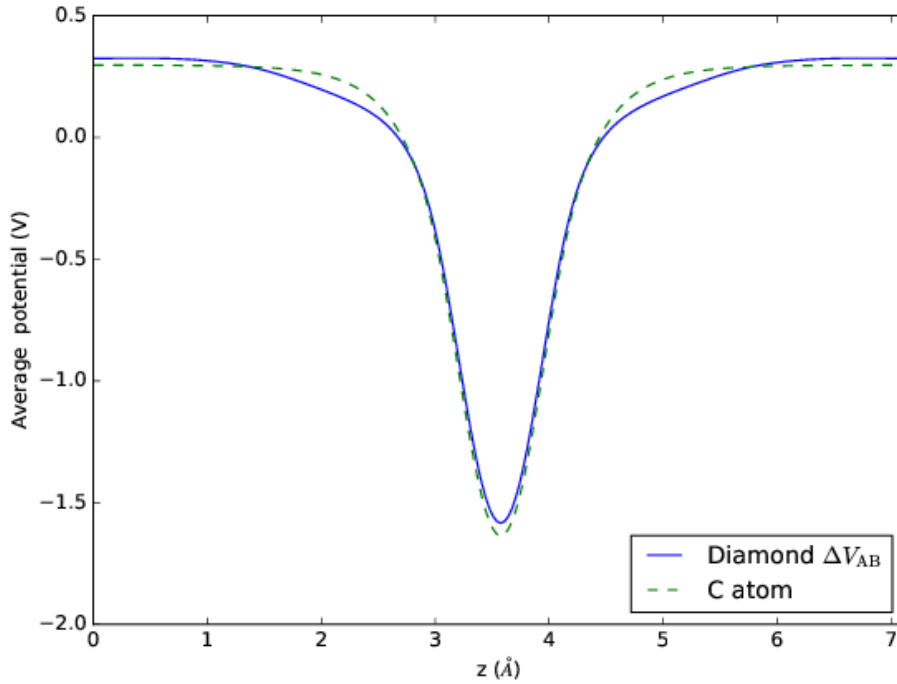


Figure 5.8: Comparison between the ΔV_{AB} alignment component of a $2 \times 2 \times 2$ supercell of diamond when a carbon atom is removed, with the potential of a carbon atom placed in an empty periodic cell of the same size. In this example, $\Delta V_{AB}(z=0) = 0.325$ V and $V_{C \text{ atom}}(z=0) = 0.297$ V.

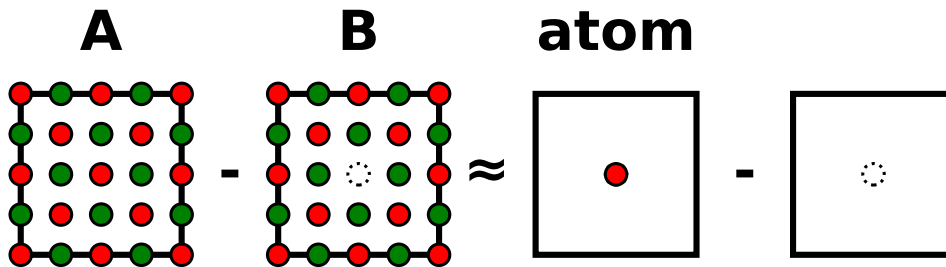


Figure 5.9: Schematic diagram of the approximation of ΔV_{AB} potential alignment component, as in Fig. 5.8. Our results show that this is approximated by a calculation on an isolated atom. This is justified as shown in the diagram, because the crystal appears to play only a secondary role. It changes the electrostatic distribution of charge associated with the atom, but this is a modification rather than a total change in character. The case of an isolated atom is simple enough to attack analytically, and predicts that the potential shift introduced will be volume dependent, as in Eq. 5.13.

5.2. POTENTIAL ALIGNMENT AND ITS CAUSES

Table 5.2: Comparison between alignment constants calculated between configurations A and B, with the potential alignment introduced by an isolated atom of the type being removed. The percentage errors reveal that there is a strong relationship between the alignment constants, but that this is a significant variance. The V_{atom} terms scale ideally with inverse volume. The ΔV_{AB} potential alignment terms retain an approximate inverse volume scaling, but the introduced noise prevents highly accurate extrapolation via Eq. 2.25.

System	Supercell	ΔV_{AB} (V)	V_{atom} (V)	Error (%)
Diamond (C vacancy)	1×1×1	-1.87	-2.35	-25.4
	2×2×2	-0.32	-0.30	8.4
	3×3×3	-0.10	-0.09	15.7
	4×4×4	-0.05	-0.04	18.4
MgO (O vacancy)	1×1×1	-0.98	-1.24	-26.7
	2×2×2	-0.12	-0.15	-32.7
	3×3×3	-0.03	0.05	-31.5
	4×4×4	-0.02	-0.02	-20.5
	5×5×5	-0.01	-0.01	-15.2
SnO ₂ (Sn vacancy)	1×1×1	-3.73	-3.44	7.9
	2×2×2	-0.66	-0.59	10.0
	3×3×3	-0.23	-0.16	28.6
	4×4×4	-0.10	-0.07	32.7

of the average potential does not introduce a meaningful potential shift between configuration B and C.

In some other materials, such as MgO, $\Delta V_{\text{BC}}(\mathbf{r})$ is large far from the defect. However, it never tends to a constant value, making it difficult to select a far region for Eq. 5.4. In turn, this will damage the approximation made in Eq. 5.5.

When the contribution of ΔV_{BC} to ΔV_{PA} is entirely neglected, our corrections appear to perform as reliably for both examples where ΔV_{BC} is large and small. This suggests that this component does not in fact introduce a significant potential alignment shift. We can justify this observation using the following argument – as the number of electrons and ions in the cell is kept fixed, as well as their total density, there is not a large change in the neglected average potential. We note that the ΔV_{BC} is large in materials where the original formulation of the FNV method is believed to perform poorly, and is the alignment component most strongly altered by the use of the KO far averaging method [81]. It would be interesting to explore in detail how the KO sampling method affects the different alignment components

we define.

5.2.3.3 The ΔV_{CD} component

Finally, we consider the potential difference ΔV_{CD} , between the charged defect and a neutral reference structure (as defined in Fig. 5.6). We observe the following relationship between our corrective potential, as introduced in Eq. 4.3, and the ΔV_{CD} potential alignment component,

$$\Delta V_{\text{CD}}(\mathbf{r}) \approx 2\varepsilon v_{\text{PBC}}(\mathbf{r}). \quad (5.7)$$

The electrostatic potential difference present in the DFT calculation is experienced by all the electrons in the calculation and therefore is not screened, whereas the interaction model v_{PBC} is experienced only by the additional defect charge and hence is screened by the dielectric constant ε (which is ε_0 when the ionic structure is relaxed, ε_∞ when it is held fixed). Although this factor of ε is justified by this electrostatic argument, it is not included in the derivation of the FNV method[87]. We note that the factor of two in this expression is due to double counting of the electron Hartree potential in CASTEP, and may not be required in other codes depending on the electrostatic convention used (this factor is not required in CP2K). Finally, only the periodic part of the interaction model, v_{PBC} , contributes. The periodic DFT calculation does not contain the isolated component of the image interaction, v_{iso} – as a result, ΔV_{CD} does not contain enough information to infer E_{corr} .

An example of this behavior is shown in Fig. 5.10. Across the defects we considered in this paper in isotropic dielectrics, we find Eq. 5.7 is satisfied to within 1% (for a material with an anisotropic dielectric, ε should be replaced with a tensor, but I haven't explored how this would be done). This correspondence demonstrates that the potential alignment component ΔV_{CD} is already fully incorporated in our interaction correction and need not be considered separately. Note that this is the only part of potential alignment that is influenced by the jellium background present in charged calculations.

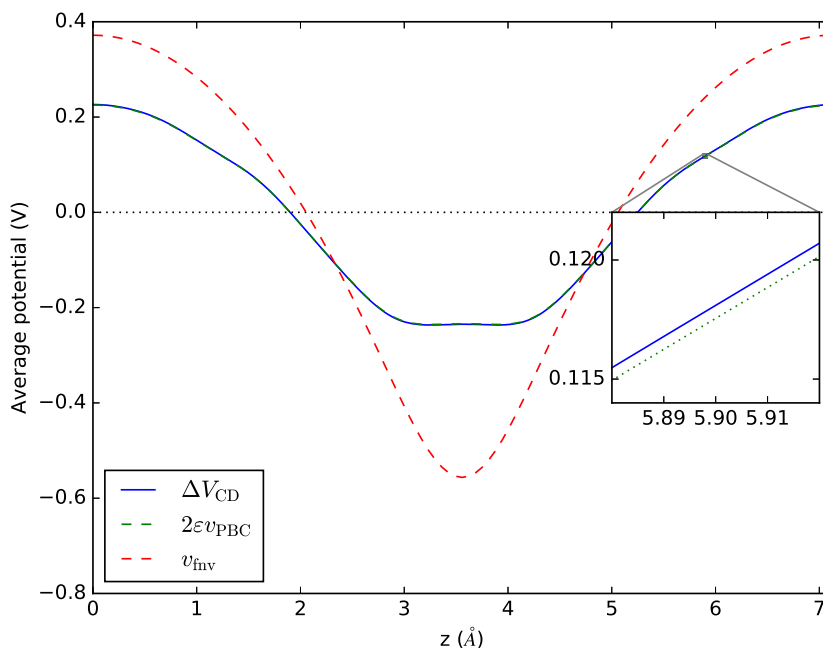


Figure 5.10: Comparison of the ΔV_{CD} alignment component of a V_{C}^2 defect in a $2 \times 2 \times 2$ supercell, with the correction potentials constructed. The inset shows a $\times 50$ magnification.

5.2.3.4 Discussion of all components

We show an example of the finite-size scaling resulting when the various components of potential alignment are used to perform alignment corrections, in Fig. 5.11. We switch to the example of an oxygen vacancy in MgO, as ΔV_{BC} is significant for this system. In contrast, the ΔV_{AB} component is relatively small in this case. These results demonstrate that alignment with ΔV_{AB} makes an improvement to the size scaling, but that the ΔV_{BC} and ΔV_{CD} components appear to do more harm than good. As we have argued, inclusion of ΔV_{CD} is expected to be harmful as this component is already fully included in the electrostatic correction. The negative contribution of the ΔV_{BC} contribution requires some further discussion.

The accurate determination of ΔV_{BC} is challenging for some materials, where we can not evaluate Eq. 5.4 reliably. This equation requires the selection of a region of the supercell that reproduces bulk properties, but if relaxation of the defect ionic structure leads to long-range effects, we cannot identify such a region. For the example of diamond, we recover a bulk-like region (i.e. ΔV_{BC} tends to a constant

5.2. POTENTIAL ALIGNMENT AND ITS CAUSES

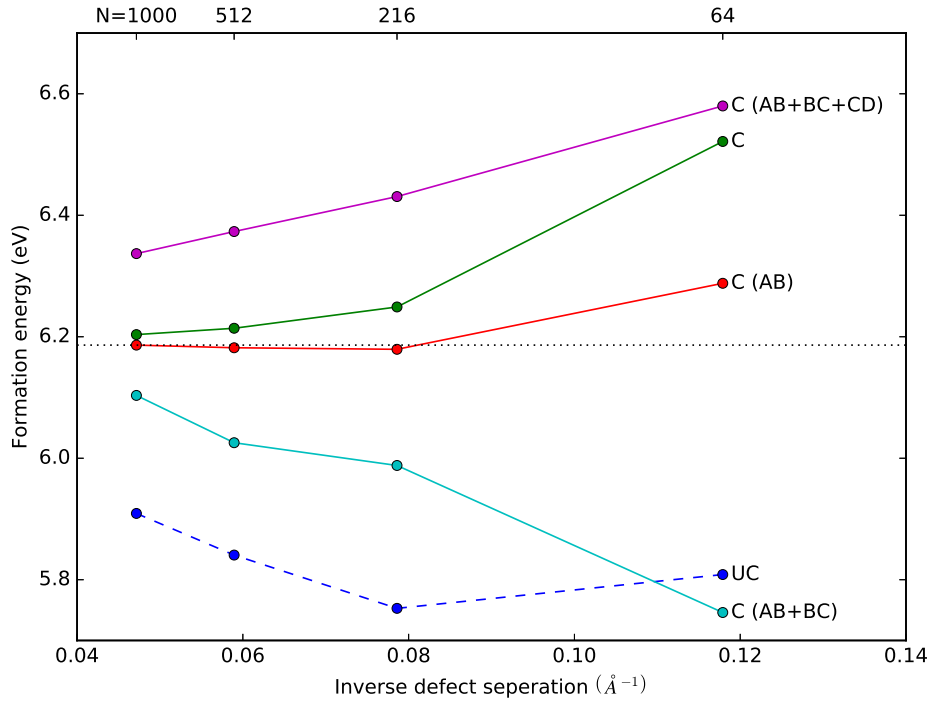


Figure 5.11: Finite-size convergence of the formation energy of the V_{O}^{+2} defect in MgO, depending on the potential alignment utilized. Results are shown without any correction (UC, blue dashed line) and with the screened Poisson electrostatic correction proposed in Chapter 4 (C, dark green line). Additionally, results also including a potential alignment correction are shown. Using only the ΔV_{AB} component (red line) yields the best finite-size scaling. Additionally including the ΔV_{BC} (cyan line) and ΔV_{CD} (purple line) components appears to make the scaling worse. A dotted line is shown for the result of the screened Poisson correction and ΔV_{AB} potential alignment for the largest supercell, to demonstrate how little size dependence remains in these results.

far from the defect) and find that $\Delta V_{\text{BC}} \sim 0$. In the case of MgO, I was not able to identify such a region, and the planar average I apply is certainly not sophisticated enough to accurately determine ΔV_{BC} . However, the results in Fig. 5.11 very strongly suggest that $\Delta V_{\text{BC}} \sim 0$. If this is the case, it is best not to include the ΔV_{BC} component in the potential alignment correction.

Considering the above results, the ΔV_{AB} component is both the most significant source of potential alignment error (once an electrostatic correction has been consistently applied) and the most well behaved component. Almost any far averaging procedure used in Eq. 5.4 will unambiguously determine this component because the modification to the electrostatic potential is local to the defect site and does

not lead to long range changes in the material. It is worth looking at this potential alignment term in more detail.

5.2.4 Finite-size scaling of the ΔV_{AB} component

Returning to the ΔV_{AB} component, simple model calculations can demonstrate that adding or removing an atom to form a defect in periodic DFT leads to a potential shift. Consider an isolated atom in a large cubic box. If the atom is neutral, we expect that the same energy will be calculated under isolated and periodic boundary conditions – as well separated neutral atoms do not interact. In fact, this is the behavior we observe. Using CP2K [46, 47, 107, 108], the same DFT calculation can be performed with both boundary conditions [109, 110]. For a calculation on a Sn atom in a 10 Å cubic box, the total energy is only modified by 0.5 meV. However, as shown in the first panel of Fig. 5.12, the electrostatic potential contains a significant shift of 0.33 V. This shift is observed to be sensitive to the details of the DFT calculation, depending on atom type, pseudopotential and xc functional. This sensitivity to the pseudopotential used is also observed in ΔV_{AB} , as shown in Table 5.3 for the example of diamond. This shift is introduced by neglect of the average potential.

This same argument, that the change in boundary conditions between the two calculations introduces an alignment shift can also be made mathematically. First, consider the constraints that the boundary conditions place on the electrostatic potential of a neutral atom,

$$\langle V_{\text{atom}}^{\text{PBC}}(\mathbf{r}) \rangle = 0 \quad (5.8)$$

$$V_{\text{atom}}^{\text{iso}}(\mathbf{r} \rightarrow \infty) = 0 \implies \langle V_{\text{atom}}^{\text{iso}}(\mathbf{r}) \rangle = C \quad (5.9)$$

where $\langle V_{\text{atom}}^{\text{PBC}}(\mathbf{r}) \rangle$ is the average electrostatic potential of the isolated atom under periodic boundary conditions. For the same system under isolated boundary conditions, $V_{\text{atom}}^{\text{iso}}(\mathbf{r})$, we do not require an average potential of zero, and instead have the average value C .

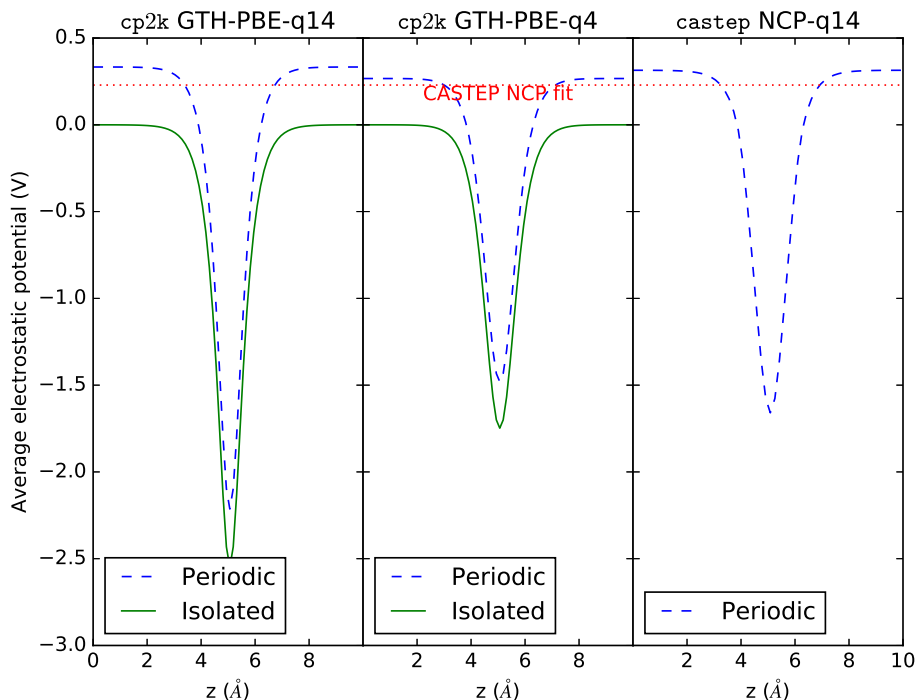


Figure 5.12: Electrostatic potential of an Sn atom at the center of a 10 Å cubic box, using different pseudopotentials and DFT codes. In solid green, the potential under isolated boundary conditions is shown (only available for CP2K). The blue dashed line shows the potential when periodic boundary conditions are applied. The red dotted line shows the potential alignment predicted from the atomic radius, by the fit in Fig. 5.13. For each individual pseudopotential, the electrostatic potentials are identical in shape for both boundary conditions, but the potential in the periodic system is shifted upwards by ΔV_{atom} . The convention of setting $\langle V \rangle = 0$, introduces this shift ΔV_{atom} far from the atom, as the isolated atom has a non-zero average potential. Equivalently, calculations on atoms using isolated boundary conditions are always correctly referenced to the vacuum level, but this level is shifted within the PBC calculations. From left to right, $V_{\text{atom}} = 0.33, 0.27$ and 0.31 V.

However, in both cases we are describing the same physical situation and should still calculate the same energy. This requires that the only difference between the two potentials is a uniform shift,

$$V_{\text{atom}}^{\text{PBC}}(\mathbf{r}) + \langle V_{\text{atom}}^{\text{iso}} \rangle = V_{\text{atom}}^{\text{iso}}(\mathbf{r}). \quad (5.10)$$

A uniform shift in the electrostatic potential of a charge neutral system does not change its energy. Following this reasoning, we would like to understand how this potential shift introduced by PBC scales with the size of our simulation supercell.

In the case of isolated boundary conditions, the vacuum level remains well defined, so this shift must be a non-physical change in the PBC potential. We can calculate this shift as,

$$\langle V_{\text{atom}}^{\text{iso}}(\mathbf{r}) \rangle = \frac{1}{\Omega} \int_{\Omega} V_{\text{atom}}^{\text{iso}}(\mathbf{r}) d\mathbf{r} \quad (5.11)$$

where the average is performed by taking an integral over the simulation cell of volume Ω . Note, however, that we can infer a lot about $V_{\text{atom}}^{\text{iso}}(\mathbf{r})$ using our knowledge of isolated atoms – it must be some kind of local well that binds electrons. As a local potential, it is only non-zero near the atom being considered. As long as our isolated box is large enough for the potential to properly decay to zero at the edges, then the actual size of the box doesn't affect the shape of this potential at all. This is equivalent to stating that,

$$\int_{\Omega} V_{\text{atom}}^{\text{iso}}(\mathbf{r}) d\mathbf{r} = \alpha_{\text{atom}} \quad (5.12)$$

where the integral given in Eq. 5.11 evaluates to a constant α_{atom} , which is a property of the atom independent of the size of the simulation cell. Different choices of atom, pseudopotential and xc functional will all have their own consistent value of α_{atom} across any large simulation supercell considered. By combining Eq. 5.10, 5.11 and 5.12 we discover the following size dependence for the non-physical potential shift,

$$\Delta V_{\text{atom}} = \langle V_{\text{atom}}^{\text{iso}}(\mathbf{r}) \rangle = \frac{\alpha_{\text{atom}}}{\Omega}. \quad (5.13)$$

Hence, this potential shift scales as a constant over the volume Ω . When we recall Eq. 2.23, this leads to an alignment correction of $q\Delta V$, and in fact would then explain a_3 term in Eq. 2.25. Clearly this example is simpler than the actual situation of removing an atom from a lattice, and leads to an ideal volume-dependent contribution to the total energy. When the defect is present within a material, this volume scaling is only approximately maintained.

As this potential shift is associated with isolated atoms, it is worth exploring if any atomic properties can be used to predict it. We find that atomic radius

5.2. POTENTIAL ALIGNMENT AND ITS CAUSES

is the best predictor, as illustrated in Fig. 5.13 (I used atomic radii calculated by Ghosh and Biswas [111], using Slater orbitals). This suggests that this kind of potential alignment is likely to be more significant in calculations involving heavier elements. An important consequence of this argument is that we expect this component of potential alignment to swap sign when considering interstitials rather than vacancies, as we swap from removing a potential well to adding a potential well. This behavior can be observed in the results of Shim *et al.* [77] and Taylor and Bruneval [78], although these authors ascribe this behavior to different mechanisms (change in screening behavior and defect state hybridization, respectively).

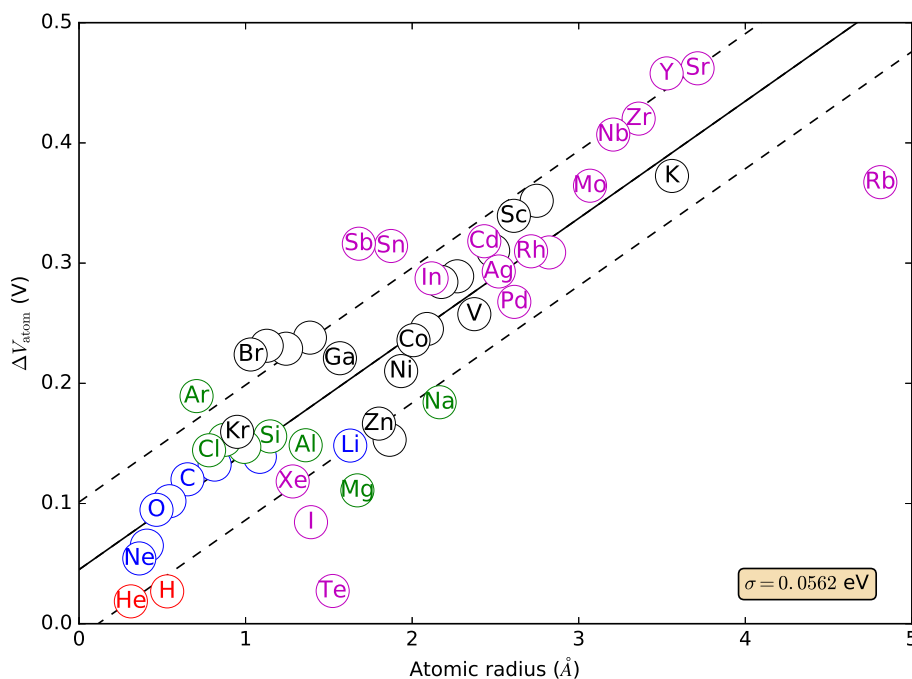


Figure 5.13: Comparison between the potential alignment shift introduced by an isolated atom in a 10 Å cubic box, with the atomic radius of that species. Elements from the same row of the periodic table share the same color. We find the potential alignment constants are dependent on pseudopotential and XC functional used, but that all choices produced similar linear fits, to that shown by the solid black line ($m = 0.097 \text{ V}/\text{\AA}$, $c=0.045 \text{ V}$). One standard deviation is shown by the dashed black line. Atomic radius is a characteristic of the element, rather than the particular DFT approximations used.

Table 5.3: Dependence of the ΔV_{AB} neutral alignment component on pseudopotential, for the example of a $2 \times 2 \times 2$ diamond supercell containing a carbon vacancy.

Pseudopotential definition	$\Delta V_{AB}(V)$
c-opt	0.249
USP	0.324
NCP	0.362
QC5	0.327

5.2.5 Model system: classical structureless atom

In light of the discovered role of atomic radius on the prediction of the ΔV_{AB} component, it is useful to explore if this feature can be captured by simple models. We consider a very simple classical model of an atom, made of two uniformly charged spheres as shown in Fig. 5.14. The first sphere has total charge Q_A , and the second sphere has a total charge of Q_B . In order to consider a charge neutral system we additionally require that $Q_A = -Q_B$.

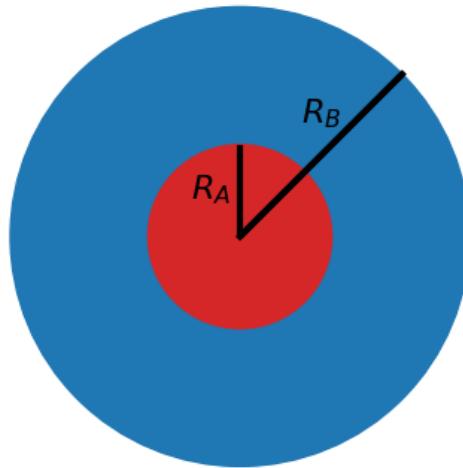


Figure 5.14: Schematic representation of the model atom, as a 2D slice of the 3D sphere. A positively charged red sphere sits inside a larger negatively charged blue sphere. Both spheres are uniformly charged (and overlap inside the red sphere). The origin of our co-ordinate system is placed at the center of the spheres.

The electrostatic potential of this model can be derived analytically, allowing us to consider the potential alignment shift associated with the model. The well known solution for the electrostatic potential of a uniform sphere of radius R is given as,

$$v(\mathbf{r}) = \begin{cases} r > R & - \int_{\infty}^r \frac{kQ}{r^2} dr^3 = \frac{kQ}{r} \\ r < R & - \int_{\infty}^R \frac{kQ}{r^2} dr^3 - \int_R^r \frac{kQ}{R^3} r dr^3 = \frac{kQ}{2R} \left(3 - \frac{r^2}{R^2} \right), \end{cases} \quad (5.14)$$

where Q is the total charge of the sphere being considered, and k is Coulomb's constant, $k = \frac{1}{4\pi\epsilon_0}$.

The total electrostatic potential for a system of two such uniform spheres follows directly from Eq. 5.14 and is,

$$v(\mathbf{r}) = \begin{cases} r > R_A, r > R_B & \frac{kQ_A}{r} + \frac{kQ_B}{r} \\ r > R_A, r < R_B & \frac{kQ_A}{r} + \frac{kQ}{2R_B} \left(3 - \frac{r^2}{R_B^2} \right) \\ r < R_A, r < R_B & \frac{kQ_A}{2R_A} \left(3 - \frac{r^2}{R_A^2} \right) + \frac{kQ}{2R_B} \left(3 - \frac{r^2}{R_B^2} \right), \end{cases} \quad (5.15)$$

where we additionally require that $R_A < R_B$.

Some example sphere models and their calculated electrostatic potentials are shown in Fig. 5.15. This yielded Fig. 5.16, which shows the averaged values of the potentials calculated as R_B is varied.

These models demonstrate that it is charge separation between positive and negative charge that drives the introduction of a potential shift. If electrons are close to the atomic nucleus, they will screen it and will not lead to a potential well. As the electrons are pulled further from it, the screening is reduced and the potential well becomes deeper.

5.2.6 Environment dependence of potential alignment

The correlation between atomic radius and the ΔV_{atom} potential alignment shift provides a hint that the effective radius of an atom within a material might help predict the ΔV_{AB} alignment radius. This effective radius can be expected to depend on the chemical environment of the atom in question.

5.2. POTENTIAL ALIGNMENT AND ITS CAUSES

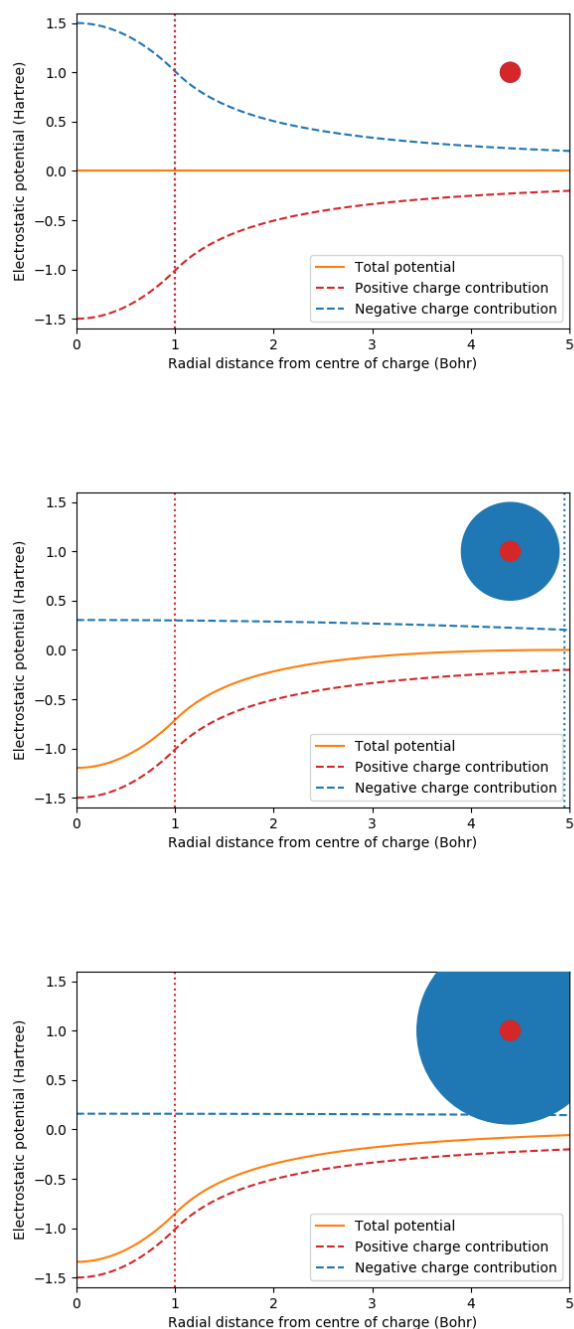


Figure 5.15: Example sphere models (upper right), and their observed electrostatic potentials (as given in Eq. 5.15). Total charges of $Q_A = -1$ and $Q_B = 1$ a.u. were employed. For all three figures $R_A = 1.0$ Bohr, and R_B takes a value of 1.0, 4.95 and 9.45 Bohr respectively. It is observed that as the sphere of negative charge is increased in radius that the depth of the total electrostatic potential well increases. Both the total potential, and the individual contributions of the positive and negative charge are shown.

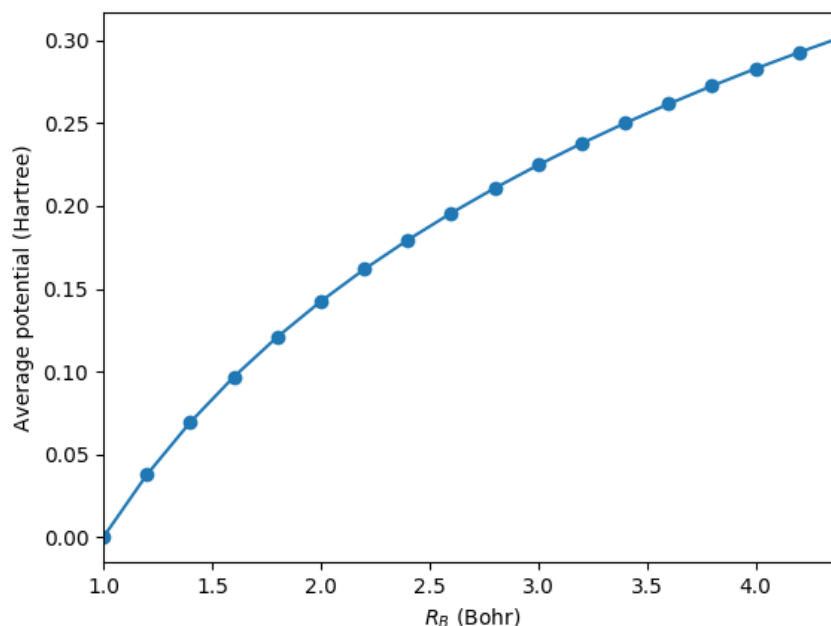


Figure 5.16: Dependence of the calculated average electrostatic potential of the model on the R_B parameter, which is the radius of the outer sphere representing electrons. R_A is held fixed at 1 Bohr. Total charges of $Q_A = -1$ and $Q_B = 1$ a.u. were employed. As R_B is increased, the average potential is observed to also increase. The potentials are averaged over a sphere of radius 9.4 Bohr.

As a descriptor of chemical environment, I found that the Bader charge [112] associated with an atom was the most successful descriptor. I used the Henkelman Bader analysis program to calculate the required Bader charges [113, 114, 115].

Example calculations where the same oxygen pseudoion was removed from different chemical environments are shown in Fig. 5.17, and a similar set of calculations for magnesium pseudoions is shown in Fig. 5.18. In both cases, the alignment factor α is plotted, which is defined as $\alpha = \Delta V \Omega$, where Ω is the total supercell volume. This is required so that simulation cells of different sizes can be compared directly.

From these results, it is clear that there are systematic patterns present in the alignment shifts introduced by particular atoms. However, none of the descriptors I have investigated are strong enough predictors to infer this shift ahead of time. A direct calculation of ΔV_{AB} can clearly absorb some of this environmental dependence

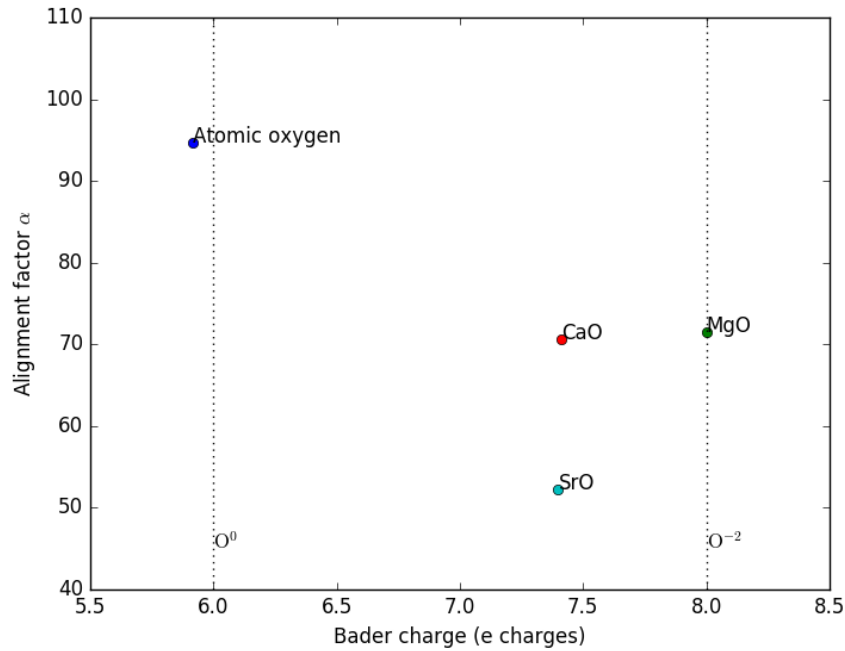


Figure 5.17: The ΔV_{AB} alignment shift introduced by the removal of an oxygen atom from the indicated chemical systems, as related to the Bader charge of the atom. Negative relative charges on the considered oxygen atom are consistent with a reduction in the produced alignment shift.

which is not present in the direct calculation of ΔV_{atom} .

Conclusions: Considering the decomposition we introduce, the AB component is found to be the most important. Changes in the number of atoms in the cell introduces a non-physical shift of the electrostatic potential, which is found to be related to the radius of the atoms involved. The CD component is related to electrostatics, and we were able to predict it exactly from the density difference. The role of the BC component was less clear, and made the observed finite-size errors larger when included directly.

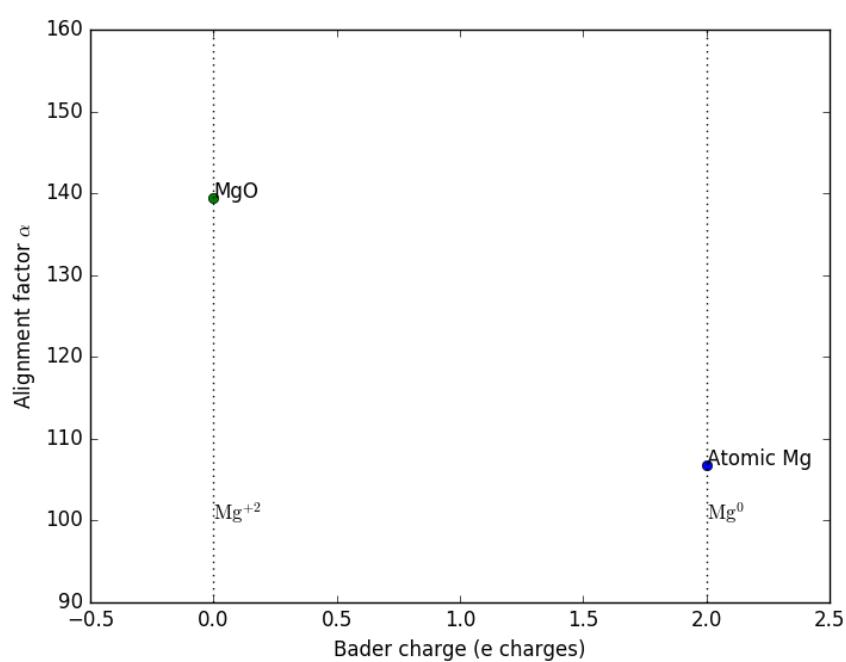


Figure 5.18: The ΔV_{AB} alignment shift introduced by the removal of a magnesium atom from the indicated chemical systems, as related to the Bader charge of the atom. Positive relative charges on the considered magnesium atom are consistent with an increase in the produced alignment shift.

Chapter 6

Application of methods in the bulk

Aims: In this chapter, I discuss charged defect formation energy calculations for a diverse range of defects and materials, and then explore how the electrostatic corrections (introduced in Chapter 3) and potential alignment corrections (of Chapter 5) vary between the different examples.

Results The new correction method introduced in Chapter 4 is very well predicted by the LZ correction method, and produces essentially identical electrostatic corrections between positive and negative charge states. This suggests that the defect charge present for negative and positive states is essentially similar and cuts against the argument that improvements to the electrostatic corrections should treat negative and positive states differently. Generally, I observe that negative and positive vacancies demonstrate quite different finite-size dependence. This doesn't seem to be caused by the electrostatic corrections, and instead can be understood as a potential alignment effect. Partial cancellation can occur between the electrostatic corrections and potential alignment corrections for some charge states. In terms of the applied electrostatic corrections, it remains difficult to distinguish the performance of the competing MP, LZ and FNV methods, although the methods do lead to different corrections for the examples considered.

6.1 Overview of bulk calculations

As our first realistic problem, I studied the formation energies of defects in the bulk. In order to understand the required corrections, I considered a diverse range of ma-

materials and defects. First, I looked at the V_C defect in Diamond. Diamond is an example of a covalent crystal, and the V_C center is an example of a defect where the defect charge is placed on broken bonds leading to the defect site. Additionally, the defect supports both negative and positive charge states, allowing us to explore if the polarization around the defect is distinct between positive and negative defects. Another advantage is that this example has been widely used as a test system. Previous work reported that the MP correction is not able to well treat this defect [77], but the FNV method was reported to overcome these difficulties [88].

Secondly, I considered the example of the V_O defect in MgO, historically called the F-center. This defect is one of the most well studied charged defects. It is considered to have a relatively simple electronic structure, as the neutral defect contains two electrons in s-like orbitals, at the defect site. In spite of this, this defect can be difficult for present correction methods, as MgO is an ionic material. This leads to long range atomic relaxations that cause difficulties for FNV-style methods.

As our final bulk example, we considered the V_{Sn} defect, as a challenging example of a more complex defect. SnO_2 has an anisotropic dielectric and a non-cubic unit cell. Recent work predicts that the formation of this defect is energetically unfavorable. However, some authors expect this defect to be abundant in SnO_2 surface. We wanted to explore if the use of other correction methods would make the defect easier or harder to form.

For these calculations, we initially restricted ourselves to the PBE functional. As a semi-local functional, this method can be applied cheaply and to larger super-cells. This is a great advantage in understanding finite-size scaling. However, this will produce defect formation energies that are in very poor agreement with experiment, as exchange plays an important role in the localization of defect states. Once we have achieved a firmer understanding of the finite-size scaling of our PBE results, we can then explore the role that XC functional plays in the finite size scaling.

6.2 Case study: Vacancies in bulk diamond

Diamond is a wide bandgap material [116]. It crystallizes in the diamond structure that bears its name, and its conventional cubic unit cell has an experimentally reported lattice constant of 3.57 Å [117]. Its band gap is reported as 5.45 eV at 0K [118]. Experimental measurements of diamond's dielectric response report a static constant of $\epsilon_0=5.5$ [119].

In order to calculate defect formation energies in diamond, I used a planewave basis with the CASTEP code. Previous work has demonstrated that \mathbf{k} -point sampling plays an important role in describing charged vacancy defects in diamond, which was suggested to be due to the ability of \mathbf{k} -point sampling to enforce incorrect electronic symmetry on defect states [45].

As a result I used a high quality \mathbf{k} -point sampling for diamond, equivalent to a $24\times 24\times 24$ Monkhorst-Pack [43] sampling of the conventional unit cell. I selected a planewave cutoff energy of 2000 eV, chosen to produce a comparable accuracy to this \mathbf{k} -point sampling. I used a norm-conserving pseudopotential with 4 valence electrons.

The above parameters would be considered to be overconverged for general usage. My rationale for this is that in studying the finite-size convergence displayed by these defects, it is helpful if basis set and Brillouin zone sampling errors can be converged out. This also should help the reliability of any extrapolations performed.

I used density functional perturbation theory (DFPT) [72, 73] as implemented in the CASTEP code [74], to calculate diamond's dielectric properties. I calculated a high frequency dielectric constant of $\epsilon_\infty=5.76$ and a static dielectric constant of $\epsilon_0=5.76$. As these numbers are identical, atomic relaxation doesn't appear to play an important role in the dielectric response of diamond. The justification for this is that carbon atoms are in a neutral charge state in diamond, so they don't move in response to an external field. This is a 5% overestimate of the experimentally reported value.

An understanding of the formation energies of different charge states of carbon vacancies is of technological interest, as they are suggested to play a key role in

6.2. CASE STUDY: VACANCIES IN BULK DIAMOND

stabilizing the diamond structure (in thermodynamic competition with graphite) in the CVD deposition of diamond films [120, 121].

First I considered the formation energies of carbon vacancies when the atomic structure is held constant around the defect. These are still physically meaningful energies to calculate, and this corresponds to the energy costs for a process that occurs on a timescale too fast for atomic relaxation to take place. These results are shown in Figs. 6.1-6.4 (a).

Looking at Fig. 6.1 (a), it can be seen that applying the MP correction by itself (green line) appears to be a significant overcorrection. This is the case for the +2 defect in Fig. 6.2 too. The behavior observed in Fig. 6.3 and 6.4. The behavior is more consistent when considering the combination of the MP and ΔV_{AB} corrections.

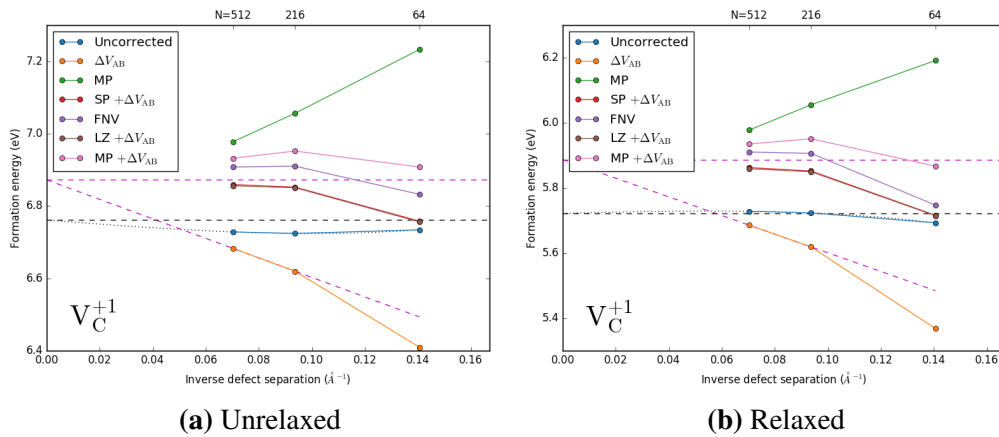


Figure 6.1: Formation energy diagrams of the V_C^{+1} defect in diamond. Uncorrected denotes formation energies calculated using Eq. 2.23, without any explicit corrections. ΔV_{AB} denotes results where AB potential alignment has been performed. MP denotes the Makov-Payne correction, SP (screened Poisson) denotes the correction of Eq. 4.1, LZ denotes the Lany-Zunger correction, and FNV denotes the Freysoldt-Neugebauer-van de Walle correction. Additionally, a linear extrapolation from the two best aligned results (red dashed line) and a traditional extrapolation in terms of inverse volume and length is shown (dotted black line).

6.2. CASE STUDY: VACANCIES IN BULK DIAMOND

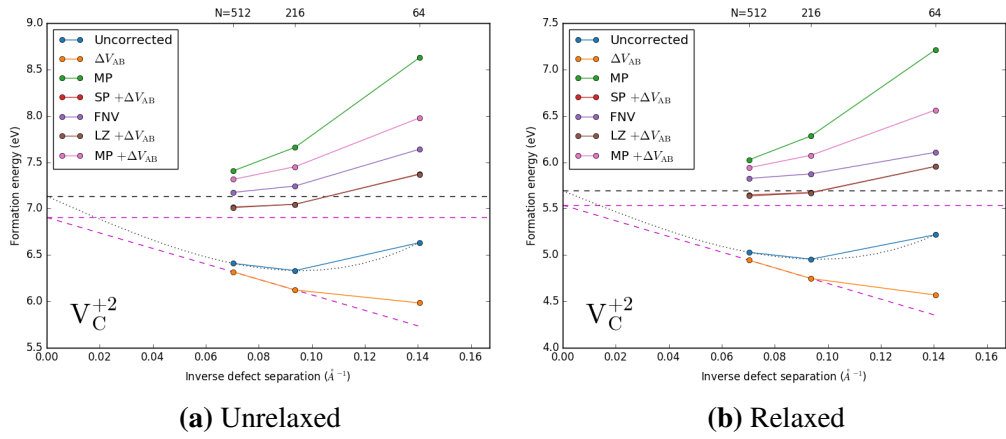


Figure 6.2: Formation energy diagrams of the V_C^{+2} defect in diamond. Follows the same notation as Fig. 6.1.

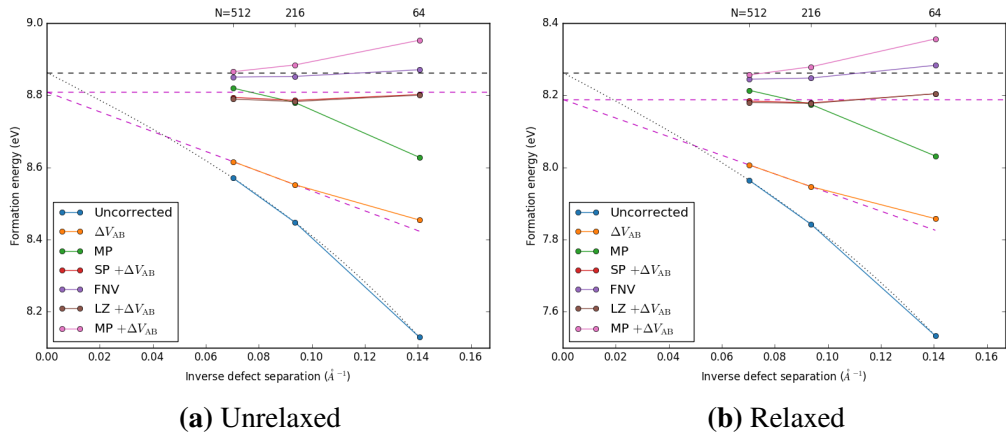


Figure 6.3: Formation energy diagrams of the V_C^{-1} defect in diamond. Follows the same notation as Fig. 6.1.

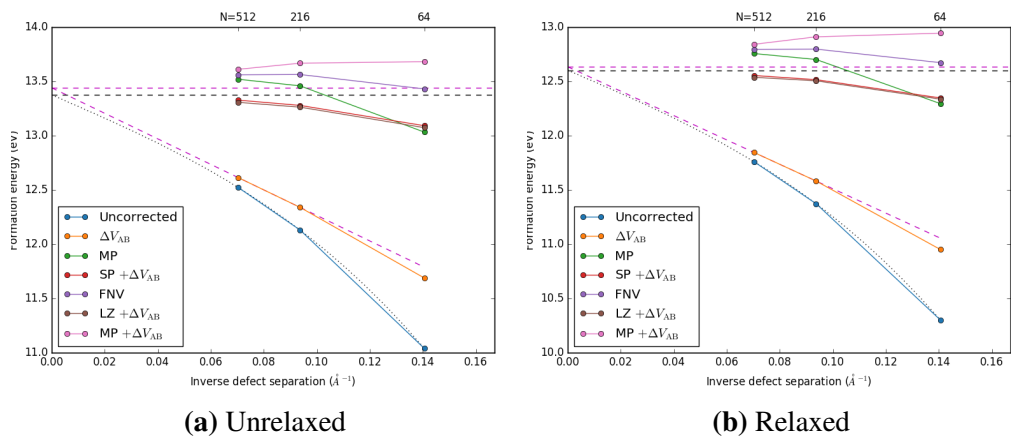


Figure 6.4: Formation energy diagrams of the V_C^{-2} defect in diamond. Follows the same notation as Fig. 6.1.

When looking at the uncorrected formation energies (blue lines) it is clear that the negative and positive charge states look quite different in their behavior. In terms of the understanding of potential alignment I have developed in Chapter 5, this can be understood quite straightforwardly.

The electrostatic corrections are always positive for cubic cells, because the jellium background in these cells is overstabilizing the charged defects. In contrast, the sign of the ΔV_{AB} potential alignment correction flips between the positive and negative charge states.

This partial cancellation can clearly be misleading, as exemplified by Fig. 6.1a. In this case, the uncorrected data appears to be almost size independent, suggesting that the required corrections vanish in this case.

Even with the high quality parameters used in these calculations, it doesn't seem that the extrapolations performed are particularly consistent, supporting different correction schemes amongst the examples considered.

Then, I performed geometric relaxations of the defect geometry. This lowers the energy required to form a defect, and more realistically describes processes where the defect geometry is allowed sufficient time to relax to its lowest energy geometry. These results are shown in Figs. 6.1-6.4 (b).

It should be observed that for these plots, the unrelaxed and relaxed defects display similar behavior. This is likely because the static dielectric constant ϵ_0 and the high frequency dielectric constant ϵ_∞ are equal. This demonstrates that the corrections required for unrelaxed and relaxed defects can be similar, at least for some examples.

For all the examples shown in Figs. 6.1-6.4, the LZ and SP corrections are found to be almost identical. This is unexpected, as the SP calculations have access to significantly more information from the host DFT calculations. The LZ calculation uses the supercell length L and the dielectric constant ϵ . The calculation of the SP correction additionally requires the defect charge distribution $\rho(\mathbf{r})$.

6.3 Case study: Vacancies in bulk MgO

Next, I considered MgO, an ionic crystal with a wide band gap. It has the rock-salt structure, with a lattice constant of 4.22 Å [122]. It has a band gap of 7.7 eV [123]. The high frequency dielectric constant of MgO has been reported experimentally as $\epsilon_\infty=3.18$ [124], and its static dielectric constant has been measured as $\epsilon_0=9.83$ [125]. Hence, atomic relaxation approximately triples the strength of the dielectric response in MgO, quite a difference to diamond.

Again, I used the CASTEP code and a planewave basis to simulate MgO. For this material, I used the PBEsol functional, as it leads to better experimental agreement. A planewave cutoff of 844 eV was employed, along with a \mathbf{k} -point sampling equivalent to a $4\times 4\times 4$ sampling of the conventional unit cell. Using this parameterization, the lattice constant was calculated as 4.24 Å, which was a 0.5 % overestimate of the experimentally reported value. I also calculated a band gap of 4.5 eV, which was a 43 % underestimate of the experimentally reported value.

Using DFPT, I then calculated the dielectric properties of MgO. For the high frequency dielectric response, a value of $\epsilon_\infty=3.19$ was found, a 0.3% overestimate of the experimental value. The calculated value of the static dielectric constant was $\epsilon_0=9.41$, a 4.3% underestimate of the experimental value.

Calculated formation energies of the V_{O}^{+1} defect in MgO are shown in Fig. 6.5. The ΔV_{AB} alignment correction is relatively more significant for the relaxed defect. The MP method appears to perform better for the unrelaxed defect, where as the SP and LZ methods appear to be more effective for the relaxed defect. The FNV correction is slightly smaller than the MP correction for the unrelaxed defect, but increases once relaxation is allowed.

6.4. CASE STUDY: VACANCIES IN BULK SnO_2

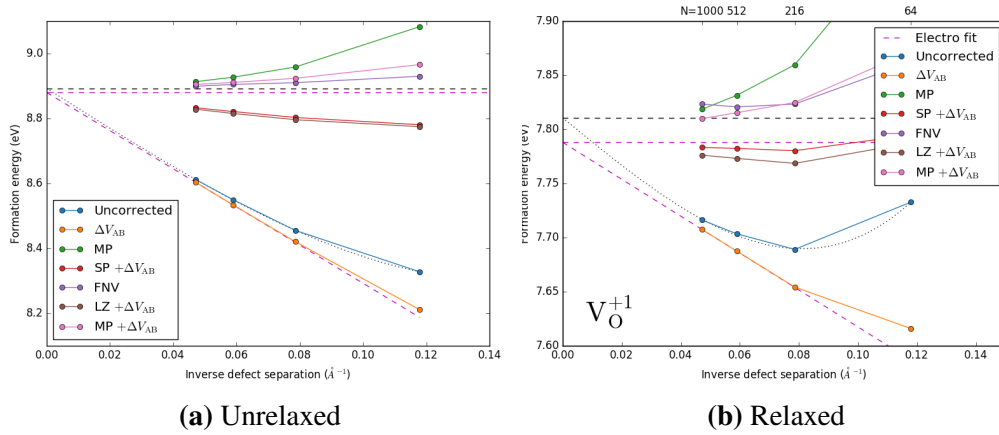


Figure 6.5: Formation energy diagrams of the V_O^{+1} defect in MgO. Follows the same notation as Fig. 6.1.

Similar plots for the V_O^{+2} defect in MgO are shown in Fig. 6.6. Generally speaking, this example seems to favor the smaller correction schemes. Definitely, the MP correction appears to be too large for the unrelaxed defect. The FNV method is more similar to the MP method for this higher charge state. The LZ and SP method appear to perform more reliably for the relaxed defect in this case.

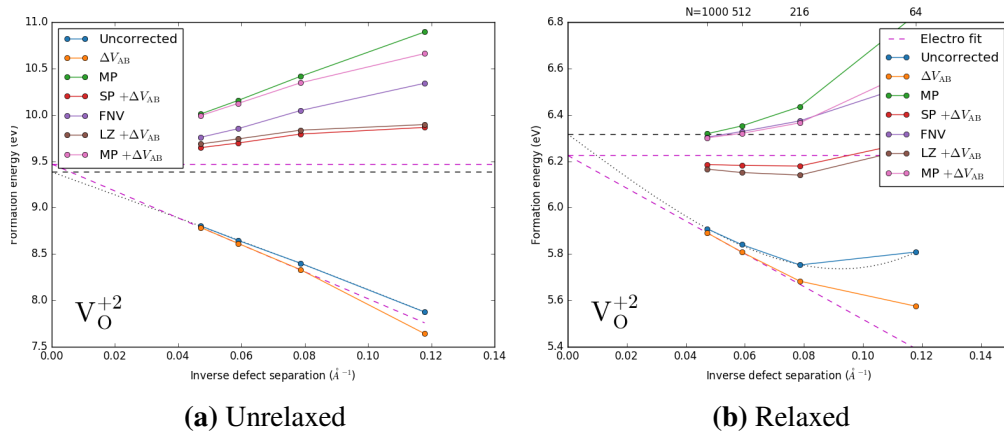


Figure 6.6: Formation energy diagrams of the V_O^{+2} defect in MgO. Follows the same notation as Fig. 6.1.

6.4 Case study: Vacancies in bulk SnO_2

Finally, I considered SnO_2 , a transparent conducting oxide [126]. It has the rutile crystal structure, with lattice constants that have been determined experimentally as $a=4.74 \text{ \AA}$ and $b=3.19 \text{ \AA}$ [127]. The band gap of SnO_2 has been reported ex-

perimentally as 3.6 eV [128]. Unlike, the other materials considered, SnO_2 has an anisotropic dielectric tensor, meaning that the strength of its dielectric response is different along different crystallographic directions. The static dielectric constants have been reported experimentally as $\epsilon_0^{xx}=\epsilon_0^{yy}=14.0$, and $\epsilon_0^{zz}=9.0$ [129], although a relatively large uncertainty of ± 2 was reported on the value of ϵ_0^{zz} . In contrast, the high frequency dielectric constant is not reported to be anisotropic, and has been measured as 4.64 [130].

To simulate SnO_2 , I used CASTEP and a planewave basis, with a cutoff energy of 2100 eV. I used a \mathbf{k} -point sampling equivalent to a $4 \times 4 \times 8$ MP grid in the unit cell. Using these parameters, the lattice constants of SnO_2 were calculated as $a=4.78 \text{ \AA}$ and $b=3.20 \text{ \AA}$, which was a 0.9% and 0.3% overestimate, respectively. This slight overestimate of the lattice constants is very typical of the PBE functional. I also calculated a band gap of 2.04 eV, which was a 43 % underestimate of the experimentally reported bandgap.

Using DFPT, I calculated the following dielectric tensors for SnO_2 at the PBE level,

$$\epsilon_\infty = \begin{pmatrix} 4.46 & 0 & 0 \\ 0 & 4.46 & 0 \\ 0 & 0 & 4.87 \end{pmatrix}, \quad \epsilon_0 = \begin{pmatrix} 13.11 & 0 & 0 \\ 0 & 13.11 & 0 \\ 0 & 0 & 10.72 \end{pmatrix},$$

which are in agreement with the values reported experimentally. The calculated value of ϵ_∞ is almost isotropic, with the experimentally reported value lying between the two values I calculated. For the static dielectric constant, the identical values of ϵ_0^{xx} and ϵ_0^{yy} lie within the experimental error bars. The worst agreement is for the value of ϵ_0^{zz} , which is calculated to be 13% higher than the highest experimentally reported value. It has been suggested that differences in SnO_2 film composition can introduce large uncertainties into these properties [131], so this agreement seems reasonable given the known experimental challenges.

Figure 6.7 shows formation energy diagrams for the unrelaxed and relaxed V_{Sn}^{-4} defect in SnO_2 . Compared to the other examples we considered, the ΔV_{AB}

6.5. FIGURES OF MERIT

alignment component was larger in this case (as expected based on the argument developed in Sec. 5.2.4). For both cases, the anisotropic MP correction appears to overestimate the magnitude of the required correction. Both the LZ and SP correction appear to be more effective for the case where relaxation is allowed. This example of a high dielectric material demonstrates that potential alignment can be the larger correction for materials of this kind.

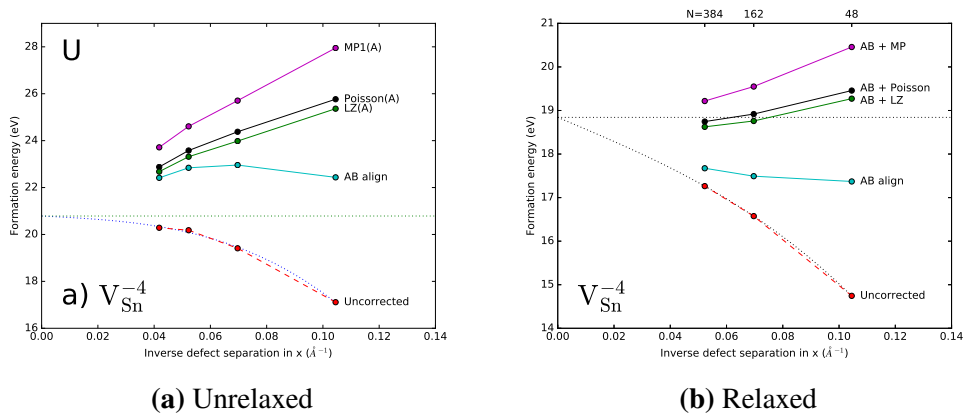


Figure 6.7: Formation energy diagrams of the V_{Sn}^{-4} defect in SnO_2 . Follows the same notation as Fig. 6.1. This example demonstrates a large ΔV_{AB} alignment term. By eye, it appears that the MP correction is too large in this case, and that the LZ and SP methods are more effective.

6.5 Figures of merit

I wanted to make an attempt to quantify the performance of the methods considered above more mathematically. As a measure of success of the correction methods, I looked at the energy difference between the two largest supercells considered. For unrelaxed defects, this metric is shown in Tab. 6.1, and for relaxed defects it is shown in Tab. 6.2. Although this is an indirect method of success, it is clear that if the corrections were fully successful, all finite size dependence should be removed and the calculated energy difference would be zero.

A criticism of this approach is that it is not proved that other sources of finite-size error to defect electrostatics and potential alignment have fully converged out of the two largest cells (e.g. there could be incomplete geometric relaxation in the case of formation energies for relaxed defects). The possibility of remaining errors

6.5. FIGURES OF MERIT

does complicate the analysis, as it is possible that these errors are systematic and cloud the comparison. In all cases, the largest supercells considered were chosen due to computational constraints, rather than an observation of size convergence.

When looking at Tab. 6.1, it can be seen that adding just an ΔV_{AB} alignment correction increases the observed error. However, when the alignment is combined with the MP correction, this leads to an improvement over just performing the MP correction. By this measure, it remains a challenge to differentiate between the success of the LZ and FNV corrections, which both appear to be improvements over the MP method. As both of these corrections are different, this suggests that this approach is not sufficiently powerful to make a clear judgement of the success of the considered methods.

Host Defect	diamond V_C^{+1}	diamond V_C^{+2}	diamond V_C^{-1}	diamond V_C^{-2}	MgO V_O^{+1}	MgO V_O^{+2}	mean
Uncorr.	0.0021	0.0388	0.0616	0.1969	0.0642	0.1649	0.0881
Uncorr. + AB	0.0316	0.0977	0.0321	0.1378	0.0752	0.1868	0.0935
MP	0.0394	0.1273	0.0206	0.0306	0.0189	0.1672	0.0672
MP + AB	0.0100	0.0684	0.0094	0.0283	0.0079	0.1453	0.0449
LZ	0.0267	0.0766	0.0327	0.0812	0.0027	0.0831	0.0505
LZ + AB	0.0027	0.0177	0.0033	0.0223	0.0132	0.0611	0.0201
FNV	0.0012	0.0347	0.0009	0.0015	0.0045	0.1198	0.0271

Table 6.1: Energy difference between the two largest supercells considered for all materials and defects considered, that produced cubic supercells. This table is for the unrelaxed defect formation energies. All figures in eV.

Tab. 6.2 demonstrates similar behavior for the relaxed defects considered. Again, including just a ΔV_{AB} alignment correction leads to a larger mean error, but when combined with the MP correction, the performance of the MP method is enhanced. By this measure, the FNV and LZ methods are hard to distinguish, although both methods lead to different corrections.

It is important to note that the new correction method introduced is very similar to the existing LZ method, which makes no use of the DFT density. This strongly suggests that the exact details of the density response across the defects considered is not important electrostatically. In the next chapter I look at these input densities

6.5. FIGURES OF MERIT

Host Defect	diamond V_C^{+1}	diamond V_C^{+2}	diamond V_C^{-1}	diamond V_C^{-2}	MgO V_O^{+1}	MgO V_O^{+2}	mean
Uncorr.	0.0026	0.0369	0.0612	0.1936	0.0111	0.0640	0.0616
Uncorr. + AB	0.0335	0.0989	0.0302	0.1316	0.0220	0.0858	0.0670
MP	0.0390	0.1292	0.0197	0.0275	0.0172	0.0490	0.0469
MP + AB	0.0080	0.0672	0.0113	0.0345	0.0062	0.0270	0.0257
LZ	0.0263	0.0786	0.0324	0.0782	0.0079	0.0125	0.0393
LZ + AB	0.0047	0.0166	0.0014	0.0162	0.0031	0.0106	0.0087
FNV	0.0020	0.0249	0.0016	0.0010	0.0013	0.0290	0.0100

Table 6.2: Energy difference between the two largest supercells considered for all materials and defects considered, that produced cubic supercells. This table is for the relaxed defect formation energies. All figures in eV.

in more detail, and try and understand them better. Then, I can look at how well these densities support the other correction methods.

Conclusions: For the examples considered, the introduced screened Poisson correction method based on calculation of $\rho(\mathbf{r})$ produces essentially identical results to the existing Lany-Zunger method. This demonstrates that using a more realistic description of the defect charge density is not sufficient to produce an improved correction. The LZ method uses only the volume of the supercell and the dielectric constant, so these results provide evidence that the defect charge $\rho(\mathbf{r})$ can be predicted using only these parameters.

Chapter 7

Structure of the bound charges

Aims: The classical concept of the bound charge allows insights into the density differences observed between neutral and charged defects in the previous chapter. In this chapter, I explore the ability of classical electrostatics to explain these observed charged differences, and what electrostatic errors should be introduced as a result.

Results: Once the classical electrostatic argument is developed, it can be seen that it is in strong agreement with density differences from DFT, as long as the presence of an approximately uniform bound depletion charge is postulated, as assumed in the derivation of the LZ method. In the classical picture this charge should be expelled to the surfaces of the crystal (indeed, this behavior is observed in DFT slab models), so it represents another non-physical charge like the neutralizing jellium background that should be absent in the infinite supercell limit. The above understanding allows simple electrostatic models to be constructed. In past derivations of electrostatic correction methods, some electrostatic interactions are neglected. However, calculations show that the inter-supercell interactions should be minimal for cubic supercells, allowing the evaluation of all energy components under isolated boundary conditions. In such an approach, the terms previously neglected in the derivation of the MP and LZ methods are found to be significant, and lead to a large reduction in the electrostatic correction as the dielectric constant is increased. Hence, attempts to improve the electrostatic lead to the prediction of far smaller errors than are expected empirically.

7.1 Classical electrostatics

Another useful description of the problem of charged defects within a dielectric is given by classical electrostatics [132, 133, 134]. This theory is justified through its remarkable success in describing diverse materials. Classical electrostatics doesn't provide an atomic level description, but instead provides a *macroscopic* description of the physics of a material. In principle, our quantum mechanical description using DFT can be more accurate, because it more faithfully reproduces the real physics. However, we should expect that our quantum mechanical results will be in good agreement with a classical electrostatics description, at a macroscopic level.

7.1.1 Electrostatics in vacuum

All of classical electrostatics is described through Gauss' law,

$$\nabla^2 v(\mathbf{r}) = \frac{\rho(\mathbf{r})}{\epsilon_{\text{vac}}}, \quad (7.1)$$

where ρ is the electrostatic charge density, v is the electrostatic potential and ϵ_{vac} is the vacuum permittivity. If we can specify the position of all negative and positive charges within a system, we can use Eq. 7.1 to calculate the electrostatic potential anywhere in space.

The simplest solution of Eq. 7.1 is for an isolated point charge in vacuum, producing,

$$v(\mathbf{r}) = \frac{1}{4\pi\epsilon_{\text{vac}}} \frac{q}{r}, \quad (7.2)$$

where q is the charge of the point charge, and r is the distance from the point charge.

A very important feature of classical electrostatics is that it obeys linear superposition. Hence, if the position of every charge in the system is known, we can add together the potentials generated by each particle by Eq. 7.2 and produce the correct solution of Eq. 7.1.

7.1.2 Electrostatics within a dielectric

One of the remarkable tools of classical electrostatics is the concept of the dielectric constant. Namely, within a dielectric material, Eq. 7.2, is simply modified to,

$$v(\mathbf{r}) = \frac{1}{4\pi\epsilon\epsilon_{\text{vac}}} \frac{q}{r}, \quad (7.3)$$

where we have introduced the dielectric constant ϵ , which is always larger than unity for static problems [135].

This produces an equivalent description to Eq. 7.1, where the electric charges associated with the material containing the point charge would have been considered explicitly. Eq. 7.3 introduces an extremely powerful description, as otherwise we would need to understand how every other charge in the system has moved in response to the introduction of the point charge, and then evaluate Eq. 7.2 for the new distributions. This is a far more complex procedure.

In order to understand the origins of Eq. 7.3, it is useful to introduce the concept of electrostatic multipoles.

7.1.3 The multipole expansion

Multipole expansions [132, 133] provide a useful way to understand classical electrostatics for complex charge distributions. This method uses spherical harmonics, which by construction, are functions that obey the Poisson equation on a sphere. In order to use this method, we require a charge distribution $\rho(\mathbf{r})$ which is only non-zero within a sphere of radius R , centered on the origin. In this case, the potential outside this sphere can then be expanded as,

$$\Phi(\mathbf{r}) = \frac{1}{4\pi\epsilon_{\text{vac}}} \sum_{l=0}^{\infty} \sum_{m=-l}^l \frac{4\pi}{2l+1} q_{lm} \frac{Y_{lm}(\theta, \phi)}{r^{l+1}}, \quad (7.4)$$

where the functions $Y_{lm}(\theta, \phi)$ are spherical harmonics. This introduces the constants q_{lm} , which are the multipole moments of the charge distribution $\rho(\mathbf{r})$. These can be calculated directly as,

$$q_{lm} = \int Y_{lm}^*(\theta', \phi') r'^l \rho(\mathbf{r}') d\mathbf{r}'. \quad (7.5)$$

Eqs. 7.4 and 7.5 are useful computationally, but are not very easy to work with or visualize.

Instead, this expression can be expanded in rectangular coordinates by taking a Taylor expansion of $\frac{1}{|\mathbf{r}-\mathbf{r}'|}$ around $\mathbf{r}'=\mathbf{0}$, producing the following expansion,

$$\phi(\mathbf{r}) = \frac{1}{4\pi\epsilon_0} \left[\frac{q}{r} + \frac{\mathbf{p} \cdot \mathbf{r}}{r^2} + \frac{1}{2} \sum_{i,j} Q_{ij} \frac{r_i r_j}{r^3} + \dots \right], \quad (7.6)$$

this is the form of the multipole expansion that is most commonly used in condensed matter physics. It introduces the following moments,

$$\text{monopole} \quad q = \int_{\Omega} \rho(\mathbf{r}') d^3\mathbf{r}' \quad (7.7)$$

$$\text{dipole} \quad \mathbf{p} = \int_{\Omega} \rho(\mathbf{r}') \mathbf{r}' d^3\mathbf{r}' \quad (7.8)$$

$$\text{quadrupole} \quad \mathbf{Q} = \int_{\Omega} \left[3r'_i r'_j - (r')^2 \delta_{ij} \right] \rho(\mathbf{r}') d^3\mathbf{r}' \quad (7.9)$$

This expansion can be continued, but the terms become significantly more complicated. As a result, this is done only very rarely.

Eq. 7.6 demonstrates that the lowest non-zero moment of a charge distribution will make the most significant contribution to the interaction far from the source charge distribution, as it will be the lowest order power of r and will fall off with distance more slowly.

7.1.4 The polarization density

Returning to the problem of a point charge placed in an ideal dielectric, we consider a dielectric body which is electrically neutral. This body has no monopole moment, and hence, the most significant part of its response to an additional charge must be the formation of dipoles, which act to reduce, or *screen*, the interaction with the

point charge. We can define the polarization introduced by the charge as,

$$\mathbf{P}(\mathbf{r}) = \frac{d\mathbf{p}}{dV}, \quad (7.10)$$

where \mathbf{P} is the polarization, and \mathbf{p} is the dipole moment per volume element. As well as looking at this polarization as a dipole density, we can also look at it as the electric charge density that produces this dipole,

$$\nabla \cdot \mathbf{P}(\mathbf{r}) = -\rho_{\text{bound}}(\mathbf{r}), \quad (7.11)$$

where ρ_{bound} has been introduced, the change in the charge density within the dielectric induced by the polarization.

To be more explicit, we label the total electrostatic charge density as,

$$\rho_{\text{total}} = \rho_{\text{free}} + \rho_{\text{bound}}, \quad (7.12)$$

where the total electric charge within the dielectric ρ_{total} , is made up of charge that has been placed in the dielectric, ρ_{free} , and the charge introduced by the polarization of the dielectric, ρ_{bound} . In the context of charged defects we will encounter exactly this situation, where a charged defect represents a free charge that is placed within a dielectric.

Within this new notation, we can restate Gauss's law in Eq. 7.1 as,

$$\nabla \cdot \mathbf{E}(\mathbf{r}) = \frac{\rho_{\text{total}}(\mathbf{r})}{\epsilon_{\text{vac}}}, \quad (7.13)$$

where we are being explicit about the fact that this definition works on both the free charge we have placed in the dielectric, and the polarization charge that arises as a result of it.

Combining Eqs. 7.11, 7.12 and 7.13 leads to another useful expression, that

$$\nabla \cdot \mathbf{D}(\mathbf{r}) = \rho_{\text{free}}(\mathbf{r}) \quad (7.14)$$

where we have introduced the electric displacement \mathbf{D} , which itself has been defined as,

$$\mathbf{D}(\mathbf{r}) = \epsilon_{\text{vac}}\mathbf{E}(\mathbf{r}) + \mathbf{P}(\mathbf{r}). \quad (7.15)$$

Taken above, we have a set of equations that describe polarization within a material. Their practical utility can be limited to realistic problems due to the difficulty in determining ρ_{total} , which clearly requires a self consistent solution of the above equations in order to be known. Secondly, although these equations resemble Maxwell's equations in vacuum, they are in practice more difficult to solve as we have no constraint on the curl of the displacement field, $\nabla \times \mathbf{D}$. Still, in high symmetry situations, direct application of these equations is possible.

In linear dielectrics (by definition), we have the following additional direct relationship between the electric displacement vector and the electric field,

$$\mathbf{D}(\mathbf{r}) = \epsilon\epsilon_{\text{vac}}\mathbf{E}(\mathbf{r}), \quad (7.16)$$

that the electric displacement field within the material is just the total electric field divided by the dielectric constant.

7.1.5 Ideal problem: Point charge in an infinite dielectric

Using the ideas introduced above, we can consider the ideal problem of a single point charge (a free charge in the language introduced above) placed in an infinite linear dielectric continuum. This is a standard derivation in electrostatics. First, let us use the fact that we are considering a linear dielectric, and combine Eqs. 7.14 and 7.16, yielding,

$$\nabla \cdot \mathbf{E} = \frac{\rho_{\text{free}}(\mathbf{r})}{\epsilon\epsilon_{\text{vac}}}. \quad (7.17)$$

We can take this result, and then use Eq. 7.13 to produce,

$$\rho_{\text{free}}(\mathbf{r}) = \epsilon\rho_{\text{total}}(\mathbf{r}). \quad (7.18)$$

Finally, we can combine Eq. 7.18 with Eq. 7.12, to produce the final result,

$$\rho_{\text{bound}}(\mathbf{r}) = -\left(1 - \frac{1}{\epsilon}\right)\rho_{\text{free}}(\mathbf{r}), \quad (7.19)$$

which is valid everywhere within the dielectric, and hence is true through all space.

In our ideal continuous dielectric, a bound charge is placed on every free charge, reducing its effective magnitude. For the point charge we are considering, we can see that a smaller bound charge of opposite sign sits on the same site. This naturally leads to Eq. 7.3, where the interaction with the point charge is reduced by a factor of ϵ . The above mathematical description demonstrates how this behavior is achieved within the material.

Note that this ideal example is “unrealistic” in the sense that the total bound charge is non-zero, breaking charge conservation. It is usual to state that the balancing positive bound charge has been “expelled to infinity”. As the dielectric continuum is infinite, there is no natural place to put this balancing charge.

7.1.6 Ideal problem: Point charge in a dielectric sphere

One of the non-physical aspects of the derivation in Sec. 7.1.5 can be removed by making the region containing the dielectric finite. We next consider a sphere of ideal linear dielectric material, of radius R , with a point free charge placed at its centre. The derivation in Sec. 7.1.5 is still valid within the dielectric medium, so we still expect to have accumulated a screening bound charge at the centre of the sphere.

As the polarization \mathbf{P} represents the response within the dielectric, it is clear that outside the sphere, $\mathbf{P}=0$. Another way of appreciating this point is to see that if we take Eq. 7.16 and set $\epsilon=1$, then Eq. 7.15 can only be satisfied if $\mathbf{P}=0$.

Following Landau and Lifshitz [135], we can integrate Eq. 7.11 over a volume element with negligible thickness placed on the boundary of the dielectric, such that the two areas are on either side. As we have $\mathbf{P}=0$ on the outer side, we require that, at the surface,

$$\rho_{\text{bound, s}} = \mathbf{P} \cdot \hat{\mathbf{n}}, \quad (7.20)$$

where $\hat{\mathbf{n}}$ is the surface normal, which points outward from the surface. This surface

bound charge is often labeled σ_b in the literature.

So, in order to evaluate the density of this bound charge, we need the value of \mathbf{P} at the boundary of the dielectric sphere. For our free point charge q at the centre of the sphere, we can use Eq. 7.14 to calculate the displacement field as,

$$\mathbf{D}(\mathbf{r}) = \frac{q}{4\pi r^2} \hat{\mathbf{r}}, \quad (7.21)$$

where $\hat{\mathbf{r}}$ is the unit radial vector from the centre of the sphere.

Now considering the solution inside the sphere, we can plug Eq. 7.21 into our linear dielectric relationship in Eq. 7.16, to get the \mathbf{E} field. Such a procedure yields,

$$\mathbf{E}(\mathbf{r}) = \frac{q}{4\pi\epsilon r^2} \hat{\mathbf{r}}, \quad (7.22)$$

which is valid only inside the dielectric.

Next, we can substitute Eqs. 7.21 and 7.22 into Eq. 7.15. This produces the polarization,

$$\mathbf{P}(\mathbf{r}) = \frac{q}{4\pi r^2} \left(1 - \frac{1}{\epsilon}\right) \hat{\mathbf{r}}, \quad (7.23)$$

namely that there is a radial polarization pointing along the radial normal of the sphere, with only an r dependence.

We can use Eq. 7.23 and evaluate the surface bound charge, as defined in Eq. 7.20. Using the simple result that $\hat{\mathbf{r}} \cdot \hat{\mathbf{n}} = 1$ leads to,

$$\rho_{\text{bound, s}} = \frac{q}{4\pi R^2} \left(1 - \frac{1}{\epsilon}\right), \quad (7.24)$$

that there is a surface bound charge that is evenly distributed over the surface of the sphere. We can then integrate Eq. 7.24 over the surface of the sphere to determine the total magnitude of this charge,

$$\oint_S \rho_{\text{bound, s}} d\mathbf{A} = q \left(1 - \frac{1}{\epsilon}\right). \quad (7.25)$$

This bound charge has the same magnitude, but opposite sign, to the bound

point charge already found inside the dielectric medium.

Combing the expression for the surface bound charge (Eq. 7.24) with the bound charge already found inside the dielectric (Eq. 7.19), we can see that the total bound charge distribution for the problem is given by,

$$\rho_{\text{bound}}(\mathbf{r}) = \frac{q}{4\pi R^2} \left(1 - \frac{1}{\epsilon}\right) \delta(\mathbf{r} - \mathbf{R}) - \left(1 - \frac{1}{\epsilon}\right) q \delta(\mathbf{r}). \quad (7.26)$$

The total amount of bound charge in the system is zero, as required by the law of charge conservation. This result represents the idea that charge is drawn from the surface of the dielectric in order to screen the bound charge inside the dielectric. In such a case, Eq. 7.3 will be observed, as long as we are significantly closer to the embedded free charge rather than the surface charge.

Generally speaking, we can anticipate that this first result for an infinite dielectric will be relevant for a charged defect within a bulk cell. Also, although we have used a spherical model for simplicity, we can also gain insight for the problem of defects in, or near surfaces, from the finite dielectric example we have made.

7.2 Modeling of the defect charge

I now consider how well the defects I have studied can be explained in light of the ideal electrostatics results discussed in Sec 7.1. The examples considered in Sec. 6 provide insight into the distribution of the defect charge within the supercell. As the corrections were calculated from density differences, but were found to be predicted by an analytic expression with no knowledge of the true distribution of charge within the cell, these results strongly suggest a generic density response takes place within the charged defect containing supercell. Folding in the analytic work in Sec. 7.1.5 on a classical charge in an infinite dielectric, I can attempt to decompose the defect charge into specific components.

For examples like the well localized defects I considered, I suggest that we can break up the defect charge into the following components,

$$\rho(\mathbf{r}) = \rho_{\text{q}}(\mathbf{r}) + J + \rho_{\text{s}}(\mathbf{r}) + \rho_{\text{d}}, \quad (7.27)$$

where the total defect charge $\rho(\mathbf{r})$ is made out of a defect state charge $\rho_q(\mathbf{r})$, a constant neutralizing jellium background J , a screening bound charge $\rho_s(\mathbf{r})$, and a resulting uniform bound depletion charge ρ_d . The screening charge $\rho_s(\mathbf{r})$ acts to dielectrically screen the defect. As charge conservation is obeyed by our DFT supercell, this electric charge has to have come from somewhere, and this is the opposite sign depletion charge, ρ_d .

These charge distributions have the following norms associated with them,

$$\int_{\Omega} \rho_q(\mathbf{r}) d^3\mathbf{r} = +q \quad (7.28)$$

$$\int_{\Omega} J d^3\mathbf{r} = -q \quad (7.29)$$

$$\int_{\Omega} \rho_s(\mathbf{r}) d^3\mathbf{r} = -\left(q - \frac{q}{\epsilon}\right) \quad (7.30)$$

$$\int_{\Omega} \rho_d(\mathbf{r}) d^3\mathbf{r} = +\left(q - \frac{q}{\epsilon}\right), \quad (7.31)$$

where the magnitude of ρ_q and J depends only on the charge state of the defect, and where ρ_s and ρ_d additionally depend on the dielectric constant, ϵ . For an atom in vacuum ($\epsilon = 1$), both ρ_s and ρ_d would be expected to have a norm of zero.

The four components of the total defect charge are graphically summarized in Fig. 7.1.

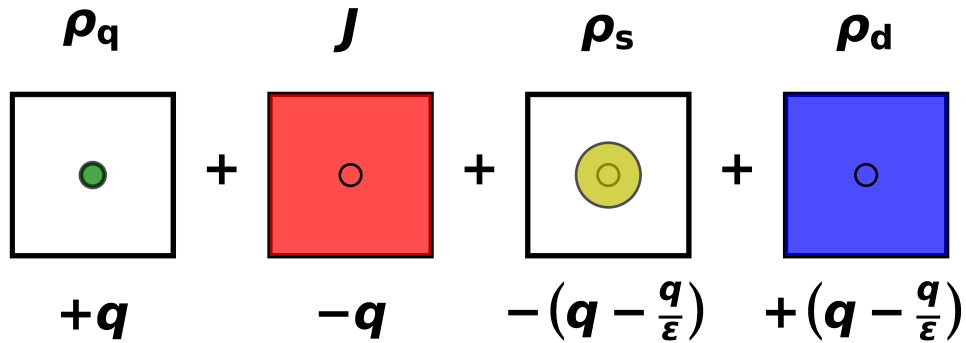


Figure 7.1: Schematic illustration of the charge decomposition introduced in Eq. 7.27. The magnitudes of the charge components are shown below the figure. The localized charges, ρ_q and ρ_s are well localized with respect to the size of the simulation cells.

In order to make direct contact between the definitions given in Eq. 7.27, and the actual charge models we construct through DFT density differences, we need to

7.2. MODELING OF THE DEFECT CHARGE

introduce some further definitions (at this point, only J and ρ_d are unambiguously defined as uniform charge densities.). We can proceed by defining ρ_q as the charge associated with the KS defect states that have been occupied (for a negative defect) or unoccupied (for a positive defect) to reach the required charge state. This would produce the following definition,

$$\rho_q(\mathbf{r}) = \sum_i^N \left| \phi_i^d(\mathbf{r}) \right|^2, \quad (7.32)$$

where a sum over i is performed over all N KS orbitals that have changed occupation with respect to the neutral defect state.

I note that there is still some choice available in the definition given in Eq. 7.32. We could calculate the density from the KS wavefunction of the neutral defect, or from within the charge state of interest. Additionally, similar to the construction of the charge model, we could make different choices of the ionic geometry considered. However, I will take the wavefunctions of the neutral defect state as our choice, as this means that defect induced polarization is explicitly excluded from the definition of ρ_q .

A definition for the bound depletion charge is also needed. I chose to define this as a uniform charge across the whole supercell, following the definition used in the derivation of the Lany-Zunger method. Hence,

$$\rho_d(\mathbf{r}) = \frac{1}{\Omega} \left(q - \frac{q}{\epsilon} \right) \quad (7.33)$$

where this formula is only valid within the supercell.

Once the choices given by Eq. 7.32 and Eq. 7.33 are made, only ρ_s requires a definition. We can use Eq. 7.27 to define it as the remaining charge,

$$\rho_s = \rho(\mathbf{r}) - \rho_q(\mathbf{r}) - J - \rho_d. \quad (7.34)$$

Of course, when using this definition, we need to check that ρ_s does in fact look like a screening charge. Practically, this means that the charge distribution should

be centered on the defect site, and that it should tend to zero far from the defect, at least for supercells large enough to contain a finite-size converged screening charge.

With the above charge components defined, we can look at how rapidly these components converge with the size of the defect containing supercell.

7.3 Defect charge in the bulk

When looking at the example of the V_O^{+1} defect in MgO, this charge model is found to explain the observed densities. Once smoothing is applied to the ρ_s density, it is observed to be well localised on the defect state, as a classical screening density should be. Two examples are shown in Fig. 7.2 and Fig. 7.3.

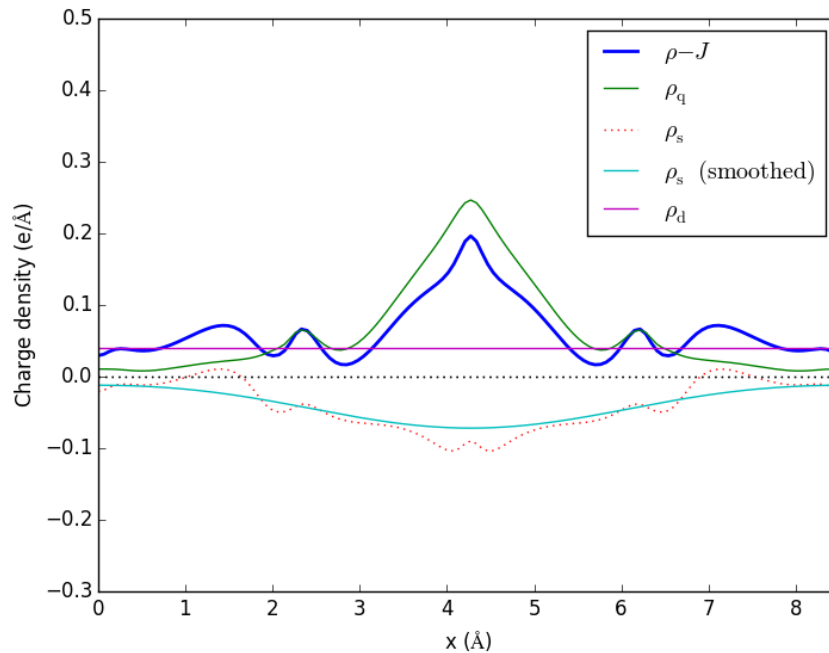


Figure 7.2: Defect density components of the V_O^{+1} defect in a $2 \times 2 \times 2$ supercell of MgO. The total defect charge neglecting jellium ($\rho - J$) is shown by the blue line. The defect free charge (ρ_q) is shown by the green line. The screening charge (ρ_s) is shown by the red dotted line, which when smoothed becomes the cyan line. The depletion charge (ρ_d) is shown by the red line.

7.3. DEFECT CHARGE IN THE BULK

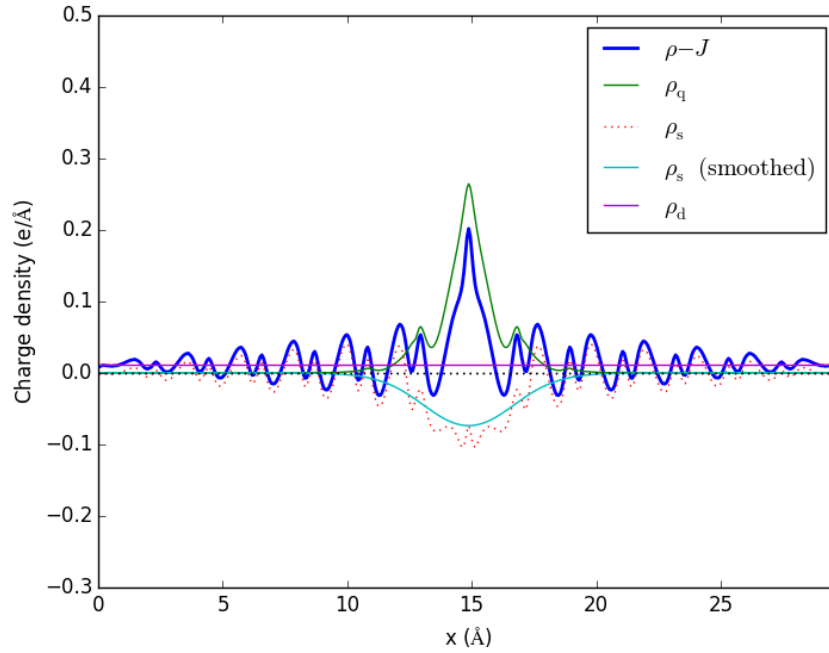


Figure 7.3: Defect density components of the V_O^{+1} defect in a $7 \times 7 \times 7$ supercell of MgO. The same notation is used as in Fig. 7.2.

The similarity of different densities can be compared by introducing a density overlap, $\Delta\rho_{ab}$, defined as [136],

$$\Delta\rho_{ab} = 1 - \frac{1}{q_a + q_b} \int |\rho_a - \rho_b| d^3\mathbf{r}, \quad (7.35)$$

where the similarity between the two densities ρ_a and ρ_b is calculated. The total charge of the densities q_a and q_b is also used. The definition in Eq. 7.35 returns one if the two charge distributions are identical, and zero if there is zero overlap between the two densities.

As shown in Fig. 7.4, this allows us to explore how quickly convergence of the defect free charge ρ_q and the total defect charge neglecting jellium (ρ -J) is achieved as the size of the supercell is increased. The jellium background is removed, as it introduces a supercell size dependence into ρ that is easily understood and removed. As the form of either of these charges in the limit of an infinite supercell is unknown, I compare with the largest supercell I calculated. It can then be inferred from the gradient of the density norm if the density in the large supercell can be

considered converged – if a density has converged, then the overlap integral should stop changing with supercell size.

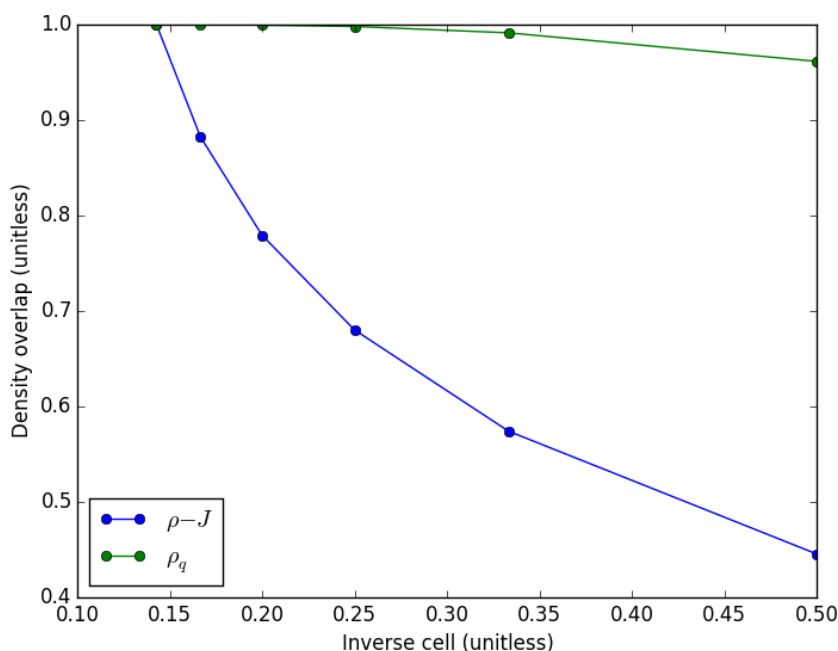


Figure 7.4: The density overlap (defined in Eq. 7.35) is considered separately for both the defect charge (excluding jellium) and for the defect free charge (defined in Eq. 7.32). The comparisons are made with respect to the densities of the $7 \times 7 \times 7$ supercell, so the overlaps are one by definition for this cell. It can be seen directly that convergence of the defect free charge ρ_q is achieved rapidly, but that convergence of the defect charge $\rho - J$ is slow. From the gradient, it is clear that even in a $7 \times 7 \times 7$ supercell, that a fully converged defect charge has not been achieved. The V_O^{+1} defect in bulk MgO is considered.

These results confirm the idea that the description of the defect free charge (equivalently, the KS orbitals associated with the charged defect) within DFT supercells converges rapidly, but that the total change in the density converges only very slowly with system size, due to the significantly enhanced size-dependence of the bound charges present in the supercell.

7.4 Calculation of the dielectric constant from the density response

Our confidence in our model of the density response (as described in Sec. 7.2) is increased due to the fact that it can be used to directly infer the dielectric constant of the host dielectric, using only the defect density. This is a strong demonstration of the consistency of the argument as a whole, and also demonstrates that the formation of a single point defect is not responsible for a significant change in the dielectric constant of the host system. This particular point is not obvious, and defect-induced changes in the dielectric constant have been suggested in the past. This correspondence is explore in more detail in this section.

In order to determine the dielectric constant, we use the following procedure:

1. Calculate the electronic density difference between the neutral defect and the charged defect, yielding $\rho(\mathbf{r})$
2. Apply a Gaussian smearing of $\sigma=2.25a$ to smooth out the long range polarization, where a is the unit cell length.
3. Identify the smoothed density at the edge of the cell as the density of the bound depletion charge ρ_d , and use Eq. 7.36 to calculate the dielectric.

Where ϵ is calculated as,

$$\epsilon = \left[1 - \frac{\rho_d \Omega}{q} \right]^{-1}, \quad (7.36)$$

where ρ_d is the density of the bound charge, Ω is the volume of the supercell, and q is the formal charge state of the defect.

As expected, using the above procedure and holding the atomic positions fixed yields ϵ_∞ . Some examples of dielectric constants calculated in this way are shown in Tab. 7.1, where we observe an average absolute relative error of less than 2%, when compared with DFPT.

Material	ϵ_∞ (DFPT)	ϵ_∞ (Eq. 7.36)	Relative error (%)
KCl	2.33	2.40	2.82
LiF	2.09	2.08	-0.59
MgO	3.19	3.23	1.18
NaCl	2.53	2.51	-0.87
SrO	3.85	3.87	0.38
CaO	3.86	3.67	-4.87

Table 7.1: Comparison of the dielectric constants calculated using DFPT, and by inspection of the defect density via Eq. 7.36, for +1 vacancy defects in $3 \times 3 \times 3$ supercells of the listed materials. The strong agreement between the dielectric constants calculated through the two methods justifies the developed charge model.

7.5 Role of boundary conditions and jellium

The discussion in Secs. 7.2 and 7.3 demonstrates that we can predict the density change introduced when a defect is charged. It is natural to then wonder about the electrostatic energies of this kind of charge model. In particular, we can ask a simple question about which kind of interaction is larger: the interactions with image supercells or the interactions with the artificial jellium background within the host supercell? In this section, I will attempt to answer this question.

As stated in Eq. 4.1, electrostatic corrections can be generated as the difference in energy between a given charge distribution ρ under both periodic and isolated boundary conditions. When PBC is utilized, the charge distribution includes an implicit jellium background that is absent when the energy is computed under isolated boundary conditions. Hence, this energy change can be understood as a two step process. Starting with the electrostatic energy of the system under isolated boundary conditions, we first add a jellium background (contained within the supercell), and then change the boundary conditions from isolated to periodic, allowing interaction with charge in neighbouring supercells – inter-supercell interactions. How clearly these two ideas can be separated is not obvious, because it is unclear how the inclusion of a jellium background effects the inter-supercell interactions.

In order to further probe this aspect of the problem, I introduce a new energy term, E_{iso}^J , namely the electrostatic energy of a charge distribution that does include a jellium background, whilst still subject to isolated boundary conditions. Then the

7.5. ROLE OF BOUNDARY CONDITIONS AND JELLIUM

following two energy terms can be constructed,

$$\epsilon_{\text{jel}} = E_{\text{iso}} - E_{\text{iso}}^J, \quad (7.37)$$

$$\epsilon_{\text{PBC}} = E_{\text{iso}}^J - E_{\text{PBC}}, \quad (7.38)$$

where ϵ_{jel} is the intra-supercell interaction between the defect charge and the neutralizing jellium, and ϵ_{PBC} is the inter-supercell interaction between both defect charge and the neutralizing jellium background. Substituting both Eqs. 7.37 and 7.38 into Eq. 4.1 produces an alternative definition for the electrostatic correction,

$$E_{\text{corr}} = \epsilon_{\text{jel}} + \epsilon_{\text{PBC}}, \quad (7.39)$$

which makes it clear that this correction is composed of two distinct energy components. By comparing these two terms, I can see if the corrections I have been constructing are dominated by inter-supercell or intra-supercell interactions directly.

Example calculations quickly demonstrate that for bulk cubic supercells, ϵ_{jel} is significantly larger than ϵ_{PBC} . Two examples for the F^+ center in MgO are shown in Fig. 7.5.

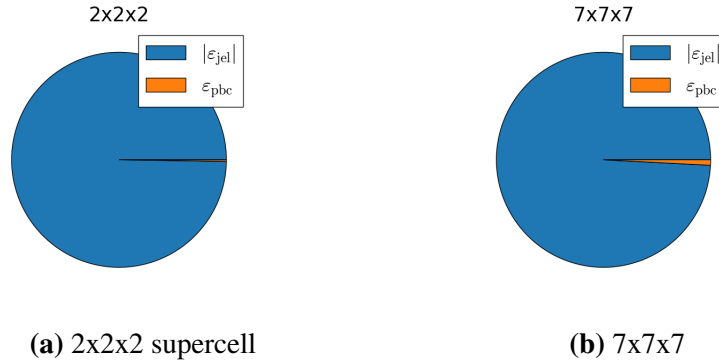


Figure 7.5: Comparison between the inter-supercell and intra-supercell interactions present in an electrostatic correction calculated using the definitions introduced in Eqs. 7.37 and 7.38.

These results suggest that inter-supercell interactions are actually only a minor source of finite-size error. This result can be justified using multipole arguments. Considering an isolated supercell, the use of a jellium background ensures

a monopole moment of zero for the combination of the defect charge and this neutralizing charge. Also, when the cell is cubic and the defect is placed at the centre of the cell, along each crystallographic axis neither direction can be preferred due to the high symmetry of the system. This ensures a net dipole moment of zero too. Hence, inter-supercell interactions are at least quadrupolar, and don't appear to be very strong.

Such an argument quickly suggests that the use of cubic supercells will suppress the ϵ_{PBC} energy term, representing inter-supercell interactions. These interactions might be more significant if the cell shape is varied away from this.

7.6 New derivations of point charge corrections

As discussed in Sec. 7.2, our DFT results suggest that a generic density response is generated across diverse materials, which only depends on the dielectric constant. This density response is in accordance with the screening charge arguments introduced in the ideal argument for a charge in an infinite dielectric introduced in Sec. 7.1.5. The only modification required was the introduction of a uniform depletion charge, as in the ideal problem it was assumed that this charge was expelled to infinity.

Additionally, our calculations in Sec. 7.5 suggested that periodic interactions surprisingly play only a very minor role in charge corrections for cubic cells. This introduces an enormous mathematical simplification, as we can solve our electrostatic equations under isolated boundary conditions. In this section, I will assume that we can consider the isolated problem only, and see how well the expressions I derive agree with previous results based on periodic approaches, such as Ewald summation [31].

7.6.1 Mathematical preliminaries

The simplest density description we can employ is to use only point charges and uniform backgrounds. For mathematical simplicity, we will also limit ourselves to cubic supercells, of unit length. Using the above arguments, for a defect of charge

q , this produces the following charge model,

$$\rho(\mathbf{r}) = \rho_q(\mathbf{r}) + \rho_s(\mathbf{r}) + J(\mathbf{r}) + \rho_d(\mathbf{r}), \quad (7.40)$$

where $\rho_q(\mathbf{r})$ is the defect free charge, $\rho_s(\mathbf{r})$ is the bound screening charge, $J(\mathbf{r})$ is the jellium background, and $\rho_d(\mathbf{r})$ is the bound depletion charge.

Using point charges to describe the local charges, and uniform charges to describe the delocalized charges yields,

$$\rho(\mathbf{r}) \approx q\delta(\mathbf{r} - \mathbf{r}_0) - \left(q - \frac{q}{\epsilon}\right)\delta(\mathbf{r} - \mathbf{r}_0) - \frac{q}{\Omega} + \frac{\left(q - \frac{q}{\epsilon}\right)}{\Omega}, \quad (7.41)$$

which is only valid within the cube, as the uniform charges are zero outside the volume Ω .

To use this model to derive a correction, we also need the potentials generated by the charges under isolated boundary conditions. We already introduced an exact expression for the potential of a point charge in Eq. 7.2, but we still require the potential of a uniform charge background, which under isolated boundary conditions becomes an isolated cube of charge.

Thankfully, the potential due to a uniform cube of charge has already been studied in detail. As derived in [137], we can use the interior multipole expansion in terms of cubic harmonics to describe this potential. The first two terms of this expansion yield,

$$\phi_c(\mathbf{r}) = 3\log(3^{1/2} + 2) - \frac{\pi}{2} - \frac{2\pi}{3}r^2 + \dots, \quad (7.42)$$

where we have considered a unit cube with a charge of unity, and the origin of the coordinate system is at the centre of the cube. This expansion is accurate within the unit cube, but is not valid outside the cube [137].

It is useful to introduce ϕ_0 as the potential at $\mathbf{r}=0$ in Eq. 7.42, producing,

$$\phi_0 = 3\log(3^{1/2} + 2) - \frac{\pi}{2}, \quad (7.43)$$

7.6. NEW DERIVATIONS OF POINT CHARGE CORRECTIONS

where $\phi_0 \approx 2.380$ numerically.

Eq. 7.42 then simplifies to,

$$\phi_c(\mathbf{r}) = \phi_0 - \frac{2\pi}{3}r^2 + \dots \quad (7.44)$$

As we have both point charges and uniform cubes in Eq. 7.41, it is helpful to derive the energy of a uniform cube of charge in the potential of another uniform charge, and also the energy of a point charge placed at the centre of a uniform cube of charge.

The energy of a point charge in the potential of a unit cube follows directly from Eq. 7.44 as,

$$E_{pj} = \frac{q_p q_j \phi_0}{2}, \quad (7.45)$$

where q_p is the charge of the point charge, and q_j is the charge on the unit cube.

The energy of a uniform cubic charge in the potential of another uniform cube requires an integration over the volume of the cube, Ω . Labeling the cubic charge experiencing the potential as having magnitude q_j , and the magnitude of the cubic charge producing the potential as $q_{j'}$ yields an integral of the form,

$$E_{jj'} = \frac{1}{2} \int_{\Omega} \frac{q_j}{\Omega} q_{j'} \phi_c(\mathbf{r}) d\Omega, \quad (7.46)$$

which is only valid in the volume Ω .

Using Eq. 7.44 and substituting it into Eq. 7.46, then integrating over the cube leads to the following expression for the energy,

$$E_{jj'} = \frac{1}{2} \left(\phi_0 - \frac{\pi}{6} \right) q_j q_{j'}, \quad (7.47)$$

where a uniform cube of charge q_j sits in the potential of a uniform cube with charge $q_{j'}$.

We can then use these definitions, and the superposition principle, to evaluate the total electrostatic energy of all of our interaction charge distributions, which in

this context will be,

$$E_{\text{tot}} = \sum_i \sum_j \frac{1}{2} \int_{\Omega} \rho_i(\mathbf{r}) v_j(\mathbf{r}) d\Omega, \quad (7.48)$$

where the indices i and j run over all charge distributions considered, to generate all the relevant pairs of interactions.

7.6.2 Solution in vacuum

If we consider the electrostatic energy components present in the absence of a dielectric medium, there are four non-zero components, as both ρ_s and ρ_d are zero, according to the definition given in Eq. 7.41.

Although there are four terms, only three of them demonstrate finite-size dependence. The defect free charge ρ_q is size independent, so it directly follows that the energy term E_{qq} is also size independent. This is fortunate, because it represents a self interaction of a point charge, which is not well defined.

Considering the remaining terms, we also note that $E_{qJ} = E_{Jq}$. So, we need to evaluate the size-dependent energy,

$$E_{\text{FS}} = E_{qJ} + E_{Jq} + E_{JJ} = 2E_{qJ} + E_{JJ}, \quad (7.49)$$

where we have introduced E_{FS} , as the component of the total electrostatic energy that demonstrates finite-size dependence.

Our expression for the energy of a point charge in a cube in Eq. 7.45 allows us to evaluate E_{qJ} as,

$$E_{qJ} = -\frac{q^2 \phi_0}{2}. \quad (7.50)$$

Likewise, using our expression for the energy of a cubic density in the potential of a cubic density in a cube, Eq. 7.47, produces for E_{JJ} ,

$$E_{JJ} = \frac{1}{2} \left(\phi_0 - \frac{\pi}{6} \right) q^2. \quad (7.51)$$

Substituting Eq. 7.50 and Eq. 7.51 into Eq. 7.49 yields,

$$E_{\text{FS}} = -q^2\phi_0 + \frac{1}{2} \left(\phi_0 - \frac{\pi}{6} \right) q^2, \quad (7.52)$$

$$E_{\text{FS}} = -\frac{q^2}{2} \left(\phi_0 + \frac{\pi}{6} \right) \quad (7.53)$$

The term in the brackets in Eq. 7.53 is a numerical constant equal to 2.9036. In fact, this is almost the relevant Madelung constant for this problem, $\alpha_M=2.837$. Hence, we have calculated a 2% overestimate of the result of an Ewald summation.

Ewald summation provides an exact result for the system we are interested in. To derive Eq. 7.53 we introduced two approximations, neglecting all image interactions and only considering the first two terms of the multipole expansion in Eq. 7.44. This correspondence demonstrates that these two approximations introduce only minor errors in the calculated total energy.

To my knowledge, the derivation above hasn't been discussed in the literature on charged defects. However, this derivation in the absence of a dielectric is a known result in the literature on Wigner crystallization [138]. I note that this derivation is significantly simpler than the corresponding derivation using Ewald summation.

7.6.3 Solution in a dielectric medium

Ewald summation can also be used to derive the appropriate correction formula when the density can be described by the density model given in Eq. 7.41. This model can be simplified to,

$$\rho(\mathbf{r}) = \frac{q}{\epsilon} \delta(\mathbf{r} - \mathbf{r}_0) - \frac{q}{\epsilon\Omega}, \quad (7.54)$$

which looks like a point charge embedded in a jellium background, where both charges have a total magnitude of $\frac{q}{\epsilon}$.

As this is the same charge model used in the Madelung correction, it has the same solution. The only difference from the traditional derivation is that the mag-

nitude of the charges is decreased. Hence, the correction produced is

$$E_{FS} = -\frac{q^2 \alpha_M}{2\epsilon^2}, \quad (7.55)$$

which only differs from the traditional MP correction by the factor of ϵ^2 in the denominator, rather than a factor of ϵ . In practice, this will produce a significantly smaller correction, which quickly tends to zero as ϵ increases.

7.7 Bound surface charges

The observation of the depletion bound charge within periodic DFT calculations is always slightly indirect. Partly, this reflects the non-physical nature of this charge. Classical electrostatics predicts that it should be expelled to surfaces, rather than drawn uniformly from the host crystal. In fact, this behavior is observed in DFT, making the bound surface charge more visible. Whenever a charged defect is formed within a slab model, the surfaces (no matter how far physically separated) become charged. The observed charge density at the surfaces is in good agreement with the classical prediction, depending on the dielectric of the material being considered. In this section, I will use the unrelaxed V_O^+ defect in films of MgO as an illustrative example of this behavior. Some example defect charges for this system are shown in Fig. 7.6.

In terms of these density models, it can be seen that the density can be broken up into two components, in accordance with the model described in Fig. 7.1. This is shown in Fig. 7.7.

Conclusions: It has been demonstrated that the classical electrostatics concepts of free and bound charges well describes the charge densities observed in DFT calculations. The approximation made in the MP, LZ and FNV methods that the electronic charge difference caused by the formation of a charged defect is well localized to the center of the DFT supercell is not consistent with the requirement of charge conservation. The presence of a net screening charge around the defect requires the formation of a bound depletion charge that acts to strongly reduce the calculated electrostatic errors, which should produce smaller finite-size errors than

7.7. BOUND SURFACE CHARGES

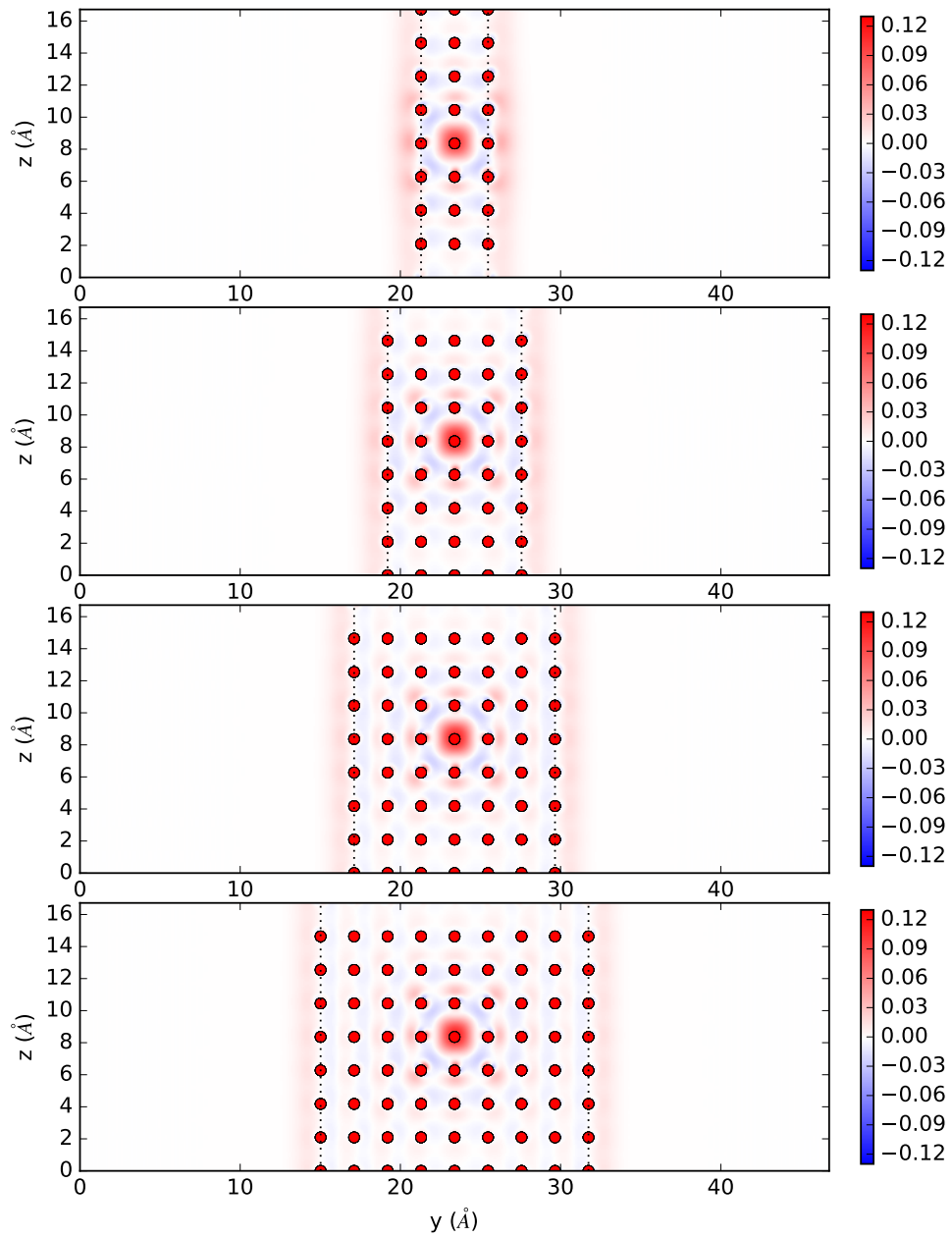


Figure 7.6: Defect charge models for the unrelaxed V_O^+ defect in MgO slabs. The red markers denote atoms. The charge density is shown in $e\text{\AA}^{-2}$. The models demonstrate a bound surface depletion charge that only weakly depends on the number of layers contained in the model.

predicted by the existing methods.

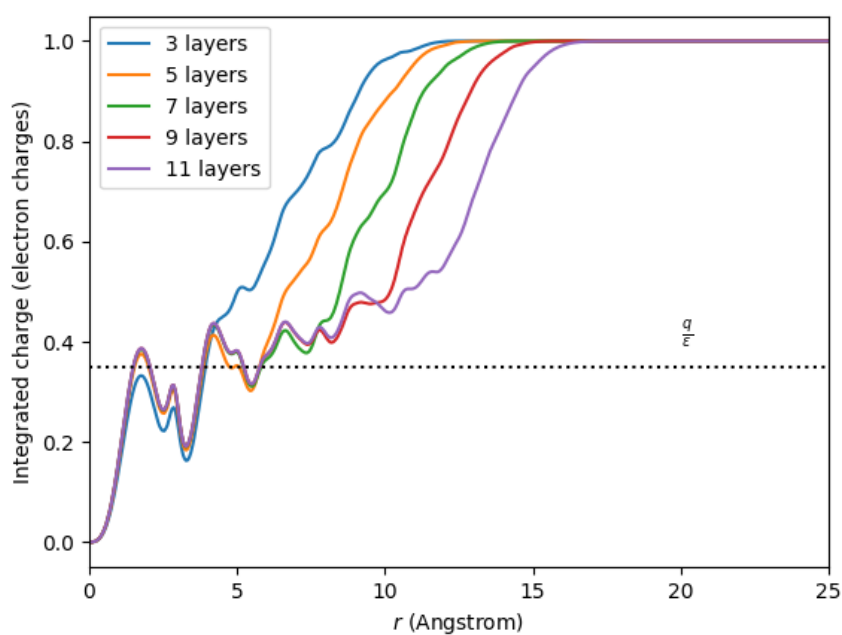


Figure 7.7: Total charges (excluding the jellium background), integrated radially from the defect site. The density shows two regions, firstly a near region $\sim 5 \text{ \AA}$ in radius that is not highly sensitive to the number of layers and which contains approximately $\frac{q}{\epsilon}$ of charge. Secondly, the charge outside this sphere is sensitive to the number of MgO layers in the model, and moves further from the defect as the surface is moved further away. This can be interpreted as the first region containing the screened defect ($\rho_q + \rho_s$), and the second region the surface depletion charge, ρ_d .

Chapter 8

Less electrostatic errors

Aims: In the previous chapter, I derived an electrostatic correction that is significantly smaller than the traditional Makov-Payne correction. This new expression is too small to explain the observed size dependence, so if the derivation is correct, then the large errors introduced must have another source. In this chapter, I start to develop an argument that the exchange-correlation energy of the bound screening charge is responsible for a larger error than electrostatics in dielectric materials. Very simple examples of unrelaxed vacancy defects in cubic supercells are considered. Although this is a significant simplification on many problems of present interest, it is notable that even for these simplified examples the traditional approach does not appear to be fully consistent.

Results: It is discussed that the electrostatic models introduced in Chapter 7 only require a small modification in order to match the observed ΔV_{CD} components (that component introduced by the system becoming formally charged), but that this has only a very small impact on the electrostatic correction calculated. With this done, the ΔV_{CD} components for the example defects appear to be well understood, along with the required alignment correction. Once both ΔV_{AB} alignment corrections and convergence of the \mathbf{k} -point sampling is achieved, it is observed that the remaining finite-size errors are almost entirely linear with respect to inverse length of the supercell. Still, this remaining error is larger than that derived on electrostatic grounds in chapter 7, and in better agreement with the existing MP and LZ corrections. However, the new electrostatic correction is a good predictor of the finite-size

dependence of the formation energy when the exchange-correlation energy component is removed. A finite-size error caused by XC would require a localized charge within the supercell that is too compressed in small supercell models. The bound screening charge fits this description, and as the magnitude of this charge depends on the dielectric constant, this could produce the observed dependence on dielectric constant. For the defects considered, an empirical correction is constructed, representing the combined electrostatic and XC errors. This correction is observed to be similar to the LZ method in form, and is similar to the average of the MP and LZ correction methods. It is suggested that this could be an improved bulk correction formula, although its transferability to relaxed defects, or more complex example systems, is not yet demonstrated.

8.1 Improving electrostatic models through potential alignment

The electrostatic correction derived in Chapter 7 appears to poorly reproduce the observed finite size dependence in actual DFT calculations. So it is natural to attempt to improve the electrostatic model by making it more realistic. The electrostatic correction given in Eq. 7.55 is based on a model using only point charges and uniform backgrounds. Point charge models are too simplistic to fully reproduce the ΔV_{CD} alignment component observed in DFT calculations. In this section, we look at the improvements required to reproduce this potential, and the energetic consequences of such an improvement.

Use of point charges introduces a discontinuity into the electrostatic potential, so this is a clear shortcoming of the model to predict the actual DFT potential differences that are observed. As in the FNV approach, where a comparison with DFT potentials is made, we should replace point charges with Gaussian charge models. If these Gaussian charges remain well localised within the supercell, then the change in the interaction energy introduced by this change should be small. Such a change naturally introduces the parameter σ , which describes the width of the Gaussian distribution considered.

8.1. IMPROVING ELECTROSTATIC MODELS THROUGH POTENTIAL ALIGNMENT

Recall that a Gaussian charge distribution can be defined as,

$$\rho(\mathbf{r}) = \frac{q}{\sigma^3 (2\pi)^{\frac{3}{2}}} \exp\left(\frac{-r^2}{2\sigma^2}\right), \quad (8.1)$$

where q is the total charge of the Gaussian, and σ is the width of the Gaussian distribution.

The density in Eq. 8.1 has an analytic solution for the electrostatic potential under isolated boundary conditions. This potential is simply,

$$v(\mathbf{r}) = \frac{1}{4\pi\epsilon} \frac{q}{r} \operatorname{erf}\left(\frac{r}{\sqrt{2}\sigma}\right). \quad (8.2)$$

The density model of Eq. 7.40, containing point and uniform charges can be converted into Gaussian and point charges directly. The only choice is whether the contribution from the free charge and from the bound screening charge should have the same value of σ , or if these two charges require different values.

For simplicity, we consider only the case where both density contributions have the same value of σ . This would produce the new density model,

$$\rho(\mathbf{r}) = \frac{q}{\epsilon\sigma^3 (2\pi)^{\frac{3}{2}}} \exp\left(\frac{-r^2}{2\sigma^2}\right) - \frac{q}{\epsilon\Omega}, \quad (8.3)$$

where q is now the charge state of the defect being considered. The density model contains two free parameters, ϵ and σ . The value of the dielectric constant ϵ is known using DFPT, but this still leaves the value of σ unknown. This parameter can be fitted numerically to best reproduce the available DFT electrostatic potential.

An approximate expression for the potential of a uniform cube of charge was given in Eq. 7.44. Combining this expression with Eq. 8.2 yields the following model potential v ,

$$v(\mathbf{r}) \approx \frac{1}{4\pi\epsilon} \frac{q}{\epsilon r} \operatorname{erf}\left(\frac{r}{\sqrt{2}\sigma}\right) - \frac{q}{\epsilon} \left(\phi_0 - \frac{2\pi}{3} r^2\right), \quad (8.4)$$

where the approximation is made in the multipole expression for the potential of a

8.1. IMPROVING ELECTROSTATIC MODELS THROUGH POTENTIAL ALIGNMENT

uniform cube of charge.

Having both an expression for the model density in Eq. 8.3, and the model potential in Eq. 8.4, it is straightforward to evaluate the total energy for a given model. Again, this expression is for isolated boundary conditions. However, as the model in Eq. 8.3 has a total charge of zero, the average value of the potential in Eq. 8.4 has no effect on the total energy. We still make the assumption that the intersupercell interactions are negligible, and then mimic the DFT boundary conditions by setting the average of the model potential to zero.

As shown in Figs. 8.1- 8.4, this model can then well reproduce the observed ΔV_{CD} potential difference. As always, the conventional unit cell is not well described by the model. It is observed that the best value of the σ parameter increases with supercell size, but as shown in Fig. 8.5, it appears that it tends to a finite value in the limit of an infinite supercell.

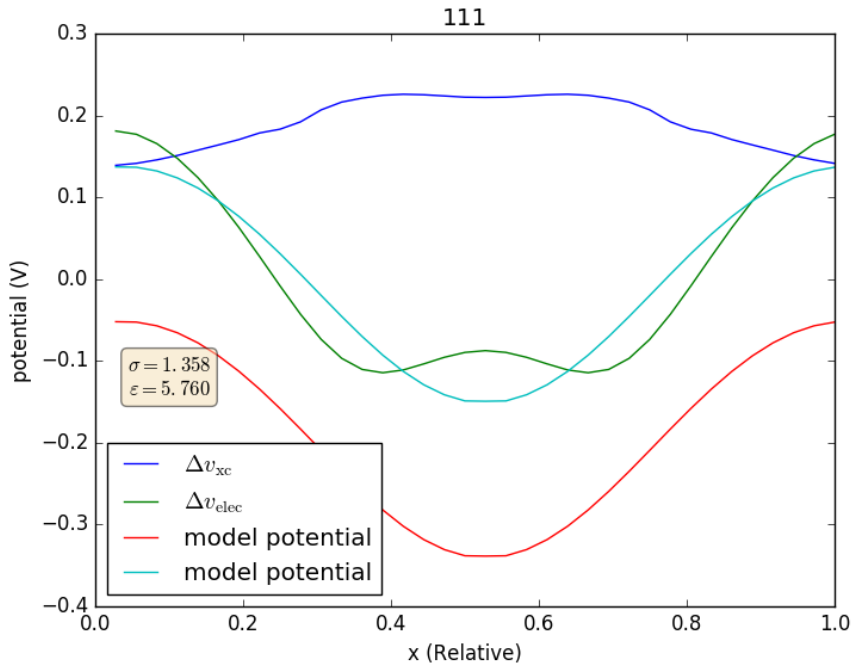


Figure 8.1: Comparison between optimized electrostatic model (Eq. 8.4, cyan line) and DFT CD alignment component (green line), for a $1 \times 1 \times 1$ supercell of diamond, containing a V_C^+ defect. The model potential is also shown when its average value is not neglected (red line). The change in the XC potential is also shown (dark blue line).

8.1. IMPROVING ELECTROSTATIC MODELS THROUGH POTENTIAL ALIGNMENT

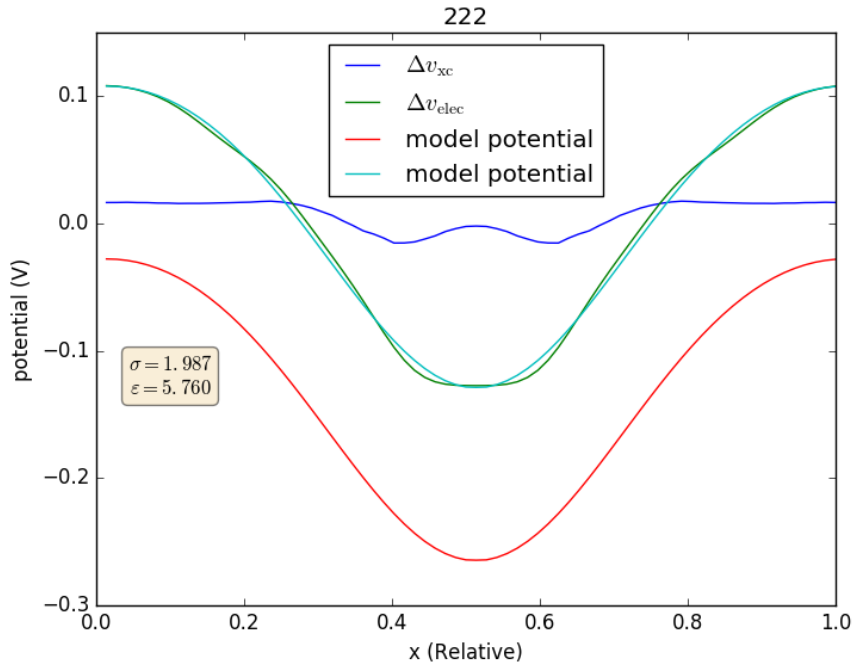


Figure 8.2: Comparison between optimized electrostatic model and DFT CD alignment component, for a $2 \times 2 \times 2$ supercell of diamond, containing a V_C^+ defect. The same notation as in Fig. 8.1 is used.

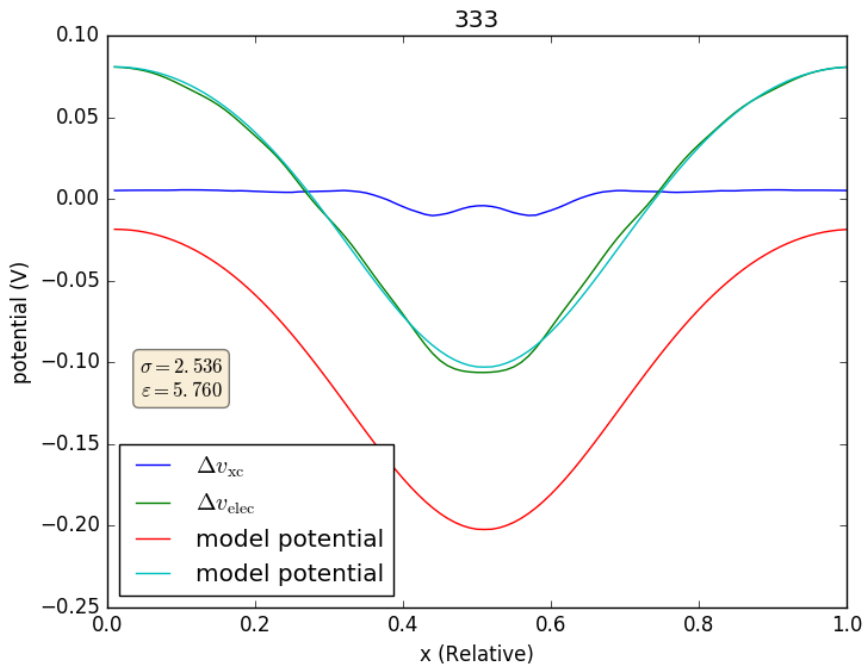


Figure 8.3: Comparison between optimized electrostatic model and DFT CD alignment component, for a $3 \times 3 \times 3$ supercell of diamond, containing a V_C^+ defect. The same notation as in Fig. 8.1 is used.

8.1. IMPROVING ELECTROSTATIC MODELS THROUGH POTENTIAL ALIGNMENT

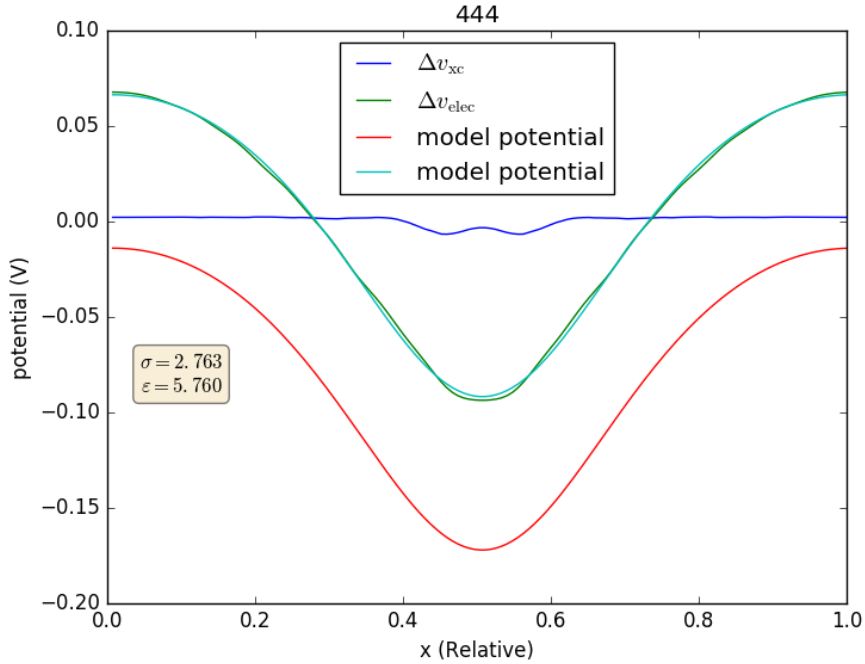


Figure 8.4: Comparison between optimized electrostatic model and DFT CD alignment component, for a $4 \times 4 \times 4$ supercell of diamond, containing a V_C^+ defect. The same notation as in Fig. 8.1 is used.

The parameter σ can be interpreted as describing the width of the bound screening charge in this example. In small supercells it is too compressed on the defect site, but as the size of the model is increased, it spreads out slightly. However, it would eventually saturate with supercell size, rather than spreading out infinitely.

What kind of energy change does the σ parameter represent? The models can be used to calculate correction energies, which are in good agreement with the prediction of Eq. 7.55. As shown in Tab. 8.1, introducing this Gaussian smearing has only a very minor impact on the calculated corrections. Additionally, this energy difference gets smaller with increasing supercell size, both in absolute energy, and as a fraction of the total correction.

Previous attempts [88] to improve the FNV correction method have looked at using more complex charge models to match the potential difference, by introducing exponential functions to Gaussian models. The results in this section demonstrate an improved model with only one free parameter, but again the results also demonstrate that the electrostatic correction becomes significantly smaller when this is

8.1. IMPROVING ELECTROSTATIC MODELS THROUGH POTENTIAL ALIGNMENT

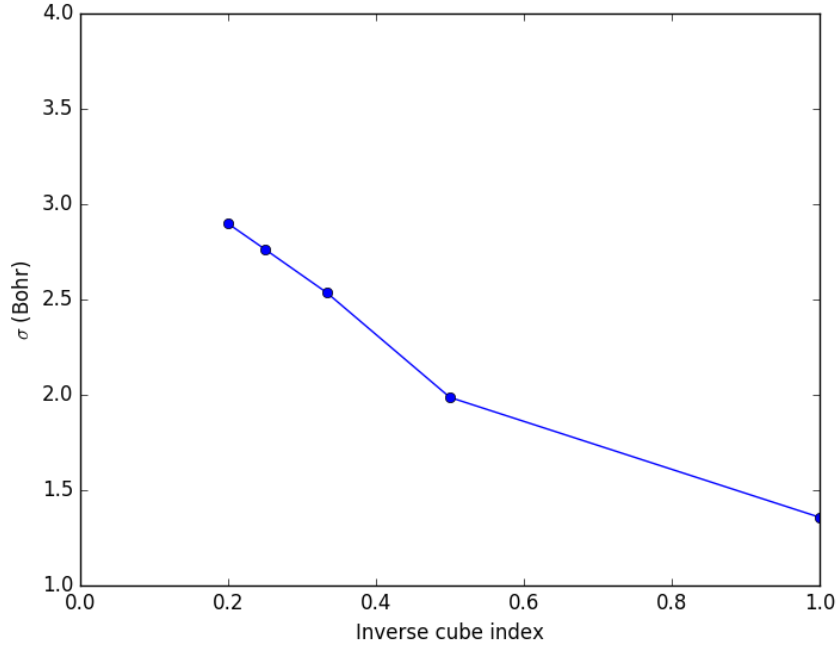


Figure 8.5: Dependence of calculated optimal value of σ on supercell size for the example of a V_C^+ defect in diamond.

supercell	E_{FS} (eV)	E_{model} (eV)	Relative error	f error
$1 \times 1 \times 1$	0.173	0.142	21.7%	0.031
$2 \times 2 \times 2$	0.087	0.080	8.1%	0.013
$3 \times 3 \times 3$	0.058	0.055	4.9%	0.008
$4 \times 4 \times 4$	0.043	0.042	2.4%	0.004
$5 \times 5 \times 5$	0.035	0.034	1.0%	0.002

Table 8.1: Calculated correction energies for the considered diamond supercells containing a V_C^+ defect. The relative error between the correction given by Eq. 7.55, and the energy calculated from the density model in Eq. 8.3 is shown. On electrostatic grounds, the change in the width of the bound screening charge doesn't significantly alter the error expected for large cells.

8.2. FURTHER EXAMPLE SYSTEMS

Material	\mathbf{k} -points	E_{cut} (eV)	a (Exp.) (Å)	a (Theory) (Å)
NaCl	5x5x5	707.50	5.57 [139, 140]	5.69
KCl	5x5x5	326.54	6.28 [141]	6.34
LiF	10x10x10	849.00	4.03[142]	4.00
CaO	7x7x7	843.55	4.79 [143, 144]	4.78
SrO	7x7x7	843.55	5.16 [145]	5.12

Table 8.2: DFT parameters used to calculate the additional systems. \mathbf{k} -points is the Monkhorst-Pack grid used for the conventional unit cell, and E_{cut} is the cut-off energy of the planewave basis employed. The calculated equilibrium lattice constants are compared with their experimentally reported values.

done.

These arguments strengthen the case made in Chapter 7 that electrostatic errors should be smaller than traditionally expected. Using such arguments, we can also understand the observed potential differences. Although a width parameter, σ , is required to well reproduce the potentials, it seems to have only a very minor role in the electrostatic correction implied by the model calculations. It is noteworthy that σ is dependant on supercell size, and this is another result that suggests that the size of the distribution of the bound screening charge is finite-size dependant.

8.2 Further example systems

In this section, it was useful to introduce a further range of materials. This allowed examples over a wider range of dielectric constants. Additional calculations were carried out for NaCl, KCl, LiF, CaO and SrO. These are all ionic materials, which are qualitatively similar to MgO. They all support vacancy defects that are expected to be similar to the F-centre in MgO. The PBEsol XC functional was used for all the examples considered in this chapter, as it leads to an improved agreement with the experimental bulk lattice constant over the PBE functional. The calculated formation energies were found to be sensitive to the \mathbf{k} -point sampling employed, so careful convergence of this was required. The calculated properties are given in table 8.2.

8.3. APPLYING LINEAR EXTRAPOLATION

Material	ϵ_∞ (Exp.)	ϵ_0 (Exp.)	ϵ_∞ (DFPT)	ϵ_0 (DFPT)
NaCl	2.25 [146]	5.89 [147]	2.53	6.50
KCl	2.20 [148]	4.81 [147]	2.32	5.89
LiF	-	8.3[149]	2.09	9.80
CaO	3.27 [150]	11.95 [151]	3.86	15.42
SrO	3.59 [152]	16.2 [153]	3.85	17.88

Table 8.3: Comparison between experimentally measured and calculated dielectric properties for the additional systems considered.

8.3 Applying linear extrapolation

Following on from the work on potential alignment discussed in Chapter 5, it can be observed that the magnitude of non-linear finite-size scaling observed once a ΔV_{AB} alignment correction has been applied is greatly reduced, if convergence with respect to \mathbf{k} -point sampling is also carried out. This enables a more reliable calculation of the finite-size dependence observed in the calculations.

Neglecting other sources of error, approximating the remaining finite size error as linear would yield,

$$E_f(L \rightarrow \infty) = E_f(L) + fE_{MP} + q\Delta V_{AB} \quad (8.5)$$

where E_{MP} is a linear error, scaled by a prefactor f . (This is a slight recasting of Eq. 3.14.) As discussed, the MP approximation would then produce $f = 1$, and for cubic systems, the LZ method would predict $f = 0.63 + 0.39\epsilon^{-1}$. The electrostatic derivation of chapter 7 would predict $f = \epsilon^{-1}$. In all three cases, this f value would be understood as belonging to an electrostatic correction. These three approximations to f are shown in Fig. 8.6. It is instructive to compare these predictions with f values calculated from actual DFT calculations on charged defects.

To calculate the parameter f , the two largest supercells available are taken, and an effective value of f is calculated directly using Eq. 8.5. This assumes that the remaining error (once alignment is applied) is linear with respect to the inverse supercell length. For such an approach to be useful, we require that the value of f converges as larger cells are considered.

Table 8.4 shows an example of this. The calculated value of f is found to

8.3. APPLYING LINEAR EXTRAPOLATION

converge for the larger models, but only when \mathbf{k} -point convergence is achieved, and potential alignment is performed.

Supercells	$f(\mathbf{k}\text{-point} + \text{AB})$	$f(\Gamma\text{-point} + \text{AB})$	$f(\mathbf{k}\text{-point})$
2, 3	0.83	1.20	0.51
3, 4	0.90	0.92	0.75
4, 5	0.92	0.88	0.82

Table 8.4: Calculated f values for the V_{O}^{+} vacancy in MgO, using respectively both \mathbf{k} -point sampling and AB potential alignment, using Γ -point sampling and AB potential alignment, and using \mathbf{k} -point sampling but neglecting potential alignment. If the finite-size errors were perfectly inverse length dependent, then f would be a constant, independent of cell size. It can be directly observed that the use of both AB potential alignment and \mathbf{k} -point sampling causes the remaining finite-size errors to be significantly closer to ideal linear errors, as the size dependence of f is greatly reduced.

Several examples of these linear fits for vacancy defects in the +1 charge state are shown in Figs. 8.7, 8.8 and 8.9. It is noteworthy that the relative importance of ΔV_{AB} potential alignment and of \mathbf{k} -point sampling varies considerably across the examples considered.

8.3. APPLYING LINEAR EXTRAPOLATION

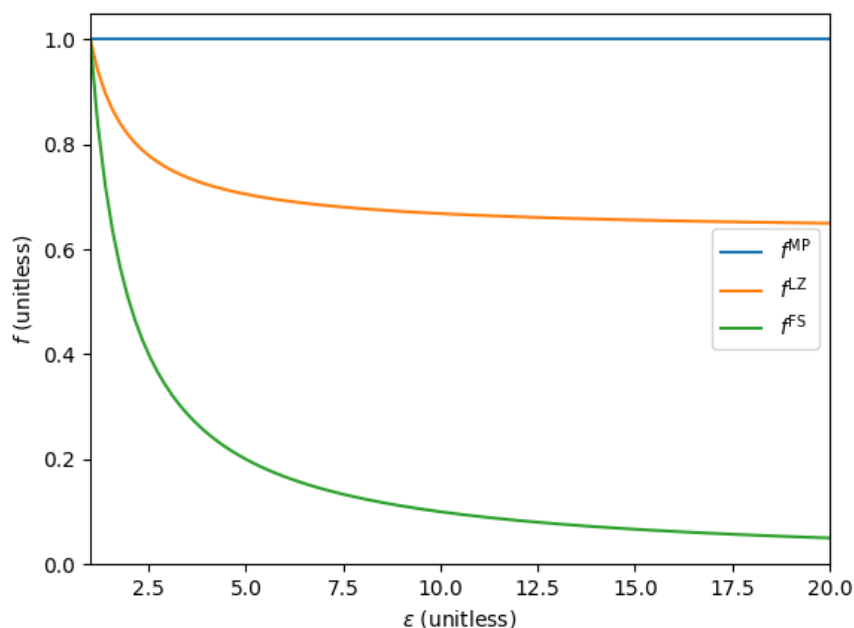


Figure 8.6: Available analytic approximations to f on electrostatic grounds. Both the Makov-Payne and Lany-Zunger are significantly larger than the electrostatic correction previously derived in this thesis (FS). All three terms reduce to the known Madelung correction at the limit of $\epsilon = 1$ i.e. in the absence of a dielectric.

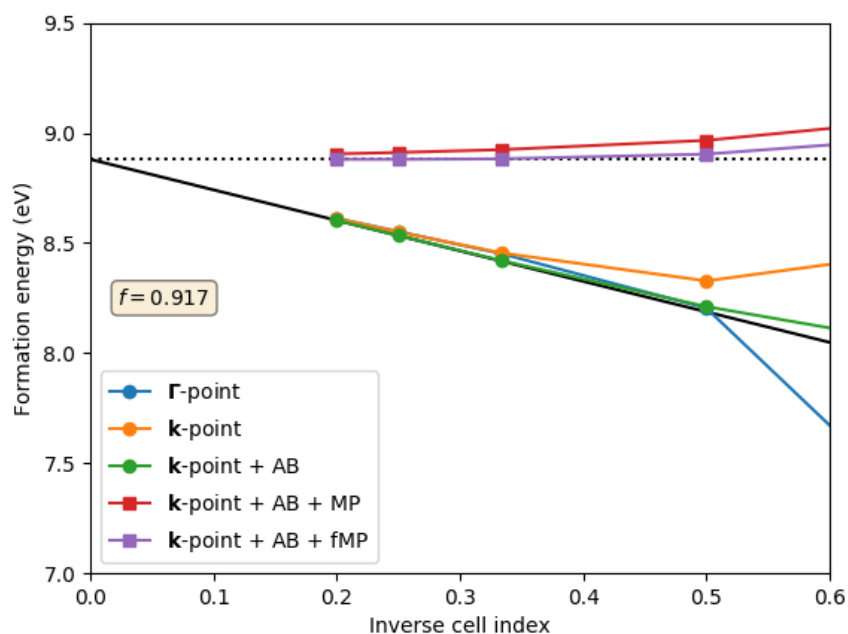


Figure 8.7: Finite-size dependence of the formation energy of the unrelaxed V_O^+ defect in MgO. Formation energies are shown using Γ -point sampling (blue), using a Monkhorst-Pack k -point sampling (orange), using a Monkhorst-Pack k -point sampling and AB potential alignment (green), the same with the addition of a MP correction (red) and finally when the MP correction is reduced by the calculated f -value (purple).

8.3. APPLYING LINEAR EXTRAPOLATION

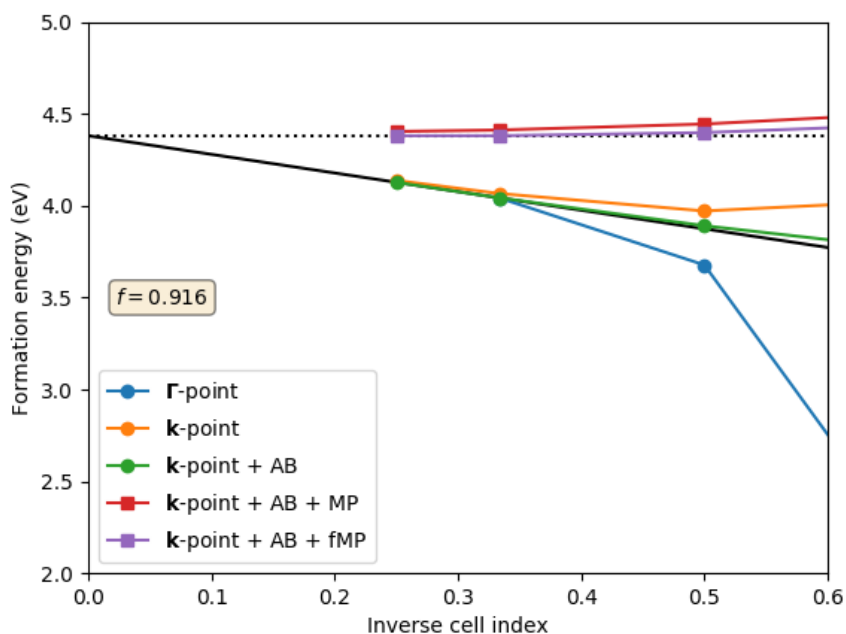


Figure 8.8: Finite-size dependence of the formation energy of the unrelaxed V_O^+ defect in CaO. Note the importance of **k**-point sampling in reaching a linear regime.

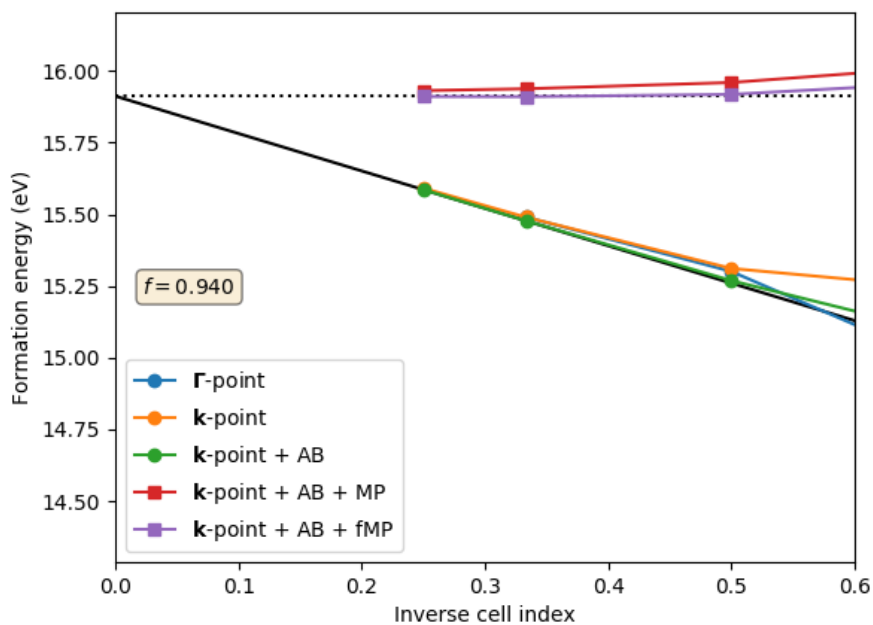


Figure 8.9: Finite-size dependence of the formation energy of the unrelaxed V_{Cl}^+ defect in KCl. Same notation as Fig. 8.7.

8.3. APPLYING LINEAR EXTRAPOLATION

The combined data for the examples considered is shown in Fig. 8.10. It can be seen that the MP and LZ methods are significantly better predictors of f than the electrostatic correction formula derived in Chapter 7. Either this derivation is incorrect, or there are other significant sources of linear finite-size error present in the calculations.

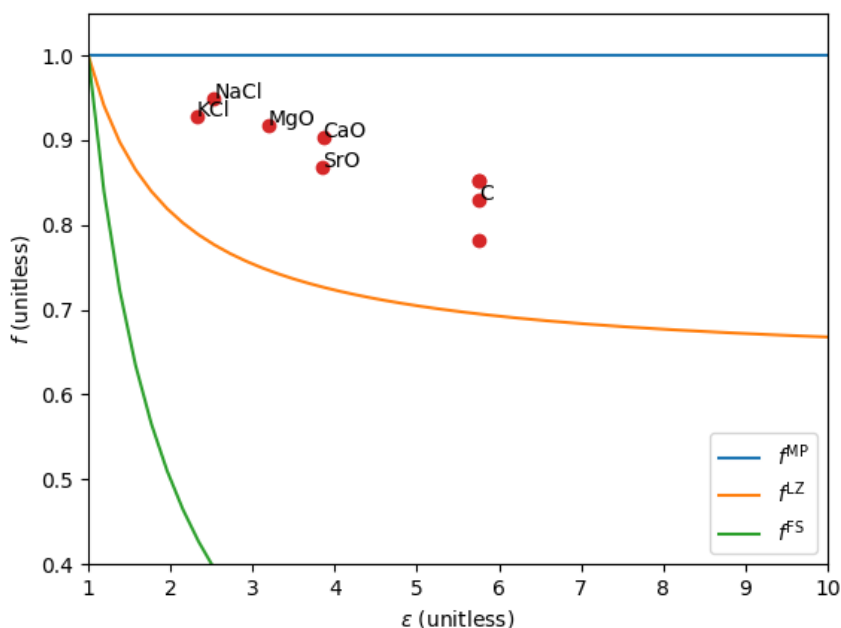


Figure 8.10: The red points show the extrapolated f values for the different defects considered. The dielectric constants are calculated using DFPT. The calculated defects fall between the predictions of the Makov-Payne and the Lany-Zunger correction. All observed f values are significantly larger than would be predicted by the electrostatic derivation we carried out (yielding Eq. 7.55), here denoted as f^{FS}

It is worth looking at the size dependence in f in more detail, to see how reliable approximating it as a constant is. Some example plots are shown in Fig. 8.11, using MgO and LiF as an illustrative example. Relaxation effects will be considered later in this chapter.

It can be seen that the remaining size dependence in f beyond the $3 \times 3 \times 3$ supercell is small (the rightmost points in the plots are the f -value calculated from the $2 \times 2 \times 2$ and $3 \times 3 \times 3$ supercell). Additionally, the data is well described by a fit of the

form:

$$f(L) = f + aL^{-3}, \quad (8.6)$$

where the value of f is almost finite-size independent, but contains an inverse volume dependant term that falls off quickly. This is similar to the traditional extrapolation formula, but this volume dependant term is present in the gradient of the formation energy, rather than the formation energy itself.

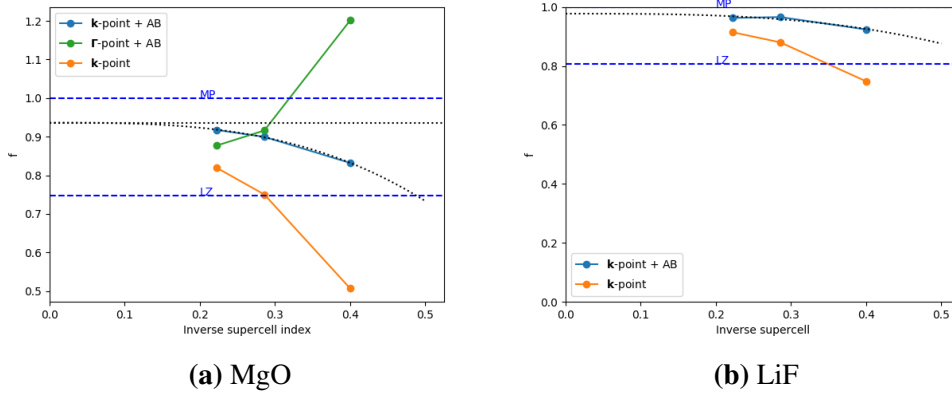


Figure 8.11: Demonstrated f -value size dependence for unrelaxed vacancy defects in MgO and LiF. The points are plotted at the average size of the two supercells that the f -value was evaluated from. The f -values calculated using both potential alignment and \mathbf{k} -point sampling (orange line) and with only \mathbf{k} -point sampling (blue line). The blue dashed lines show the predictions of the MP and LZ methods. An extrapolation is performed according to Eq. 8.6.

The data in Fig. 8.11 demonstrates that including AB potential alignment reduces the observed size dependence in f .

8.4 Separating the exchange-correlation energy

Test calculations where the exchange-correlation energy is neglected appear to show significantly reduced finite-size dependence. This naturally suggests that exchange-correlation might play an important role in the observed finite-size dependence of charged defects. However, a detailed comparison between defect formation energies calculated both with PBEsol and without any XC functional is quite challenging in practice, as the complete removal of E_{xc} represents a significant perturbation of the wavefunction of the whole system. In many cases, the defect state is no longer

8.4. SEPARATING THE EXCHANGE-CORRELATION ENERGY

a well localized gap state, precluding a meaningful comparison. As an additional complication, there is strain introduced if the lattice constant is not reoptimized for the change in XC. This means that when the two cases are compared, both ϵ and L will change, clouding the comparison.

Instead, it is simpler to look at the change in the exchange-correlation energy E_{xc} as a charged defect is formed. As a defect formation energy is typically calculated as a total energy difference, $E_f = E_{\text{defect}}^{\text{DFT}} - E_{\text{bulk}}^{\text{DFT}}$ (as introduced in Eq. 2.23), I define the same energy difference considering only the change in the exchange-correlation energy,

$$\Delta E_{xc} = E_{\text{defect}}^{xc} - E_{\text{bulk}}^{xc}, \quad (8.7)$$

where E_{defect}^{xc} is the xc energy calculated for a supercell containing a charged defect, and E_{bulk}^{xc} is the energy of an equivalent bulk supercell.

In principle, as DFT is a self-consistent field method, this makes it possible for individual energy terms to be mixed together in quite complex ways. However, it would still be anticipated that a substantive part of the energy change introduced by XC would still be present in the E_{xc} term.

Using the V_{O}^+ defect in MgO within the CP2K code as an example, a plot of E_{xc} is shown in Fig. 8.12. Again, this term is observed to be approximately linear, although the linear regime is reached more slowly than in the case of the total formation energy. This allows the gradient to be extracted, providing a value of f_{xc} , namely that part of f that is introduced through a change in the exchange-correlation energy. These XC contributions to f are considered in more detail in table 8.5.

Taken together, the results in table 8.5 suggest an argument that the linear errors present in the supercell calculations could be made of a combined electrostatic error and an XC error, where the smaller electrostatic correction derived produces the correct limit of f as $\epsilon \rightarrow 1$ (representing vacuum), but that the XC errors actually cause a larger error within dielectric mediums.

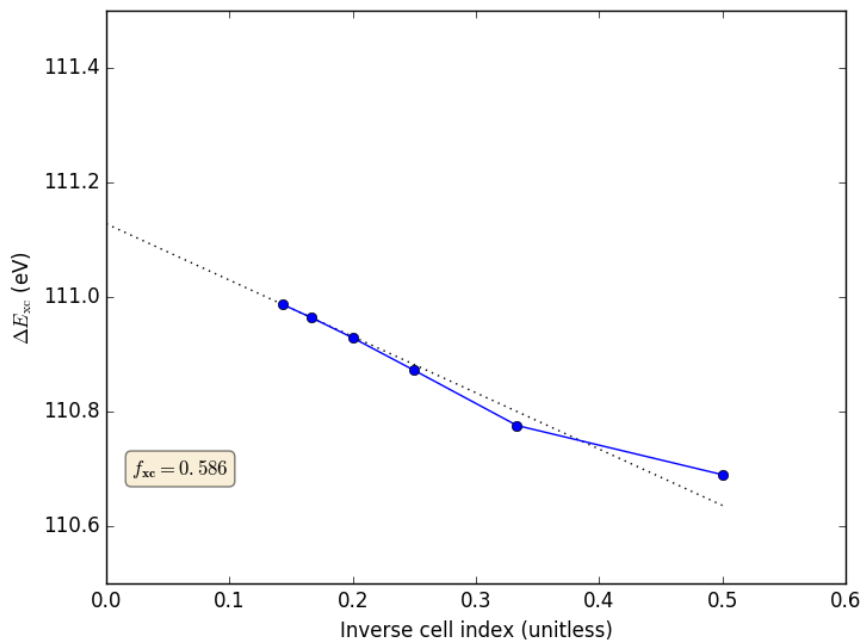


Figure 8.12: Plot of ΔE_{xc} (as defined in Eq. 8.7) against inverse supercell for the unrelaxed V_O^+ defect in MgO using CP2K. The energy term tends to linear behavior for the largest supercells considered.

Material	Supercell	ϵ_∞	f_{elec}	f_{xc}	$f_{elec} + f_{xc}$	f	Δf
KCl	4x4x4	2.32	0.43	0.49	0.92	0.93	0.01
NaCl	5x5x5	2.53	0.40	0.68	1.07	0.96	-0.11
MgO	5x5x5	3.19	0.31	0.47	0.78	0.92	0.14
SrO	4x4x4	3.85	0.26	0.63	0.89	0.87	-0.02
CaO	4x4x4	3.86	0.26	0.52	0.78	0.91	0.12
C	4x4x4	5.76	0.17	0.39	0.57	0.71	0.14

Table 8.5: Observed finite-size dependence for unrelaxed +1 vacancy defects in the listed materials. The dielectric constants ϵ_∞ are calculated using DFPT. The f_{elec} values listed are those predicted by Eq. 7.55. The values of f_{xc} and f are determined through the linear extrapolations outlined. Δf is the difference between the extrapolated f and the prediction of $f_{elec} + f_{xc}$.

8.5 Model calculations and the exchange-correlation energy

Using simple model calculations and the LDA functional, it can be demonstrated that there is an energy penalty if the bound screening charge is too constrained in the supercells considered. Using the density model already produced in Sec. 8.1, in Eq. 8.3, as well as the optimized model parameters for the example considered, the change in the XC energy can be crudely predicted. The calculated change in the XC energy was calculated at the LDA level. The results of these calculations are shown in Fig. 8.13.

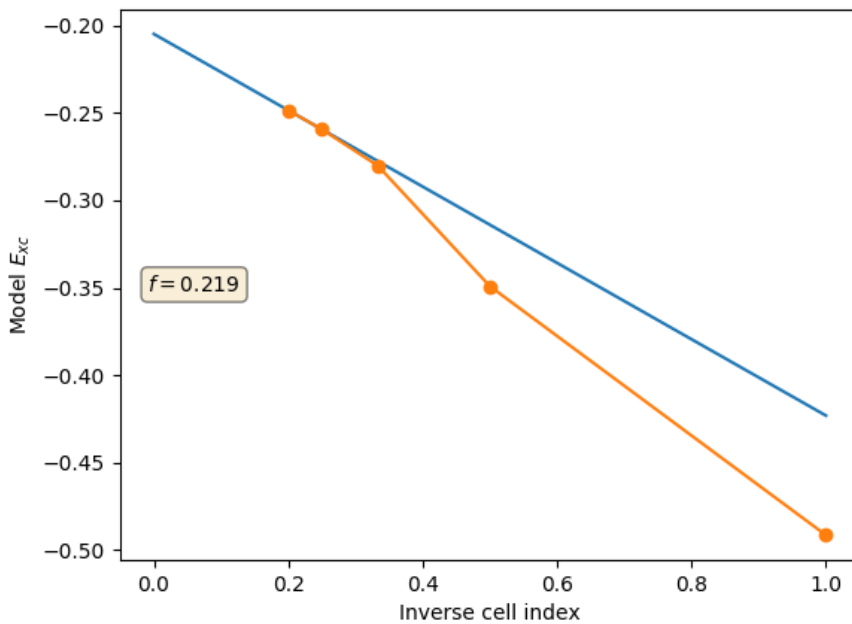


Figure 8.13: Exchange-correlation energies of the developed charge models for the V_C^+ defect. The simple model tends to linear error, but the magnitude of the error is too small to explain the XC errors seen in Tab. 8.5.

It is interesting that the error in this model does become linear. However, it is still a poor prediction of the observed XC energy change in the host DFT calculations. The exchange-correlation energy penalty is significantly harder to model than the electrostatic interactions, due to the lack of linear superposition. An accurate model most likely needs to incorporate a realistic description of all electronic

charge located around the defect, which is no simple task. This is in contrast to the electrostatic picture, where we can use linear superposition to treat the electrostatic model as an addition to the system.

8.6 Parameterizing a new bulk correction

Using the definition of f given through Eq. 8.5, the dependence of f on the dielectric constant can be investigated. An example of this for the available unrealaxed vacancy defects is shown in Fig. 8.14.

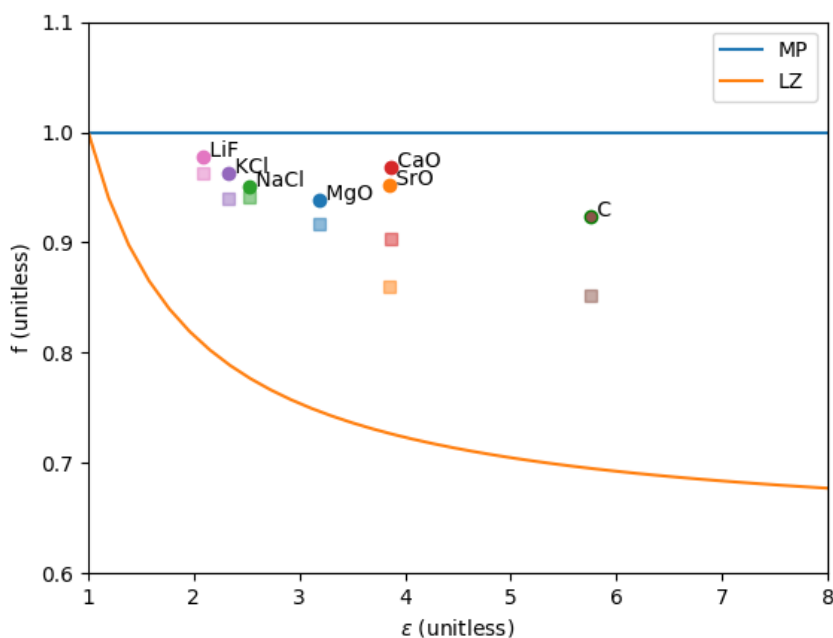


Figure 8.14: Dependence of extrapolated f -values on dielectric constant for the +1 vacancy defects, compared against the predictions of the MP and LZ correction methods. All the calculated values fall between the two correction methods, and lie nearer to the MP method. The round markers show the f -value extrapolated using Eq. 8.6, and the squares show the largest supercell calculated. For LiF, KCl, NaCl and MgO, a 5x5x5 supercell was calculated, and the extrapolation only changes the value slightly. For CaO, SrO and C, the largest supercell calculated was 4x4x4, and the extrapolation has a larger impact.

The dielectric constant ϵ is not well suited directly to constructing approximations, as it can vary from one to infinity. Instead, the magnitude of the bound charge is a slightly more natural variable, which is defined as $1 - \epsilon^{-1}$ and that varies from zero to one. The observed dependence in terms of this variable is shown in Fig. 8.15.

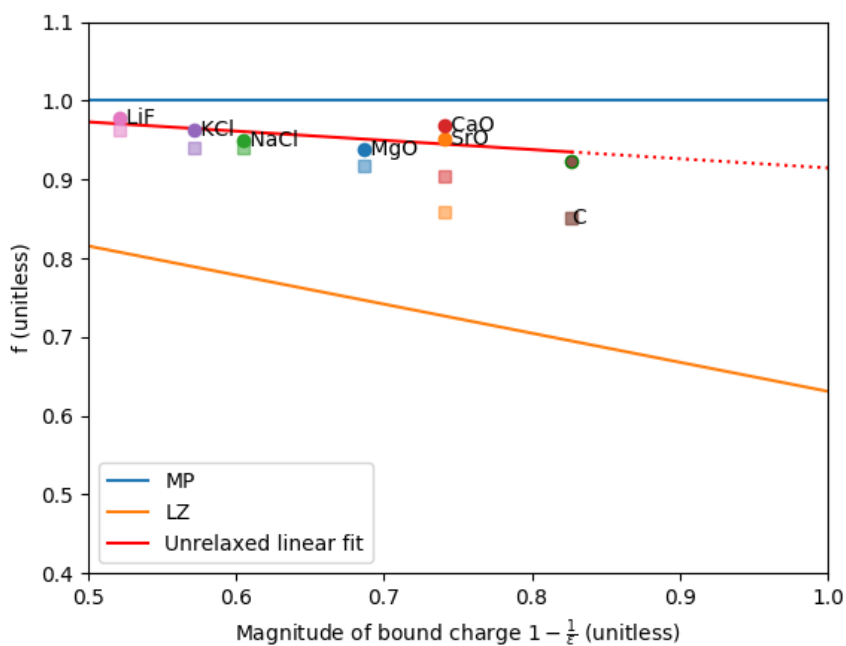


Figure 8.15: The same data as Fig. 8.14, but plotted against the magnitude of the bound charge. A linear fit to the data is shown, as defined through Eq. 8.8. For this fit, $A = 1.03$ and $B = -0.11$.

The data shown in Fig. 8.15 supports a linear fit. This produces a formula to predict f that takes the form,

$$f = A + B \left(1 - \frac{1}{\epsilon} \right), \quad (8.8)$$

where A and B are constants determined through the fit. Both the MP and LZ method take this form; the MP method is the choice of $A = 1, B = 0$, and for cubic supercells the LZ method is $A = 1.0, B = -0.37$.

For the unrelaxed defects shown in Fig. 8.15, this produces values of $A = 1.03$ and $B = -0.11$, which are able to describe available data well. One shortcoming of this fit is that the correct limit is not retained at $\epsilon \rightarrow 1$, which would require a value of $A = 1.0$. It is encouraging that this limit is almost reproduced by the fit. This suggests that the form of the LZ method is a good choice, but that the LZ method overestimates the reduction in the f -value as the size of the supercell is increased.

8.7 Role of relaxation

Our understanding of the problem once ionic relaxation is incorporated is less developed. Both the MP and LZ methods treat unrelaxed and relaxed defects identically. As in the unrelaxed case, the finite-size dependence of the observed f -values can be inspected. This size dependence appears to be less systematic than that encountered in the unrelaxed case.

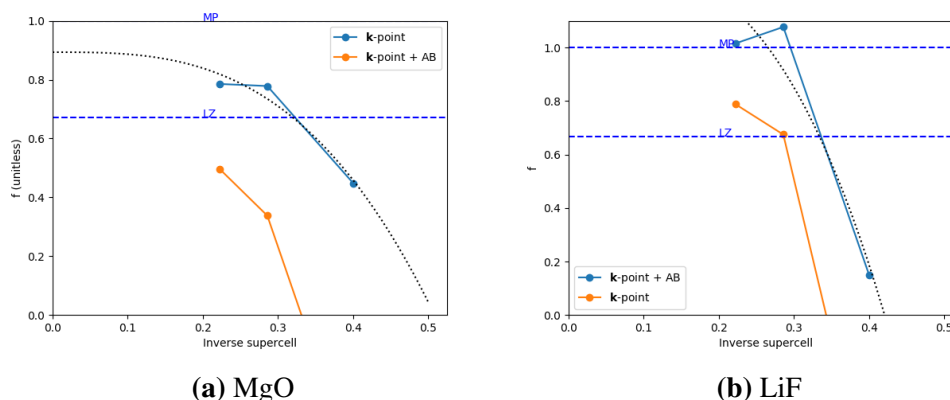


Figure 8.16: Demonstrated f -value size dependence for relaxed vacancy defects in MgO and LiF. An extrapolation according to Eq. 8.6 is shown, but it no longer appears to be reliable.

The irregular size dependence demonstrated in Fig. 8.16 prevents an extrapolation from being carried out with confidence. Hence, extrapolations on the relaxed data was not performed. This limits the confidence that can be placed on the accuracy of the calculated f -values for relaxed defects, as the remaining finite-size dependence in f is not clear. The available data is shown in Fig. 8.17.

8.7. ROLE OF RELAXATION

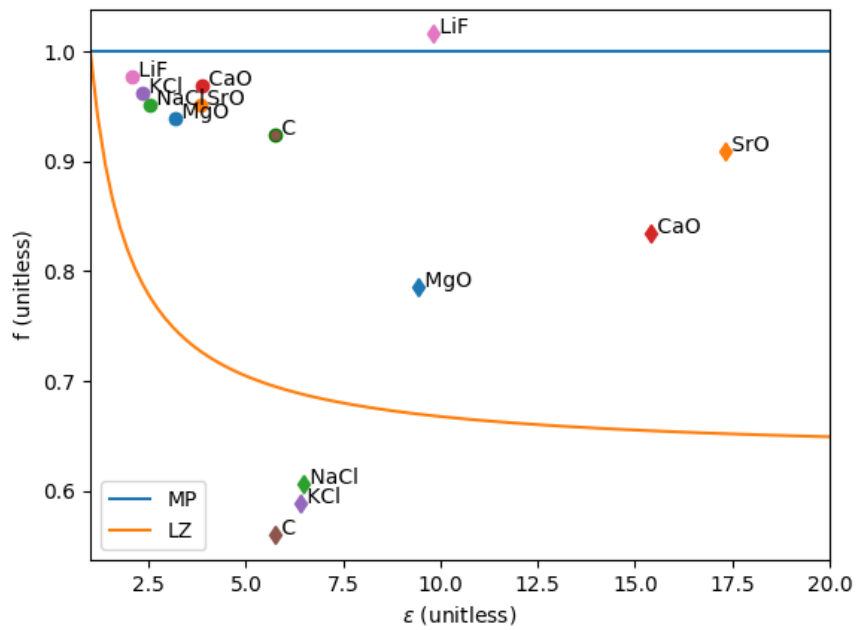


Figure 8.17: Observed dependence of f -values on dielectric constant, for both unrelaxed (circles) and relaxed (diamonds) vacancy defects. Due to the lack of a reliable extrapolation, the relaxed defects are expected to display larger errors.

8.7. ROLE OF RELAXATION

Still, a fit to the linear function in Eq. 8.8 can still be performed for the available relaxed defects. This produces values of $A = -2.07$ and $B = 3.20$. This linear fit is shown in Fig. 8.18. This fit has quite a different form, as it displays significantly greater dependence on the dielectric constant ϵ .

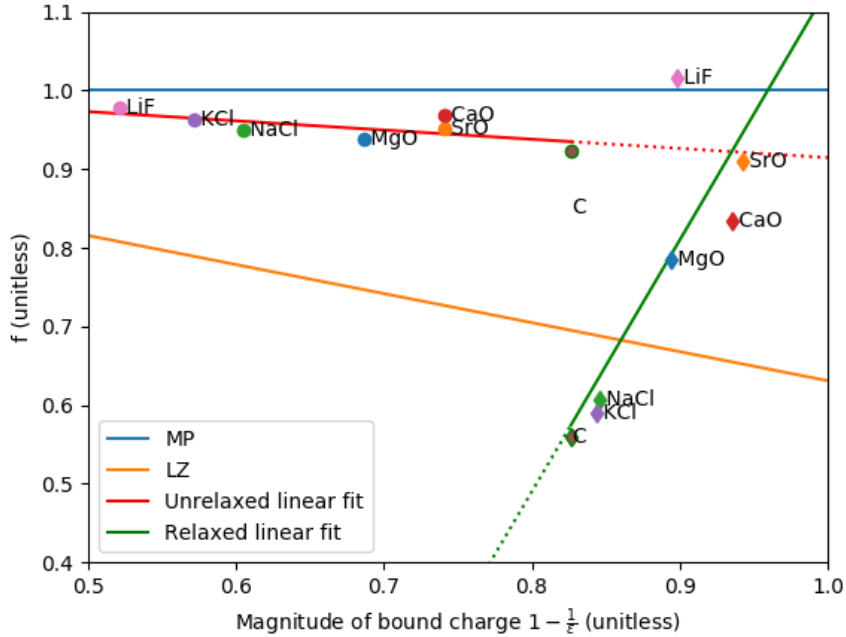


Figure 8.18: Observed dependence of f -values on magnitude of the bound charge, for both unrelaxed (circles) and relaxed (diamonds) vacancy defects. Due to the lack of a reliable extrapolation, the relaxed defects are expected to display larger errors. Linear fits are shown to both datasets, which display different behavior

The justification for this fit to the relaxed defects remains unclear. Certainly, the process of ionic relaxation has the potential to interact with the screening bound charge in quite a complex way. Equally, the significant difference observed between vacancies in NaCl and KCl when compared with LiF seems hard to justify given the similarity between the defects. It is possible that larger supercells than are presently available are still needed to produce accurate results for the relaxed vacancy defects.

In the above fits, cubic crystals, vacancy defects and +1 charge states are employed. These new fits could be used as correction formulas. However, the transferability of these parameters to more general defects remains to be demonstrated. Still, it is notable that even with these simplifications, neither the LZ nor MP method

is able to reliably predict the observed f -values when ionic relaxation is allowed.

The results presented demonstrate that defining an f -value can be used to gain insight into the actual finite size dependence observed for charged defects, and that this approach can be used to fit new corrections.

Conclusions It is shown that the remaining finite-size error present once both the derived electrostatic correction and potential alignment have been performed is approximately equal to the finite-size dependence in the exchange-correlation energy on formation of the defect. Once potential alignment and \mathbf{k} -point convergence is performed, it is demonstrated that the remaining finite-size dependence can be approximated as an inverse linear term. For unreleased vacancy defects in the cubic crystals considered, the inferred error is found to be approximated as 0.9 times the MP correction. For relaxed defects, the required correction is nearer the LZ method for lower dielectrics, but increases rapidly towards the MP correction as the dielectric constant increases. These inferred corrections are interpreted as a combined electrostatic-XC term.

Chapter 9

Ionization of surfaces and surface defects

Aims: In this chapter I looked at ionization, both for bulk supercells and for surfaces. In an ionization problem, we still need to look at systems with net charge, incorporating a neutralizing jellium background. In direct contrast with the problem of charged defect formation energies, errors can be straightforwardly defined using Koopmans' theorem (KT). This enables direct tests of the supercell size dependence present in the calculated energies for the charged systems.

Results: For bulk cubic supercells, the error to obey KT is observed to be small. Calculations suggest that this could be because the state being deoccupied overlaps the jellium background. In contrast, when electrons are removed from surface slab models, this favorable overlap is no longer achieved, and a significant supercell size dependence is observed. The main component of this size dependence can be predicted using electrostatics. It is observed that the use of cubic cells for surface ionization problems leads to reduced errors. Considering KT for defects, the situation is more complex, due to the use of approximate density functionals. It is observed that a bulk defect in an infinite supercell would still fail to obey KT, most likely due to the use of an approximate XC functional. When considering surfaces, the bound screening charge looks similar to the charging observed in ionization calculations. This suggests that cubic cells might still be favorable for surface defect calculations, and it is observed that a linear extrapolation of the

charged defect formation energy can still be carried out. This is in contrast to the complex size-dependence reported in the literature, when more typical vacuum gaps are employed.

9.1 Eigenvalue vs numerical ionization approaches

In principle, calculations of workfunctions and ionization energies within DFT should be a very similar problem to the calculation of charge transition levels. In both cases, we want to understand the energy cost to add or remove electrons from our system. Both types of calculation could include formally charged calculations, introducing jellium backgrounds, and in both cases the charge density difference introduced by the exchange of electrons is manifestly dependent upon the size of the supercell used. Additionally, potential alignment errors could be introduced in both cases, if we compare the energy of neutral and charged systems.

We will recast the workfunction problem in the same mathematical framework as typically used in charged defect calculations. We will find that once this is done, corrections similar (but not identical) to the bulk corrections considered so far for defects are now required for surface workfunction problems. Then, I will look at the bulk case.

The ionisation energy I is the energy cost to remove an electron from a DFT cell, and is defined as,

$$I = E_{-1}^{\text{DFT}} - E_0^{\text{DFT}} \quad (9.1)$$

where E_0^{DFT} is the energy of a neutral supercell, and E_{-1}^{DFT} is the energy of the supercell with one electron removed.

However, Eq. 9.1 is not used often in practice, as it requires an additional calculation. Ionization energies can instead be calculated using Koopmans' theorem (a restatement of 2.22),

$$I = -\epsilon_{\text{homo}}, \quad (9.2)$$

where the energy required to remove one electron I is equal to the negative value of the highest occupied molecular orbital, ϵ_{homo} .

The expression in Eq. 9.2 leads directly to the standard textbook expression for

the workfunction,

$$w_{\varepsilon} = -e\phi - \varepsilon_{\text{homo}}, \quad (9.3)$$

where the workfunction w_{ε} is given relative to the potential of the vacuum ϕ . Under isolated boundary conditions $\phi=0$, but this constraint is lost when using PBC and repeated slab models. This introduces a slight difference to charged defect formation energies, as these are conventionally referenced to the valence band maximum of the material, instead of the unknown vacuum potential. In both cases, the essential point is that the calculated energies must be referenced to some well defined energy level in order to be meaningful, as out of the box, surface and bulk calculations are referenced to the average potential of the calculation supercell. This is an energy scale without any direct physical significance. Using Eq. 9.3 successfully sidesteps the problems inherent to actually introducing a jellium background into the system, as only properties calculated from the charge neutral system are required.

Rather than using Eq. 9.3, we could also use Eq. 9.1 to carry out an ionization calculation in an analogous way to a formation energy calculation,

$$w_I = E_{-1}^{\text{DFT}} - E_0^{\text{DFT}} - e\phi, \quad (9.4)$$

where E_0^{DFT} is the energy of a neutral supercell, and E_{-1}^{DFT} is the energy of the supercell with one electron removed.

It is important to compare and contrast Eq. 9.4, for ionization, and Eq. 2.23 for defects. Eq. 2.23 is more complex, because contains chemical potentials for the exchange of ions, as well as two finite-size correction terms. In the defect case, we would also allow atomic relaxation.

When comparing Eq. 9.3 and Eq. 9.4, the $-e\phi$ term is not important, as it is the same in both expressions. The definition for the workfunction given by Eq. 9.4 contains the total energy of a system with net charge (E_{-1}^{DFT}), so a neutralizing jellium background will be included when the workfunction is calculated in this way. When using Eq. 9.3, only neutral cells need to be considered.

9.1. EIGENVALUE VS NUMERICAL IONIZATION APPROACHES

In order to aid my analysis, I will introduce the following definition of the Koopmans' error, from Koopmans' condition as given in Eq. 9.2,

$$\Delta_{\text{KE}} = I + \epsilon_{\text{homo}}, \quad (9.5)$$

which follows exactly from Eq. 9.2. The numerical ionisation energy I is calculated according to Eq. 9.1. Hence, when $\Delta_{\text{KE}}=0$, Koopmans' condition is obeyed exactly. This would be the case for ideal DFT on an isolated atom or molecule, but we expect that both the use of non-physical jellium background, the use of a periodic model and failures of XC functionals can all introduce Koopmans' errors. In the case where Koopmans' condition is obeyed exactly, there should be no difference between the two definitions of the workfunction, given in Eqs. 9.3 and 9.4.

In this chapter, CP2K was used, rather than CASTEP. This was an advantageous choice for surface systems, as the cost for vacuum regions is reduced in CP2K, when compared to a pure planewave basis. The primary disadvantage is that this required Γ -point sampling. Note that the results in the previous Chapter demonstrated that MgO defects are better described by this approximation than many other examples. Secondly, when using 3D slab models, \mathbf{k} -point sampling in the surface direction is in any case undesirable, as density fluctuations across different images of the slab model is non-physical.

The use of CP2K also motivated a change from the PBEsol to PBE functional, as PBEsol pseudopotentials are not presently available. The use of more expensive hybrid functionals was avoided so that larger surface models could be constructed.

Finally, in this chapter, no atomic relaxation was carried out. Again, this is because this is a simpler case that is worth understanding first. In the future, this work can be expanded by incorporating relaxation as well. When considering Koopmans' theorem, it is only valid when the geometry is held fixed in any case, and no ionic relaxation should take place when systems are ionized anyway.

9.2 KT for ionization of the bulk

First we considered the ionisation of bulk supercells. In this case we can not directly calculate a workfunction as the potential of vacuum is unknown. Instead, I used the definitions in this section with the vacuum potential set to zero. This doesn't allow comparison with experiment, but we can still assess the similarity between the two definitions given in Eq. 9.3 and Eq. 9.4.

In Fig. 9.1, the VBM eigenvalue and the numerical ionization energy (calculated via Eq. 9.1) for cubic bulk cells of MgO are shown. The eigenvalue converges with respect to supercell size more rapidly, although in this case, both definitions show very little finite-size dependence. Equally, it does not appear that the two definitions would produce the same ionization energy for an infinite supercell, although the difference in energies is very small.

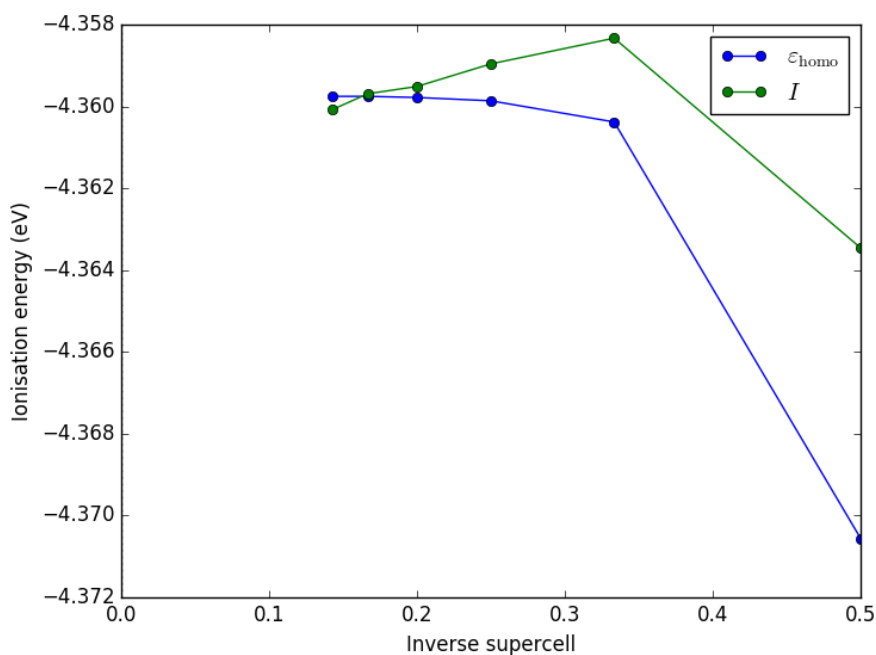


Figure 9.1: Comparison between the highest occupied molecular orbital ϵ_{homo} and the ionization energy I (Eq. 9.1) for different cubic supercells of MgO. The eigenvalue displays less finite-size dependence compared to the ionization energy.

Using Eq. 9.5 to define the Koopmans' error as the difference between these two definitions yields Fig. 9.2. This makes it easier to perform an extrapolation to the infinite limit, as the Koopmans' error has an approximately linear dependence

on supercell size. This produces a very small error of a couple of meV. Hence, for the case of bulk ionization, there is very little difference between the definitions of Eq. 9.3 and Eq. 9.4.

It is possible to construct an electrostatic correction for this situation. It is clear that in the limit of an infinite supercell, there should be no change in the Hartree energy on removal of an electron. This is the case because the two charge densities involved, the VBM state being deoccupied, and the neutralizing jellium background, are both delocalized across the supercell. This means that both these charge densities tend to a value of zero as the size of the model goes to infinity. So, any change in the Hartree interaction on removal of an electron could be identified as an error.

It is appropriate to calculate the electrostatic interaction between the jellium background and the change in electronic charge density between the charged and uncharged supercells considered, yielding E_{PBC} (as defined in Eq. 4.5). This energy can then be evaluated using the `DEFECT_SOLVER` code. Such calculations produce the corrections shown in Fig 9.2.

These corrections should tend to zero as the size of the supercell tends to infinity, following the argument made for the Hartree energy, and this behavior is shown by the corrections. Even for small supercells, these interactions are small. As shown in Fig. 9.3, these corrections are small for all supercells and get smaller as the supercell is made larger.

All of the errors considered in this section are very small, which means that numerical errors are harder to control. Still, the evidence suggests that these errors are strictly speaking finite size dependant, and lead to non-zero errors for the infinite supercell. In practice, these errors are small enough that they are often ignored, and it can be seen that the favorable overlap between the state being deoccupied and the neutralizing jellium background leads to the calculated values of E_{PBC} to be in meV.

There is an important conceptual point in the fact that, although local functionals are often described as being perfectly Koopmans compliant for delocalized states, there is still a formal error to obey Koopmans' condition for infinite super-

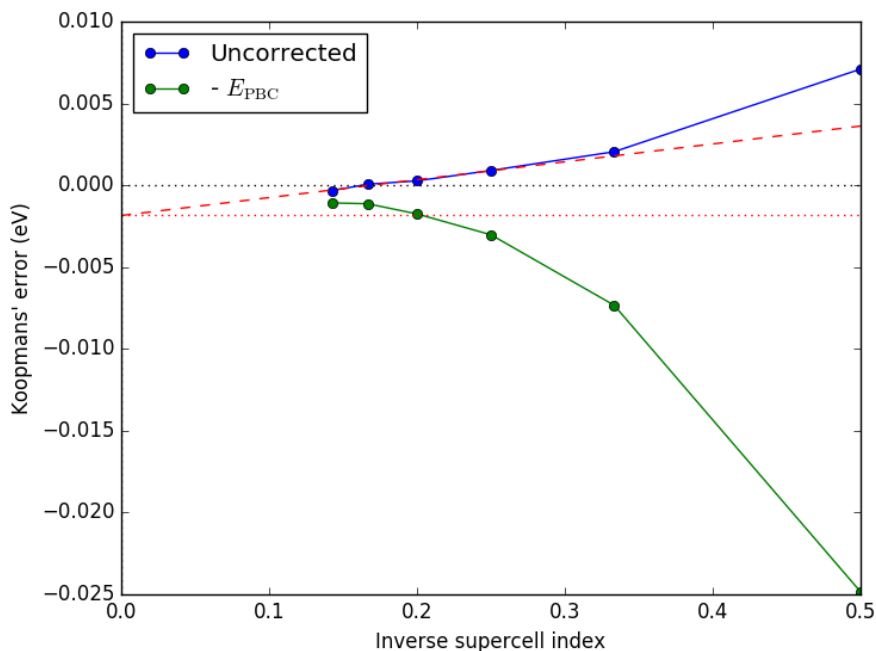


Figure 9.2: Koopmans' errors calculated for bulk MgO supercells, using the PBE functional. The Koopmans' error is small for all the supercells considered, and does display finite-size dependence. A linear extrapolation to the four largest supercells is shown in red, which predicts a Koopmans' error of 0.0018 eV for an infinite supercell. Addition of an E_{PBC} correction (Eq. 4.5) does reduce the inferred error for larger supercells.

cells. It would be hoped that improved density functionals reduce this error further, although it is already so small at the PBE level of theory that such an improvement would be hard to make.

Another confusing conceptual point is that it is not clear if a small Koopmans error for small bulk supercells would actually be displayed by the universal functional. The Koopmans' error is small in this case because the jellium background is screening the electrostatic interaction with the band state. But this screening is entirely a non-physical effect, so it seems uncomfortable that it is principally responsible for observed Koopmans' compliance. In any case, the inferred Koopmans' compliance of an infinite cell is better defined, and maintaining this property should be important for improved functionals.

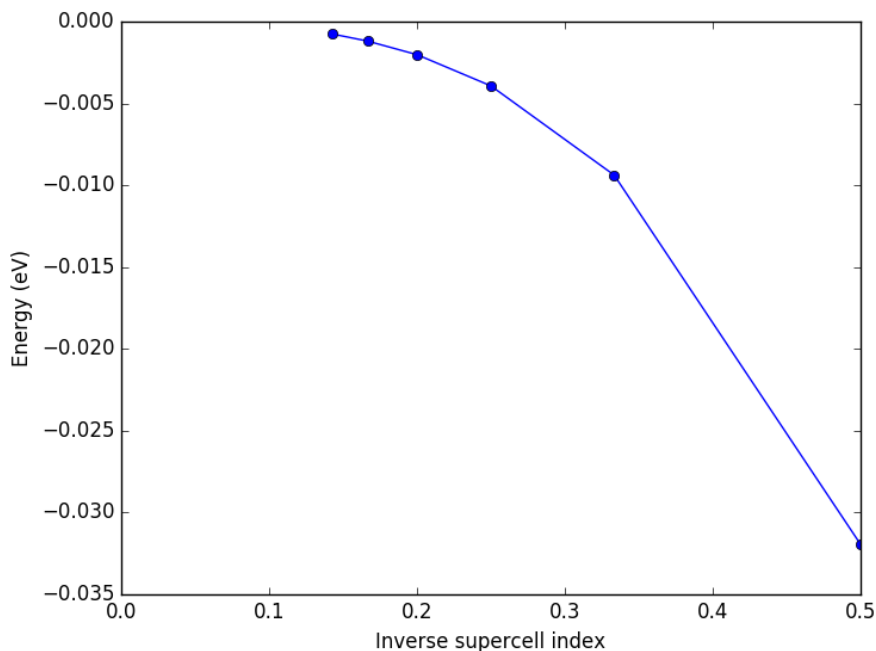


Figure 9.3: Calculated $-E_{PBC}$ corrections calculated from the density differences between a bulk supercell and an equivalent supercell of the same size with an electron removed. The interaction energy is low because the deoccupied state is a negative charge delocalized across the whole cell, immersed in a positive jellium background delocalized across the whole supercell. The similarity of the two charge distributions leads to almost complete screening, with the interaction only present because the bulk state is not perfectly uniform.

9.3 KT for ionization of surfaces

When looking at surfaces, there are many parameters that can be varied in the construction of surface models. Unlike in the bulk case, cubic cells are used only very rarely when considering surface problems. This is due to the need for a sufficiently large vacuum gap and number of layers to reproduce properties of the surface of interest. In order to understand the role of these parameters in more detail, several datasets were considered where these descriptors were systematically varied.

9.3.1 Workfunction dependence on number of layers

First, the number of layers contained in the model was varied. This is shown pictorially in Fig. 9.4. The use of a constant supercell size allows for a direct comparison of potentials and density models, but disadvantageously means that the larger models considered have the smallest vacuum gaps.

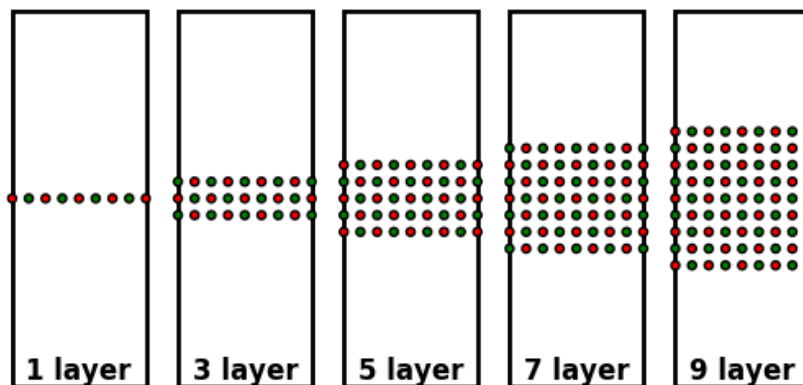


Figure 9.4: Example surface unit cells in the layers data set. A constant supercell is applied to a model that contains varying numbers of layers, effectively leading to a reduction in vacuum gap as the number of layers increases. A constant 4×4 surface net is maintained across the dataset.

As is shown in Fig. 9.5, the work function calculated using the two approaches is not identical. The workfunction is over an electron volt higher for a monolayer when the energy difference formula of Eq. 9.4 is employed. However, it looks like the difference in energy between the two methods decreases as the amount of material in the model increases.

It is important to note that the orthodox workfunction definition given in Eq. 9.3 achieves a converged value far more rapidly with respect to the model size. This validates the traditional wisdom on workfunction calculations. As the eigenvalue approach avoids the inclusion of a jellium background, it seems plausible that it is an interaction with jellium that reduces the quality of the total energy approach, in a way analogous with the problem of charged defects in the bulk.

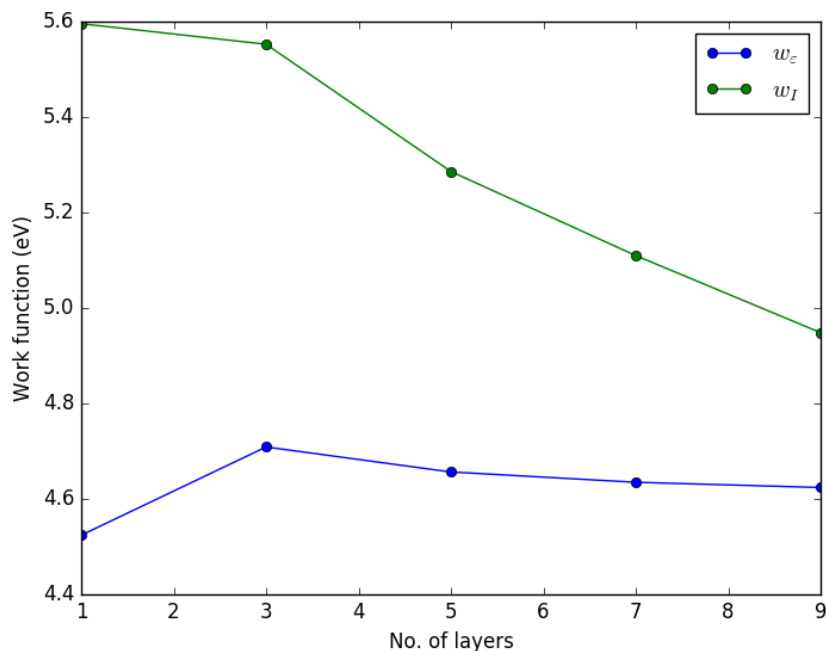


Figure 9.5: Comparison between work function values for the layers dataset using both eigenvalue (Eq. 9.3) and numerical ionisation definitions (Eq. 9.4). In blue, the w_ϵ definition quickly converges with respect to the number of MgO layers contained in the model. In contrast, w_I definition converges significantly slower, as shown by the green line. According to both definitions, the monolayer is an outlier.

Direct application of the correction method defined in Eq. 4.1 produces poor results. Instead only applying the periodic part of the correction appears to be more fruitful. The inclusion of the interaction under isolated boundary conditions, E_{iso} , is unhelpful as this term should go to zero for an infinite supercell. This is in contrast with bulk defects, where a localized charge is present within the supercell even when its size is taken to infinity. This is demonstrated in Fig. 9.6, using the definition of the Koopmans' error given in Eq. 9.5. We note that solving Poisson's equation for vacuum or including dielectric screening makes almost no difference to the correction. In the rest of this section, a vacuum dielectric is used in the corrective calculations. This seems to be more appropriate, as a delocalized electronic state doesn't correspond to the classical concept of a free charge. Equally, the numerical difference between the two approaches is minimal for all the examples that were considered.

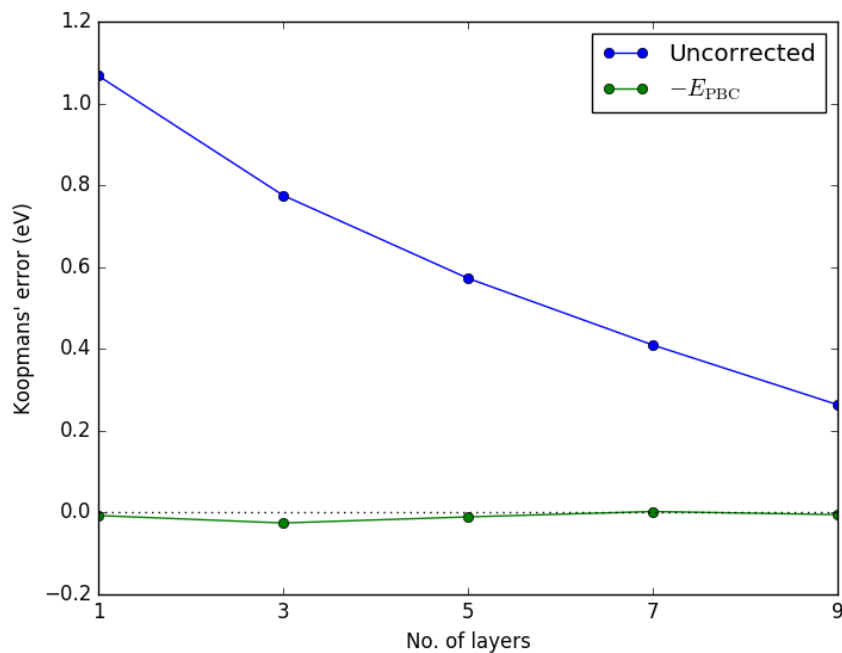


Figure 9.6: Koopmans' errors, as defined in Eq. 9.5, for the layers dataset. Addition of a E_{PBC} correction to the numerical ionization energy removes most of the Koopmans' error demonstrated by the dataset.

9.3.2 Workfunction dependence on vacuum gap size

As we now have a tentative understanding of the finite-size errors introduced into this kind of calculation, we wanted to explore the role of other descriptors of the simulation cell on the errors introduced. Next we consider the role the size of the vacuum gap on the introduced electrostatic interactions. These supercells are shown graphically in Fig. 9.7.

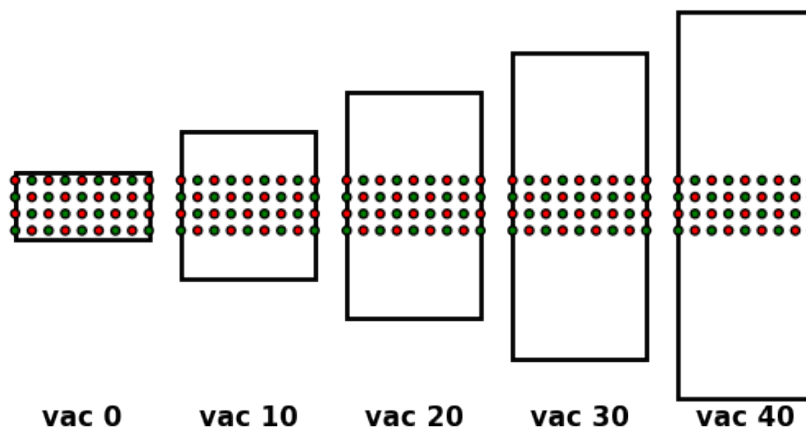


Figure 9.7: Example surface unit cells in the gap scan data set. A four layer system is considered in supercells with various vacuum gap sizes. A surface net of 4×4 is maintained across the calculations. The vacuum gap is defined as the extra separation over a bulk supercell, rather than the standard definition of separation between surface layers (using the standard definition yields a non-zero vacuum gap in the bulk case). Hence, vac 0 represents a rectangular bulk supercell. Note that an even number of layers is required to avoid a stacking fault in the bulk limit.

For this dataset only, we avoid the standard definition of vacuum gap as the separation between surface layers. Instead we take the separation between layers in the bulk as the zero of the vacuum gap. This makes it easier to compare with a rectangular bulk cell, demonstrating direct correspondence with the behavior in the bulk. This comparison requires models that contain an even number of layers, in order to avoid the formation of a stacking fault in the model.

As demonstrated by the Koopmans' errors in Fig. 9.8, increasing the size of the vacuum gap appears to increase the errors described by E_{PBC} . This kind of divergent behavior was already reported by Komsa *et. al.* [89] in the context of charged defects, although it appears defects are not required to see the behavior.

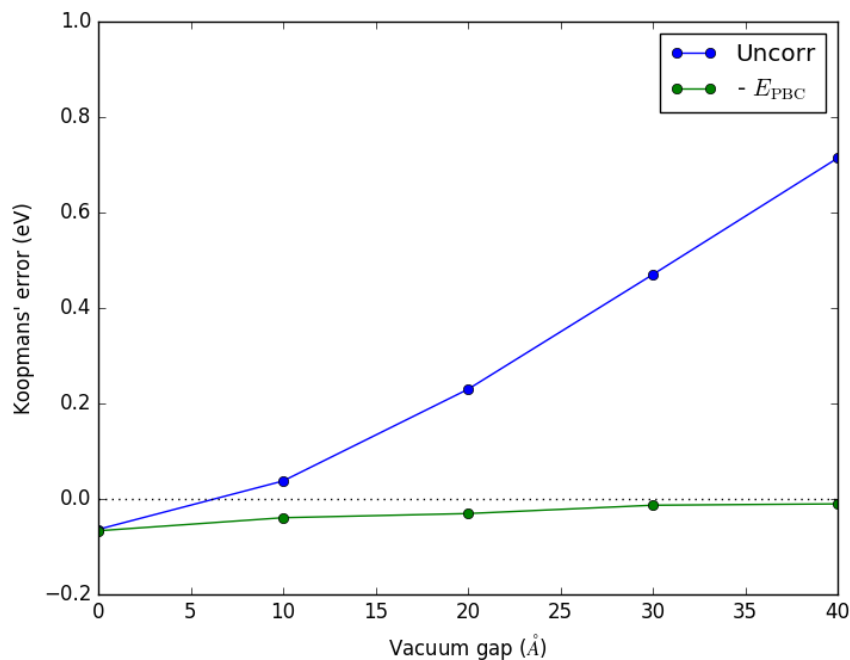


Figure 9.8: Dependence of the calculated Koopmans' error on the size of the vacuum gap. Uncorrected results (blue line) are contrasted with a periodic correction, E_{PBC} (green line).

9.3.3 Workfunction dependence on cubic volume

Our bulk calculations already suggested the surprising result that image interactions are almost negligible for cubic bulk cells. Additionally, the results above show larger errors are introduced when the vacuum gap is increased and the elongation of the cell is enhanced. For these reasons, we considered cubic surface models as well. These cubic models are shown in Fig. 9.9. A three layer model was employed for these calculations, as the data in Fig. 9.6 appeared to suggest this was sufficient to qualitatively reproduce the surface case.

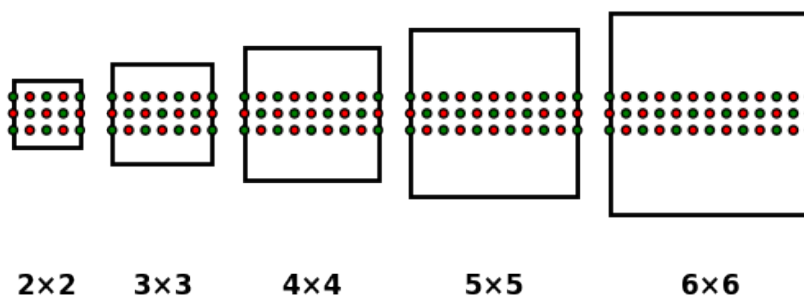


Figure 9.9: Example surface unit cells in the cubic data set. A three layer system is considered in supercells of various sizes, which are always constructed to be cubic. The size of the surface net and the size of the vacuum region increase in lockstep. Observe that this produces vacuum gaps that are smaller than would normally be considered acceptable in the literature.

The calculated workfunctions for these cubic surface systems are shown in Fig. 9.10. In this example, the two approaches produce more similar results. Additionally, the error does not seem to increase as the size of the vacuum region increases. This demonstrates that it is not a large vacuum gap itself that leads to a large divergence between the two methods, but instead elongating the cell and accompanying jellium background.

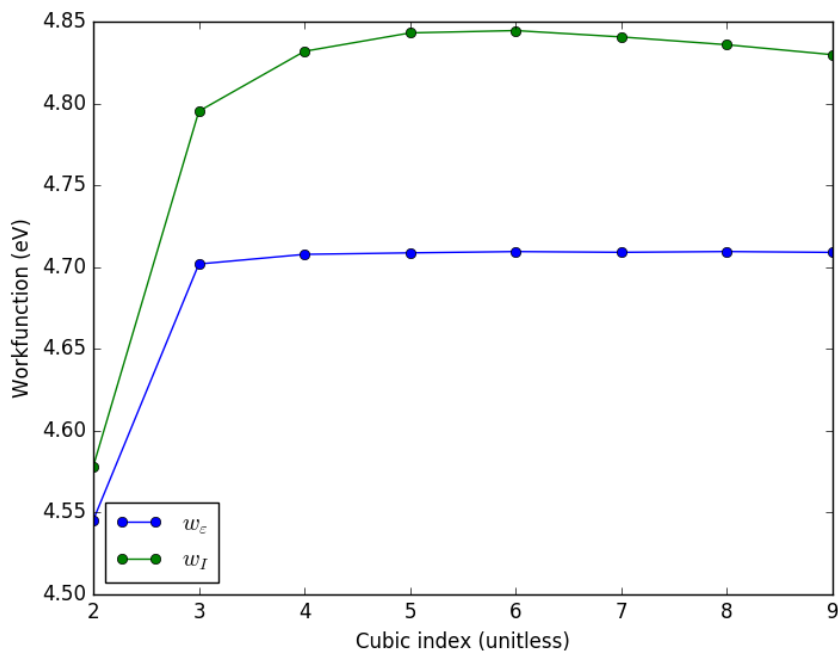


Figure 9.10: Calculated workfunctions following the definitions given in Eqs. 9.3 and 9.4. The eigenvalue definition shows very little finite-size dependence, and the total energy definition is mildly concave. The two methods differ in the calculated value of the workfunction by ~ 0.1 eV.

The resultant error to obey Koopmans' condition is shown in Fig. 9.11. Again, application of an E_{PBC} correction is successfully able to reduce the majority of the supercell size dependence. This demonstrates the electrostatic origin of the observed errors. Although the Koopmans' error has a complex dependence on the size of the supercell model, it is observed that the quality of the corrected data improves with supercell size.

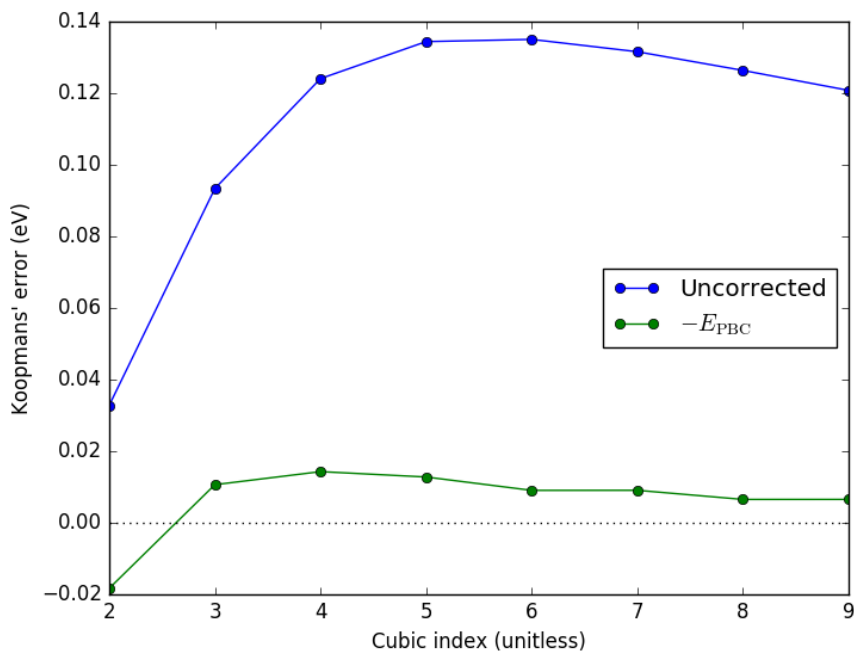


Figure 9.11: Koopmans' errors, as defined in Eq. 9.5, for the cubic dataset. Addition of a E_{PBC} correction to the numerical ionization removes the majority of the observed Koopmans' error. Equally, the observed Koopmans' errors are small in comparison to the calculations performed with a large vacuum gap ($> 15 \text{ \AA}$).

The calculated electrostatic corrections for this system are shown in Fig. 9.12. It is clear that the required E_{PBC} corrections are significantly smaller for cubic supercells than for rectangular supercells (contrast the large corrections required in Fig. 9.8). The electrostatic corrections calculated are not straightforward, and are defined by the cell size, controlling the density of the neutralizing jellium background, along with where the DFT calculation chooses to remove electronic density upon the removal of an electron.

9.3. KT FOR IONIZATION OF SURFACES

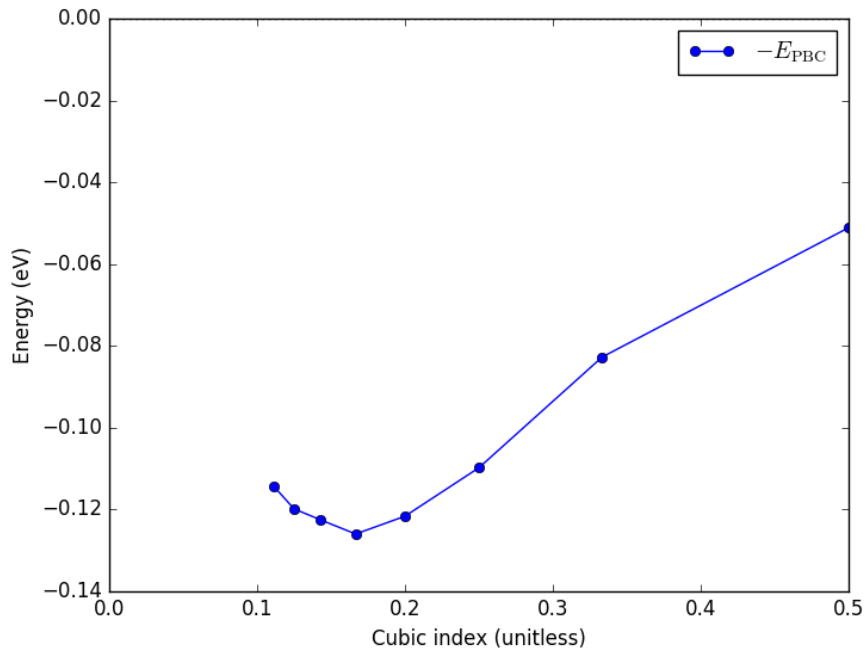


Figure 9.12: Calculated electrostatic corrections with respect to inverse supercell size. The form of the curve is quite complex, and does not demonstrate a systematic improvement. The requirement that the correction term tends to zero as $L \rightarrow \infty$ suggests that the correction drops off quite rapidly for larger models.

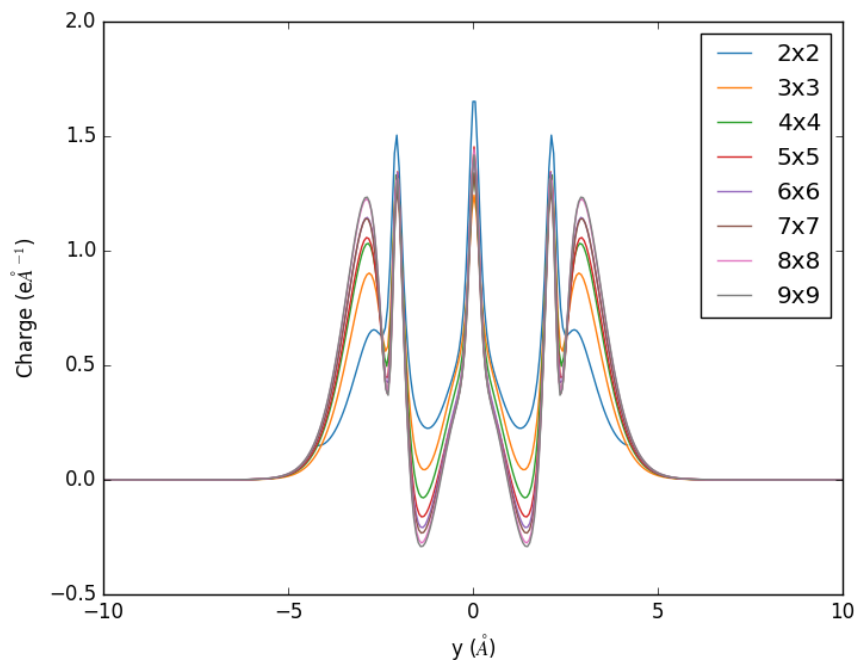


Figure 9.13: Observed changes in the electronic density as electrons are removed from the cubic slab models, averaged along the y -axis (the surface normal). The three layers of the slab are clearly visible, and as the size of the box is increased, the total amount of charge placed on the surfaces increases.

One ingredient of the complex behavior observed in Fig 9.12 is how the density change upon removal of an electron depends on the size of the surface net (and hence supercell shape), as shown in Fig. 9.13. There is a systematic trend of placing more charge on the surfaces as the size of the model increases. This could be justified using the argument that too small a surface causes the surface charge to be concentrated, giving it a higher interaction with itself. This would lead to an interaction that systematically decreases as the supercell is made larger.

We note that cubic supercells are essentially never used in surface calculations, due to a widespread belief that a larger vacuum region is beneficial. This is undoubtedly the case for neutral calculations, but our results suggest that this in fact a very poor choice for surface ionization problems. Whether this is the case for defect calculations remains to be demonstrated.

For the workfunction calculations considered above, we are well served by the

following approximation (where the definition of Δ_{KE} was given in Eq. 9.5),

$$\Delta_{KE} \approx -E_{\text{PBC}}, \quad (9.6)$$

namely that the electrostatics is incorrect for a DFT supercell containing net charge, and that all extra Hartree interactions present in the charged cell should be removed in order to produce Koopmans' compliance. This is the case because both the density of the jellium background and the surface state being deoccupied tend to zero as the volume of the simulation cell increases, so any non-zero interaction between these densities can be directly interpreted as a finite-size error.

The work presented in this chapter so far clearly demonstrates that the removal of electrons from ideal surfaces using an approach based on DFT total energies introduces important errors that are suppressed for bulk ionization energy calculations. This raises a warning that the dominant source of error for charged surface defect calculations might differ in an analogous way.

9.4 KT for charged defects in the bulk

As shown in Fig. 9.14, significant Koopmans' errors are calculated when an electron is removed from a localized defect state, even when a cubic geometry is maintained.

In general, large Koopmans' errors are anticipated in this case, due to failures of approximate density functionals to well describe self interaction errors on well localized states like defect orbitals [154, 155, 86].

It can be seen in Fig. 9.14 that a Koopmans' error of over an electron volt is expected even if an infinite supercell model was utilized. Additionally, the Koopmans' error displays a strong finite-size dependence. There is some error cancellation between these two components, leading to smaller observed Koopmans' errors for smaller supercells.

It is constructive to split the Koopmans' error into a size-independent part and a size-dependant part, yielding,

$$\Delta_{KE}(L) = \Delta_{KE}^{\infty} + \Delta'_{KE}(L), \quad (9.7)$$

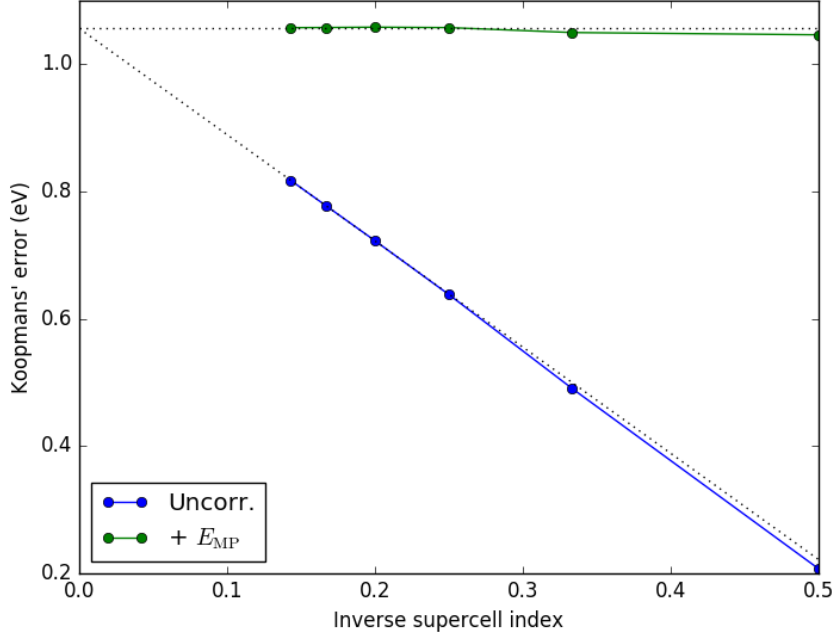


Figure 9.14: Finite-size dependence of the calculated Koopmans' errors for removal of an electron from an F-center in a bulk MgO supercell. The observed finite-size dependence appears to be dominated by a L^{-1} term. The total error increases with supercell size, saturating at a value of 1.06 eV. Additionally, the Makov-Payne correction well approximates the observed finite-size dependence (the low dielectric of this example yields $f \approx 1$).

where $\Delta_{\text{KE}}^{\infty}$ is the Koopmans' error of an infinite supercell, and Δ'_{KE} is a finite-size dependant component of the Koopmans' error.

Then, for this example it is observed that,

$$\Delta'_{\text{KE}}(L) \approx E_{\text{corr}}, \quad (9.8)$$

i.e. that the same finite-size correction required for the formation energy is also observed in the failure to obey Koopmans' condition. The remaining $\Delta_{\text{KE}}^{\infty}$ component is not a finite-size effect, and hence must be interpreted as a failure of the PBE functional employed. A further discussion of the functional dependence of these errors is deferred to the future work section.

9.5 Applying linear extrapolation to surfaces

Returning to the problem of surfaces, we considered if linear extrapolation can be used to infer corrections for surface systems, where there is less confidence in the performance of available correction methods. To this end, a set of models of MgO slabs containing a F^+ defect were constructed, where the number of bulk layers is varied, as shown in Fig 9.4. The objective of this test is to recover the bulk formation energies, as the number of layers in the employed model approaches infinity. This is a robust test of the consistency of the calculations, given that the accuracy of both bulk and surface problems remains difficult to directly demonstrate. The calculations in this section have suggested that the large errors often reported in the literature on surface defects could in part be due to not using cubic cells, as would be done in the equivalent bulk calculations.

The Komsa-Pasquarello (KP)[89] correction is also applied to the calculated formation energies. This is the extension of the MP correction to surfaces.

First, we considered a defect in the monolayer system. In this case, when using the PBE functional, the unoccupied defect state is resonant with the surface VBM. This prevents the formation of a well localised defect. As a result, the F^+ centre does not appear to be stable in a monolayer of MgO. It is excluded from the following results.

Next, a three layer system was considered, with an F-centre at the centre of the middle layer. The observed finite-size dependence of the formation energies is shown in Fig. 9.15.

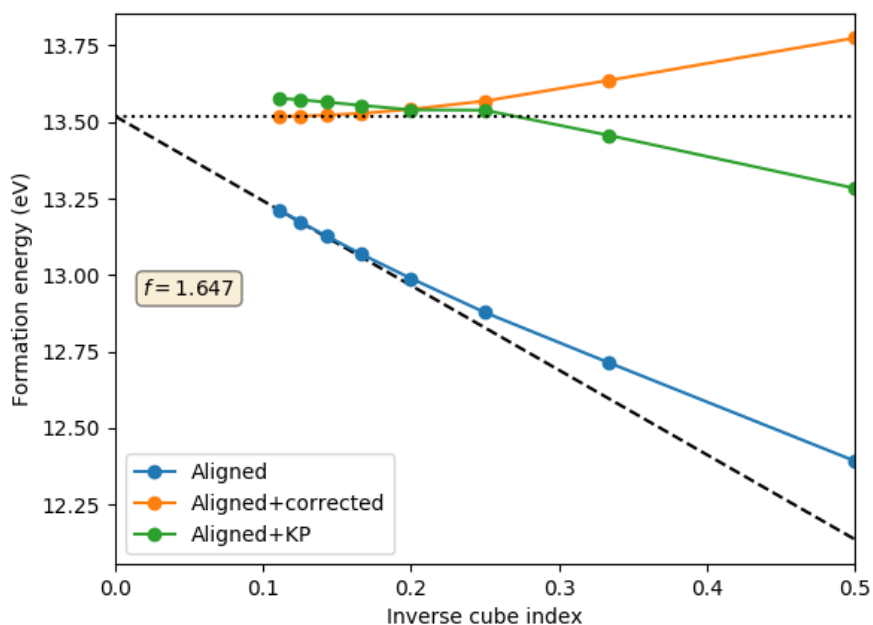


Figure 9.15: Dependence of the formation energy on size of the cubic model employed for a trilayer of MgO. Data is shown only with AB potential alignment (blue line), both with potential alignment and the addition of a fE_{MP} correction (green line), and finally with both AB alignment and the Komsa *et al.* electrostatic correction (orange line). The behavior appears to become linear once large enough cells are considered, and a fit of the Makov-Payne correction to the best two cells yields the shown fit, along with a value of $f = 1.65$, showing enhancement of the finite-size error with respect to the bulk case.

The data for the pentalayer system, shown in Fig. 9.16, shows the same trend of tending to a linear error as the size of the supercells is increased.

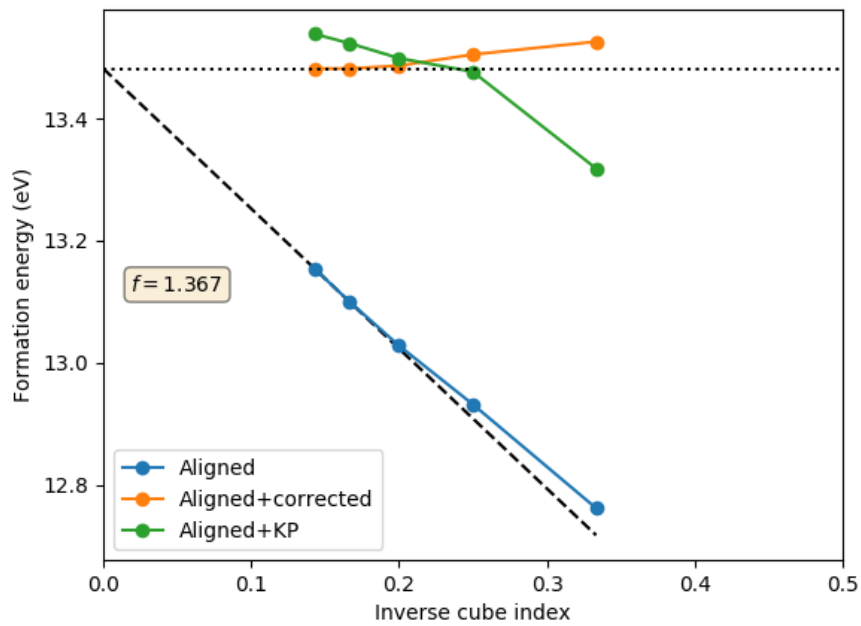


Figure 9.16: Dependence of the formation energy on size of the cubic model employed for a pentalayer of MgO. Same notation as Fig. 9.15. Linear behaviour is achieved significantly more rapidly than in the trilayer case in Fig. 9.15, but the implied correction is not as large.

Similar behavior is also observed for the heptalayer, as demonstrated in Fig. 9.17.

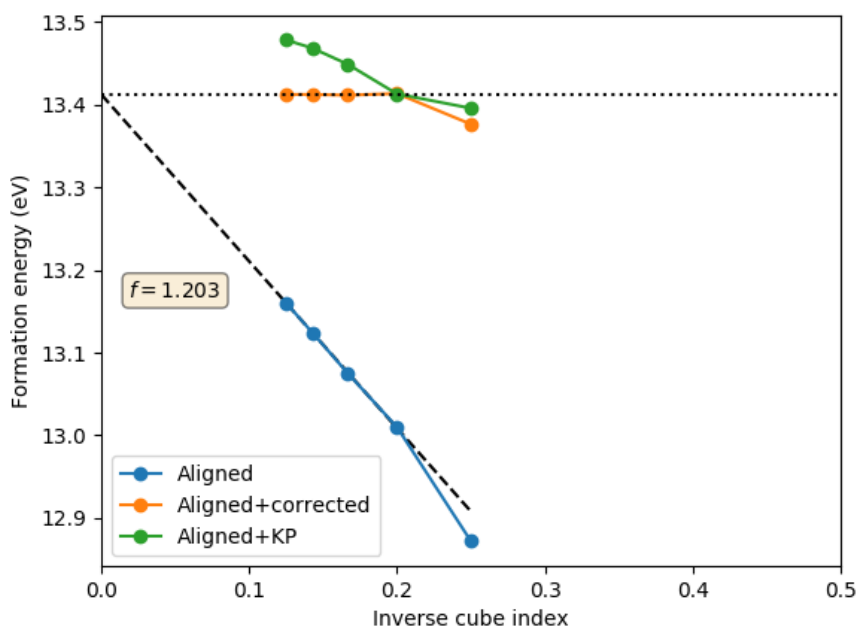


Figure 9.17: Dependence of the formation energy on size of the cubic model employed for a heptalayer of MgO. Same notation as Fig. 9.15. Again, linear scaling is quickly achieved, with a further reduction in the value of f calculated.

Across the considered examples, the KP method is reasonably successful in absolute terms. However, the method is less reliable for larger cells. As a result, trying to extrapolate the corrected values to the limit of an infinite supercell would give quite a poor result. The method appears to be more successful for the thinner slab models.

To make a comparison, all the surface formation energies need to be referenced to a common energy scale. The bulk calculations have been referenced to the energy of the valence band maximum, ϵ_{VBM} , whereas the surface calculations have all been referenced to the vacuum potential. The simplest way to solve this problem is to work out what potential relative to the vacuum the average potential within a crystal of MgO represents.

To do this, the average potential within an MgO slab was compared with the value of the vacuum potential. An example of this is shown in Fig. 9.18, for the example of an $8 \times 8 \times 8$ cubic supercell of the heptalayer system. A Gaussian smoothing is applied to the electrostatic potential. Then, the value of the smoothed function in

the middle of the slab is taken as the inferred value of the average potential in the bulk.

When calculating this potential, it is important that enough MgO layers are included to reproduce the bulk system. In this case, the potential is already well converged for a trilayer.

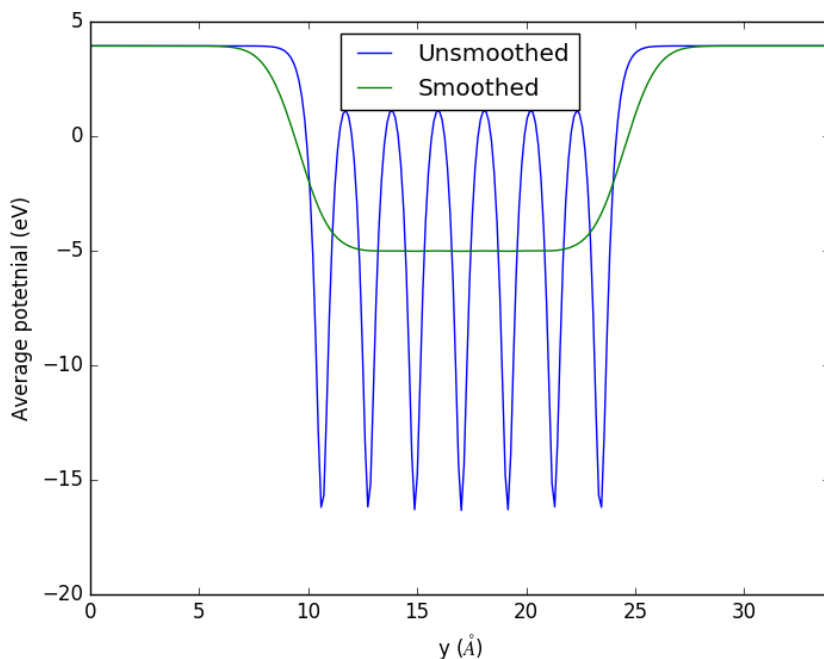


Figure 9.18: Average electrostatic potential (blue line) along the y -axis, for a $8 \times 8 \times 8$ cubic supercell containing a heptalayer of MgO. A smoothed electrostatic potential (green line) is also shown. The average value of the potential within the MgO system is inferred as the difference between the smoothed potential in the middle of the vacuum gap and in the middle of the slab model.

Once this potential referencing has been completed, the defect formation energies between the bulk and slab systems can be directly compared. This comparison is shown in Fig. 9.19.

As would be expected, the formation energy of the electrically neutral F^0 center quickly reproduces its bulk value, as the number of layers in the model is increased. This is the same behavior we want to achieve with the charged F^+ center.

The suggested approach is able to restore this property to the formation energies of the F^+ center too. This shows that we have a consistent description of the

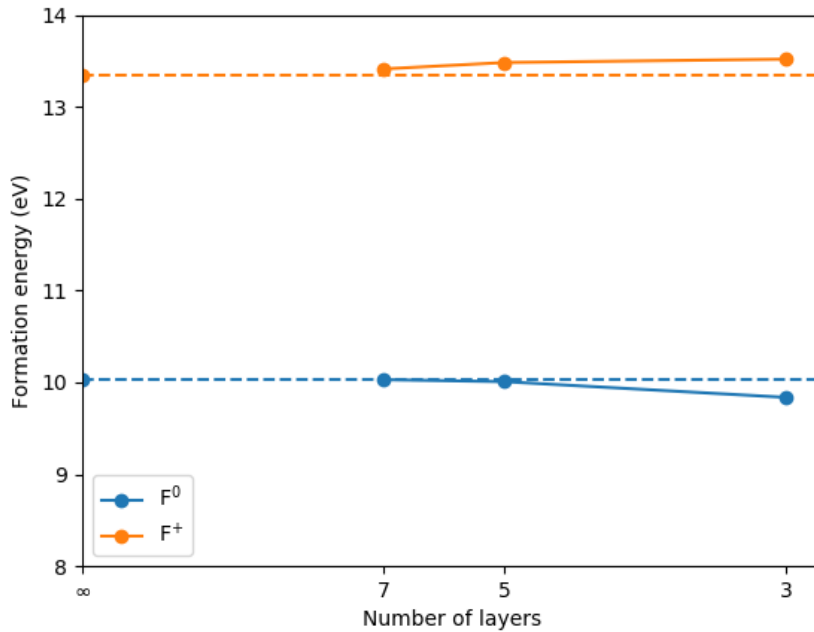


Figure 9.19: Comparison between formation energies calculated in the bulk, and for layered systems. The dashed lines and squares show the formation energies calculated in the bulk. The round markers show the formation energies calculated for the layered systems. The charged formation energies shown have been corrected with AB potential alignment, and with MP electrostatic corrections, that have been scaled based on a linear fit of f based on the two largest cubic supercells considered. Both the uncorrected formation energies for the F^0 and the corrected values for the F^+ center converge to the bulk values as the number of layers in the model is increased. The formation energies for the charged defects are referenced to the vacuum level, rather than the more typical ϵ_{VBM} .

problem.

The layered systems require larger corrections than bulk systems of the same size would. Equally, as the number of layers in the model is increased, the magnitude of the electrostatic corrections decreases. These observations could be simply justified in terms of intra-supercell interaction with the neutralizing jellium background. The jellium background interacts most strongly with charge placed at the center of the cell. Hence, the corrections are larger the closer the surface bound charge in the models is to the center of the supercell. As the number of layers is increased, the surfaces are moved away from the center of the cell, and the unwanted interactions are reduced. In all cases, the bound charge is constrained by the surface

to sit nearer to the center of the cell than would be the case in bulk calculations.

Although further work is needed, these results suggest that the linear approximation utilized to understand bulk defects can still be applied to surfaces. An important requirement of this is that cubic cells are used, in order to avoid large electrostatic interactions with image cells.

Conclusions: Calculating the ionization energies of surface slabs demonstrates that cubic cells show reduced errors to obey KT, and that the observed errors are electrostatic in origin. Considering charged defects, the size-dependant error to obey KT is well approximated by the required correction for the formation energy, when the potential alignment term is neglected. The linear extrapolation method introduced for charged defects in bulk supercells in Chapter 8 can be reliably applied to surface slab models too, when cubic supercells are employed. These calculations demonstrate that the surface Komsa-Pasquarello correction method is effective, but that it does not display systematic improvement with supercell size. The internal consistency of the bulk and surface correction methods developed in this thesis is demonstrated using the example of oxygen vacancies in MgO.

Chapter 10

Conclusions

10.1 General Conclusions

I have considered the finite-size dependence observed in the defect formation energies of point defects with net electrostatic charge for a diverse range of defects and materials. Both the traditional bulk case and the more complex surface case have been considered. Several general rules describe these calculations.

Firstly, an approximately volume dependent error term is introduced through the introduction of a potential alignment error whenever the number of atoms in a supercell is modified. These errors are present in typical charged defect calculations, due to the exchange of atoms with an external reservoir. It was discovered that this potential shift can be approximated using only the atomic radius of the atoms being exchanged. However, this relationship is approximate, as atomic alignment shifts are observed to be very sensitive to the exact pseudopotential employed, meaning that reference calculations are required to understand the magnitude of these errors for a specific example. This new argument in practice provides strong agreement with what is sometimes termed the traditional approach to potential alignment, allowing the source of these errors to be more clearly understood. This source of error appears to change little between bulk and surface calculations.

In order to better understand the defect electrostatics of charged defects, a new correction method was constructed based on electrostatic charge differences, and the DEFECT_SOLVER code was developed to evaluate this correction. This method

10.1. GENERAL CONCLUSIONS

produced results similar to the known Lany-Zunger method, but also allowed calculation of a corrective potential. The correspondence of this electrostatic potential with part of the observed potential alignment within DFT demonstrated that this part of the potential shift present in DFT calculations is introduced by defect electrostatics. It also demonstrated that the FNV method uses only a poor approximation of this difference. Surprisingly, these calculations also predicted that the inter-supercell interactions present in the DFT supercells were almost zero, enabling corrections to be constructed under isolated boundary conditions.

Following on from these calculations, the defect density was analyzed in detail and was in strong agreement with the predictions of classical electrostatics. As well as charge associated with the defect state and a jellium background, a predictable bound charge was also present in the cells. This new understanding of the supercell dependant density response, in combination with the observed minor role played by inter-supercell interactions, was used in order to derive an electrostatic correction from first principles.

Unexpectedly, this derivation suggested that electrostatic corrections should be substantively smaller than present methods predict. The resolution of this seeming paradox was suggested to be the key role that exchange-correlation plays in the observed finite-size dependence. However, as this is not well understood presently, this introduces a strong disconnect between the derivations of present correction methods and the finite-size dependence actually observed in practical calculations. Simple models failed to predict this term accurately.

In spite of these complexities, it was observed that once both potential alignment and \mathbf{k} -point convergence has been satisfactorily performed, that the remaining finite-size error for cubic supercells is well predicted by a linear term. This term looks like a scaled Makov-Payne correction. For almost all of the considered bulk examples, the MP correction was an overestimate. Two new linear fits to the results were constructed. For unreleased defects, the MP correction was a slight overestimate. For relaxed defects, the errors swapped from LZ-like to MP-like as the dielectric constant was increased.

Similar calculations were carried out for surface slab models, where there is additional freedom in selecting the size of the vacuum region. Surface ionization calculations were carried out first, where the use of generalized Koopmans' theorem suggested that large vacuum regions introduced large unwanted interactions, due to a dilution of the jellium background. This suggested that the convergence problems normally reported for surface defects are due to the lack of a cubic supercell, rather than being intrinsic to the surface problem. Most of the cases still showed linear electrostatic errors, but they were typically enhanced with respect to the bulk case.

Taken together, these advances allow progress towards the consistent calculation of charged defect formation energies both in the bulk and in surfaces. This was demonstrated using the F-centre in MgO as an example, where it was possible to recover the bulk surface formation energies from slab model calculations.

The main limitations of the above studies was the use of local functionals, combined with a focus on unrelaxed defects. Even with these simplifications of the problem, modifications to existing methods were still required in order to understand the results. Further work is required to extend the developed arguments to more challenging cases. Initial calculations suggest that the use of hybrid functionals does slightly alter the observed finite-size dependence, beyond those changes introduced by modification of the dielectric constant. Present analytic correction methods are typically justified as electrostatic errors, so do not incorporate any functional dependence.

10.2 Avenues for future work

In this section, I discuss the most promising avenues for future work arising from the results presented in this thesis. Firstly, I consider the role hybrid functionals play in the finite size behavior demonstrated for charged defects in the bulk. It appears that further work is required to understand this, with the possibility that different exchange correlation functions produce finite-size errors that scale differently with the size of the model considered. Secondly, I discuss the neglect of atomic relax-

ation in our results on surface charged defects. Finally, for surface defects, the alternative use of 2D boundary conditions is discussed.

10.2.1 Hybrid functionals and defect states

It seems likely that a complete understanding of Koopmans' condition for charged defects also requires a resolution of the self-interaction problem present on the defect state. Hybrid functionals provide a tool that is capable of this, in principle. The problem is confused because hybrid functionals are normally calibrated using Koopmans' condition, but as demonstrated in this thesis, failures to obey Koopmans' condition can also be introduced by finite size effects. Great care is required to avoid mixing up these errors.

See reference [156] for an example study where the DFT+U method was parameterized for a defect to remove its Koopmans' error. Such an approach implicitly assumes that XC functional failure rather than finite-size electrostatics introduces Koopmans' error. If there are finite-size errors in such calculations, then they will incorrectly be mixed into the self interaction correction that is constructed.

As demonstrated in Fig. 10.1, modifying the exchange-correlation functional has a significant impact on the finite size dependence. Echoing the results of Sec. 7, setting the exchange-correlation functional to zero significantly reduces the finite-size errors in total energies calculated using cubic cells.

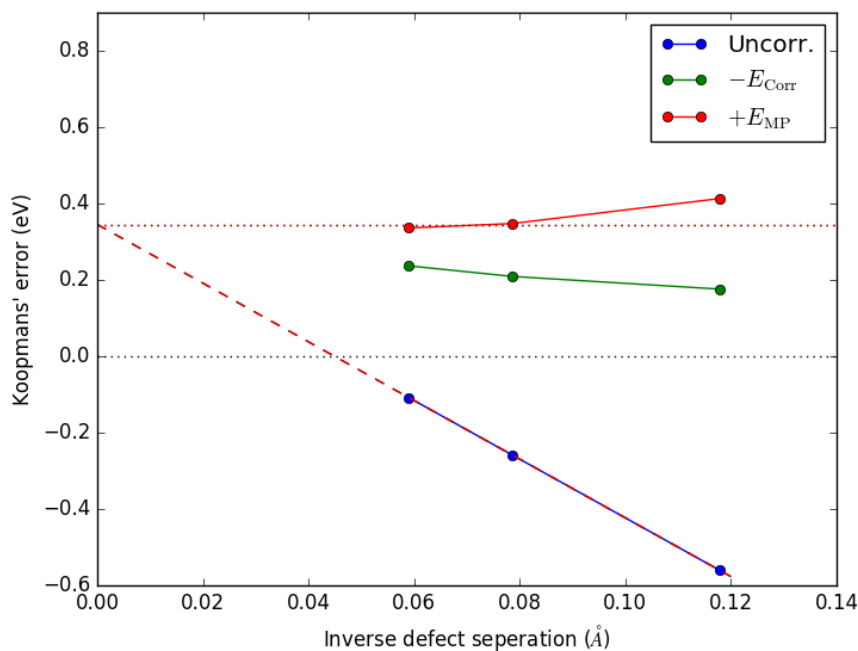


Figure 10.1: Finite-size dependence of the calculated Koopmans' errors for the removal of an electron from the F-centre in a bulk MgO supercell, using the PBE_TC_LRC functional. The observed behavior is qualitatively similar to that seen for the PBE functional in Fig. 9.14, but the limit of the error is significantly reduced. This suggests a improved description of the self interaction error on the state.

In contrast, the differences observed between popular solid state functionals is significantly smaller. This suggests that these functionals interact with the delocalized bound charge and with the jellium in a similar way. This agreement between a diverse range of functionals acts to conceal the result that the strong electrostatic errors present in total energies is introduced by the calculation of E_{xc}

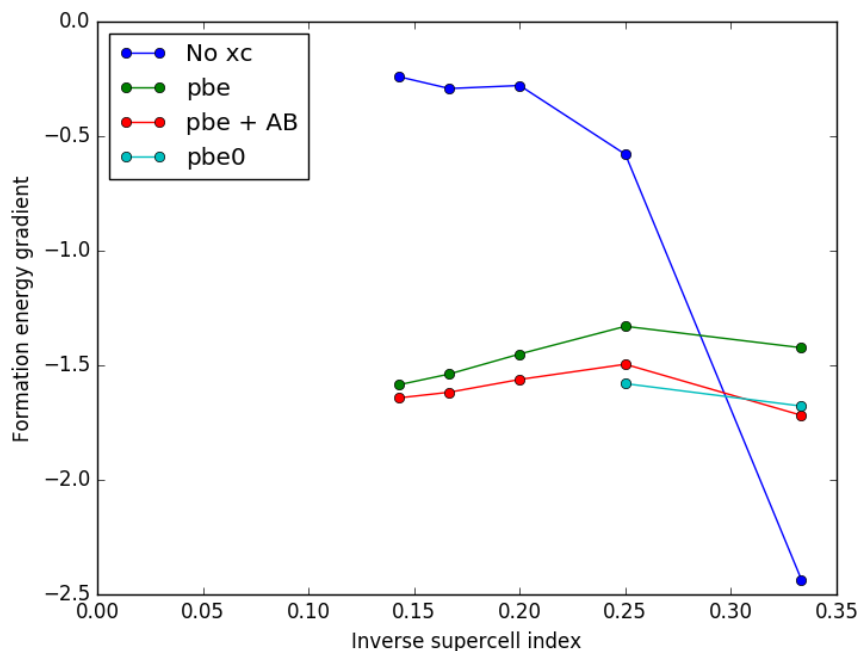


Figure 10.2: Gradient in the formation energy with cubic supercell volume. Calculations without XC demonstrate significantly weaker finite-size dependence than calculations including it. There is a change in finite-size scaling moving from PBE to PBE0, but is significantly smaller. In this case, the use of Fock exchange slightly increases the observed finite-size dependence.

10.2.2 Role of ionic relaxation for surfaces

The surface calculations in Chapter 9 have a significant shortcoming in that ionic relaxation is not included. Further work is required to understand the effects of ionic relaxation for the surface calculations. It seems reasonable that similar behavior will be observed as in Chapter 8 for bulk defects – that the required f -values will be modified, but that approximately inverse linear errors will still be observed. It remains to be demonstrated how successful the Komsa-Pasquarello correction will remain once atomic relaxation is incorporated.

10.2.3 Comparison with 2D boundary conditions

Surface defect formation problems can also be approached using 2D boundary conditions, rather than using periodic electrostatics and jellium backgrounds. Such approaches are based on wavelet solvers, and can be expected to be used more widely in the future. It would clearly be interesting to develop a clearer understanding of

the links between 2D and 3D calculations, in order to understand which approach converges to the limit of an infinite supercell most rapidly. One additional advantage of 2D boundary conditions is the ability to describe defects with dipole moments, which are artificially suppressed in 3D boundary conditions. Corrections for these errors are well known for neutral systems, but significantly less work has been done for systems with net charge.

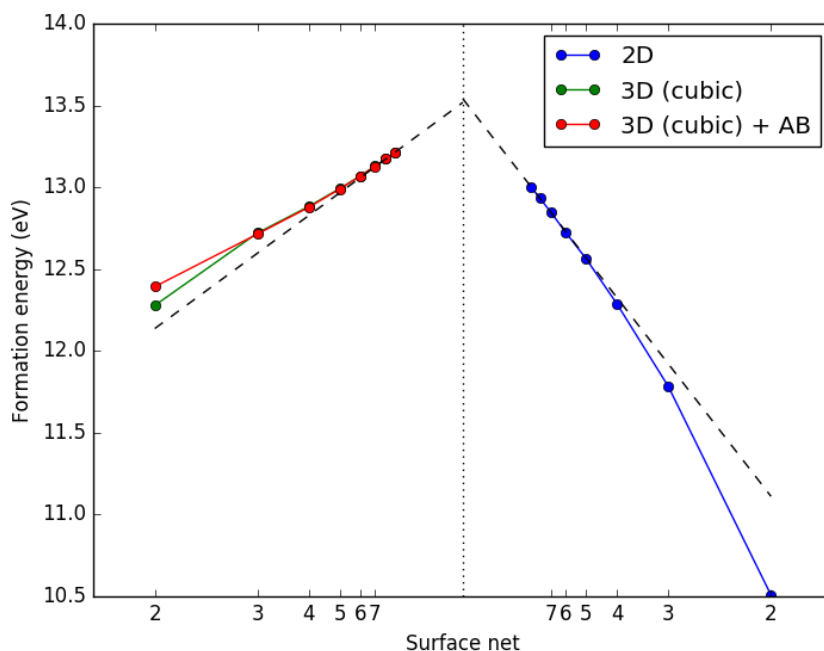


Figure 10.3: Formation energy dependence on supercell shape for an unrelaxed F^+ defect in an MgO trilayer, under two different boundary conditions. On the left, 3D boundary conditions (with ΔV_{AB} alignment) and a cubic supercell are employed. On the right, 2D boundary conditions (an essentially infinite vacuum gap) is utilized. Note that potential alignment is not required in the 2D case, as these calculations are correctly referenced to the vacuum level. A linear fit to the largest three cells is shown for both boundary conditions. The extrapolations approximately agree, but the 2D results have a higher gradient, suggesting that the encountered errors are larger under 2D boundary conditions. Formation energies are referenced to the vacuum level rather than the bulk VBM, and hence are not directly comparable with bulk formation energies.

A comparison between 3D and 2D boundary conditions used to calculate the defect formation energies of a F^+ centre in a trilayer of MgO, without ionic relaxation, is shown in Fig. 10.3. It is observed that both boundary conditions can be used

10.2. AVENUES FOR FUTURE WORK

to extrapolate the same size converged formation energy, although the agreement is not fully unambiguous. It is notable that the errors under 3D boundary conditions (with cubic cells) appear to be smaller.

The 2D case contains no jellium background, and no interactions with image slabs in the vacuum direction. For these reasons, it would be reasonable to expect the method to converge more rapidly. In contrast, the results suggest that the neutralizing jellium background in this case does more good than harm, and should be maintained. This can be understood as the jellium background acting to screen the interactions between the image defects, which strongly interact under 2D boundary conditions.

There is no fundamental reason that a cubic jellium background cannot be incorporated into the 2D boundary conditions case, and it is possible that combining the two methods in this way might produce the best of both worlds – both the electrostatics of 3D boundary conditions, with the beneficial properties of 2D boundary conditions of no interactions across the vacuum region and the possibility of forming a dipole. It would be interesting to look at this in the future.

Bibliography

- [1] Charles Kittel et al. *Introduction to solid state physics*. Wiley New York, 1976.
- [2] Norman Neill Greenwood and Alan Earnshaw. *Chemistry of the Elements*. Elsevier, 1984.
- [3] Wolfgang M Arden. The international technology roadmap for semiconductors—perspectives and challenges for the next 15 years. *Current Opinion in Solid State and Materials Science*, 6(5):371–377, 2002.
- [4] International technology roadmap for semiconductors. Executive report, 2015.
- [5] Mark Z Jacobson. Review of solutions to global warming, air pollution, and energy security. *Energy & Environmental Science*, 2(2):148–173, 2009.
- [6] Augustin Joseph McEvoy, Luis Castaner, and Tom Markvart. *Solar cells: Materials, manufacture and operation*. Academic Press, 2012.
- [7] Peter T. Landsberg. *Recombination in Semiconductors*. Cambridge University Press, 1992.
- [8] We Shockley and WT Read Jr. Statistics of the recombinations of holes and electrons. *Physical review*, 87(5):835, 1952.
- [9] Re N Hall. Electron-hole recombination in germanium. *Physical review*, 87(2):387, 1952.

Bibliography

- [10] Arvind Shah, Pedro Torres, Reto Tscharner, Nicolas Wyrsh, and Herbert Keppner. Photovoltaic technology: The case for thin-film solar cells. *science*, 285(5428):692–698, 1999.
- [11] Neil W Ashcroft and N David Mermin. *Solid state physics*. Holt-Saunders, 1976.
- [12] FA Kröger and HJ Vink. Relations between the concentrations of imperfections in crystalline solids. In *Solid state physics*, volume 3, pages 307–435. Elsevier, 1956.
- [13] DTJ Hurle. Charged native point defects in GaAs and other iii–v compounds. *Journal of crystal growth*, 237:1621–1627, 2002.
- [14] Harold Max Rosenberg. *The solid state: an introduction to the physics of crystals for students of physics, materials science and engineering*. Oxford Univ. Press, 1988.
- [15] Christoph Freysoldt, Blazej Grabowski, Tilmann Hickel, Jörg Neugebauer, Georg Kresse, Anderson Janotti, and Chris G. Van de Walle. First-principles calculations for point defects in solids. *Rev. Mod. Phys.*, 86:253–305, Mar 2014.
- [16] Max Born and Robert Oppenheimer. Zur quantentheorie der molekeln. *Annalen der Physik*, 389(20):457–484, 1927.
- [17] Paul Güttinger. Das verhalten von atomen im magnetischen drehfeld. *Zeitschrift für Physik*, 73(3-4):169–184, 1932.
- [18] W Pauli. Principles of wave mechanics. *Handbuch der Physik*, 24:162, 1933.
- [19] Hans Hellmann. *Einführung in die quantenchemie: Texte imprimé*. F. Deuticke, 1937.
- [20] Richard Phillips Feynman. Forces in molecules. *Physical Review*, 56(4):340, 1939.

- [21] Max Born and Kun Huang. *Dynamical theory of crystal lattices*. Clarendon press, 1954.
- [22] S Kais, DR Herschbach, and RD Levine. Dimensional scaling as a symmetry operation. *The Journal of Chemical Physics*, 91(12):7791–7796, 1989.
- [23] Christopher J Cramer. *Essentials of computational chemistry: theories and models*. John Wiley & Sons, 2013.
- [24] C David Sherrill and Henry F Schaefer III. The configuration interaction method: Advances in highly correlated approaches. In *Advances in quantum chemistry*, volume 34, pages 143–269. Elsevier, 1999.
- [25] Chr Møller and Milton S Plesset. Note on an approximation treatment for many-electron systems. *Physical Review*, 46(7):618, 1934.
- [26] Lars Hedin. New method for calculating the one-particle Green’s function with application to the electron-gas problem. *Physical Review*, 139(3A):A796, 1965.
- [27] Wilfried G Aulbur, Lars Jönsson, and John W Wilkins. Quasiparticle calculations in solids. *Solid State Physics*, 54:1–218, 2000.
- [28] Ferdi Aryasetiawan and Olle Gunnarsson. The GW method. *Reports on Progress in Physics*, 61(3):237, 1998.
- [29] Pierre Hohenberg and Walter Kohn. Inhomogeneous electron gas. *Physical review*, 136(3B):B864, 1964.
- [30] Richard M Martin. *Electronic structure: Basic theory and practical methods*. Cambridge university press, 2004.
- [31] Paul P Ewald. Die berechnung optischer und elektrostatischer gitterpotentiale. *Annalen der physik*, 369(3):253–287, 1921.

- [32] David Borwein, Jonathan M Borwein, and Keith F Taylor. Convergence of lattice sums and madelung constant. *Journal of mathematical physics*, 26(11):2999–3009, 1985.
- [33] JS Blakemore. *Solid State Physics*. Saunders, 1974.
- [34] Yu-Ning Wu, X.-G. Zhang, and Sokrates T. Pantelides. Fundamental resolution of difficulties in the theory of charged point defects in semiconductors. *Phys. Rev. Lett.*, 119:105501, Sep 2017.
- [35] Chris G Van de Walle and Richard M Martin. Absolute deformation potentials: Formulation and ab initio calculations for semiconductors. *Physical review letters*, 62(17):2028, 1989.
- [36] John Bardeen. Theory of the work function. II. The surface double layer. *Physical Review*, 49(9):653, 1936.
- [37] Conyers Herring and MH Nichols. Thermionic emission. *Reviews of modern physics*, 21(2):185, 1949.
- [38] Leonard Kleinman. Comment on the average potential of a Wigner solid. *Physical Review B*, 24(12):7412, 1981.
- [39] LN Kantorovich. Elimination of the long-range dipole interaction in calculations with periodic boundary conditions. *Physical Review B*, 60(23):15476, 1999.
- [40] LN Kantorovich and II Tupitsyn. Coulomb potential inside a large finite crystal. *Journal of Physics: Condensed Matter*, 11(32):6159, 1999.
- [41] RA Evarestov and VP Smirnov. Band and localized states in finite and infinite crystals. *Physica status solidi (b)*, 180(2):411–421, 1993.
- [42] Robert A Evarestov. *Quantum chemistry of solids: the LCAO first principles treatment of crystals*, volume 153. Springer Science & Business Media, 2007.

- [43] H. J. Monkhorst and J. D. Pack. Special points for Brillouin-zone integrations. *Phys. Rev. B*, 13:5188–5192, 1976.
- [44] Clas Persson, Yu-Jun Zhao, Stephan Lany, and Alex Zunger. n-type doping of CuInSe_2 and CuGaSe_2 . *Physical Review B*, 72(3):035211, 2005.
- [45] Jihye Shim, Eok-Kyun Lee, Young Joo Lee, and Risto M. Nieminen. Density-functional calculations of defect formation energies using the supercell method: Brillouin-zone sampling. *Phys. Rev. B*, 71:245204, Jun 2005.
- [46] Joost VandeVondele, Matthias Krack, Fawzi Mohamed, Michele Parrinello, Thomas Chassaing, and Jürg Hutter. Quickstep: Fast and accurate density functional calculations using a mixed gaussian and plane waves approach. *Computer Physics Communications*, 167(2):103–128, 2005.
- [47] Jürg Hutter, Marcella Iannuzzi, Florian Schiffmann, and Joost VandeVondele. Cp2k: Atomistic simulations of condensed matter systems. *Wiley Interdisciplinary Reviews: Computational Molecular Science*, 4(1):15–25, 2014.
- [48] John P Perdew and Karla Schmidt. Jacobs ladder of density functional approximations for the exchange-correlation energy. In *AIP Conference Proceedings*, volume 577, pages 1–20. AIP, 2001.
- [49] W. Kohn and L. J. Sham. Self-consistent equations including exchange and correlation effects. *Phys. Rev.*, 140:A1133–A1138, Nov 1965.
- [50] D. M. Ceperley and B. J. Alder. Ground state of the electron gas by a stochastic method. *Phys. Rev. Lett.*, 45:566–569, Aug 1980.
- [51] G. Ortiz and P. Ballone. Correlation energy, structure factor, radial distribution function, and momentum distribution of the spin-polarized uniform electron gas. *Phys. Rev. B*, 50:1391–1405, Jul 1994.

- [52] O. Gunnarsson and B. I. Lundqvist. Exchange and correlation in atoms, molecules, and solids by the spin-density-functional formalism. *Phys. Rev. B*, 13:4274–4298, May 1976.
- [53] John P Perdew, Adrienn Ruzsinszky, Lucian A Constantin, Jianwei Sun, and Gábor I Csonka. Some fundamental issues in ground-state density functional theory: A guide for the perplexed. *Journal of chemical theory and computation*, 5(4):902–908, 2009.
- [54] John P. Perdew, Kieron Burke, and Matthias Ernzerhof. Generalized gradient approximation made simple. *Phys. Rev. Lett.*, 77:3865–3868, Oct 1996.
- [55] Kieron Burke. Perspective on density functional theory. *The Journal of chemical physics*, 136(15):150901, 2012.
- [56] J. P. Perdew, K. Burke, and M. Ernzerhof. Perdew, burke, and ernzerhof reply:. *Phys. Rev. Lett.*, 80:891–891, Jan 1998.
- [57] John P. Perdew, Adrienn Ruzsinszky, Gábor I. Csonka, Oleg A. Vydrov, Gustavo E. Scuseria, Lucian A. Constantin, Xiaolan Zhou, and Kieron Burke. Restoring the density-gradient expansion for exchange in solids and surfaces. *Phys. Rev. Lett.*, 100:136406, Apr 2008.
- [58] Philipp Haas, Fabien Tran, and Peter Blaha. Calculation of the lattice constant of solids with semilocal functionals. *Physical Review B*, 79(8):085104, 2009.
- [59] Axel D Becke. Density-functional thermochemistry. III. The role of exact exchange. *The Journal of chemical physics*, 98(7):5648–5652, 1993.
- [60] Carlo Adamo and Vincenzo Barone. Toward reliable density functional methods without adjustable parameters: The PBE0 model. *The Journal of chemical physics*, 110(13):6158–6170, 1999.

- [61] John P Perdew, Matthias Ernzerhof, and Kieron Burke. Rationale for mixing exact exchange with density functional approximations. *The Journal of chemical physics*, 105(22):9982–9985, 1996.
- [62] Jonathan H. Skone, Marco Govoni, and Giulia Galli. Self-consistent hybrid functional for condensed systems. *Phys. Rev. B*, 89:195112, May 2014.
- [63] G Strinati. Application of the Greens functions method to the study of the optical properties of semiconductors. *La Rivista del Nuovo Cimento (1978-1999)*, 11(12):1–86, 1988.
- [64] Giovanni Onida, Lucia Reining, and Angel Rubio. Electronic excitations: density-functional versus many-body Green’s-function approaches. *Rev. Mod. Phys.*, 74:601–659, Jun 2002.
- [65] Manuel Guidon, Jurg Hutter, and Joost VandeVondele. Auxiliary density matrix methods for Hartree-Fock exchange calculations. *Journal of chemical theory and computation*, 6(8):2348–2364, 2010.
- [66] Manuel Guidon, Jurg Hutter, and Joost VandeVondele. Robust periodic Hartree-Fock exchange for large-scale simulations using gaussian basis sets. *Journal of chemical theory and computation*, 5(11):3010–3021, 2009.
- [67] Tjalling Koopmans. Über die zuordnung von wellenfunktionen und eigenwerten zu den einzelnen elektronen eines atoms. *Physica*, 1(1-6):104–113, 1934.
- [68] C-O Almbladh and Ulf von Barth. Exact results for the charge and spin densities, exchange-correlation potentials, and density-functional eigenvalues. *Phys. Rev. B*, 31(6):3231, 1985.
- [69] Ulrike Salzner and Roi Baer. Koopmans springs to life, 2009.
- [70] MJP Hodgson, JD Ramsden, TR Durrant, and RW Godby. Role of electron localization in density functionals. *Physical Review B*, 90(24):241107, 2014.

- [71] Aron J. Cohen, Paula Mori-Sánchez, and Weitao Yang. Fractional charge perspective on the band gap in density-functional theory. *Phys. Rev. B*, 77:115123, Mar 2008.
- [72] Stefano Baroni, Paolo Giannozzi, and Andrea Testa. Greens-function approach to linear response in solids. *Physical Review Letters*, 58(18):1861, 1987.
- [73] Stefano Baroni, Stefano De Gironcoli, Andrea Dal Corso, and Paolo Giannozzi. Phonons and related crystal properties from density-functional perturbation theory. *Reviews of Modern Physics*, 73(2):515, 2001.
- [74] Keith Refson, Paul R. Tulip, and Stewart J. Clark. Variational density-functional perturbation theory for dielectrics and lattice dynamics. *Phys. Rev. B*, 73:155114, Apr 2006.
- [75] S. B. Zhang and John E. Northrup. Chemical potential dependence of defect formation energies in GaAs: Application to Ga self-diffusion. *Phys. Rev. Lett.*, 67:2339–2342, Oct 1991.
- [76] C. W. M. Castleton, A. Höglund, and S. Mirbt. Managing the supercell approximation for charged defects in semiconductors: Finite-size scaling, charge correction factors, the band-gap problem, and the ab initio dielectric constant. *Phys. Rev. B*, 73:035215, Jan 2006.
- [77] Jihye Shim, Eok-Kyun Lee, Y. J. Lee, and R. M. Nieminen. Density-functional calculations of defect formation energies using supercell methods: Defects in diamond. *Phys. Rev. B*, 71:035206, Jan 2005.
- [78] Samuel E. Taylor and Fabien Bruneval. Understanding and correcting the spurious interactions in charged supercells. *Phys. Rev. B*, 84:075155, Aug 2011.

- [79] Hannu-Pekka Komsa, Tapio T. Rantala, and Alfredo Pasquarello. Finite-size supercell correction schemes for charged defect calculations. *Phys. Rev. B*, 86:045112, Jul 2012.
- [80] Stephan Lany and Alex Zunger. Assessment of correction methods for the band-gap problem and for finite-size effects in supercell defect calculations: Case studies for ZnO and GaAs. *Phys. Rev. B*, 78:235104, Dec 2008.
- [81] Yu Kumagai and Fumiyasu Oba. Electrostatics-based finite-size corrections for first-principles point defect calculations. *Phys. Rev. B*, 89:195205, May 2014.
- [82] M Leslie and NJ Gillan. The energy and elastic dipole tensor of defects in ionic crystals calculated by the supercell method. *J. Phys. Condens. Matter*, 18(5):973, 1985.
- [83] G. Makov and M. C. Payne. Periodic boundary conditions in *ab initio* calculations. *Phys. Rev. B*, 51:4014–4022, Feb 1995.
- [84] Samuel T. Murphy and Nicholas D. M. Hine. Anisotropic charge screening and supercell size convergence of defect formation energies. *Phys. Rev. B*, 87:094111, Mar 2013.
- [85] Ismaila Dabo, Boris Kozinsky, Nicholas E. Singh-Miller, and Nicola Marzari. Electrostatics in periodic boundary conditions and real-space corrections. *Phys. Rev. B*, 77:115139, Mar 2008.
- [86] Stephan Lany and Alex Zunger. Accurate prediction of defect properties in density functional supercell calculations. *Model. Simul. Mater. Sci. Eng.*, 17(8):084002, 2009.
- [87] Christoph Freysoldt, Jörg Neugebauer, and Chris G. Van de Walle. Fully *Ab Initio* finite-size corrections for charged-defect supercell calculations. *Phys. Rev. Lett.*, 102:016402, Jan 2009.

- [88] Christoph Freysoldt, Jörg Neugebauer, and Chris G Van de Walle. Electrostatic interactions between charged defects in supercells. *Phys. Status Solidi B*, 248(5):1067–1076, 2011.
- [89] Hannu-Pekka Komsa and Alfredo Pasquarello. Finite-size supercell correction for charged defects at surfaces and interfaces. *Phys. Rev. Lett.*, 110:095505, Feb 2013.
- [90] Lev Kantorovich. *Quantum theory of the solid state: An introduction*, volume 136. Springer Science & Business Media, 2004.
- [91] Lucian Anton et al. computer code DL_MG. the Numerical Algorithms Group Ltd., 2013.
- [92] Lucian Anton, Jacek Dziedzic, Chris-Kriton Skylaris, and Matt Probert. Multigrid solver module for ONETEP, CASTEP and other codes, 2013.
- [93] James C Womack, Lucian Anton, Jacek Dziedzic, Phil J Hasnip, Matt IJ Probert, and Chris-Kriton Skylaris. Dl.mg: A parallel multigrid poisson and poisson–boltzmann solver for electronic structure calculations in vacuum and solution. *Journal of chemical theory and computation*, 14(3):1412–1432, 2018.
- [94] Reuben D Budiardja and Christian Y Cardall. Parallel FFT-based poisson solver for isolated three-dimensional systems. *Computer Physics Communications*, 182(10):2265–2275, 2011.
- [95] Ulrich Trottenberg, Cornelius W Oosterlee, and Anton Schuller. *Multigrid*. Academic press, 2000.
- [96] Matteo Frigo and Steven G Johnson. The design and implementation of fftw3. *Proceedings of the IEEE*, 93(2):216–231, 2005.
- [97] R W Hockney. The potential calculation and some applications. *Methods Comput. Phys.*, 9:136–211, 1970.

- [98] JW Eastwood and DRK Brownrigg. Remarks on the solution of poisson's equation for isolated systems. *Journal of Computational Physics*, 32(1):24–38, 1979.
- [99] JA Maruhn, TA Welton, and CY Wong. Remarks on the numerical solution of poisson's equation for isolated charge distributions. *Journal of Computational Physics*, 20(3):326–335, 1976.
- [100] William H Press, Saul A Teukolsky, William T Vetterling, and Brian P Flannery. Numerical recipes in fortran (cambridge, 1992).
- [101] K Fuchs. A quantum mechanical investigation of the cohesive forces of metallic copper. *Proc. R. Soc. A*, 151(874):585–602, 1935.
- [102] J Ihm, Alex Zunger, and Marvin L Cohen. Momentum-space formalism for the total energy of solids. *J. Phys. C*, 12(21):4409, 1979.
- [103] John P Perdew, Robert G Parr, Mel Levy, and Jose L Balduz Jr. Density-functional theory for fractional particle number: Derivative discontinuities of the energy. *Phys. Rev. Lett.*, 49(23):1691, 1982.
- [104] Roland Gillen and John Robertson. A hybrid density functional view of native vacancies in gallium nitride. *J. Phys. Condens. Matter*, 25(40):405501, 2013.
- [105] Fumiyasu Oba, Shigeto R. Nishitani, Seiji Isotani, Hirohiko Adachi, and Isao Tanaka. Energetics of native defects in ZnO. *J. Appl. Phys.*, 90(2):824–828, 2001.
- [106] D. B. Laks, C. G. Van de Walle, G. F. Neumark, P. E. Blöchl, and S. T. Pantelides. Native defects and self-compensation in ZnSe. *Phys. Rev. B*, 45:10965–10978, May 1992.
- [107] Joost VandeVondele and Juerg Hutter. Gaussian basis sets for accurate calculations on molecular systems in gas and condensed phases. *The Journal of chemical physics*, 127(11):114105, 2007.

- [108] M Krack. Pseudopotentials for H to Kr optimized for gradient-corrected exchange-correlation functionals. *Theoretical Chemistry Accounts: Theory, Computation, and Modeling (Theoretica Chimica Acta)*, 114(1):145–152, 2005.
- [109] Luigi Genovese, Thierry Deutsch, Alexey Neelov, Stefan Goedecker, and Gregory Beylkin. Efficient solution of Poissons equation with free boundary conditions. *The Journal of chemical physics*, 125(7):074105, 2006.
- [110] Luigi Genovese, Thierry Deutsch, and Stefan Goedecker. Efficient and accurate three-dimensional Poisson solver for surface problems. *The Journal of chemical physics*, 127(5):054704, 2007.
- [111] Dulal C Ghosh and Raka Biswas. Theoretical calculation of absolute radii of atoms and ions. Part 1. The atomic radii. *International Journal of Molecular Sciences*, 3(2):87–113, 2002.
- [112] R. F. W. Bader. *Atoms in molecules: A quantum theory*. Oxford university press, 1990.
- [113] Min Yu and Dallas R Trinkle. Accurate and efficient algorithm for Bader charge integration. *The Journal of chemical physics*, 134(6):064111, 2011.
- [114] Edward Sanville, Steven D Kenny, Roger Smith, and Graeme Henkelman. Improved grid-based algorithm for Bader charge allocation. *Journal of computational chemistry*, 28(5):899–908, 2007.
- [115] Graeme Henkelman, Andri Arnaldsson, and Hannes Jónsson. A fast and robust algorithm for Bader decomposition of charge density. *Computational Materials Science*, 36(3):354–360, 2006.
- [116] Lawrence S Pan and Don R Kania. *Diamond: electronic properties and applications*. Springer Science & Business Media, 2013.

Bibliography

- [117] T Yamanaka and S Morimoto. Isotope effect on anharmonic thermal atomic vibration and κ refinement of 12c and 3c diamond. *Acta Crystallographica Section B*, 52(2):232–238, 1996.
- [118] KP ODonnell and X Chen. Temperature dependence of semiconductor band gaps. *Applied physics letters*, 58(25):2924–2926, 1991.
- [119] Landolt-Börnstein New Series. Group iii, vol 17a, ed o madelung, 1982.
- [120] Y Bar-Yam and TD Moustakas. Theory and experiment: defect stabilization of diamond films through multiple-regrowth. *MRS Online Proceedings Library Archive*, 162, 1989.
- [121] Y Bar-Yam and TD Moustakas. Defect-induced stabilization of diamond films. *Nature*, 342(6251):786, 1989.
- [122] Satoshi SASAKI, Kiyoshi FUJINO, and Yoshio TAKÉUCHI. X-ray determination of electron-density distributions in oxides, MgO, MnO, CoO, and NiO, and atomic scattering factors of their constituent atoms. *Proceedings of the Japan Academy, Series B*, 55(2):43–48, 1979.
- [123] Sadao Adachi. *Optical constants of crystalline and amorphous semiconductors: numerical data and graphical information*. Springer Science & Business Media, 1999.
- [124] Orson L Anderson and Paul Glynn. Measurement of compressibility in polycrystalline MgO using the reflectivity method. *Journal of Physics and Chemistry of Solids*, 26(12):1961–1967, 1965.
- [125] Mary Wintersgill, John Fontanella, Carl Andeen, and Donald Schuele. The temperature variation of the dielectric constant of pure CaF₂, SrF₂, BaF₂, and MgO. *Journal of Applied Physics*, 50(12):8259–8261, 1979.
- [126] Chitra Agashe and SS Major. Effect of heavy doping in SnO₂: F films. *Journal of materials science*, 31(11):2965–2969, 1996.

Bibliography

- [127] Werner H Baur and Aijar A Khan. Rutile-type compounds. IV. SiO_2 , GeO_2 and a comparison with other rutile-type structures. *Acta Crystallogr. Sec. B*, 27(11):2133–2139, 1971.
- [128] K Reimann and M Steube. Experimental determination of the electronic band structure of SnO_2 . *Solid State Commun.*, 105(10):649–652, 1998.
- [129] HJ Van Daal. The static dielectric constant of SnO_2 . *Journal of Applied Physics*, 39(9):4467–4469, 1968.
- [130] M Ali Yıldırım, Sümeyra Tuna Yıldırım, Emine Fedakar Sakar, and Aytunç Ateş. Synthesis, characterization and dielectric properties of SnO_2 thin films. *Spectrochimica Acta Part A: Molecular and Biomolecular Spectroscopy*, 133:60–65, 2014.
- [131] S Goldsmith, E Çetinörgü, and RL Boxman. Modeling the optical properties of tin oxide thin films. *Thin Solid Films*, 517(17):5146–5150, 2009.
- [132] John David Jackson. *Classical electrodynamics*. Wiley, 1999.
- [133] Roald K Wangsness. *Electromagnetic fields*. Wiley, 1986.
- [134] Edward M Purcell and David J Morin. *Electricity and magnetism*. Cambridge University Press, 2013.
- [135] LD Landau, JS Bell, MJ Kearsley, LP Pitaevskii, EM Lifshitz, and JB Sykes. *Electrodynamics of continuous media*, volume 8. Elsevier, 2013.
- [136] P. M. Sharp and I. D’Amico. Metric space formulation of quantum mechanical conservation laws. *Phys. Rev. B*, 89:115137, Mar 2014.
- [137] Gerhard Hummer. Electrostatic potential of a homogeneously charged square and cube in two and three dimensions. *Journal of electrostatics*, 36(3):285–291, 1996.

Bibliography

- [138] BRA Nijboer and Th W Ruijgrok. On the energy per particle in three- and two-dimensional Wigner lattices. *Journal of statistical physics*, 53(1-2):361–382, 1988.
- [139] Viktor N Staroverov, Gustavo E Scuseria, Jianmin Tao, and John P Perdew. Erratum: Tests of a ladder of density functionals for bulk solids and surfaces [phys. rev. b 69, 075102 (2004)]. *Physical Review B*, 78(23):239907, 2008.
- [140] Dwight E Gray et al. *American institute of physics handbook*. 1972.
- [141] Victor L Cherginets, Vyacheslav N Baumer, Sergey S Galkin, Lidiya V Glushkova, Tatyana P Rebrova, and Zoya V Shtitelman. Solubility of Al_2O_3 in some chloride- fluoride melts. *Inorganic chemistry*, 45(18):7367–7371, 2006.
- [142] H Ott. Xi. die strukturen von MnO , MnS , AgF , NiS , SnJ_4 , SrCl_2 , BaF_2 ; präzisionsmessungen einiger alkalihalogenide. *Zeitschrift für Kristallographie-Crystalline Materials*, 63(1-6):222–230, 1926.
- [143] Otfried Madelung. *Semiconductors: data handbook*. Springer Science & Business Media, 2012.
- [144] DK Smith. Dk smith and hr leider, j. appl. crystallogr. 1, 246 (1968). *J. Appl. Crystallogr.*, 1:246, 1968.
- [145] Maarten C Verbraeken, Emmanuelle Suard, and John TS Irvine. Structural and electrical properties of calcium and strontium hydrides. *Journal of Materials Chemistry*, 19(18):2766–2770, 2009.
- [146] AJ Dekker. Solid state physics prentice-hall. *Englewoods Cliffs, NJ*, 1957.
- [147] Carl Andeen, John Fontanella, and Donald Schuele. Low-frequency dielectric constant of LiF , NaF , NaCl , NaBr , KCl , and KBr by the method of substitution. *Physical Review B*, 2(12):5068, 1970.

Bibliography

- [148] RP Lowndes and DH Martin. Dielectric dispersion and the structures of ionic lattices. *Proceedings of the Royal Society of London. Series A. Mathematical and Physical Sciences*, 308(1495):473–496, 1969.
- [149] N Veeraiah. Dielectric properties of lif single crystals x-ray irradiated under dc fields. *Journal of materials science*, 22(6):2017–2022, 1987.
- [150] IM Boswarva. Semiempirical calculations of ionic polarizabilities and van der waals potential coefficients for the alkaline-earth chalcogenides. *Physical Review B*, 1(4):1698, 1970.
- [151] MA Subramanian, RD Shannon, BHT Chai, MM Abraham, and MC Wintersgill. Dielectric constants of beo, mgo, and cao using the two-terminal method. *Physics and chemistry of minerals*, 16(8):741–746, 1989.
- [152] George Earl Pynchon and EF Sieckmann. Refractive index of strontium oxide. *Physical Review*, 143(2):595, 1966.
- [153] M Galtier, A Montaner, and G Vidal. Phonons optiques de cao, sro, bao au centre de la zone de brillouin á 300 et 17k. *Journal of physics and chemistry of solids*, 33(12):2295–2302, 1972.
- [154] John P Perdew and Alex Zunger. Self-interaction correction to density-functional approximations for many-electron systems. *Physical Review B*, 23(10):5048, 1981.
- [155] Paula Mori-Sánchez, Aron J Cohen, and Weitao Yang. Many-electron self-interaction error in approximate density functionals, 2006.
- [156] Stephan Lany. Predicting polaronic defect states by means of generalized Koopmans density functional calculations. *Physica status solidi (b)*, 248(5):1052–1060, 2011.